

UNIVERSITY OF CALIFORNIA, SAN DIEGO

Coseismic and Postseismic Deformations Associated With the 1992 Landers,
California, Earthquake Measured by Synthetic Aperture Radar Interferometry

A dissertation submitted in partial satisfaction of the requirements
for the degree of Doctor Of Philosophy in Earth Sciences

by

Evelyn J. Price

Committee in charge:

David T. Sandwell, Chair
James Arnold
Yehuda Bock
J. Bernard Minster
Hubert Staudigel


1999

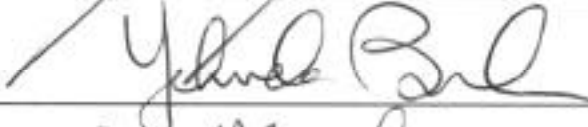
Copyright


Evelyn J. Price, 1999


All rights reserved.


The dissertation of Evelyn Jeanne Price is approved, and it
is acceptable in quality and form for publication on microfilm:











Chair

University of California, San Diego

1999

This dissertation is dedicated to my parents:

Dr. Albert M. Price and Virginia L. Price

"Not everything that I do with my roast chicken is necessarily scientific. Many aspects of my method are based on my feeling and experience. For instance, I *always* give my bird a generous butter massage before I put it in the oven. Why? Because I think the chicken likes it- and, more important, *I* like to give it."

Julia Child

TABLE OF CONTENTS

Signature Page.....	iii
Dedication.....	iv
Epigraph.....	v
Table of Contents.....	vi
List of Figures.....	xii
List of Tables.....	xvi
Acknowledgements.....	xvii
Vita.....	xix
Abstract.....	xxii
Chapter 1. An Introduction to Deformation Studies Using Synthetic Aperture Radar Interferometry and the 1992 Landers, California, Earthquake.....	1
1.1. Synthetic Aperture Radar Interferometry.....	1
1.2. Deformation of Southern California and the Landers Earthquake.....	14
1.3. References.....	20
Chapter 2. Active Microwave Remote Sensing and Synthetic Aperture Radar.....	21
2.1. The Interaction of Electromagnetic Energy With the Earth's Surface.....	21
2.1.1. Electromagnetic Wave Propagation in a Lossless, Source-Free Medium.....	21
2.1.2. Electromagnetic Wave Propagation in a	

Lossy, Source-Free Medium.....	22
2.1.3. Electromagnetic Wave Propagation in a Conducting (High-Loss) Source-Free Medium.....	23
2.1.4. The Reflection Coefficient of Horizontally Polarized Electromagnetic Waves.....	24
2.1.5. The Radar Equation.....	26
2.1.6. Backscatter.....	27
2.1.7. The Relationship Between EM Interactions, SAR Processing, and InSAR algorithms.....	28
2.2. Matched Filter Convolution and Pulse Compression.....	29
2.2.1. The Signal to Noise Ratio.....	30
2.2.2. Matched Filter Design.....	30
2.2.3. The Pulse Compression of a Linear-FM Chirp Radar Return Signal.....	32
2.3. SAR Processing Theory.....	36
2.3.1. The Description of an Imaging Radar.....	36
2.3.2. The Range Resolution of a SLAR.....	38
2.3.3. The Azimuth Resolution of a SLAR.....	40
2.3.4. An Example of SLAR Resolution: ERS-1 and ERS-2 Imaging Radars.....	40
2.3.5. The Range Resolution of Imaging Radars Whose Transmitted Signal is a Linear-FM Chirp.....	40
2.3.6. SAR: Synthesizing the Aperture.....	43
2.4. The Implementation of the SAR Processor.....	50

2.4.1. Loading the Processing Parameters and Data.....	52
2.4.2. Range Compression.....	53
2.4.3. Estimation of the Doppler Centroid Frequency.....	55
2.4.4. Range Migration.....	56
2.4.5. Azimuth Compression.....	59
2.5. References.....	63
Chapter 3. Small-scale deformations associated with the 1992 Landers, California, earthquake mapped by synthetic aperture radar interferometry phase gradients.....	65
(see reprint insert)	
3.1 Introduction.....	
3.1.1. Landers Earthquake Observations.....	
3.1.2. Regional Tectonics.....	
3.1.3. SAR and InSAR.....	
3.1.4. Effects of Propagation Medium on Range Delay.....	
3.2 Data processing.....	
3.2.1 Estimation of Interferometer Baselines from Orbital Knowledge.....	
3.2.2 Interferogram Filtering.....	
3.2.3 Phase Gradient Computation.....	
3.3 Interferogram Interpretation and Transformation of Displacement and Deformation Gradient Into the Satellite Reference Frame.....	

3.4. Results.....	
3.4.1 End of the Main Rupture.....	
3.4.2 Calico Fault and Newberry Fractures.....	
3.4.3 Barstow Aftershock Cluster and Coyote Lake..	
3.5. Discussion.....	
3.6. Conclusions.....	
3.Appendix A. Interferometer Geometry and Equations.....	
3.A1. Range Difference Due to Spheroidal Earth.....	
3.A2. Range Difference Due to Topography on a Spheroidal Earth.....	
3.A3. Range Difference for Topography and Deformation on a Spheroidal Earth.....	
3.A4. Scale Factors for Interferograms Which Have Had the Flat Earth Correction Applied.....	
3.Appendix B. Low-Pass and Gradient Filters.....	
3.Acknowledgements.....	
3.References.....	
Chapter 4. Vertical displacements on the 1992 Landers, California earthquake rupture from InSAR and finite-fault elastic half-space modeling.....	67
4.1. Abstract.....	67
4.2. Introduction.....	68
4.3. Interferometric Method.....	70
4.3.1 Scaling Vertical and Horizontal	

Displacements into the Satellite LOS.....	77
4.4. Data Processing and Reduction.....	81
4.5. Modeling Method.....	89
4.6. Results.....	90
4.6.1. Interferometric Observations.....	90
4.6.2. Forward Modeling Results.....	98
4.6.3. Inverse Modeling Results.....	99
4.6.4. Moment Analysis of the Slip Model.....	104
4.6.5. Resolution Analysis of the Vertical Slip Model.....	105
4.7. Discussion.....	107
4.7.1. A Comparison Between the Field Measured and the Interferometrically Measured Vertical Slip.....	107
4.7.2. Did the Iron Ridge Fault Stop the Rupture?.....	109
4.7.3. A Comparison Between Modeled Vertical Displacements and Modeled Right-lateral Slip.....	111
4.7.4. Interpretation - transient and long-term strain fields.....	112
4.8. Conclusions.....	116
4.9. References.....	118
Chapter 5. Postseismic Deformation Following the 1992 Landers, California Earthquake.....	123

5.1. Introduction.....	123
5.2. Postseismic Deformation Mechanisms.....	126
5.2.1. Deep Afterslip.....	126
5.2.2. Viscoelastic Rebound.....	128
5.2.3. Fault Zone Collapse.....	131
5.2.4. Pore Fluid Pressure Re-equilibration.....	132
5.3. Data Processing and Reduction.....	132
5.4. Modeling Method.....	136
5.5. Results.....	138
5.5.1. Interferometric Observations.....	138
5.5.2. Modeling Results.....	141
5.5.2.1. Slip Models.....	141
5.5.2.2. Forward Predictions.....	144
5.5.2.3. Variance Reduction.....	144
5.5.2.4. Moment Analysis.....	150
5.6. Discussion.....	150
5.6.1. Comparison of LOS Displacements with GPS Horizontal Displacements.....	150
5.6.2. Postseismic Deformation Mechanisms.....	153
5.7. Conclusions.....	154
5.8. References.....	156
Chapter 6. Conclusions.....	159

LIST OF FIGURES

Chapter 1.

Figure 1.1. The locations, types, and data sources of published InSAR surface Change studies.....	2
Figure 1.2. The geometry of a simple interferometer.....	5
Figure 1.3. A SAR system configuration.....	6
Figure 1.4. The ERS SAR receiving stations.....	8-9
Figure 1.5. InSAR geometry.....	10
Figure 1.6. The limitations of InSAR displacement measurements.	13
Figure 1.7. The ERS frames and published studies over S. California	16
Figure 1.8. The InSAR and USGS DEM.....	17

Chapter 2.

Figure 2.1.1. The reflection and transmission of an EM wave.....	25
Figure 2.2.1. The power spectrum of an ERS-like transmitted pulse	34
Figure 2.2.2. The result of matched filtering a Linear FM Chirp.....	35
Figure 2.3.1. The imaging radar geometry.....	36
Figure 2.3.2. The orbital configuration.....	38
Figure 2.3.3. The SLAR geometry.....	39
Figure 2.3.4. The center of an ERS-like transmitted pulse.....	42
Figure 2.3.5. The along-track geometry.....	45
Figure 2.3.6. The lines of constant range and Doppler shift.....	46

Figure 2.3.7. The relative range offset in successive radar pulses....	47
Figure 2.3.8. The power spectrum of the along-track filter.....	49
Figure 2.4.1. The diagram of a SAR processing algorithm.....	51

Chapter 3.

Plate 1. The 60-meter digital elevation model.....	
Plate 2. The coseismic interferogram.....	
Figure 1. Earth and Radar rectangular coordinate systems and rotation matrix.....	
Figure 2. The coseismic phase gradient.....	
Plate 3. An enlargement of the rupture area.....	
Plate 4. An enlargement of the Mojave Valley area.....	
Plate 5. An enlargement of the Coyote Lake and Barstow Cluster area.....	
Figure A1. InSAR geometry. No topography. No displacement....	
Figure A2. The InSAR geometry.....	
Figure B1. Filters.....	

Chapter 4.

Figure 4.1. The ERS-1 and ERS-2 imagery used in this chapter.....	71
Figure 4.2. The coseismic interferogram.....	72-73
Figure 4.3a. The InSAR geometry.....	75
Figure 4.3b. The geometry for projecting horizontal displacements	

into the across-track direction.....	76
Figure 4.4a. The radar LOS displacement scale factor.....	78-79
Figure 4.4b. The horizontal displacement scale factor.....	78-79
Figure 4.5. The synthetic coseismic interferogram.....	82-83
Figure 4.6. The residual LOS displacement.....	84-85
Figure 4.7. The inverse model predictions.....	86-87
Figure 4.8. Across-rupture profiles of displacement and topography	94-95
Figure 4.9. Along-rupture profiles of displacement and topography	96-97
Figure 4.10. The plot of misfit versus roughness.....	100
Figure 4.11. The vertical slip models for various roughness.....	101
Figure 4.12. The vertical and dextral slip models.....	103
Figure 4.13. The resolution analysis.....	106
Figure 4.14. The interpretation and vertical displacement map.....	114-115
Chapter 5.	
Figure 5.1. The SAR imagery used in this study.....	125
Figure 5.2. Postseismic deformation mechanisms.....	127
Figure 5.3a. The 5-215 day interferogram.....	129
Figure 5.3b. The 40-355 day interferogram.....	130
Figure 5.3c. The 355-1253 day interferogram.....	135
Figure 5.4. The model parameterization.....	137
Figure 5.5a. The 5-215 day afterslip model.....	140

Figure 5.5b. The 40-355 day afterslip model.....	142
Figure 5.5c. The 355-1253 day afterslip model.....	143
Figure 5.6a. The 5-215 day model predictions.....	145
Figure 5.6b. The 40-355 day model predictions.....	146
Figure 5.6c. The 355-1253 day model predictions.....	147
Figure 5.7a. The data histograms.....	148
Figure 5.7b. The residual histograms.....	149
Figure 5.8. The data and model profiles along the USGS geodetic array	151

LIST OF TABLES

Chapter 1.

Table 1.1. The civilian SAR satellites used for InSAR studies	4
---	---

Chapter 2.

Table 2.4.1. The SAR processing parameters.....	54-55
---	-------

Chapter 5.

Table 5.1. InSAR pairs considered in this study.....	133
--	-----

ACKNOWLEDGEMENTS

There are many people and organizations that contributed to my experience in graduate school. I'd first like to thank those who contributed directly to the realization of this dissertation. At the top of the list is my advisor and chair of the thesis committee, David Sandwell, who supported my research, acted as an advocate on my behalf, and allowed me relative freedom in the pursuit of new and interesting science during my 6 years of graduate school. Next are two other members of the committee: Yehuda Bock and Bernard Minster. Yehuda's interest in my studies of postseismic deformation was a welcome motivating factor. Bernard's skills as an editor, enthusiasm for the InSAR method, and advice regarding my professional career are much appreciated. I'd also like to recognize the contributions of Hubert Staudigel and James Arnold who asked thought-provoking questions during the qualifying and final exams.

In addition to my committee, there are several people at IGPP who contributed to the scientific quality and defense of this dissertation. Duncan Agnew previewed Chapter 3 before it was sent to the journal and made suggestions that contributed substantially to the manuscript. Hadley Johnson provided the basic framework and impetus for the geodetic inversions performed in Chapters 4 and 5. Karen Scott did an excellent job of formatting Chapter 3 for journal publication. Suzanne Lyons, Lydie Sichoix, and David McMillan listened to a practice version of my oral defense presentation and their constructive criticisms significantly improved its clarity and organization. Finally, I'd like to thank Lydie and Suzanne for being understanding, friendly, and generous computer-lab-mates during my last few months of thesis writing.

Outside of IGPP, a few people contributed substantially to this dissertation. Professor Howard Zebker of Stanford University provided us with versions of computer code for InSAR processing and expressed much interest in our work. One of the main ideas in Chapter 4, to subtract *Wald and Heaton's* dextral slip model from the coseismic interferogram to look for vertical slip on the Landers earthquake rupture, came from Dr. Wayne Thatcher of the U.S. Geological Survey. Professor Roland Bürgmann of the University of California at Berkeley provided the GPS

displacements of *Freymueller et al.*, [1994] and his comments contributed significantly to the quality of Chapter 4.

My entire academic experience at IGPP rode on the inertia created by my first year of classes. I thank the professors who taught those classes for raising my awareness of geophysical methods to a level appropriate for high quality research. I also thank my fellow classmates Greg Anderson, Keith Richards-Dinger, Harm Van Avendonk, and Lois Yu for their comradery and dedication to excellence during that first year and beyond.

Outside of academic pursuits, the enjoyment of my time in graduate school was catalyzed by a number of friends, associates, and organizations. Rob Sohn redefined, for me, the meaning of friendship and proved to be a most capable recreational companion. Vera Schulte-Pelkum paid half the rent and provided the much-needed distractions that galvanized me for the final thesis crunch. Though a recent one, my good friend Chris Small affirmed my tendencies towards individuality and original thought. Two organizations associated with UCSD provided the facilities for an occasional escape from the daily grind. The Mission Bay Aquatic Center made available an array of boats for my sailing pleasure. Fat Baby Glass Works and its staff, especially Sergeant Eva, allowed me to explore my artistic capabilities and fascination with blown glass.

The text of Chapter 3, in part or in full, is a reprint of the material as it appears in *Journal of Geophysical Research*. I was the primary researcher and author and the co-author listed on the publication directed and supervised the research which forms the basis for that chapter. Many of the figures in this dissertation were made using the Generic Mapping Tools (GMT) software provided by *Wessel and Smith*, [1991].

Vita

March 26, 1970	Born, Philadelphia, Pennsylvania
1992	A.B., Princeton University
1992-1993	Lab Assistant, Woods Hole Oceanographic Institution
1993-1999	Research Assistant, Scripps Institution of Oceanography, University of California, San Diego
1999	Ph. D., University of California, San Diego

PUBLICATIONS

- Price, E.J. and D.T. Sandwell, Small-scale deformations associated with the 1992 Landers, California, earthquake mapped by synthetic aperture radar interferometry phase gradients, *J. Geophys. Res.*, *103*, 27001-27016, 1998.
- Sandwell, D.T. and E.J. Price, Phase gradient approach to stacking interferograms, *J. Geophys. Res.*, *103*, 30183-30204, 1998.
- Phipps Morgan, J., W.J. Morgan, and E. Price, Hotspot melting generates both hotspot volcanism and hotspot swell?, *J. Geophys. Res.*, *100*, 8045-8062, 1995.
- Williams, C.A., C. Connors, F.A. Dahlen, E.J. Price, and John Suppe, Effect of the brittle-ductile transition on the topography of compressive mountain belts on Earth and Venus, *J. Geophys. Res.*, *99*, 19947-19974, 1994.

ABSTRACTS

- Price, E.J., SAR interferogram displacement maps constrain depth, magnitude, and duration of postseismic slip on the 1992 Landers, California earthquake rupture, *Eos Trans. AGU*, *80* (17), Spring Meet. Suppl., S77, 1999.
- Price, E.J., and D.T. Sandwell, Postseismic deformation following the 1992 Landers, California, earthquake measured by SAR interferometry, *Eos Trans. AGU*, *79* (45), Fall Meet. Suppl., F36, 1998.

Price, E.J., InSAR observations of spatial deformation anomalies associated with the 1992 Landers, California M 7.3 earthquake, *Eos Trans. AGU*, 78 (45), Fall Meet. Suppl., F157, 1997.

Price, E.J., and D.T. Sandwell, Small, linear displacements directly related to the Landers 1992 earthquake mapped by InSAR, *Eos Trans. AGU*, 77 (46), Fall Meet. Suppl., F50, 1996.

Price, E.J., and D.T. Sandwell, Phase unwrapping of SAR interferograms using an FFT method. Application of the method to prediction of topography, *Eos Trans. AGU*, 76 (46), Fall Meet. Suppl., F64, 1995.

Price, E.J., C. Connors, F. A. Dahlen, J. Suppe, and C. A. Williams, Accretionary wedge mechanics on Venus: A brittle/ductile critical taper model, *23rd Lunar and Planetary Sciences Conference proceedings*, part 3, 1105, 1992.

FIELDS OF STUDY

Major Field: Earth Sciences

Studies in Applied Mathematics
Professors William Young and Glen Ierley

Studies in Geodynamics
Professors Jason Phipps-Morgan and David Sandwell

Studies in the Geology of Convergent Plate Margins
Professors James Hawkins, Paterno Castillo, and Kevin Brown

Studies in Geomagnetism and Paleomagnetism
Professors Robert Parker and Catherine Constable

Studies in Geophysical Data Analysis
Professors Catherine Constable and Duncan Agnew

Studies in Geophysical Inverse Theory
Professor Robert Parker

Studies in Marine Geology and Geophysics
Professors Jason Phipps-Morgan, David Sandwell, John Sclater, and Edward Winterer

Studies in Numerical Methods
Professor Glen Ierley

Studies in the Physics of Earth Materials
Professors Duncan Agnew and Freeman Gilbert

Studies in Satellite Remote Sensing
Professor David Sandwell

Studies in Seismology
Professors Peter Shearer, Freeman Gilbert, Bernard Minster, and John Orcutt

ABSTRACT OF THE DISSERTATION

Coseismic and Postseismic Deformations Associated With the 1992 Landers,
California, Earthquake Measured by Synthetic Aperture Radar Interferometry

by

Evelyn J. Price

Doctor of Philosophy in Earth Sciences

University of California, San Diego, 1999

Professor David T. Sandwell, Chair

This dissertation focuses on using a relatively new technology called Synthetic Aperture Radar Interferometry (InSAR) to measure the displacements of the Earth's surface during the coseismic and postseismic deformation phases of the 1992 Landers, California, earthquake. An introduction to InSAR and its application to movements of the Earth's surface are given in Chapter 1. In Chapter 2, microwave

remote sensing and the range-Doppler Synthetic Aperture Radar (SAR) processing algorithm are discussed. In Chapter 3, the "phase gradient" method is used to map fractures and triggered slip on faults induced by the Landers earthquake. In Chapter 4, we investigate the vertical component of displacement on the Landers earthquake rupture and generate a coseismic vertical displacement map using a combination of InSAR displacement maps and elastic half-space modeling. In Chapter 5, we map displacements of the Earth's surface during the postseismic phase of deformation using InSAR measurements and predict these displacements assuming that the deformation mechanism is after-slip in an elastic half-space. Chapter 6 lists the main conclusions of Chapters 3,4, and 5.

Chapter 1

An Introduction to Deformation Studies Using Synthetic Aperture Radar

Interferometry and the 1992 Landers, California, Earthquake

1.1. SYNTHETIC APERTURE RADAR INTERFEROMETRY

This dissertation focuses on using a relatively new remote sensing technology called "InSAR" to map movements of the Earth's surface caused by the 1992 Landers, California, earthquake. InSAR, an acronym for Interferometric SAR, is a method of combining imagery collected by imaging radar systems on board airplane or satellite platforms to map the elevations, movements, and changes of the Earth's surface. To measure the movements of the Earth's surface, "repeat-pass" InSAR, using imagery collected by satellite-borne radar, is employed. It is called "repeat-pass" because an image of an area taken at one time, the "reference" time, is combined with images taken at other times, the "repeat" times, by the same radar.

The applications of InSAR extend well beyond the study of earthquakes. InSAR detectable movements of the Earth's surface can be due to natural phenomena including earthquakes, volcanoes, glaciers, landslides (Figure 1.1), and salt diapirism; or anthropogenic phenomena including groundwater and petroleum extraction, watering of farms, or underground explosions. InSAR detectable changes in the Earth's surface can be due to fires, floods, forestry operations, moisture changes, vegetation growth, and ground shaking. Hence, applications include mitigation and assessment of natural and man-made hazards and quantification of the impact of human interaction with natural resources.

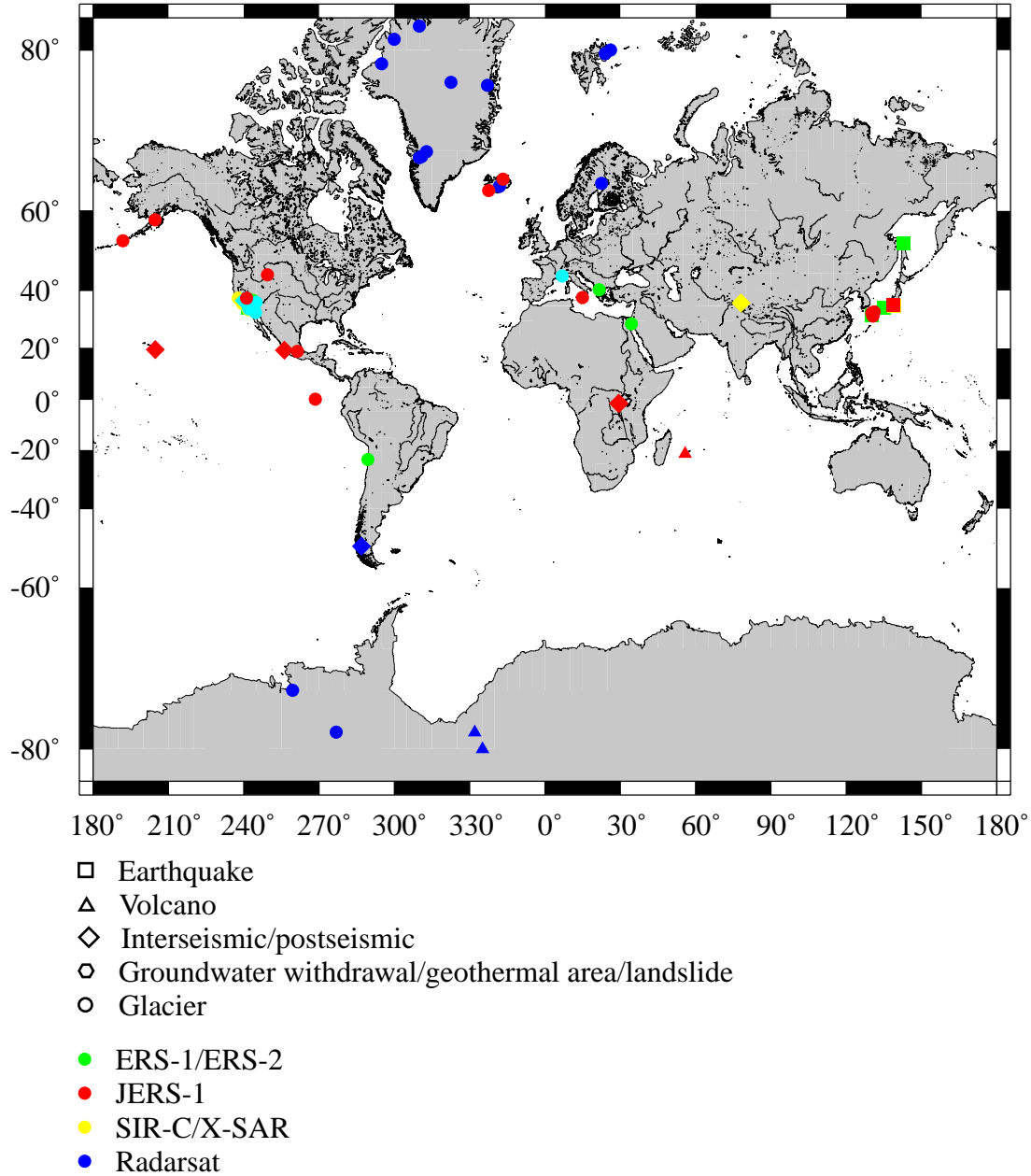


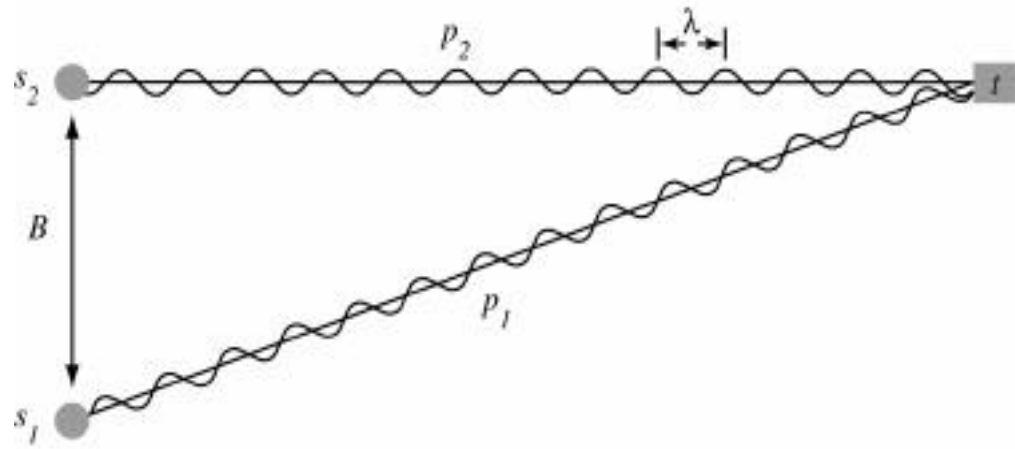
Figure 1.1. The locations, types, and data sources of published InSAR surface change studies.

The first study that demonstrated the usefulness of InSAR for measuring movements of the Earth's surface was published by *Gabriel et al.*, [1989]. They used imagery collected by an L-band radar system aboard the Seasat satellite to detect swelling of the ground due to selective watering of fields in California's Imperial Valley. However, until the publication of the spectacular displacement maps of ground movements caused by the 1992 Landers, California earthquake [*Massonnet et al.*, 1993; *Zebker et al.*, 1994] and ice movements within the Rutford Ice Stream, Antarctica [*Goldstein et al.*, 1993], the method's usefulness as a geodetic tool had gone unrecognized by the geoscience community. Since that time, a multitude of workers have used data from the ERS, JERS, Radarsat, and the Space shuttle's SIR-C/X-SAR radar imaging systems (Table 1.1) to study earthquakes, volcanoes, glaciers, landslides, ground subsidence, and plate boundary deformation (Figure 1.1).

Before discussing how InSAR works, it is illuminating to consider how an interferometer, for example one that might be found in a physics laboratory, measures a distance difference. A basic, two-sensor interferometer is used to measure the difference in the lengths of two paths (Figure 1.2). The interferometer is composed of two electromagnetic field sensors, s_1 and s_2 , separated by a known distance called the baseline B . One path p_1 begins at sensor s_1 and ends at the target t . Another path p_2 begins at sensor s_2 and ends at t . A sinusoidal signal is transmitted by sensor s_1 , reflected off the target, and received at both sensors. This sinusoidal signal has amplitude and phase. If the triangle whose sides are p_1 , p_2 , and B is not isosceles the phases of the reflected signals received back at s_1 and s_2 will be different. The difference in the lengths of p_1 and p_2 can be computed by differencing the phases of the two reflected signals and

Table 1.1. The civilian SAR satellites used for InSAR studies.

Satellite	Agency/Country	Launch Year	Frequency Band (GHz)	Altitude (km)	Repetition Period (days)	Incidence Angle	Swath Width (km)	Resolution (m)
Seasat	NASA/USA	1978	L (1.3)	800	3	23°	100	23
ERS-1	ESA	1991	C (5.3)	785	3, 35, 168	23°	100	25
JERS-1	NASDA/Japan	1992	L (1.2)	565	44	35°	75	30
SIR-C	NASA/USA	1994	X (9.7), C (5.2), L (1.3)	225	variable	15°-55°	15-90	10-200
ERS-2	ASI/Italy ESA	1995	C (5.3)	785	35	23°	100	25
Radarsat	Canada	1995	C (5.3)	792	24	20°-50°	50-500	28



$$\phi = \frac{4\pi}{\lambda} (p_2 - p_1)$$

Figure 1.2. The geometry of a simple interferometer. λ is the wavelength of the signal transmitted by sensor s_1 . The other symbols are described in the text.

multiplying by the wavelength of the sinusoidal signal. The phase difference ϕ is a measure of the path length difference in wavelengths.

As a satellite platform orbits the Earth the imaging radar system on board maps out a swath on the Earth by transmitting and receiving pulses of microwave electromagnetic energy (Figure 1.3). This mapping is repeated after a number of days determined by the orbital characteristics of the satellite (Table 1.1). The radar's antenna is pointed to the side at an angle called the "look angle" and the beam pattern is determined by the antenna's dimensions and the frequency of the transmitted signal. After the signal data is collected, it is transmitted to Earth and received at a number of

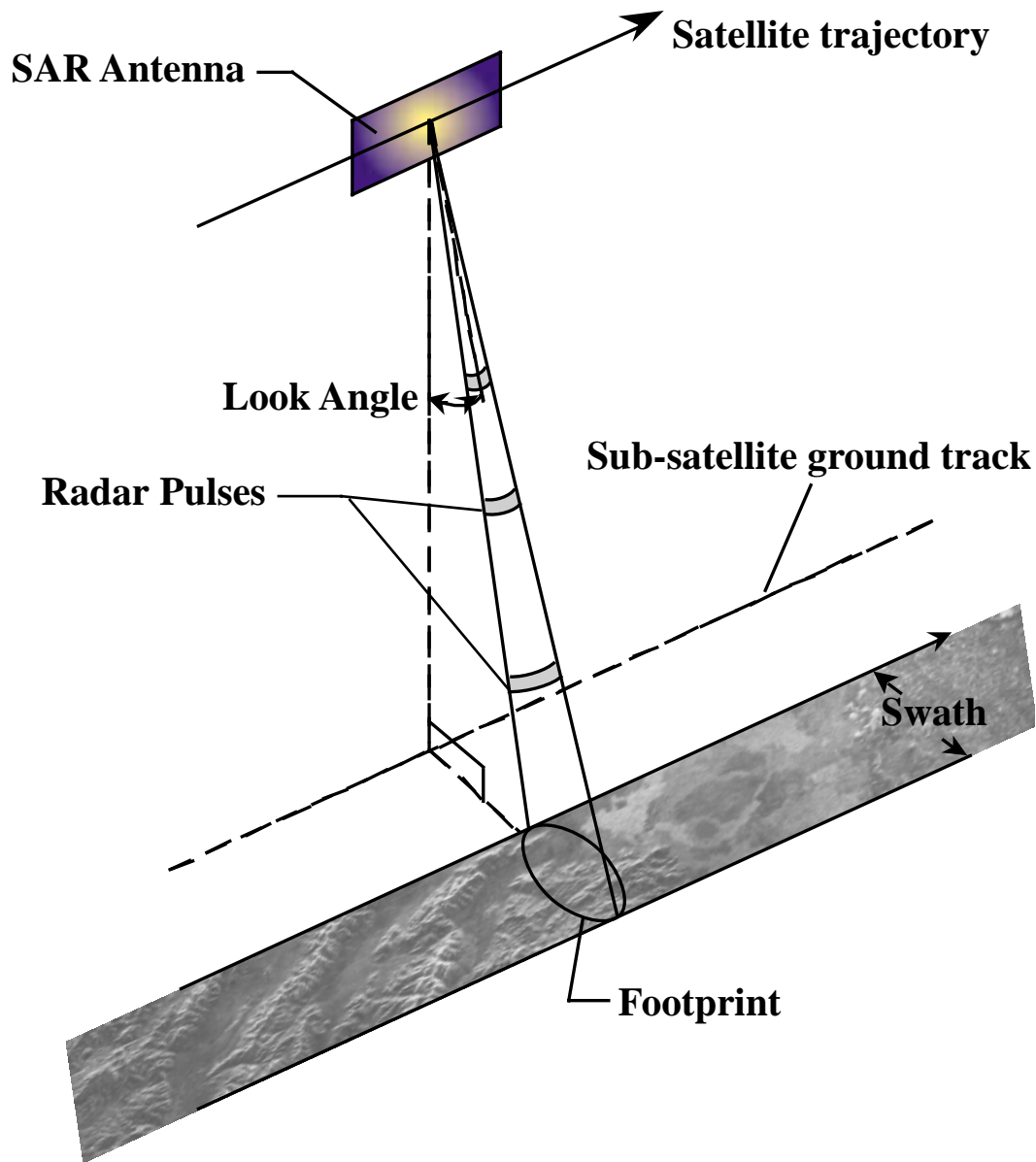


Figure 1. 3. A SAR system configuration. As the satellite orbits the Earth, the imaging radar maps out a swath on the ground by transmitting electromagnetic pulses at a fixed repetition frequency and recording their echoes. The ERS-1 and ERS-2 radars look to the side with an average look angle of 20° . Although the radar footprint is quite large, computer processing of the signal data improves the image resolution. The swath-width of the ERS-1 and ERS-2 SAR systems is 100 km.

strategically located data receiving stations (Figure 1.4). The data are then processed into high-resolution imagery using algorithms based on the signal's characteristics and the satellite orbit: this is described in Chapter 2. The high-resolution imagery is an array of complex numbers representing the amplitudes and phases of the radar signal reflected from patches of ground corresponding to pixels in the image.

After radar imagery has been collected more than once over a particular location on the Earth, consecutive images can be combined to detect topography and surface change using the InSAR method. The InSAR method utilizes the "phase coherent" part of the radar's signal, the spatial separation of the positions of the satellite during its two passes over the same area (Figure 1.5), and knowledge of the wavelength of the signal emitted by the radar system to form an interferometer. Because randomly oriented scatterers within an image resolution element have reflected the signal detected by the radar, the phase of the detected signal has both a random part and a deterministic part. The random part is "incoherent" while the deterministic part is "coherent." If the random part of the phase in the reference image is different from that of the corresponding phase in the repeat image, the coherence of the phase difference in the interferogram is lost. An imaging radar interferometer is capable of measuring changes in the round-trip distances, or range changes, of the electromagnetic signals traveling between the satellite and targets on the ground at the times of the reference and repeat passes of the satellite.

The observed range change can be due to a variety of factors including the geometry of imaging, topography, displacements of the Earth's surface, changes in atmospheric refraction, and noise. The measurements forming maps of interferometric phase, which is proportional to range change, are sometimes expressed as portions of a

Figure 1.4. The ERS SAR receiving stations. This figure is adapted from http://earth1.esrin.esa.it/f/eo3.324/groundstations_map_230997.gif.

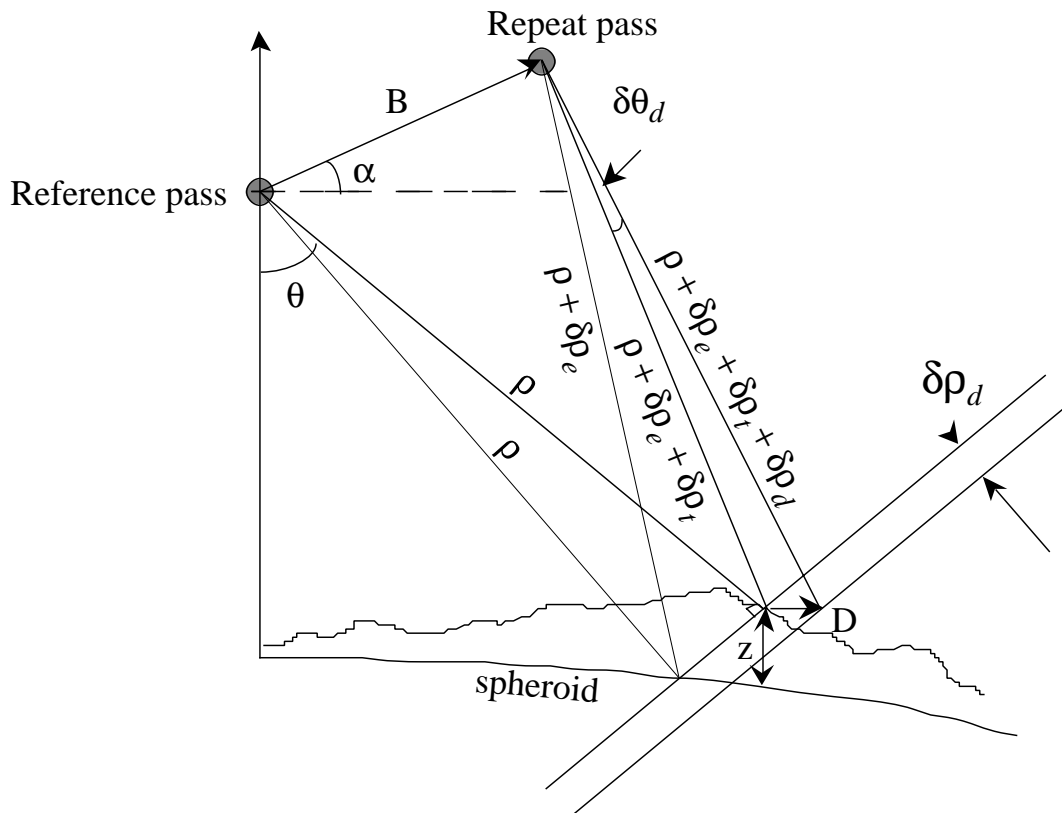


Figure 1.5. The InSAR geometry for a spheroidal Earth with topography and surface deformation. In this diagram, ρ is the range from the "reference" satellite pass to a location on the surface of the Earth at elevation z , $\rho + \delta\rho_e + \delta\rho_t$ is the range from the "repeat" satellite pass to the same location, $\rho + \delta\rho_e + \delta\rho_t + \delta\rho_d$ is the range from the repeat pass of the satellite to the same piece of Earth if it has been displaced by D , θ is the look angle, α is the baseline elevation angle, B is the baseline length. The subscripts e , t , and d refer to the "reference Earth", topography, and displacement respectively. When measuring ground displacement using space-based InSAR, the three range rays in the figure can be considered parallel to each other making $\delta\theta_d$ essentially zero. The InSAR measured component of the displacement, D , is that which is in the direction of the satellite line-of-sight (LOS). This displacement is equal to $\delta\rho_d$.

phase cycle or "wrapped" and sometimes "unwrapped" and converted to range change. The basic information that an interpreter of a wrapped interferogram needs to know is the amount of range change per 2π increment of phase, also called a "fringe", which is equal to one half of the wavelength of the signal transmitted by the radar. For example, this number is 28 mm in ERS C-band interferometry. Because using a computer algorithm to add the appropriate number of 2π increments to each phase measurement, called "unwrapping the phase", sometimes results in a loss of signal over an area that has visually interpretable fringes, leaving the phase wrapped is sometimes advantageous. While fringes in an interferogram may be observable by the naked eye, computer phase unwrapping methods will fail if the level of the noise in an area of the interferogram is too high.

The range of spatial and temporal scales over which the InSAR method can be applied is dependent on the radar's wavelength and swath width, and the pixel size and noise characteristics of the radar imagery data. The amount of time that an interferogram may span while retaining "phase coherence" is controlled by the characteristics of the surface (e.g., vegetated or barren). Phase coherence is a measure of the correlation between the phase returned from a target in the reference image and the corresponding phase in the repeat image. Over time, the movement of scatterers or a change in the dielectric properties within a patch of ground will cause the phase of the signals returned from that patch to be uncorrelated with the phase of previously returned signals. This is called "phase decorrelation". If this happens, the interferometric phase cannot be recovered. Phase decorrelation can be linear with time or can be seasonally dependent.

In spite of this effect, interferograms spanning as much as seven years have been computed for dry desert locations.

The spatial dimensions of detectable deformation signals are limited by five parameters (Figure 1.6): the pixel size, the swath width, the upper and lower limits of the amount of deformation gradient, and the phase and atmospheric noise levels. These parameters bound a pentagon in a plot of the width of a deformation signal versus the amount of range change or displacement in the direction of the satellite line-of-sight (LOS) caused by the deformation event. The bounds on the pentagon are not hard limits since, for example, the phase measurements can be improved by stacking properly filtered interferograms. While the bounds represented in Figure 1.6 correspond to the ERS-1 and ERS-2 C-band systems, the bounds shift depending on the radar system parameters. The pixel size and swath width bounds are physical limitations on the spatial wavelength of the deformation signal that can be measured. Deformation signals with spatial wavelengths smaller than an image pixel or much larger than the size of an image scene cannot be detected with InSAR alone. The locations of the steep and shallow deformation gradient bounds are respectively set by the criteria of 1 interferometric fringe per pixel and 1 fringe per scene. For the ERS systems, each fringe represents 28 mm of LOS displacement, the resolution is 30 m, and the swath width is 100 km giving approximate bounds of 10^{-3} on the steepest displacement gradient and 10^{-7} on the shallowest displacement gradient detectable. Atmospheric noise and phase noise levels limit the smallest LOS displacement signal that can be measured at any spatial wavelength. Phase noise can prohibit the measurement of a displacement signal smaller than a few millimeters. Atmospheric noise is spatially variable and can have magnitudes

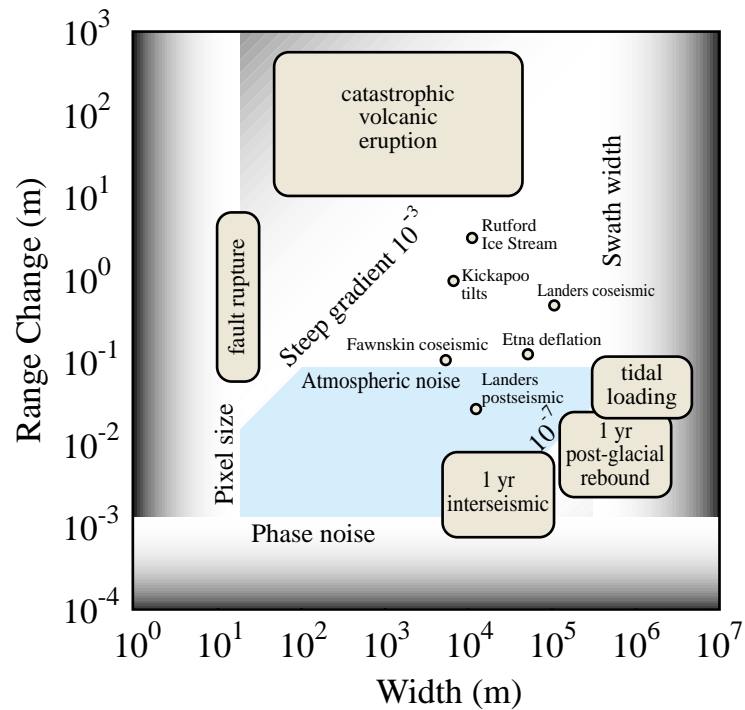


Figure 1.6. The limitations of measuring displacements of the Earth's surface using InSAR. Representative deformation events and mechanisms are plotted. The abscissa indicates the spatial wavelength (map-view) of a displacement. The ordinate is the range change resulting from the deformation event. Modified from *Massonnet and Feigl*, [1998].

of 5 cm. While atmospheric noise does not prohibit the measurement of the deformation signal, it can contaminate it significantly leaving the interpretation open to argument.

The measurement of seismic, volcanic, and glacial displacement signals using InSAR is well documented in the literature since their associated deformation gradients fall well within the limits of the method. Representative phenomena include the coseismic and postseismic phases of the 1992 Landers earthquake cycle, aftershocks of the Landers earthquake, the deflation of Mount Etna, and flow within the Rutford Ice Stream (Figure 1.6). The displacements associated with catastrophic volcanic eruption, near-fault fault rupture, the interseismic phase of the earthquake cycle, post-glacial rebound, and tidal loading lie near the boundaries of the method's applicability. With further method development and the combination of InSAR data with other geodetic methods (e.g., *Bock and Williams*, [1997]; *Williams et al.*, [1998]; *Emardson et al.*, [1999]; *Thatcher*, [1999]), the measurement of these elusive displacement signals lies within our reach.

1.2. DEFORMATION OF SOUTHERN CALIFORNIA AND THE LANDERS EARTHQUAKE

A major strike-slip tectonic plate boundary defined by the San Andreas fault system, cuts through the state of California. The Pacific plate is to the west of the boundary and the North American plate is to the east. The two plates move past each other at a rate of 45-55 mm per year. Although much of the plate motion is accommodated by slip on the San Andreas fault itself, faulting in California is complex

(Figure 1.7). The zone of deformation extends from the coast of California through the Basin and Range Province and the Rocky Mountains.

In Southern California, approximately 14% of the strike-slip motion is transferred to the faults of the Mojave Desert Region north of the location where the San Andreas fault bends towards the west, threatening the inhabitants of Los Angeles. On June 28, 1992 the M_w 7.3 Landers, California earthquake happened in the Mojave Desert and was the largest earthquake to hit California since the 1952 M_w 7.7 Kern County earthquake. The Landers earthquake occurred within a zone of NNW striking right-lateral faults that are part of the Eastern California Shear Zone. The earthquake ruptured five major faults in the Mojave Desert by propagating northward and stepping right onto more northwestwardly oriented faults (Figure 1.8). These faults included, from south to north, the Johnson Valley fault, the Kickapoo fault, the Homestead Valley fault, the Emerson fault, and the Camp Rock fault. The maximum amount of right-lateral surface slip, 6.1 meters, was measured near Galway Lake Road on the Emerson fault. The pattern of slip on the buried rupture is inferred to have been heterogeneous by the inversion of seismic and geodetic data and may have slipped as much as 8 meters at depth. Additional immediate effects of the rupture, in the form of triggered seismicity, were apparent as far away as The Geysers in Northern California.

Geodetic measurements of the displacement of the Earth's surface due to the Landers earthquake were made using campaign and continuous GPS instruments and InSAR technology. While there is a background level of continuous movement of the crust, the geodetic measurements indicated an increase in movement during both the

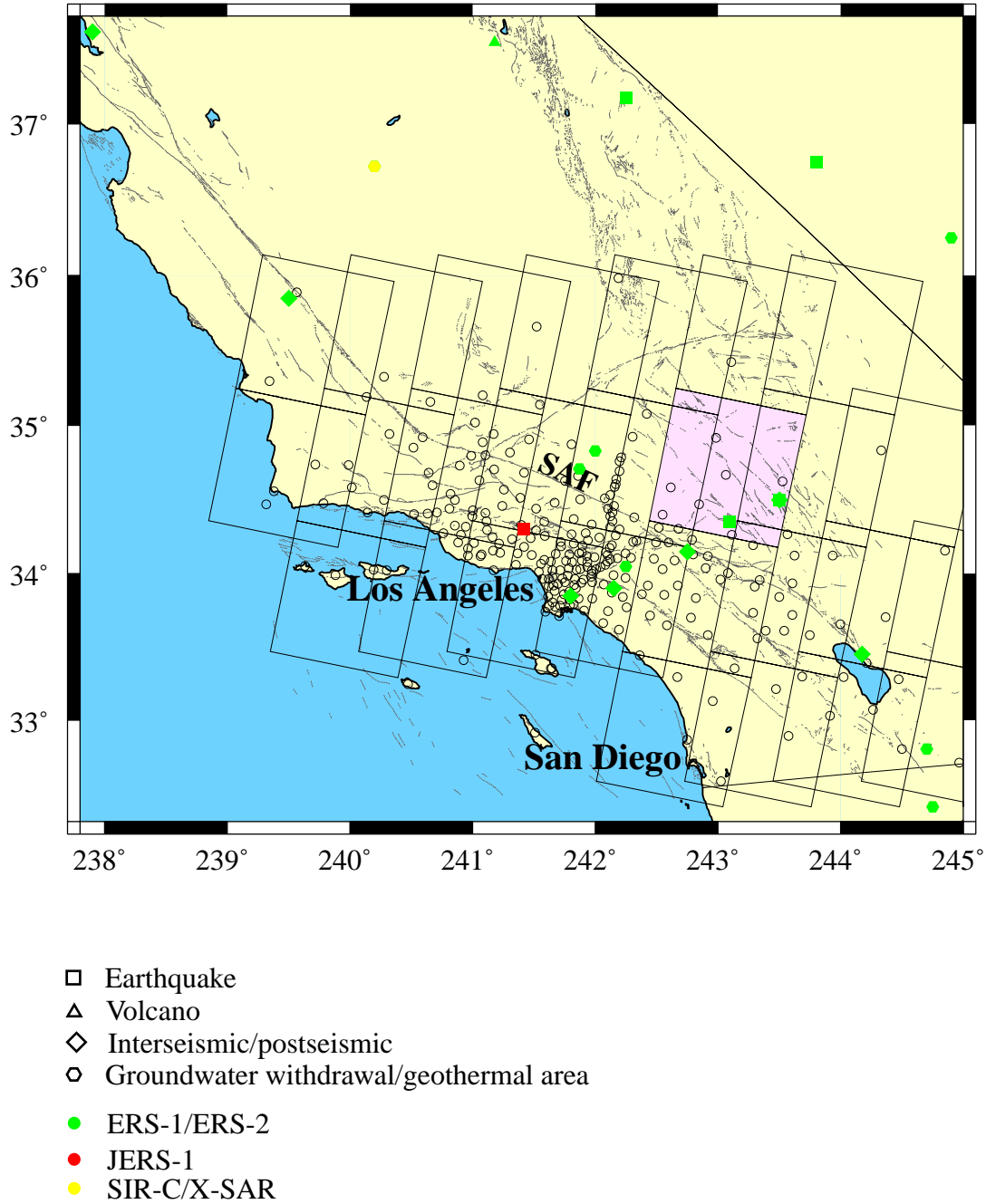


Figure 1.7. The ERS frames and published studies over Southern and Central California. This dissertation focuses on data from the region indicated by the pink frame.

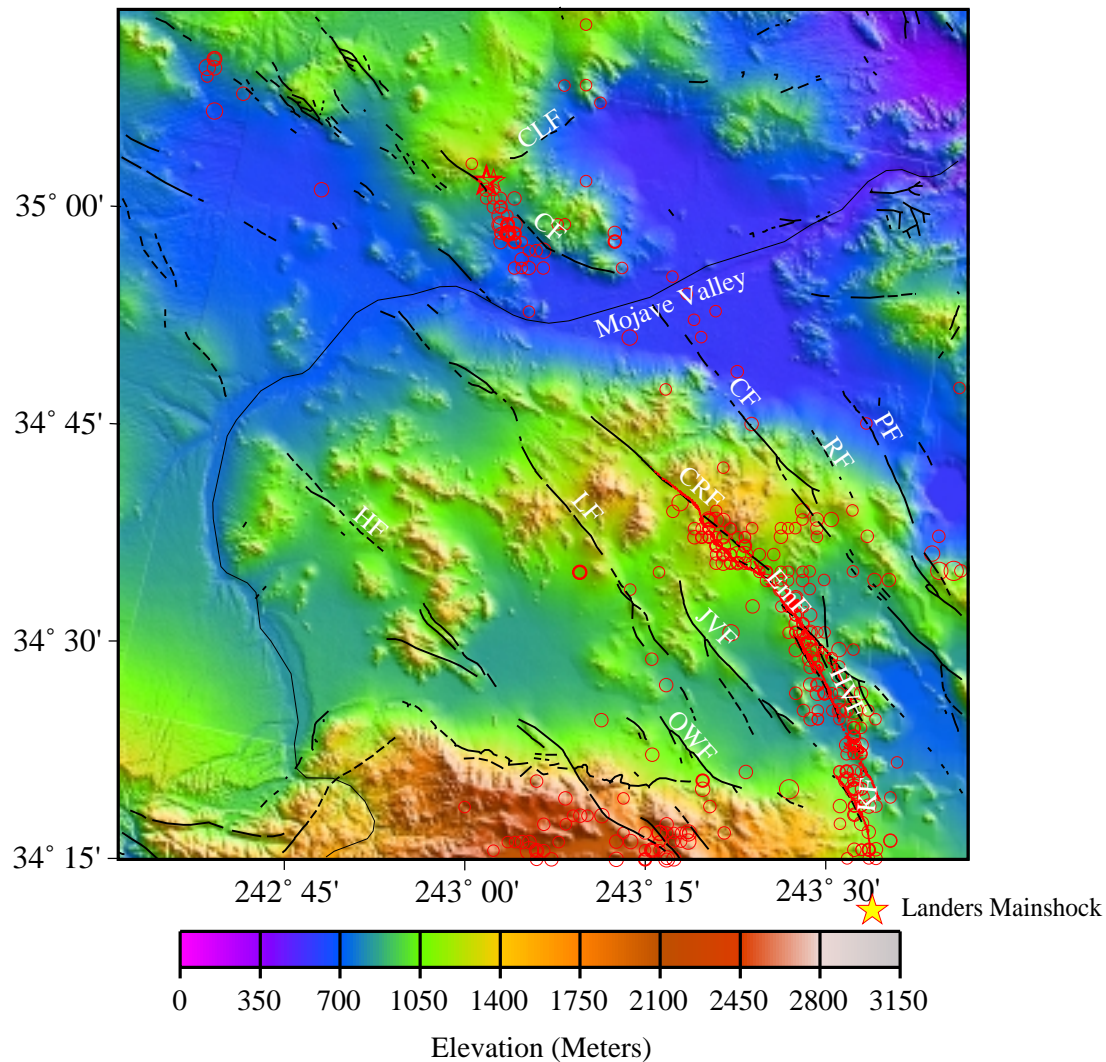


Figure 1.8. The 60 meter digital elevation model (DEM) of the study area derived from InSAR and U.S. Geological Survey (USGS) 1 degree DEM. The Landers earthquake had a magnitude of 7.3 and occurred on June 28, 1992. Shocks with $M > 3.0$ (circles and stars) occurring within 40 days after the Landers Earthquake are plotted. Stars indicate the locations of shocks near the intersection of the Barstow earthquake cluster and the Calico Fault. The Abbreviations are: Helendale Fault (HF), Old Woman Fault (OWF), Lenwood Fault (LF), Johnson Valley Fault (JVF), Emerson Fault (EmF), Camp Rock Fault (CRF), West Calico Fault (WCF), Calico Fault (CF), Rodman Fault (RF), Pisgah Fault (PF), and Coyote Lake Fault (CLF).

coseismic and postseismic phases of the Landers earthquake cycle with much of the movement increase localized near the earthquake rupture. Multiple workers have used these geodetic measurements in conjunction with physical models of the Earth's crust to successfully infer both the spatial and temporal distribution of slip on the earthquake rupture. These inferences give us a greater understanding of the mechanics and processes involved in the earthquake cycle and enhance our ability to assess earthquake hazard.

This dissertation focuses on InSAR measurements of coseismic and postseismic deformations associated with the Landers earthquake. In Chapter 3, the mapping of fractures and triggered slip on faults induced by the rupture indicate the effects of the earthquake on surrounding faults and the directions of the forces induced by the earthquake within the Earth's crust. In Chapter 4, the vertical component of displacement on the rupture is investigated. While the possibility of vertical slip on the rupture has been seismically inferred from modeling of the earthquake source, the distribution of vertical slip has not been resolved by any other method. Knowledge of the vertical slip distribution is important input to viscoelastic models of postseismic deformation. In Chapter 5, InSAR measurements and models of postseismic deformation are investigated and discussed. In the future, the InSAR method will be instrumental in helping us distinguish between the contribution of various mechanisms of postseismic deformation to the geodetic signal.

GLOSSARY OF TERMS

COHERENCE: Coherence is the spectral counterpart of correlation. As such, it is a terminology referring to the degree of correlation between two signals.

DISPLACEMENT: When a piece of the Earth moves, it is said to be displaced. The measurement of the amount that the Earth was displaced is the displacement. A map of displacements allows us to infer deformation, which is a word commonly used to refer to the change of shape of a solid.

PHASE: The phase of a periodic, sinusoidal signal measured by a sensor indicates the stage of the signal's wave-front when it intercepts the sensor. The units of phase are the same as the units used to measure angles: radians and degrees. 2 radians of phase make up one phase cycle.

PIXEL: A digital image is broken up into pixels. These pixels are samples of an image on a grid. This is done because computers are digital machines: they can't process continuous signals. The pixel size controls the resolution of the image.

RADAR: Radar is an acronym for "radio detection and ranging." Radar instruments transmit and receive signals with frequencies in the microwave portion of the electromagnetic spectrum.

SCATTERER: After a radar signal's wave-front intersects the Earth, reflectors on the ground scatter it in all directions. These reflectors are called scatterers.

1.3 REFERENCES

- Bock, Y., and S.D.P. Williams, Integrated satellite interferometry in southern California, *Eos Trans. AGU*, 78 (293), 299-300, 1997.
- Emardson, R., F. Crampe, G.F. Peltzer, and F.H. Webb, Neutral atmospheric delay measured by GPS and SAR, *Eos Trans. AGU*, 80 (17), Spring Meet. Suppl., S79, 1999.
- Gabriel, A.K., R.M. Goldstein, and H.A. Zebker, Mapping small elevation changes over large areas; differential radar interferometry, *J. Geophys. Res.*, 94 (7), 9183-9191, 1989.
- Massonnet, D., M. Rossi, C. Carmona, F. Adragna, G. Peltzer, K. Feigl, and T. Rabaute, The displacement field of the Landers earthquake mapped by radar interferometry, *Nature*, 364 (8 July), 138-142, 1993.
- Zebker, H.A., P.A. Rosen, R.M. Goldstein, A. Gabriel, and C.L. Werner, On the derivation of coseismic displacement fields using differential radar interferometry: The Landers earthquake, *J. Geophys. Res.*, 99 (B10), 19,617-19,643, 1994.
- Goldstein, R.M., H. Engelhardt, B. Kamb, and R.M. Frolich, Satellite radar interferometry for monitoring ice sheet motion: Application to an Antarctic ice stream, *Science*, 262, 1525-1530, 1993.
- Massonnet, D.M. and K. Feigl, Radar interferometry and its application to changes in the Earth's surface, *Rev. Geophys.*, 36 (4), 441-500, 1998.
- Thatcher, W., New strategy needed in earthquake, volcano monitoring, *Eos Trans. AGU*, 80 (30), 330-331, 1999.
- Williams, S., Y. Bock, and P. Fang, Integrated satellite interferometry: Tropospheric noise, GPS estimates and implications for interferometric synthetic aperture radar products, *J. Geophys. Res.*, 103 (B11), 27,051-27,067, 1998.

Chapter 2

Active Microwave Remote Sensing and Synthetic Aperture Radar

2.1. THE INTERACTION OF ELECTROMAGNETIC ENERGY WITH THE EARTH'S SURFACE

An orbiting, active microwave remote sensing instrument launches a pulse of electromagnetic energy towards the Earth; the energy travels in the form of a wave towards the Earth, interacts with the Earth's surface, and is scattered back towards the sensor. The propagation of the pulse can be described using Maxwell's equations. This pulse propagates through the Earth's atmosphere, which is considered a low-loss, refractive medium. The surface of the Earth is an interface between a refractive (low-loss) and a conducting (high-loss) medium. An understanding of the interaction with and the subsequent reflection of the electromagnetic wave off of this interface are essential to understanding the detected signal and the remote sensing data. Without going into extreme detail, the basic concepts of this interaction are illustrated here. For a more thorough treatment, the reader is referred to *Ulaby, Moore and Fung*, [1981].

2.1.1. ELECTROMAGNETIC WAVE PROPAGATION IN A LOSSLESS, SOURCE-FREE MEDIUM

Maxwell's equations in a source-free medium are:

$$\nabla \times \vec{\mathbf{E}} = -\mu \frac{\partial \vec{\mathbf{H}}}{\partial t} \quad (2.1.1a)$$

$$\nabla \times \vec{\mathbf{H}} = \epsilon \frac{\partial \vec{\mathbf{E}}}{\partial t} \quad (2.1.1b)$$

Where $\vec{\mathbf{E}}$ and $\vec{\mathbf{H}}$ are the electric and magnetic field vectors, μ and ϵ are, respectively, the permeability and the permittivity of the medium.

Some vector calculus and substitution leads to the wave equation for the electric field (the magnetic field is orthogonal to the electric field and has an analogous wave equation and solution):

$$\nabla^2 \vec{\mathbf{E}} = \mu\epsilon \frac{\partial^2 \vec{\mathbf{E}}}{\partial t^2} \quad (2.1.2)$$

If we assume harmonic time dependence ($\vec{\mathbf{E}}(\vec{\mathbf{r}}, t) = \mathbf{Re}\{\vec{\mathbf{E}}(\vec{\mathbf{r}})e^{j\omega t}\}$), this becomes

$$\nabla^2 \vec{\mathbf{E}}(\vec{\mathbf{r}}) = -\omega^2 \mu\epsilon \vec{\mathbf{E}}(\vec{\mathbf{r}}) \quad (2.1.3)$$

A solution to this equation for a horizontally (x direction) polarized wave propagating in the positive or negative z direction is:

$$E_x(z) = \mathbf{Re}\{E_{x0} \exp[\pm jkz]\} \quad (2.1.4)$$

Where k is the wavenumber, and E_{x0} is the amplitude of the electric field in the horizontal direction. In the following discussion, we consider the wave directed in the positive z direction. The wavenumber is inversely proportional to the wavelength $k = 2\pi/\lambda$. The angular frequency is $\omega = 2\pi f$. Substitution of Eqn. 2.1.4 into Eqn. 2.1.3 shows that $k = \omega\sqrt{\mu\epsilon}$, and the phase velocity of the plane wave is $v = \omega/k = 1/\sqrt{\mu\epsilon}$.

2.1.2. ELECTROMAGNETIC WAVE PROPAGATION IN A LOSSY, SOURCE-FREE MEDIUM

In a lossy, homogeneous medium, Maxwell's equations become:

$$\nabla \times \vec{\mathbf{E}} = -\mu \frac{\partial \vec{\mathbf{H}}}{\partial t} \quad (2.1.5a)$$

$$\nabla \times \bar{\mathbf{H}} = \sigma \bar{\mathbf{E}} + \epsilon \frac{\partial \bar{\mathbf{E}}}{\partial t} \quad (2.1.5b)$$

Where σ is the conductivity of the medium. Now, assuming harmonic time dependence of the electric and magnetic fields, these equations become:

$$\nabla \times \bar{\mathbf{E}}(\bar{\mathbf{r}}) = -j\omega\mu\bar{\mathbf{H}}(\bar{\mathbf{r}}) \quad (2.1.6a)$$

$$\nabla \times \bar{\mathbf{H}}(\bar{\mathbf{r}}) = (\sigma + j\omega\epsilon)\bar{\mathbf{E}}(\bar{\mathbf{r}}) \quad (2.1.6b)$$

Now, to simplify further algebraic manipulations, a physical parameter called the "dielectric constant" can be defined as $\epsilon_c = \epsilon - j\sigma/\omega$. An analogous quantity to the dielectric constant in the atmosphere is the index of refraction. If the relative dielectric constant is $\epsilon_r = \epsilon_c/\epsilon_0$, where ϵ_0 is the permittivity of free space, then the complex refractive index is $n^2 = \epsilon_r = \epsilon_r' - j\epsilon_r''$. Note that $\epsilon_r' = \epsilon/\epsilon_0$ and $\epsilon_r'' = \sigma/\omega\epsilon_0$.

After some substitutions and vector calculus, a wave equation for the electric field is obtained as above (Eqn. 2.1.2). A solution to this wave equation for the horizontally polarized electric field propagating in the z direction is:

$$E_x(z) = \text{Re}\{E_{x0} \exp[-jk_c z]\} \quad (2.1.7)$$

Where $k_c = \omega\sqrt{\mu\epsilon_c}$ and is analogous to the wavenumber in the loss-less medium. Now, the exponent in Eqn. 2.1.7 has both a real and an imaginary part:

$$E_x(z) = E_{x0} \exp(-\alpha z - j\beta z) \quad (2.1.8)$$

Where α is the "attenuation constant" which determines how the amplitude of the wave is attenuated as it propagates in the medium and β is the new phase constant.

2.1.3. ELECTROMAGNETIC WAVE PROPAGATION IN A CONDUCTING (HIGH-LOSS),

SOURCE-FREE MEDIUM

In a conducting (high-loss) medium (such as the Earth), $\sigma \gg \omega\epsilon$. Then, $j\omega\sqrt{\mu\epsilon_c} = \sqrt{j\omega\mu\sigma} = \sqrt{\omega\mu\sigma/2} + j\sqrt{\omega\mu\sigma/2}$ and $\alpha = \beta = \sqrt{\omega\mu\sigma/2}$. Now the phase constant, β , is different from the phase constant in the lossless case, $k = \omega\sqrt{\mu\epsilon}$. The "skin depth" (d_s) in the conducting medium is the distance the wave travels in the medium before its amplitude is decreased by $1/e$. The skin depth is $d_s = \sqrt{2/\omega\mu\sigma}$.

2.1.4. THE REFLECTION COEFFICIENT OF HORIZONTALLY POLARIZED ELECTROMAGNETIC WAVES

When an electromagnetic wave encounters an interface between two media with different impedance $\eta = \sqrt{\mu/\epsilon}$, part of the wave energy is reflected and part of it is transmitted (Figure 2.1.1). The way in which the wave is reflected and transmitted is described by the reflection and transmission coefficients at the interface. The reflection and transmission coefficients are derived by matching the phase of the incident, reflected, and transmitted waves and requiring that the sums of the reflected and transmitted electric and magnetic field amplitudes equal the incident electric and magnetic field amplitudes at the interface, respectively. For the ERS SAR application, it is illuminating to write down the reflection and transmission coefficients for horizontally polarized (electric field vector is horizontal) incident and reflected waves:

$$R_{HH} = \frac{\eta_2 \cos\theta_1 - \eta_1 \cos\theta_2}{\eta_2 \cos\theta_1 + \eta_1 \cos\theta_2} \quad (2.1.9a)$$

$$T_{HH} = \frac{2\eta_2 \cos\theta_1}{\eta_2 \cos\theta_1 + \eta_1 \cos\theta_2} \quad (2.1.9b)$$

Where η_1 is the impedance of medium 1, η_2 is the impedance of medium 2, θ_1 is the angle

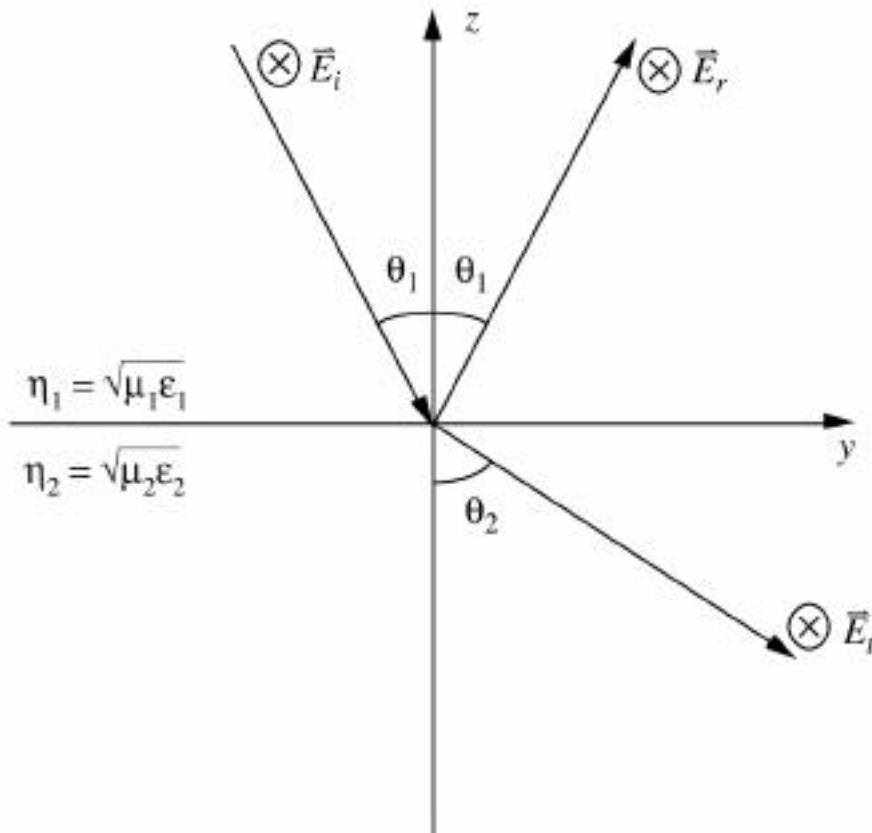


Figure 2.1.1. The reflection and transmission of an electromagnetic wave incident from a medium with impedance η_1 on a medium with impedance η_2 . The magnetic field vector is not shown but is everywhere perpendicular to the electric field vector (which points into the page) and the direction of wave propagation.

of incidence, and θ_2 is the angle of refraction for the transmitted wave (see Figure 2.1.1).

Note that if ϵ is complex, so is the reflection coefficient. At zero incidence, the incident and reflected waves travel in opposite directions and are related to each other by:

$$E_i = E_0 \exp[jkz] \quad (2.1.10a)$$

$$E_r = R_{HH} E_0 \exp[-jkz] \quad (2.1.10b)$$

Where E_i is the incident electric field and E_r is the reflected field. In this case, the z direction is vertical and the incident wave impinges on the interface from above.

2.1.5. THE RADAR EQUATION

When an imaging radar signal encounters the boundary between the atmosphere and the Earth, it is reflected in all directions due to the multiple orientations of "scatterers" within a patch on the Earth. The radar instrument detects and records that part of the signal that is reflected back at the radar. The radar equation describes the relationship between the power transmitted, P_T , by an isotropically radiating radar antenna with gain G , and the power received by the radar antenna, P_R , from an isotropically reflecting target. The basic radar equation is [Levanon, 1988]:

$$P_R = \frac{P_T G^2 \lambda^2 \sigma}{(4\pi)^3 R^4} \quad (2.1.11)$$

Where λ is the wavelength of the signal, R is the range from the antenna to a target with radar cross-section σ . The radar cross-section of a target is the area of a target that, if it reflected isotropically, would return the same amount of power as the real target (real targets usually don't reflect isotropically).

The radar equation can be derived by first writing down the expressions for the transmitted power density on a sphere of radius R centered on the antenna, $\rho_T = P_T G / 4\pi R^2$, and reflected power density on a sphere of radius R centered on the target, $\rho_R = \rho_T \sigma / 4\pi R^2$. Then, the received power is equal to the product of the reflected power density and the effective area of the antenna, $P_R = \rho_R A$ where the effective area of

the antenna is $A = \lambda^2 G / 4\pi$. The effective area of the antenna is analogous to the radar cross-section of the target (e.g., if the antenna was a target of another radar, $A = \sigma$).

When imaging the Earth, the radar return signal has been reflected from a patch of ground with some average radar cross section. The normalized radar cross section, σ° , is the quantity that is most often studied in the literature when trying to determine how natural targets reflect radar signals. It is the average radar cross-section per unit surface area and is a dimensionless quantity. Sometimes it is called the "backscattering coefficient".

2.1.6. BACKSCATTER

The backscattering coefficient of a random surface can be written [Ulaby *et al.*, 1981]

$$\sigma_{rt}^\circ(\theta) = f_r(\epsilon_s, \theta) f_s(\rho(x, y), \theta) \quad (2.1.12)$$

Where θ is the angle of incidence, f_r is the "dielectric function" that describes how the backscatter amplitude depends on the dielectric constant and the incidence angle, and f_s is the "roughness function" that describes how the backscatter energy depends on surface roughness where ρ is the normalized autocorrelation of the surface height. The roughness function and the dielectric function are independent of each other. If the radar signal and return are horizontally polarized, the dielectric function is equal to the Fresnel reflectivity, $f_r = |R_{HH}(\theta)|^2$.

Because of the multiple reflections from scattering elements within the patch of Earth being imaged, the radar return has a random (non-coherent) amplitude and phase

superimposed on a mean amplitude and phase. The mean amplitude and phase give us information about the Earth's surface that we can interpret. Because of the non-coherent components, each measurement of amplitude and phase is a noisy estimate (or a random variable). The non-coherent amplitude components cause a phenomenon called "speckle" in radar amplitude images and the non-coherent phase components cause the phase of each pixel in a single radar image to lose some correlation with its neighbors.

2.1.7. THE RELATIONSHIP BETWEEN EM INTERACTIONS, SAR PROCESSING, AND INSAR ALGORITHMS

SAR processing and InSAR algorithms take advantage of the mean or the estimate of the "coherent" phase of the returned signal. Formulating a SAR processing algorithm involves first deriving filters matched to the expected return radar signal from a unit target on the ground and then applying these filters to the data. The frequency characteristics of these filters depend on the satellite orbit and the transmitted radar signal. Successful InSAR depends on the non-coherent component of the phase not changing with time. If the non-coherent part of the phase does change between consecutive imaging passes of the satellite over the same patch of ground, then a phenomenon called "phase decorrelation" occurs and the interferometric phase cannot be recovered. As can be deduced from the above discussion, if the scatterers within an Earth patch move between imaging times or the dielectric constant of the ground changes, the random component of the phase will change. Note that a gradual change in dielectric constant (such as can happen with a gradual change in soil moisture) will lead to a change

in skin depth as well as mean reflected phase. A significant change in skin depth will change volume scattering effects and hence change the non-coherent part of the phase.

2.2. MATCHED FILTER CONVOLUTION AND PULSE COMPRESSION

The "matched filter" and "pulse compression" concepts are the basis of SAR processing algorithms. These concepts are also applicable to any filtering problem that involves the attempt to recover a signal whose frequency characteristics are known from a mixture of that signal with noise. A matched filter is, surprisingly, a filter that is matched to the signal one is trying to detect. It will be shown below that the matched filter maximizes the signal to noise ratio (*SNR*). For a thorough treatment of matched filtering see *McDonough and Whalen*, [1995]. Pulse compression involves using a matched filter to compress the energy in a signal into a shorter period of time.

The matched filtering of a linear FM chirp signal is used in both the across-track (range) and along-track (azimuth) directions in the SAR processor to increase the resolution of SAR imagery by "compressing" the signal. In the range direction, the linear FM chirp is the actual signal emitted by the SAR sensor. This reduces the peak power requirement of the SAR antenna. In the azimuth direction, a linear FM chirp filter is constructed from the Doppler frequency shifts of the returns from a target as it passes through the radar's footprint with each consecutive pulse emitted by the radar. This Doppler frequency shift is proportional to the rate at which the orbiting satellite moves towards or away from the target.

2.2.1. THE SIGNAL TO NOISE RATIO

The return signal detected by a radar instrument is usually accompanied by some noise. The signal to noise ratio (*SNR*) is the ratio of the signal power to the noise power.

It is:

$$SNR = [\alpha(t)]^2 = \frac{[\{R_{sn}(t)\} - \{N(t)\}]^2}{Var\{N(t)\}} \quad (2.2.1)$$

Where E is the expected value operator, Var is the variance operator, N is the noise, and $R_{sn}(t) = s(t) + N(t)$ where R_{sn} is the detected signal and $s(t)$ is the desired signal.

2.2.2. MATCHED FILTER DESIGN

The matched filter is derived by finding a filter that maximizes the *SNR* of the detected signal in an attempt to recover the desired signal.

The filtering operation $g(t)$ is defined as the convolution of a filter with a signal

$$g(t) = \int h(t-u) R_{sn}(u) du \quad (2.2.2)$$

Where $h(t)$ is the filter and $R_{sn}(u)$ is the signal. To find the filter that maximizes the *SNR* of $g(t)$, this expression for $g(t)$ is first substituted into Eqn. 2.2.1

$$[\alpha(t)]^2 = \frac{\int h(t-u)[s(u) + N(u)] du - \int h(t-u) N(u) du}{\int h(t-u) N(u) du - \int h(t-u) N(u) du} \quad (2.2.3)$$

If the noise has zero mean and is evenly distributed in the frequency domain with power $N_0/2$ then its expected value is zero and Eqn. 2.2.3 becomes

$$[\alpha(t)]^2 = \frac{2N_0 \int_a^b h(t-u)s(u) du}{\int_a^b h^2(t-u) du} \quad (2.2.4)$$

Schwartz's inequality can now be used to find the filter that maximizes the above expression for the *SNR*. Schwartz's inequality for complex scalar functions of t is:

$$\left| \int_a^b x(t)y(t) dt \right|^2 \leq \int_a^b |x(t)|^2 dt \int_a^b |y(t)|^2 dt \quad (2.2.5)$$

Where $*$ denotes complex conjugation. Equality holds in this expression only if $x(t) = \beta y(t)$ where β is some constant. If Eqn. 2.2.5 is applied to the numerator in Eqn. 2.2.4,

$$\int_a^b h(t-u)s(u) du \leq \sqrt{\int_a^b |h(t-u)|^2 du \int_a^b |s(u)|^2 du} \quad (2.2.6)$$

Where equality will hold only if $h(t-u) = \beta s(u)$. Setting $\beta = 1$, we find that the filter that maximizes the *SNR* is the time-reversed "desired" signal that has been combined with white noise to yield the measured signal. The filter, $h(u) = s(-u)$ (at $t = 0$), is called a "matched filter" because it is matched to the signal we are trying to detect.

Note that matched filtering is a correlation operation. Substituting the matched filter, $h(u)$, into Eqn. 2.2.2 gives

$$g(t) = \int_a^b s(u-t)s(u) du + \int_a^b s(u-t)N(u) du \quad (2.2.7)$$

The first expression on the right-hand side of Eqn. 2.2.7 is the definition of the complex autocorrelation. The second expression on the right-hand side of Eqn. 2.2.7 is

the correlation of the matched filter with the noise. At time $t = 0$, the autocorrelation function is a maximum and the correlation of the signal with the noise should be relatively small. Because the matched filtering operation is a correlation, a SAR processor is sometimes referred to as a correlator.

Note also that the maximum SNR given by the matched filter is $2E/N_0$. If we substitute the matched filter into Eqn. 2.2.4, we find

$$[\alpha(t)]^2 = 2/N_0 \int s^2(u) du = 2E/N_0 \quad (2.2.8)$$

Where E is the energy in the signal and is equal to the time-integrated power s^2 .

For a thorough discussion of matched filtering, the reader is referred to *McDonough and Whalen* [1995]. For a simple explanation of matched filtering and its application to radar problems, see *Levanon*, [1988].

2.2.3. THE PULSE COMPRESSION OF A LINEAR-FM CHIRP RADAR RETURN SIGNAL

In this section, the result of matched filtering a radar return will be examined. This result allows a determination of the theoretical spatial resolution of SAR imagery. Consider an isolated point target located at a distance R from a SAR satellite. The radar emits a pulse $s(t)$ that travels to the point target and back in a time $T = 2R/c$ where c is the velocity of the electromagnetic wave and is approximately the speed of light. The impulse response of a point target is a delta function multiplied by the reflectivity of the target. The returned signal is thus the outgoing signal delayed by time T and multiplied

by some constant. Since we are here interested in deriving the resolution of the system, the constant will be neglected and the return from the target is then $s(t-T)$.

The output of the matched filtering operation is

$$g(t-T) = \int s(u-t)s(u-T) du \quad (2.2.9)$$

If the origin is shifted to time T , this becomes

$$g(t) = \int s(u-t)s(u) du \quad (2.2.10)$$

Using Rayleigh's Theorem, Eqn. 2.2.10 becomes

$$g(t) = \int |S(f)|^2 e^{-i2\pi ft} df \quad (2.2.11)$$

Where $|S(f)|^2$ is the power spectrum of the signal $s(t)$. Note that the time width of $g(t)$ determines how well the filtered signal can recover a delta function: the resolving capability of the system.

An idealized linear FM chirp signal has a power spectrum that looks like a box-car in the frequency domain (e.g. Figure 2.2.1). This is a good approximation if the product of the signal's duration and bandwidth is large (> 130) [Cook and Bernfeld, 1967; Curlander and McDonough, 1991]. Since the time-bandwidth product for the outgoing ERS signal is 575, this condition is met. Suppose that the chirp has a constant power spectral density, M , over some one-sided band so that $|f - f_c| \leq B/2$ where B is the bandwidth of the chirp signal and f_c is the central frequency of the band. Then the output of the matched filtering operation is

$$g(t) = MB e^{-i2\pi f_c t} \text{sinc}(\pi B t) \quad (2.2.12)$$

Now, the time width of $g(t)$ is $\Delta t = 1/B$ where B is in Hz (see Figure 2.2.2).

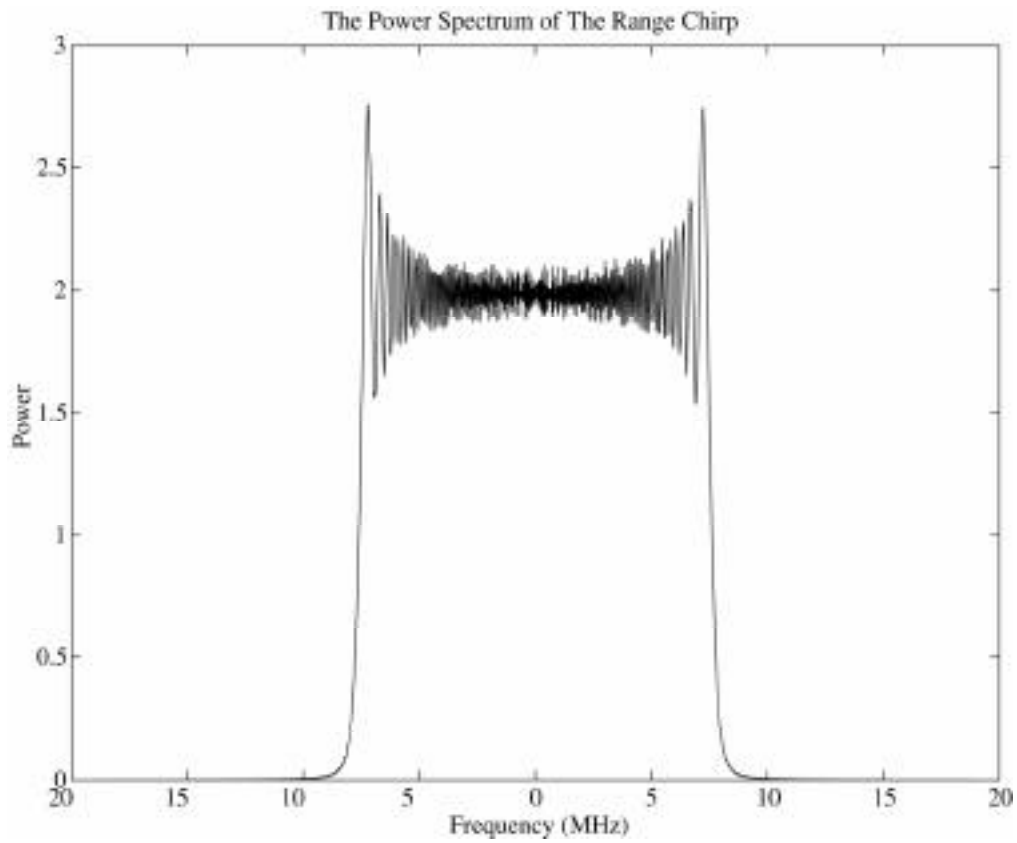


Figure 2.2.1. The power spectrum of an ERS-like transmitted pulse. The power spectrum is close to rectangular with a bandwidth equal to the product of the chirp-slope and the pulse duration.

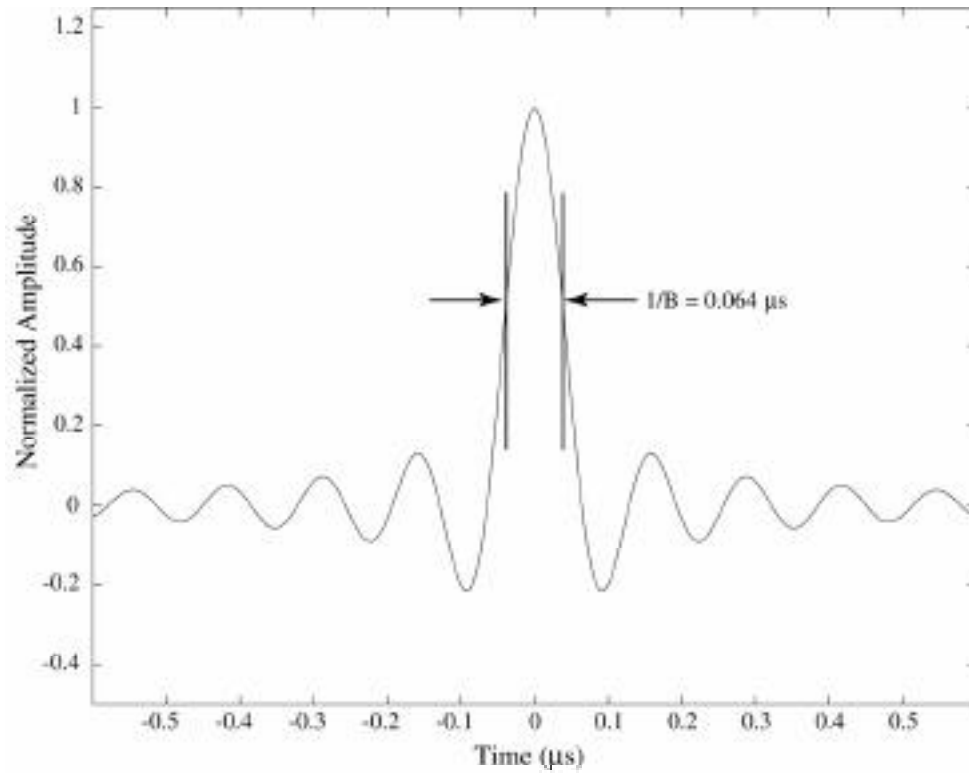


Figure 2.2.2 The result of matched filtering a Linear FM Chirp function. The time-width of the sinc function is determined by ERS-1 and ERS-2 system parameters.

2.3. SAR PROCESSING THEORY

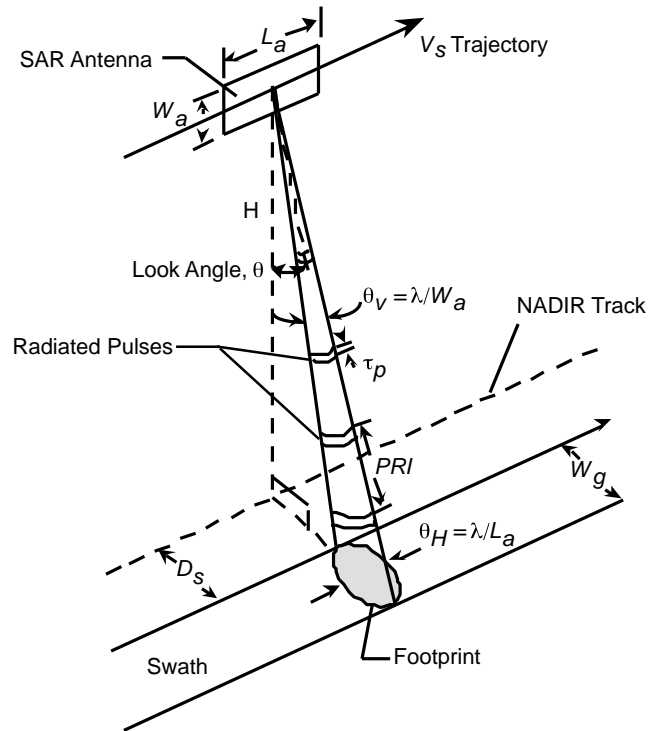


Figure 2.3.1. The imaging radar geometry. The parameters are as described in the text. The figure is adapted from *Curlander and McDonough*, [1991].

2.3.1. THE DESCRIPTION OF AN IMAGING RADAR

The geometry of an imaging radar is shown in Figure 2.3.1. The SAR antenna with width W_a and length L_a is mounted on a satellite platform that travels along a trajectory with velocity V_s that can be determined by its orbital parameters. The satellite's orbit can be found from Newton's law of gravitation and obeys Kepler's laws. The orbit

is specified by its inclination (i), ascending node (Ω), semi-major axis (a), eccentricity (e), and angular position with respect to the ascending node (ϕ) (Figure 2.3.2). The radar transmits an electromagnetic pulse, which spreads radially as it travels towards the earth according to the radar antenna's beam pattern. The angular across-track 3 dB beamwidth of the antenna, $\theta_V = \lambda/L_a$, and the angular along-track 3 dB beamwidth of the antenna, $\theta_H = \lambda/W_a$, depend on the width and length of the antenna, respectively, and the wavelength of the transmitted signal (λ) (see Figure 2.3.1). The pulse is directed at some angle off nadir (directly below the satellite) called the look angle (θ). The transmitted pulses have a duration τ_p and are repeated at a given interval (pulse repetition interval, *PRI*) that can be inverted to obtain the pulse repetition frequency (*PRF*). The sampling frequency of the imagery data is equal to the *PRF* in the along-track direction and the radar's sampling frequency (f_s) in the across-track direction. The distance between the swath and the sub-satellite track is D_s .

The antenna's beam pattern modulates the amplitude of the radar signal returns. The elliptical footprint in Figure 2.3.1 indicates the width of the swath specified by the beamwidth at which the amplitude of the signal is 3 dB below the beam center amplitude. However, many imaging radar systems (ERS-1 and ERS-2 in particular), record the signal returned from targets located outside of the 3 dB swath width and thus include returns that have been amplitude modulated by the side-lobes of the antenna beam pattern. While this kind of a system images a wide swath on the ground, it may be necessary to remove the antenna beam pattern from the data depending on the science application.

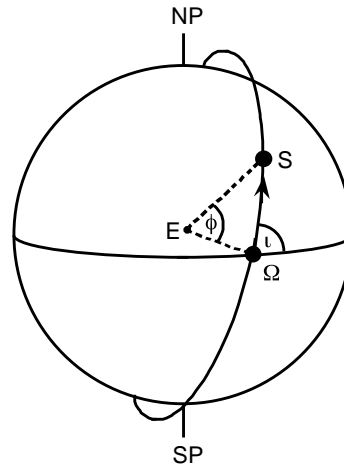


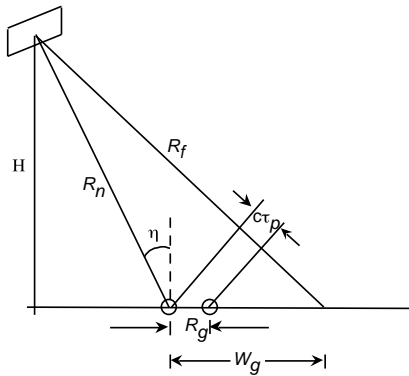
Figure 2.3.2 The orbital configuration. S is the location of the satellite, Ω is the longitude of the ascending node, ι is the orbital inclination, ϕ is the angular position of the satellite relative to the ascending node, E is the center of the Earth, NP is the North Pole, and SP is the South Pole. The figure is adapted from *Rees*, [1990].

Before launching into a description of SAR theory, it is illuminating to consider the resolution of a side-looking aperture radar (SLAR). In this case, the along-track and across-track resolutions are poor because the physical length and width of the antenna respectively limit them.

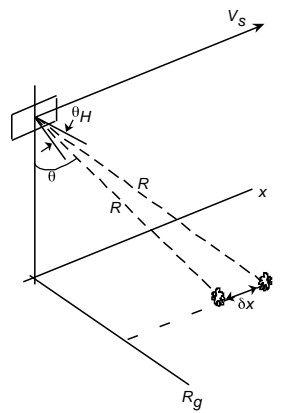
2.3.2. THE RANGE RESOLUTION OF A SLAR

The range resolution of a SLAR system is determined by the ability of the system to distinguish between two point targets on the ground in the range direction (closed circles separated by distance R_g in Figure 2.3.3a. This is dictated by the time duration of the radar pulse, τ_p , and the angle of incidence, η , such that two targets on the ground can be distinguished only if they are separated by more than one pulse-width. The range

resolution of the SLAR is then [*Curlander and McDonough, 1991*]:



a)



b)

Figure 2.3.3 The SLAR geometry. a) The configuration in the range direction. H is the height of the spacecraft, R_n is the near range, R_f is the far range, η is the incidence angle, c is the speed of light, τ_p is the pulse duration, ΔR_g is the ground range resolution, W_g is the width of the swath on the ground. b) The configuration in the along-track direction. V_s is the velocity of the spacecraft, θ_H is the along-track beam-width, θ is the look angle, R is the range, and δx is the along-track resolution. The figure is adapted from *Curlander and McDonough*, [1991].

$$R_g = \frac{c\tau_p}{2\sin \eta} \quad (2.3.1)$$

Note that the range resolution is independent of the spacecraft height.

2.3.3. THE AZIMUTH RESOLUTION OF A SLAR

The azimuth resolution of a SLAR is determined by the system's ability to distinguish between two targets in the azimuth direction. This is dictated by the along-track beam-width of the signal ($\theta_H = \lambda/L_a$) (see Figure 2.3.3b). Two targets located at the same slant range can be resolved only if they are not in the radar beam at the same time. The azimuth resolution of the SLAR is then [*Curlander and McDonough, 1991*]:

$$\delta x = R\theta_H = R\lambda/L_a \quad (2.3.2)$$

Note that the azimuth resolution for this real aperture radar decreases with increasing range and increases with antenna length. As shown below, higher along-track resolution can be obtained by coherent integration of many returns from the same target to synthesize a much longer antenna.

2.3.4. AN EXAMPLE OF SLAR RESOLUTION: ERS-1 AND ERS-2 IMAGING RADARS

The ERS-1 and ERS-2 radars have a pulse duration of .0371 ms, an average angle of incidence of 20° , a signal wavelength of .056 m, and a mean range to a target on the Earth of 850 km. Thus, the ERS-1 and ERS-2 SLARs have a 16 km range resolution and a 5 km azimuth resolution. This resolution is very low and can be significantly improved by SAR processing of the radar signal data.

2.3.5. THE RANGE RESOLUTION OF IMAGING RADARS WHOSE TRANSMITTED SIGNAL IS A LINEAR FM CHIRP

The signal transmitted by the ERS radars is a linear FM chirp (Figure 2.3.4):

$$s(t) = \text{Re} \left[E_0 e^{i2\pi(f_c t + kt^2/2)} \right], \quad |t| < \tau_p/2 \quad (2.3.3)$$

Where E_0 is the signal amplitude, f_c is the signal carrier frequency, and k is the "chirp slope". Note that the frequency of the signal sweeps through a band $-k\tau_p/2$ to $k\tau_p/2$ so that the bandwidth of the signal, B , is equal to the product of the chirp slope and the pulse duration.

After a returned radar pulse is detected, an operation called complex basebanding is performed on the pulse by the system electronics on-board the ERS satellites (see Curlander and McDonough, [1991] p.183 or Levanon, [1988] p.111-113). This operation converts the real signal to a complex signal with frequency centered about zero by shifting the spectrum of the returned signal according to the transmitted signal's carrier frequency and filtering the result to recover only the frequency band centered about zero frequency with bandwidth B (e.g. Figure 2.2.2). This operation is also called "I,Q detection" because the in-phase and quadrature components of the signal are retrieved. The raw radar data collected by the receiving stations is then an array of complex numbers with each row representing a basebanded, sampled returned pulse.

If each basebanded, returned pulse is correlated with a replica of the outgoing pulse, the output of the filtering operation $g(t)$ on a return from a point target is

$$g(t - T) = E_0^2 B \text{sinc} \pi B (t - T) \quad (2.3.4)$$

Where T is the delay of the return from the point target and the time-width of $g(t)$ is $1/B$. The value of the sinc function at its maximum is the range-compressed datum

corresponding to the return from the point target. Substituting $1/B$ for τ_p in Eqn. 2.3.1 gives:

$$R_s = \frac{c}{2B \sin \eta} \quad (2.3.5)$$

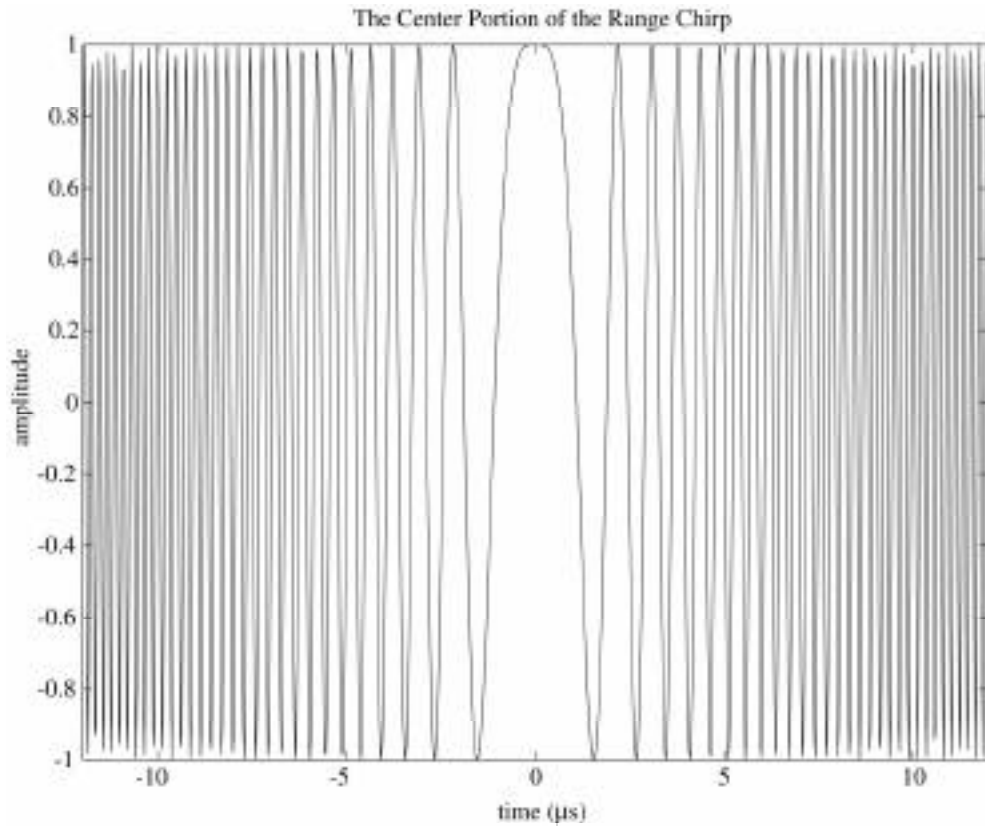


Figure 2.3.4. The center portion of an ERS-like transmitted pulse. Note that the frequency of the signal increases with increasing time away from the origin.

For the ERS radars with $\tau_p = 0.371$ ms, $k = 4.189 \times 10^{11}$ s⁻², and bandwidth $B = 15.5$ MHz give a range resolution of 24.7 m. This is a compression by a factor of 577 over a comparable SLAR system without signal processing.

Note that the return from a point target A will be spread out in the radar data over a time equal to the pulse width but the return's frequency will depend on time as specified by the transmitted chirp signal. The return from an adjacent point target B will have the same frequency spread but will have a different frequency than the return from A at any particular time with the frequency shifted according to the difference in delay (and hence

range) between the returns from A and B . Thus, the returns from two adjacent targets, A and B , can contribute to the received signal at the same time and yet can be separated because they each have a different frequency at that time.

2.3.6. SAR: SYNTHESIZING THE APERTURE

Basic antenna theory states that the resolution of the signal detected by an antenna is inversely proportional to the length of the antenna (e.g. Eqn. 2.3.2). The “synthetic aperture” in the acronym “SAR” derives from the azimuth (or along-track) processing of the signal data which synthesizes an aperture that is longer than the actual physical antenna to yield a higher resolution. The key observation that led to the ability to do SAR processing was made by *Wiley*, [1965] who realized that a Doppler frequency shift of the signal returns could be used to improve the resolution of the radar imagery in the along-track direction.

Two point targets at the same range but at slightly different angles with respect to the track of the radar have different speeds relative to the radar platform at any instant in time. These speed differences lead to a frequency shift of the signal returned from targets located fore and aft of the center of the radar beam relative to the frequency of the signal returned from a target located broadside of the radar. This Doppler frequency shift is proportional to the rate at which the range, R , between the satellite and the target changes:

$$f_D = -\frac{2}{c} \dot{R} f = -\frac{2\dot{R}}{\lambda} \quad (2.3.6)$$

Where f_D is the Doppler frequency shift, and \dot{R} is the range rate.

The range between the satellite and the target can be written (see Figure 2.3.5)

$$R^2 = (x - sV_{st})^2 + R_g^2 + H^2 \quad (2.3.7a)$$

and in a reference frame moving with the spacecraft ($s = 0$), the range rate is

$$\dot{R} = -\frac{x}{R} V_{st} \quad (2.3.7b)$$

Where x is the along-track location of the target, s is "slow time" sampled by the *PRF* (1680 Hz as opposed to fast time sampled by the system's received signal sampling frequency $f_s = 18.96$ MHz), R_g is the across-track distance between the sub-satellite ground track and the target, H is the height of the spacecraft, and V_{st} is the relative velocity between spacecraft and target. Substituting Eqn. 2.3.7b into Eqn. 2.3.5 gives

$$f_D = -\frac{2V_{st}x}{\lambda R} = -2V_{st} \sin(\theta_a) / \lambda \quad (2.3.8)$$

Where θ_a is the angle of the target off broadside, and λ is the radar wavelength. If the radar points to the side, then the ground range, R_g , can be expressed as a function of range, R , along-track location relative to boresight, x , and height, H :

$$R_g = \sqrt{R^2 - x^2 - H^2} \quad (2.3.9)$$

And it can also be expressed as a function of Doppler frequency shift:

$$R_g = \sqrt{-\frac{2V_{st}x}{\lambda f_D}^2 - x^2 - H^2} \quad (2.3.10)$$

A target can be located in across-track, along-track coordinates within one radar pulse from the slant range, frequency shift, and sign of frequency shift of the return signal. This concept can be illustrated by plotting ground range against along-track

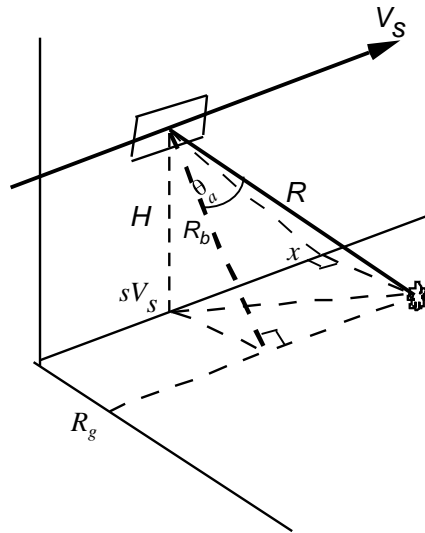


Figure 2.3.5. The along-track geometry. V_s is the spacecraft velocity, H is the height of the spacecraft, R is the range between spacecraft and target, x is the along-track position of the target, R_g is the across-track location of the target, θ_s is the along-track angular position of the target, R_b is the broadside range to the target, and s is slow time. The figure is adapted from *Curlander and McDonough*, [1991]

location for various slant ranges, and against along-track location for various Doppler centroid frequencies (Figure 2.3.6). As a target passes through the radar footprint, it appears at a different range and frequency for each consecutive pulse (Figure 2.3.7). Furthermore, if the change in frequency shift of a return from a particular target within each consecutive radar pulse (the phase history of the target) can be predicted, this information can be used to design an along-track matched filter for pulse compression in the azimuth direction.

If it is assumed that the satellite does not move significantly between transmission and reception of a radar pulse (the velocity of the satellite is approximately 7.5×10^3 m/s

while the velocity of the pulse is approximately 3×10^8 m/s), then the range to a target within each pulse can be considered constant and a change in range to a target can be

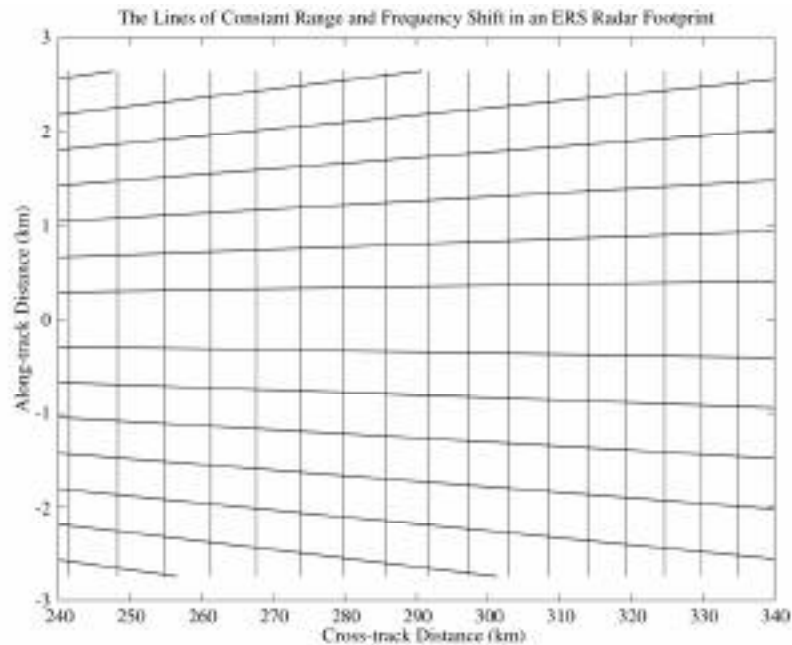


Figure 2.3.6. The lines of constant range and Doppler frequency shift in an ERS radar's footprint. The vertical lines are lines of constant range. The sub-horizontal lines are lines of constant frequency shift.

considered a function only of slow time, s so that the returned signal from a target at range R can be represented by

$$r(s) = Ae^{i4\pi R(s)/\lambda} \quad (2.3.11)$$

Where $R(s)$ is the one-way range to the target and A is the amplitude. Note that the phase of the return from a target at range $R(s)$ is $\phi(s) = 4\pi R(s)/\lambda$.

A Taylor series expansion of range as a function of slow time about the time when the target is in the center of the radar beam, s_c , can be performed retaining only the quadratic terms in the expansion. The range to the target is then

$$R(s) = R_c + \dot{R}_c(s - s_c) + \ddot{R}_c(s - s_c)^2/2 + \dots \quad (2.3.12)$$

Substituting this expression for the range as a function of along-track time (Eqn 2.3.12)

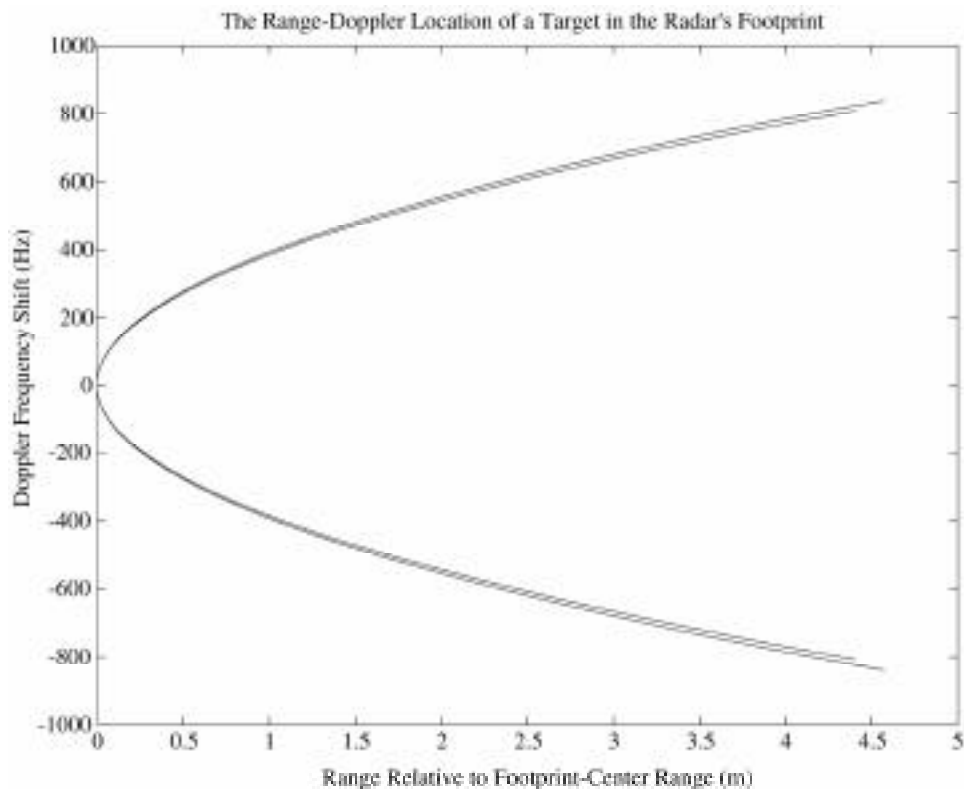


Figure 2.3. 7. The range offset relative to the range when a target is at the center of the radar beam versus the frequency shift of the return from a target as it passes through the radar's footprint. The two curves indicate the range offset and frequency shift from a target at near range and a target at far range. Note that the system's range sampling frequency gives a 7.9 m range pixel size and hence the maximum range offset for a target is less than one pixel.

into Eqn 2.3.11 gives

$$r(s) = A \exp i \frac{4\pi}{\lambda} \left[R_c + \dot{R}_c(s - s_c) + \ddot{R}_c(s - s_c)^2/2 \right] \quad (2.3.13)$$

The range rate at the center of the beam is given by Eqn 2.3.8 by substituting θ_s , the squint angle, for θ_a . The rate of the range rate can be obtained by differentiating Eqn. 2.3.7a twice with respect to the slow time, s :

$$\ddot{R} = \frac{V_{st} x - V_{st}^2 s}{R^2} \dot{R} + \frac{V_{st}^2}{R} \quad (2.3.14)$$

Because the first term on the right of Eqn 2.3.14 is 10^{-6} times the size of the second term, the rate of the range rate can be approximated as

$$\ddot{R} = \frac{V_{st}^2}{R} \quad (2.3.15)$$

The frequency of the return from the target when it is located in the center of the radar beam is the Doppler centroid frequency, f_{Dc} . The rate at which the frequency of the return from a target changes as the target passes through the radar footprint is the Doppler frequency rate, f_R . These Doppler parameters are:

$$f_{Dc} = 2 \dot{R}_c / \lambda = -2V_{st} \sin(\theta_s) / \lambda \quad (2.3.16a)$$

$$f_R = 2 \ddot{R}_c / \lambda = 2V_{st}^2 / \lambda R_c \quad (2.3.16b)$$

Substituting the Doppler centroid frequency and Doppler frequency rate into Eqn. 2.3.13 gives

$$r(s) = A e^{i \frac{4\pi}{\lambda} R_c} \exp\left\{i 2\pi \left[f_{Dc} (s - s_c) + f_R (s - s_c)^2 / 2 \right]\right\}, \quad |s - s_c| < S/2 \quad (2.3.17)$$

Where S is the SAR "integration time" determined by the amount of time a target spends within view of the satellite. This is equal to the product of the along-track footprint length and the relative velocity between the spacecraft and the ground. With reference to

Figure 2.3.1 which shows the equation for the along-track angular beamwidth (θ_H), the SAR integration time is

$$S = \frac{R_c \theta_H}{V_{st}} = \frac{R_c \lambda}{L_a V_{st}} \quad (2.3.18)$$

Figure 2.3.8 shows the power spectrum of the theoretical along-track chirp function. Note that the spectrum is centered on the Doppler centroid frequency. From

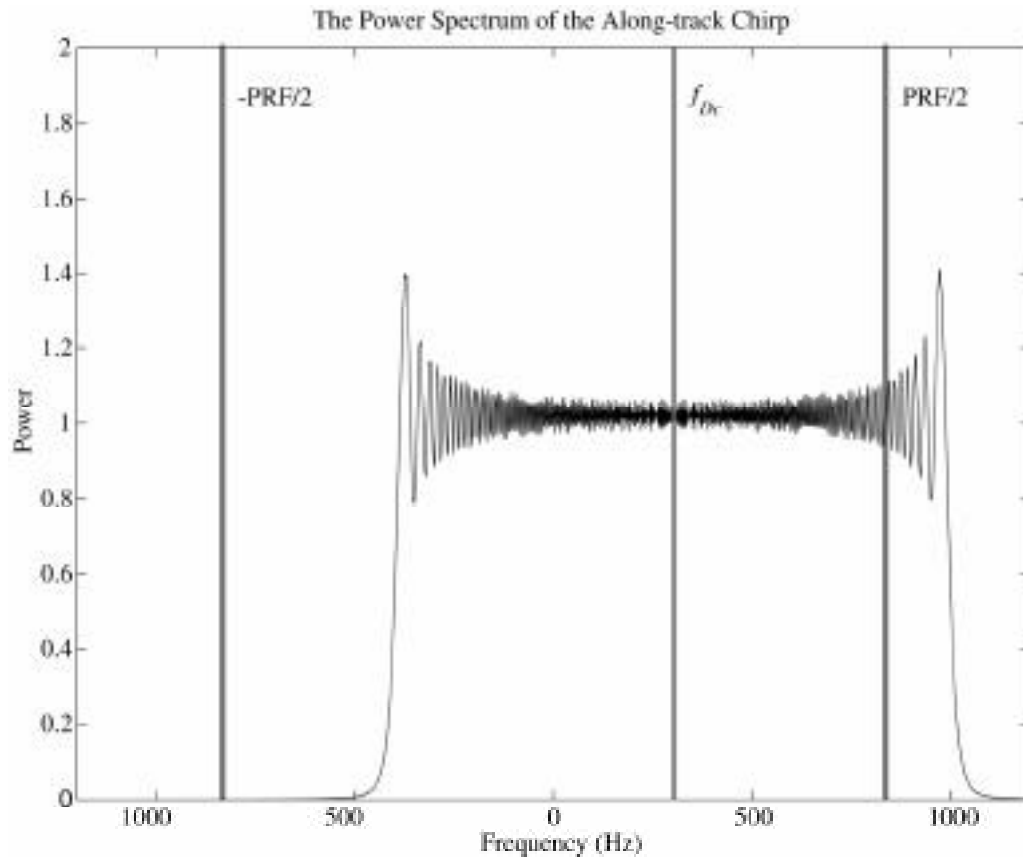


Figure 2.3.8 The power spectrum of an ERS-like along-track compression filter with Doppler centroid frequency equal to 300 Hz. Note that if the frequency of part of the signal exceeds $0.5*PRF$, it must be wrapped into the corresponding negative frequencies before applying the filter to the data.

the discussion about pulse compression (Sec. 2.2), we know that the temporal resolution of the match-filtered chirp signal data is equal to the reciprocal of the bandwidth. The along-track signal has bandwidth, B , equal to the product of the Doppler frequency rate and the integration time. Thus, the reciprocal of the bandwidth is

$$1/B = \frac{L_a}{2V_{st}} \quad (2.3.19)$$

The spatial resolution of the SAR processed data in the along-track direction is the product of the temporal resolution and the relative velocity of the spacecraft. The along-track spatial resolution, δx , is then

$$\delta x = \frac{L_a}{2} \quad (2.3.20)$$

Where, as before, L_a is the length of the antenna. This is a statement that an arbitrarily high resolution can be attained using a shorter antenna. However, there is a trade-off between antenna length and pulse width (and hence swath width) such that a lower bound on the total area of the SAR antenna for a systems like the ERS-1 and ERS-2 SARs is about 1.6 meters (see *Curlander and McDonough*, [1991]).

2.4. THE IMPLEMENTATION OF THE SAR PROCESSOR

The SAR data is sampled in the range direction by the sampling frequency (f_s) of the radar and in the along-track direction by the pulse repetition frequency (PRF). The data comes in the form of an array of complex numbers. Each row of data corresponds to one pulse of the radar while each column of data contains a sample from successive pulses at a constant range.

SAR processing consists of three basic steps: range compression, range migration, and azimuth compression (Figure 2.4.1). The range compression step involves matched filtering of the returned radar signal data with a replica of the transmitted signal. The range migration step translates the radar return from a target in successive pulses of the radar such that it falls within one column in the data set. For the ERS-1 and ERS-2 systems, the maximum translation is less than one range bin (see Figure 2.3.7 and note

that sampling is 7.9 meters in range). However, range migration is justified since a generally accepted criterion for performing this step is that the shift be greater than 1/4 of a range resolution cell [Curlander and McDonough, 1991]. The azimuth compression step involves correlating the returns from a target within successive pulses of the radar with a theoretical chirp function designed according to the expected frequency shift and phase of the returns from that target as it passes through the radar footprint. These three steps are performed on patches of data since they must operate on at least a block of data corresponding to the size of the radar footprint (1200 pulses for ERS-1 and ERS-2) and the amount of computer random access memory limits the amount of data that can be loaded. Thus, in addition to the three basic steps, a significant amount of bookkeeping is necessary.

2.4.1. LOADING THE PROCESSING PARAMETERS AND DATA

The first step performed by the SAR processor is to read in the SAR processing parameters. Sufficient parameters for SAR processing of ERS data and some representative values are shown in Table 2.4.1. The next step is to read in a block of data whose rows correspond to an area larger than the radar footprint in the along-track direction and whose number of rows is a power of 2 for efficient use of Fast Fourier Transforms (FFTs). Note that although the Fourier transform is used here, a number of other spectral transforms can be used in SAR processing algorithms.

2.4.2. RANGE COMPRESSION

After reading in the processing parameters and a block of data, we compute the range reference function (RRF). This processing step maximizes the range resolution of the imagery data. The RRF is a replica of the transmitted radar pulse that will be used as a matched filter to be correlated with each row of raw SAR data. The RRF is constructed by first computing the number of points in the filter, N , using the range sampling frequency and the pulse duration ($N = f_s \tau_p$). Noting that the signal has been stripped of its carrier frequency, we express the RRF as:

$$\text{RRF}[i] = \exp\left(\pi k t^2[i]\right), \quad -\tau_p/2 \leq t[i] \leq \tau_p/2 \quad (2.4.1)$$

Where, if $t[0] = -\tau_p/2$ and $t = 1/f_s$, then $t[i] = t[i-1] + t$, $i = 1, 2, \dots, N$; and k is the chirp-slope parameter (Table 2.4.1).

The RRF is then windowed according to the `rng_spec_wgt` and `rm_rng_band` parameters (Table 2.4.1) and padded with zeros out to the power of 2 sized vector with length greater than and nearest to the number of range samples of raw SAR data, `good_bytes_per_line` (Table 2.4.1). In the case where `good_bytes_per_line = 11232`, since each pair of bytes corresponds to one sample of complex raw SAR data, this is 8192 samples. After padding, the RRF might be shifted in frequency according to the `chirp_ext` parameter (Table 2.4.1) such that each integral increase in `chirp_ext` amounts to one negative sample shift ($-\Delta t$) of the RRF. This allows recovery of imagery data at a nearer range, R_0 , than previously allowed (since the center of the RRF corresponds to the time of the compressed radar return). After padding, the RRF is transformed into the Fourier domain using an FFT algorithm, multiplied by each row of similarly padded,

Fourier transformed raw SAR data, and the product is transformed into the time domain to complete the range compression operation.

Table 2.4.1. The SAR processing parameters

Parameter	Value	Note	Symbol
input_file	orbit_frame.raw	Name of the raw data file	
bytes_per_line	14860	Number of bytes in 1 row of raw data	
good_bytes_per_line	12632	Number of bytes of SAR data in 1 row of raw data (1 pulse)	
first_sample	412	Byte location of first sample in each row	
num_valid_az	2800	Number of rows of valid processed data in each patch	
earth_radius	6371450.5	Radius of the earth at the latitude of the area being imaged	R_e
SC_vel	7124.7	Relative velocity between spacecraft and the ground	V_{st}
SC_height	788168.5	Height of spacecraft	H
near_range	825289.6	Range to target for first sample of SAR data in each row	R_0
PRF	1679.9	Pulse Repetition Frequency (Fig. 2.3.1, $PRF = 1/PRI$)	PRF
I_mean	15.266	Mean value of real part of each sample of SAR data	
Q_mean	15.455	Mean value of imaginary part of each sample of SAR data	
rng_samp_rate	1.896e+07	Sampling frequency in the range direction	f_s
chirp_slope	4.1779e+11	The frequency rate of the transmitted signal (Eqn. 2.3.3.)	k
pulse_dur	3.71e-05	The time width of each transmitted pulse (Fig. 2.3.1.)	τ_p
radar_wavelength	0.056	The wavelength of the radar at the carrier frequency (c/f_c)	λ
first_line	1	First line of raw data to process	
num_patches	10	Number of patches of data to process	
st_rng_bin	1	First column of raw data to process	
num_rng_bins	5780	Number of columns of processed data	
az_res	4	Desired azimuth resolution.	
nlooks	1	Number of rows over which to average the processed data	
chirp_ext	0	Shifts the range filter in frequency	
rng_spec_wgt	1.0	Ratio of coefficients of hamming window for windowing range reference function in time domain	

Table 2.4.1. Cont.

rm_rng_band	0.0	Defines the percent of the bandwidth of the RRF to remove
rm_az_band	0.0	Defines the percent of the bandwidth of the ARF to remove
fd1	326.23	Constant coefficient of doppler centroid frequency
fdd1	0.0	Linear coefficient of doppler centroid frequency
fddd1	0.0	Quadratic coefficient of doppler centroid frequency
xshift	15	Integer shift of processed data in range direction
yshift	485	Integer shift of processed data in along-track direction
sub_int_r	0.923443	Fractional shift of processed data in range direction
sub_int_a	0.195221	Fractional shift of processed data in along-track direction
stretch_r	0.001464	Range stretch of processed data as a function of range
stretch_a	-0.001952	Along-track stretch of processed data as a function of range

An approximation for the relative velocity between the spacecraft and the ground is (see *Curlander and McDonough*, [1991], Eqn. B.4.12): $V_{sr} = V_s / (1 + H/R_e)^{1/2}$.

Consider a Hamming window with coefficients a and b : $w(x) = a - b \cos(2\pi x)$, $0 \leq x \leq 1$. Then, $a = \text{rng_spec_wgt}$ and $b = 1.0 - \text{rng_spec_wgt}$.

The doppler centroid frequency may vary with range. It can then be expressed:

$$f_{Dc} = f_{d1} + f_{dd1} R + f_{ddd1} R^2$$

2.4.3. ESTIMATION OF THE DOPPLER CENTROID FREQUENCY

Without knowing the attitude of the spacecraft (and hence the squint angle), or the exact location of the spacecraft and the exact location of an image point corresponding to a point on the ground, it is impossible to compute the Doppler centroid frequency directly. Instead, it may be estimated by finding the center of the power spectrum of the

raw data (e.g. Figure 2.3.8). This is done using a autocorrelation algorithm such as described by *Madsen et al.* [1989].

2.4.4. RANGE MIGRATION

During range migration the range-compressed, along-track Fourier transformed radar echoes are interpolated in the range direction such that the returns from a particular target will lie along one column in the data set. Within the limits imposed by the *PRF* the range to a target at a particular frequency can be approximated using Eqn. 2.3.12. Noting that time and frequency are locked together in the linear FM chirp signal by $s - s_c = (f - f_c)/f_R$ (note that this assumes that the range to a target as it passes through the radar footprint is sufficiently represented by the Taylor series approximation retaining only the linear and quadratic terms) and substituting the expressions for the Doppler centroid frequency and along-track frequency rate into Eqn. 2.3.12 gives

$$R(s) = R_c - \frac{\lambda}{4f_R} (f^2 - f_{Dc}^2) \quad (2.4.2)$$

The second term on the right-hand side of Eqn. 2.4.2 is the range shift of a pixel at frequency f , and mid-swath range R_c , relative to its range at beam center, in the data set. This suggests that the range migration be performed in range-Doppler space where the columns of the imagery data have been transformed into the frequency domain. The range migration can then be performed on a block of data since different targets at the same mid-swath range and frequency in successive pulses of the radar require the same amount of range shift. This shift might have both an integer and a fractional part.

Shifting by an integer is trivial. The fractional shift is performed using a process called "sinc function interpolation".

Sinc function interpolation is a way of applying the shift theorem for Fourier transforms to discrete data in the time domain. Sinc function interpolation is performed on the data rows because, within each row, the pixels require various amounts of fractional shifting (in contrast, if there was a constant shift for the entire row of data, it would be easier to transform the row into the frequency domain, apply the appropriate phase shift, and transform the row back into the time domain).

The relationship between a signal sampled at times t_k with sampling frequency f_s and the corresponding continuous frequency Fourier transform is:

$$g(t_k) = \int_{-f_s/2}^{f_s/2} G(f) e^{i2\pi f k / f_s} df, \quad t_k = k / f_s, \quad k = 0, 1, \dots, N \quad (2.4.3)$$

An infinitely high sampling frequency (and correspondingly infinite number of samples) would therefore allow us to recover the continuous signal:

$$g(t) = \int_{-W/2}^{W/2} G(f) e^{i2\pi f t} df \quad (2.4.4)$$

If the continuous signal is truly bandlimited with bandwidth $W < f_s$, the Fourier transform of the continuous signal is

$$g(t) = \int_{-W/2}^{W/2} G(f) e^{i2\pi f t} df = \int_{-W/2}^{W/2} (f/W) G(f) e^{i2\pi f t} df \quad (2.4.5)$$

With corresponding sampled signal:

$$g(t_k) = \int_{-W/2}^{W/2} (f/W) G(f) e^{i2\pi f k / f_s} df \quad (2.4.6)$$

When attempting to interpolate a sampled signal, we need only take into account the desired fraction of a sampling interval by which we wish to shift the signal without having to worry about its actual sampling frequency. We can therefore assume, for the sake of simplicity, that the sampling frequency is 1 Hz giving a bandwidth of 1 Hz for the Fourier transform of the discretized signal in to Eqn. 2.4.3. If the bandwidth is 1 Hz, the shift theorem gives

$$g(t_k - a) = \int_{-\infty}^{\infty} e^{-i2\pi f a} (f)G(f) e^{i2\pi f t_k} df = g(t_k) \text{sinc}(t_k - a) \quad (2.4.7)$$

And hence samples of the fractionally shifted, discretized signal are

$$g(t_k - a) = g(t_k) \text{sinc}(t_k - a) \quad (2.4.8)$$

For each shift a , a sinc function corresponding to $\text{sinc}(s_k - a)$ can be computed and convolved with the discretized signal to recover the value of the signal at the specified shift.

For each instance of the SAR processor, an array of sinc function filters corresponding to successively larger fractional data shifts is constructed. Because the frequency resolution of 1 Hz sampled data is the reciprocal of the number of samples ($f = 1/N$), there are N possible divisions for each space between data points (e.g. see Eqn. 2.4.7). Therefore, N sinc function filters for each fractional shift $1/N$ are computed. For each fractional shift, a , the filter is

$$s_{k+3} = \frac{-\cos(\pi k) \sin(\pi a)}{\pi(k-a)}, \quad k = -3, -2, \dots, 4 \quad (2.4.9)$$

After the filter array is constructed, the shift for each pixel in range is computed according to Eqn. 2.4.2 and the `xshift`, `sub_int_r`, and `stretch_r` parameters (Table 2.4.1),

and stored in two vectors: one contains the integer shift for each pixel while the other contains the fractional shift. Then, for each pixel, the fractional shift is used to retrieve the appropriate sinc function filter from the array of sinc functions and that 8-point filter is convolved with the data centered on the appropriate pixel. The value of this convolution at lag zero is the new interpolated data value.

2.4.5. AZIMUTH COMPRESSION

After range migration, the transformed, range-migrated columns of radar data are passed to the azimuth compression subroutine. First, the SAR integration time is computed according to Eqn. 2.3.18 and Eqn. 2.3.19 and the desired azimuthal resolution (*az_res* parameter). This determines the bandwidth of the along-track chirp. Second, an along-track pulse compression filter for each range is constructed. Third, the filter is transformed into the frequency domain, applied to the previously along-track frequency transformed data, and the product is transformed into the time domain. In the following equations the *k* index refers to indexing in the range direction while the *j* index refers to indexing in the along-track direction.

From Eqns. 2.3.18, 2.3.19, and 2.3.20, the SAR integration time can be computed from the bandwidth as a function of resolution (since we are given *az_res* in the parameter file), and the Doppler rate f_R . If the desired resolution is $\text{az_res} = \delta x'$, then the bandwidth is:

$$B = \frac{V}{\delta x'} = |f_R|S \quad (2.4.10)$$

Where S is the SAR integration time and V_{sr} is the relative velocity between the spacecraft and the target on the ground. Substituting the expression for the Doppler rate (Eqn. 2.3.16b) into Eqn. 2.4.10 gives:

$$S[k] = \frac{\lambda R_c[k]}{2 V_{sr} \delta \alpha'} \quad (2.4.11)$$

Note that S depends on the range to the target at the center of the radar beam (R_c). After computing the SAR integration time, we can compute the number of points in the azimuth compression filter. This is just $np[k] = S[k] PRF$.

The along-track filter is computed according to Eqn. 2.3.17 and simplified by setting s_c equal to zero. This does not change the frequency content of the filter but does result in a shift of the processed data in the along-track direction depending on the squint angle (and hence Doppler centroid frequency). The along-track reference function (ARF) is

$$ARF[k][j] = \exp\left\{i2\pi\left(f_{Dc}[k]s[j] + f_R[k]s[j]^2\right)\right\}, \quad -S/2 \leq s[j] \leq S/2 \quad (2.4.12)$$

Where, if $s[0] = 0$ and $s = 1/PRF$, then $s[j] = s[j-1] + s$, $j = 1, 2, \dots, np/2$ and if $s[N] = -s$, then $s[j] = s[j+1] - s$, $j = N-1, N-2, \dots, N - np/2$. Where N is an integer equal to the nearest power of 2 greater than the number of data that will be processed. Remember that the k index refers to the range direction and the j index refers to the along-track direction. The Doppler centroid frequency may vary with range according to the parameters $fd1$, $fdd1$, and $fddd1$ by

$$f_{Dc}[k] = fd1 + fdd1 R_c[k] + fddd1 R_c[k]^2 \quad (2.4.13)$$

While the Doppler rate varies across the swath according to

$$f_R = 2V_{st}^2/\lambda R_c [k] \quad (2.4.14)$$

A further refinement to the along-track matched filter is made by setting the phase of the ARF at time $s = 0$ to correspond to the actual difference between the broadside range to the target and the beam center range to the target. The difference between the mid-beam range and the broadside range is small and can be written $R_b = R_c + \delta R$. From the geometry shown in Figure 2.3.5 (with θ_a equal to the squint angle, and $x = x_c$, the relationship between the broadside range, R_b , and the range to beam center, R_c , (in a reference frame moving with the spacecraft) is

$$R_c^2 = x_c^2 + R_b^2 \quad (2.4.15)$$

Which, after substituting $R_b = R_c + \delta R$, and noting that δR is small, gives an expression for δR

$$\delta R = \frac{x_c^2}{2R_c} \quad (2.4.16)$$

If we square Eqn. 2.3.8 and do some algebraic manipulation, we find that the relationship between the square of the along-track location of the target at beam center and the Doppler centroid frequency is

$$x_c^2 = \frac{\lambda^2 R_c^2}{4V_{st}^2} f_{Dc}^2 \quad (2.4.17)$$

Substituting Eqn. 2.4.17 into Eqn. 2.4.16 and using Eqn. 2.4.14 gives the difference between the broadside range and the beam center range:

$$\delta R = \frac{\lambda f_{Dc}^2}{4f_R} \quad (2.4.18)$$

And hence the phase, ϕ , of the along-track filter at time $s = 0$ is

$$\phi = \frac{4\pi}{\lambda} \delta R = \pi f_{Dc}^2 / f_R \quad (2.4.19)$$

After the ARF is constructed, it is transformed into the frequency domain and multiplied by the corresponding column of range compressed and range migrated data. The product is then transformed into the time domain to yield the SAR processed data.

In the remainder of this dissertation, InSAR is used to map crustal deformations associated with the 1992 Landers, California earthquake. Multiple SAR-processed images covering the Landers area are combined to form interferograms. The geometry of a SAR interferometer and the technical interferometric approach are described in the appendices of Chapter 3. While the Landers earthquake has been widely studied using a variety of geophysical tools, we push the limits of the InSAR method to examine small-scale deformations as well as vertical and postseismic displacements.

2.5. REFERENCES

- Cook, C.E. and M. Bernfeld, *Radar Signals*, Academic Press, New York, 1967.
- Curlander, J.C., and R. N. McDonough, *Synthetic Aperture Radar: Systems and Signal Processing*, edited by J.A. Kong, John Wiley, New York, 1991.
- Levanon, N, *Radar Principles*, John Wiley and Sons, New York, 1988.
- Madsen, S.N., Estimating the Doppler Centroid of SAR Data, *IEEE Trans. Aerospace and Elec. Sys.*, AES-25 (2), 134-140, 1989.
- McDonough, R.N., and A.D. Whalen, *Detection of Signals in Noise*, 2nd. ed., Academic Press, San Diego, 1995.
- Rees, W.G., *Physical Principles of Remote Sensing*, Cambridge University Press, Cambridge, 1990.
- Ulaby, F. T., Moore, R.K., and A. K. Fung, *Microwave Remote Sensing: Active and Passive (in three volumes)*, Artech House, Inc., Norwood, Ma.,1981.
- Wiley, C.A., *Pulsed Doppler radar methods and apparatus*, *United States Patent, No. 3,196,436, Filed August 1954, 1965.*

Small-scale deformations associated with the 1992 Landers, California, earthquake mapped by synthetic aperture radar interferometry phase gradients

Evelyn J. Price and David T. Sandwell

Institute of Geophysics and Planetary Physics, Scripps Institution of Oceanography, La Jolla, California

Abstract. The Landers earthquake (M_w 7.3) occurred on June 28, 1992, and ruptured nearly 100 km of previously mapped and unmapped faults in the Mojave Desert. We use synthetic aperture radar interferometry (InSAR) to examine the cumulative surface deformation between April 24 and August 7, 1992, in a 100 x 100 km region surrounding the northern portion of the earthquake rupture. Also, we introduce a technique for manipulating SAR interferograms to extract short-wavelength displacement information. This technique involves computation and subsequent combination of interferometric phase gradient maps. The InSAR results show significant deformation signatures associated with faults, fractures, dry lake beds, and mountainous regions within 75–100 km of the main rupture. Using the phase gradient method, we are able to extract small-scale deformation patterns near the main rupture. Many of the preexisting, mapped faults within 50 km of the main rupture experienced triggered slip; these include the Old Woman, Lenwood, Johnson Valley, West Calico, and Calico Faults. The InSAR results also indicate right-lateral offsets along secondary fractures trending N-NE within the left-lateral zone of shear between the main rupture and the Johnson Valley Fault. Additionally, there are interesting interferogram fringe signatures surrounding Troy Dry Lake and Coyote Dry Lake that are related to deformation of dry lake beds.

1. Introduction

We use the technique of synthetic aperture radar interferometry (InSAR) to examine small-scale features in the deformation field associated with the Landers earthquake and Big Bear aftershock. Our study is spatially limited to a 100x100 km SAR data frame surrounding the northern portion of the surface rupture (Plate 1) and is limited by data availability to temporally integrate all deformations occurring between April 24 and August 7, 1992. While the coseismic and postseismic deformations associated with this earthquake have been studied by other workers using the InSAR technique [Massonnet *et al.*, 1993, 1994; Zebker *et al.*, 1994; Peltzer *et al.*, 1994; Feigl *et al.*, 1995; Peltzer *et al.*, 1996], our processing methods, which entail computation of phase gradients, bring out short-wavelength features to reveal previously unrecognized strain patterns.

Like the phase of an interferogram, the gradient of the phase depends on the topography and deformation of the Earth's surface and differences in the atmosphere at the two times of imaging. In an attempt to isolate the phase gradient due to deformation, the topographic contribution to the phase gradient can be computed using a digital elevation model or additional interferometric pairs and subsequently removed. Because we cannot yet remove atmospheric variations from an interferogram, we use ancillary geologic information in our interpretations of the phase and phase gradient. One of the many advantages of the phase gradient map is that it can be used to interpret large-scale interferogram phase variations by highlighting small-scale deformations on fractures and faults.

The gradient of the phase is important to interferometric analysis for several reasons. First, the gradient of the phase is unique and can be computed from the real and imaginary parts of the interferogram (there are no 2π ambiguities). Second, it can be used to reduce noise in topographic interferometric measurements either through averaging of phase gradients [Sandwell and Price, 1997] or by aiding in the design of filters whose width is dependent on topographic slope [Werner *et al.*, 1992]. Third, the phase gradient due to topography can be subtracted from an interferogram containing phase gradient due to both topography and deformation without first unwrapping the phase. The two components of the residual phase gradient are then proportional to two components of the deformation gradient tensor rotated into a rectangular satellite coordinate system (see section 3.1): the first is proportional to the gradient of the line-of-sight (LOS) deformation in the direction of the satellite LOS (range gradient), and the second is proportional to the gradient of the LOS deformation in the direction of the satellite groundtrack.

Phase gradients attributable to deformation show small-scale variations in deformation gradient with near total coverage of the area imaged. Strain concentrations along preexisting faults and structural features are observed allowing us to study spatial heterogeneity in the deformation field of a large earthquake. This heterogeneity has been suggested by other workers to explain deviations of geodetic measurements from those predicted by elastic models [e.g., Hudnut *et al.*, 1994; Murray *et al.*, 1993]. In this paper, this heterogeneity is mapped in a SAR data frame over part of the region affected by the Landers earthquake.

1.1. Landers Earthquake Observations

The Landers earthquake sequence is conventionally characterized by three events: the April 23, 1992, 0451 UTC, 33.94°N, 116.33°W Joshua Tree earthquake (M_w 6.1); the June 28, 1992,

Copyright 1998 by the American Geophysical Union.

Paper number 98JB01821.
0148-0227/98/98JB-01821\$09.00

1158 UTC, 34.22°N, 116.43°W Landers event (M_w 7.3); and the June 28, 1992, 1507 UTC, 34.21°N, 116.83°W Big Bear event (M_w 6.2). The data discussed in this study (Table 1) contain deformation occurring between April 24 and August 7, 1992, in an area surrounding the northern part of the rupture of the Landers event (Plate 1).

The Landers earthquake has been modeled teleseismically as a two-event phenomenon with the hypocenter conventionally placed 30–40 km north of Joshua Tree as a small, shallow (3–6 km deep) M_w 6.8 earthquake with strike 359° rupturing unilaterally to the north and provoking a larger magnitude (M_w 7.15) second event about 30 km to the north having a strike of 333° [Kanamori *et al.*, 1992]. The rupture, which was initially oriented nearly due north on the Johnson Valley Fault, changed its orientation as it propagated by stepping right onto progressively more northwestwardly oriented major faults. The earthquake ruptured nearly twenty mapped and unmapped faults; the main five of which are (from south to north) the Johnson Valley Fault, the Kickapoo Fault (sometimes called the Landers Fault), the Homestead Valley Fault, the Emerson Fault, and the Camp Rock Fault (Plate 1). The maximum measured surface displacement was 5.1 m on the Emerson Fault near Bessemer Mine Road [Hart *et al.*, 1993]. In addition to the main rupture slip, triggered slip was reported on several faults within a 100 km radius including the Pisgah, Calico-West Calico (including fractures NE of Newberry Springs), Johnson Valley, upper Johnson Valley, Lenwood, Old Woman, and Pinto Mountain Faults [Hart *et al.*, 1993].

The Landers earthquake ruptured deeper and stronger than any earthquakes previously recorded in the area. It had more than 60,000 shocks including foreshocks, coshocks, and aftershocks [Hauksson *et al.*, 1993]. Shock patterns pertinent to this study include clusters of aftershocks not on the main fault rupture. In particular, aftershock clusters in our area include the Barstow sequence, a cluster near the Calico Fault north of the Mojave Valley, a cluster on the Calico Fault just east of the rupture on the Camp Rock Fault, and seismicity associated with the Newberry fractures which are northeast of the Calico Fault in the Mojave Valley [Unruh *et al.*, 1994] (Plate 1).

1.2. Regional Tectonics

The faults of the western Mojave Desert (Plate 1) define an 80 km wide region of NNW right-lateral shear and lie within the Eastern California Shear Zone (ECSZ) [Dokka and Travis, 1990a, b; Savage *et al.*, 1990; Sauber *et al.*, 1986]. These faults have been active since about 10.6 Ma and have accommodated 9–14% of total plate motion [Dokka and Travis, 1990a] at this latitude on the Pacific-North American plate boundary. The faults of the Mojave Block are characterized as discontinuous with the only fault traversing the entire length of the Mojave from the Pinto Mountain Fault to the Garlock Fault being the Calico-Blackwater system. Faults tend to end in structurally complex zones of extension or shortening with zones of extension characteristically marked by triangular-shaped lakes and zones of shortening marked by mountains and hills [Dokka and

Travis, 1990a]. Geologically determined fault offsets show greater than 40 km of cumulative offset throughout the region south of Barstow [Dokka and Travis, 1990a], while geodetic results show most of the deformation in this region accommodated between the Helendale and Calico Faults south of Barstow (6.7 mm/yr) with negligible deformation to the east [Sauber *et al.*, 1986]. This contrast between geologic and geodetic results points to a recent westward migration of strain [Sauber *et al.*, 1986].

In spite of the surface rupture and shock characteristics of large earthquake swarms (April 10, 1947, Manix [Richter, 1947; Doser, 1990]; June 1, 1975, Galway Lake [Hill and Beeby, 1977; Fuis and Lindh, 1979]; and March 15, 1979, Homestead Valley [Hill *et al.*, 1980]) which have implied significant fault interactions, geologic results have led to block models of faulting in the Mojave with faults accommodating motion independently of each other in time and space [Garfunkel, 1974; Carter *et al.*, 1987; Dokka and Travis, 1990a]. These presumptions about the nature of faulting in the Mojave have led to underestimation of the earthquake magnitude potential in the area [e.g., Wesnousky, 1986; Hart *et al.*, 1993] and confusion as to the link between the San Andreas Fault (SAF) and the more northern parts of the ECSZ. The Landers earthquake changed these presumptions by rupturing along several faults across areas previously modeled as coherent blocks [Hart *et al.*, 1993].

1.3. SAR and InSAR

We use radar imagery data (Table 1) collected by the C-band (5.2 GHz) SAR instruments aboard the ERS-1 and ERS-2 satellites. The raw signal data are processed using a Jet Propulsion Laboratory (JPL) heritage SAR processor whose output consists of a complex signal that is a measure of the complex backscatter of a patch on the ground delayed by the travel time of the signal from sensor to target and back [see Curlander and McDonough, 1991; McDonough *et al.*, 1985]. After processing, the phase of a SAR image resolution element is the sum of several components: (1) the phase delay due to the two-way travel time between sensor and target (location of a SAR pixel on the ground), (2) a random phase component due to the complicated interference pattern produced by radar signal interaction with multiple ground scatterers within an image resolution element, and (3) additive noise.

InSAR is a method by which the phase differences of two SAR images are used to calculate the differences in range from two SAR antennae having slightly different viewing geometries to targets on the ground [Graham, 1974; Zebker and Goldstein, 1986] (Figures A1 and A2). The ERS radar interferometer is composed of either the same antenna on one platform “repeating” its orbit (e.g., ERS-1) or two antennae on different platforms having nearly the same orbit (e.g., ERS-1/ERS-2 tandem mission). The antennae are separated in both space and time (repeat-pass interferometry), and range differences can be due to a number of sources including topography, surface deformation, and atmospheric differences at the two times of imaging. The

Table 1. Data Frames and Baseline Parameters Used in this Study

Reference		Repeat		Baseline	
Satellite: Orbit_Frame	Acquisition Date	Satellite: Orbit_Frame	Acquisition Date	Length, m	Elevation Angle, α
ERS1: 5554_2907	Aug. 7, 1992	ERS1: 4051_2907	April 24, 1992	147.1	152.4
ERS1: 22932_2907	Dec. 3, 1995	ERS2: 3259_2907	Dec. 4, 1995	105.7	178.6
ERS1: 23433_2907	Jan. 7, 1996	ERS2: 3760_2907	Jan. 8, 1996	137.0	178.4

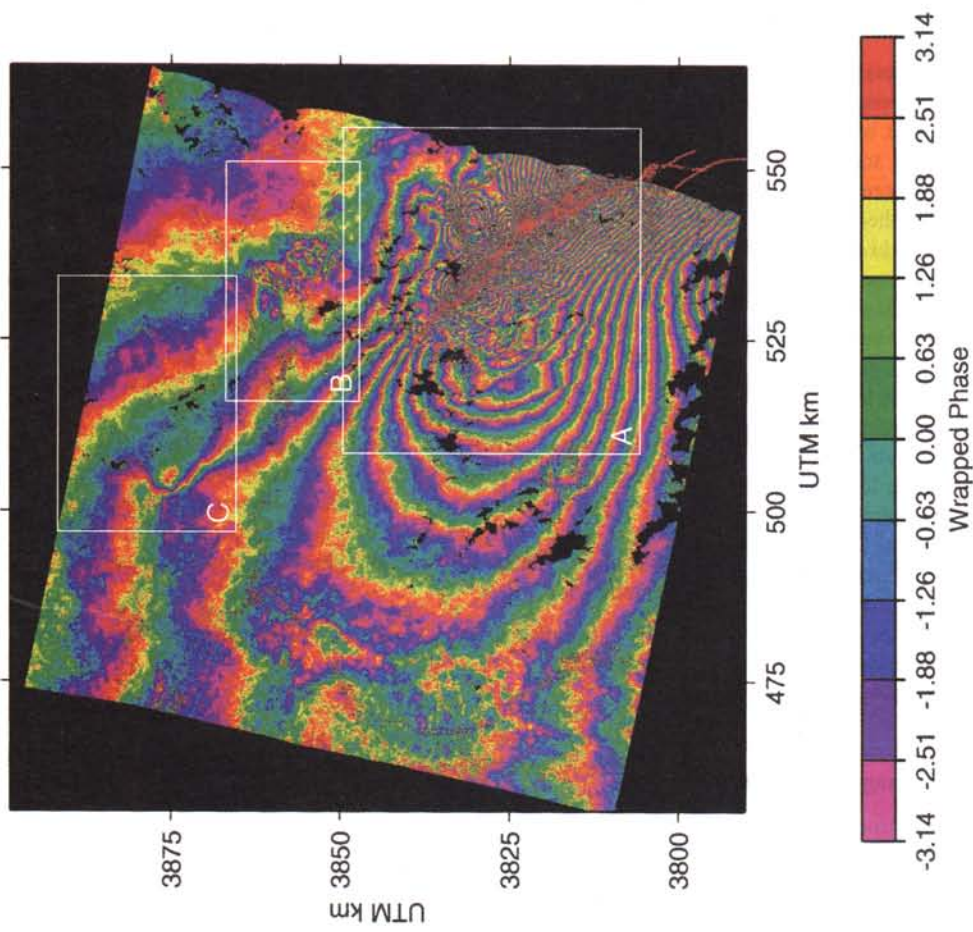


Plate 2. Interferogram deformation fringe phase. Boxes show areas A, B, and C which are discussed in the text. Red lines are field mapped earthquake rupture [Sieh *et al.*, 1993].

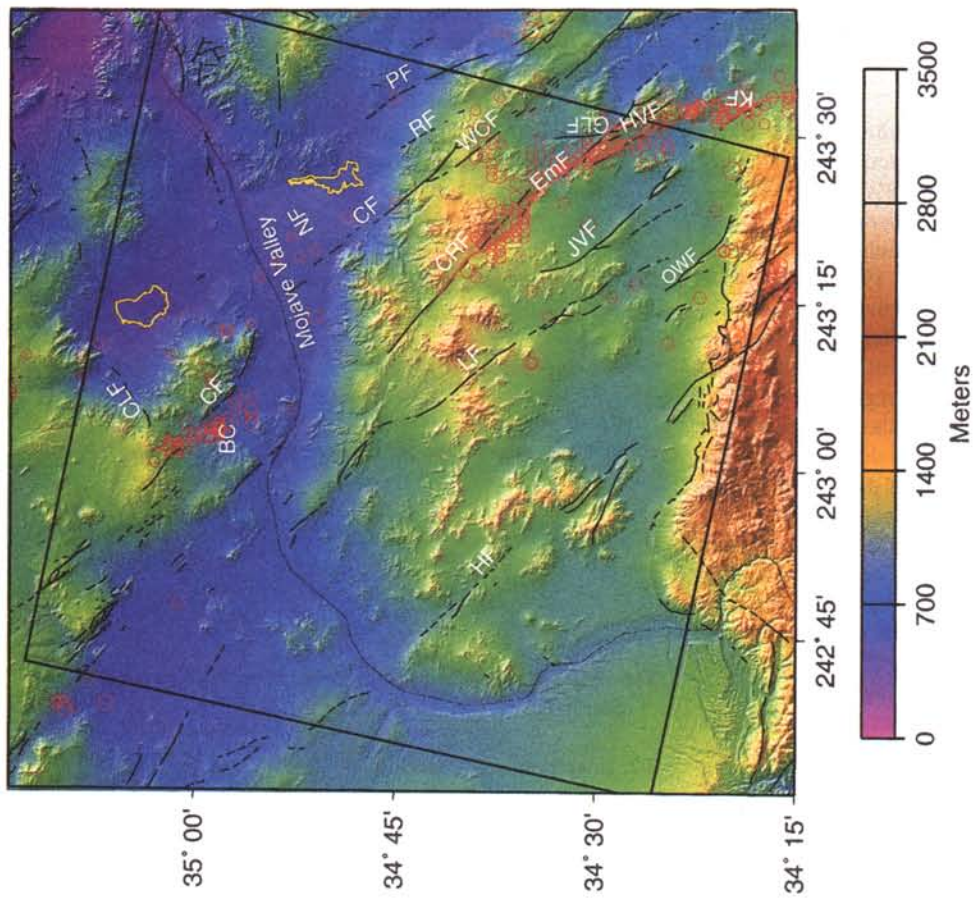


Plate 1. The 60 m digital elevation model (DEM) of the study area derived from InSAR and U.S. Geological Survey (USGS) 1° DEM. Shocks with $M > 3.0$ (circles and stars) occurring between April 24 and August 7, 1992, are plotted. Stars show shocks at the intersection of the Barstow earthquake cluster and the Calico Fault. The box indicates the position of the SAR imagery. Abbreviations are Helendale Fault (HF), Old Woman Fault (OWF), Lenwood Fault (LF), Johnson Valley Fault (JVF), Emerson Fault (EmF), Camp Rock Fault (CRF), Galway Lake Fault (GLF), West Calico Fault (WCF), Calico Fault (CF), Rodman Fault (RF), Pisgah Fault (PF), and Coyote Lake Fault (CLF). Five bench marks are plotted: Rock (ROK), Fry (FRY), Old Woman (OWN), Boulder (BDR), and Means (MNS).

line that connects the two antennae in space is called the interferometer baseline (Figures A1 and A2).

In repeat-pass interferometry, spatial coverage limitations are imposed by phase decorrelation and the geometry of imaging. Three sources of phase decorrelation have been identified as temporal decorrelation due to motion of scatterers between imaging times, spatial decorrelation that is more influential when the interferometric baseline is longer, and thermal noise in the system electronics [Goldstein *et al.*, 1988; Zebker and Villasenor, 1992]. In areas of complete spatial or temporal decorrelation (very steep topography or the area surrounding the Landers surface rupture, respectively), the phase cannot be recovered. The sensor's ability to image the terrain with geometric fidelity depends on the slope of the terrain and the look angle of the radar. "Robust" imaging of the terrain can occur only if the slope does not satisfy the criteria for geometric layover or shadowing. Because ERS-1/ERS-2 have a steep average look angle of 21°, geometric layover is a common phenomenon in mountainous areas. The black patches in Figure 2 and Plates 2-5 occur in areas where the topographic interferogram could not be unwrapped using a "tree" algorithm [e.g., Goldstein *et al.*, 1988]. They exist in the phase gradient map (which should show total coverage) because we used the topography computed from the topographic interferogram to perform orthorectification on our images.

1.4. Effects of Propagation Medium on Range Delay

Because we cannot yet remove the atmospheric signal from the topographic phase-corrected interferograms, it is important to be able to recognize atmospheric artifacts in interferograms so they are not confused with tectonic deformations. Short-wavelength atmospheric artifacts (which could be confused with small-scale tectonic deformations) typically have length scales of the order of 5-10 km and can cause as much as 10 cm of excess two-way path length (three interferogram fringes). Examples are given by Massonnet and Feigl [1995a], Rosen *et al.* [1996], and Zebker *et al.* [1997].

Regional atmospheric effects corresponding to long-wavelength ionospheric perturbations, and differences in the hydrostatic component of the troposphere manifest themselves as a planar phase trend in an interferogram [Tarayre and Massonnet, 1996]. This phase trend makes it necessary either to compute an "artificial baseline" [Tarayre and Massonnet, 1996] or to remove the long-wavelength atmospheric effect from the interferogram at some point in the data processing. If these regional effects are not removed, they will produce a constant offset in the phase gradient map which could be interpreted as a regional tilt.

Despite variations in the refractivity of the atmosphere and ionosphere, repeat-pass InSAR has proved valuable for applications involving deformation of the surface of the Earth. Several studies [Zebker *et al.*, 1994; Massonnet *et al.*, 1993] have compared coseismic deformation signatures obtained from InSAR with those measured by Global Positioning System (GPS). Zebker *et al.* [1994] found the correlation of GPS displacements with those obtained from his interferometric method to be 0.958, while Massonnet *et al.* [1993] found interferometric displacement estimates to agree with GPS measurements of displacement within 3.4 cm RMS. Also, the results of forward modeling of the large-scale ground displacement field near earthquakes agree qualitatively with InSAR fringe maps [Massonnet *et al.*, 1993; Peltzer *et al.*, 1994]. In this study, we differentiate between small, localized tectonic

deformations and atmospheric artifacts using proximity to pre-existing geologic structures as a discriminative criterion.

2. Data Processing

The basic steps of our InSAR data processing are quite standard. We process the raw radar echoes to SAR images and match the images to a subpixel level. We then form an interferogram by multiplying each complex pixel in one image by the complex conjugate of the matching pixel in the other image. Interferograms computed in this fashion have a corrugated appearance [Li and Goldstein, 1990, Figure 7] resulting from a high phase rate in range due to imaging geometry. The flat Earth correction (Appendix A) [Zebker *et al.*, 1994] removes those fringes due to Earth curvature and imaging geometry.

There are some data processing steps that are either done differently here than in previous studies or should be elaborated upon for the sake of explaining the resolution and interpretation of our results. These include estimation of baselines from orbital knowledge, image filtering, and phase gradient computation and combination.

2.1. Estimation of Interferometer Baselines From Orbital Knowledge

In contrast to previous studies, which estimated baseline parameters from imagery and topography data, we computed baselines from ERS-1/ERS-2 precise orbits provided by Scharroo and Visser [1998] (Table 1). These orbits have radial accuracies of 50 mm and crossover repeatability within 70 mm, giving an overall baseline accuracy better than 70 mm. The advantage of this approach is that surface displacements and long-wavelength atmospheric artifacts are not absorbed into the baseline estimate. Repeat orbits are usually not parallel, necessitating the computation of a new baseline at several points in azimuth within an image frame [e.g., Gabriel and Goldstein, 1988].

Let $s(t_1)$ be the vector position of the satellite at time t_1 within the timespan of the reference frame. We search the orbit over the timespan of the repeat frame for time t_2 , the time of closest approach. If $s(t_2)$ is then the vector position of the satellite within the timespan of the repeat frame, the total baseline length is

$$B = |s(t_2) - s(t_1)| \quad (1)$$

and the baseline elevation angle (α) is

$$\alpha = \tan^{-1} \left(\frac{B_V}{B_H} \right) \quad (2)$$

where B_V and B_H are the local vertical and horizontal components, respectively, of the baseline:

$$B_V = (s_2 - s_1) \cdot \frac{s_1}{|s_1|} \quad (3a)$$

$$B_H = \pm (B^2 - B_V^2)^{1/2} \quad (3b)$$

The sign of the horizontal component is positive in the direction of radar look.

2.2. Interferogram Filtering

Methods of filtering interferograms range from simple averaging over pixels (taking looks) [e.g., Gabriel *et al.*, 1989] to

spatially variable filters whose power spectra are matched to that of the local phase [Goldstein *et al.*, 1988; Werner *et al.*, 1992]. We filtered the real and imaginary parts of the complex interferogram (with pixel spacing as sampled by the radar) separately using a low-pass Gaussian 5 point by 17 point filter whose characteristics are discussed in Appendix B. Because none of the baselines of the interferograms examined in this study are longer than 150 m, we do not find in necessary to use an adaptive filter.

2.3. Phase Gradient Computation

Analysis of the phase gradient image is a new approach to studying small-scale surface deformation. The gradient of the interferogram phase is computed directly from the real and imaginary parts of an interferogram and is scaleable by any real number, whereas the phase of an interferogram, measured modulo 2π , can only be scaled by an integer. The expression for the phase gradient ($\nabla\phi$) of a complex interferogram is

$$\nabla\phi(x) = \frac{R\nabla I - I\nabla R}{R^2 + I^2} \quad (4)$$

where R and I are the real and imaginary parts, respectively, of the interferogram and ∇ denotes a gradient operator. This expression is equivalent to one obtained by Werner *et al.*, [1992], but differentiation is performed in the spatial domain rather than the frequency domain.

Averaging of phase gradient images, or stacking, to produce a topographic phase gradient model is useful for decreasing the noise level of the data and averaging out atmospheric range errors [Sandwell and Price, 1997]. Before phase gradients can be stacked, they must be scaled to some common baseline. This is done using a scale factor that is equal to the ratio of the perpendicular baselines after the flat Earth correction (Appendix A) has been applied [e.g., Zebker *et al.*, 1994]. The expression for the average phase gradient from N interferograms each having scale factor b_i (see Appendix A) is

$$\overline{\nabla\phi} = \frac{1}{N} \sum_{i=1}^N b_i \nabla\phi_i \quad (5)$$

In this study, we averaged two pairs from the ERS-1/ERS-2 tandem mission to obtain an estimate for the topographic phase gradient. We then scaled and subtracted this topographic phase gradient from the interferogram phase gradient for the ERS-1 pair which includes the earthquake (Table 1) to obtain an estimate of the phase gradient (Figure 2) related to the deformation which occurred between April 24 and August 7, 1992.

3. Interferogram Interpretation and Transformation of Displacement and Deformation Gradient Into the Satellite Reference Frame

The quantity that relates deformations and topography to InSAR geometry (Figure A2) is the difference in range to a point on the ground between repeat and reference passes of the satellite ($\delta\rho$). This change in range is related to the interferometric phase (ϕ) by

$$\phi = \phi_2 - \phi_1 = \frac{4\pi}{\lambda} \delta\rho \quad (6)$$

where ϕ_1 is the phase of a pixel in the reference image, ϕ_2 is the

phase of a pixel in the repeat image, and ρ is the range from the satellite to the target during the satellite's reference pass.

If deformation has occurred between the two times of imaging, ϕ is proportional to the sum of a geometric (flat Earth) $\delta\rho_e$, a topographic $\delta\rho_t$, and a deformation $\delta\rho_d$ contribution to the range change [Zebker *et al.*, 1994] (Appendix A)

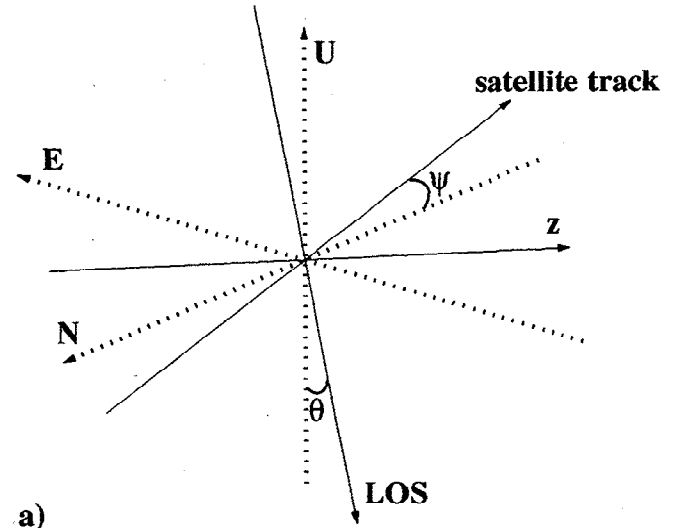
$$\phi = \frac{4\pi}{\lambda} (\delta\rho_e + \delta\rho_t + \delta\rho_d) \quad (7)$$

When the topographic and geometric phase contributions are removed, the residual phase can be assumed to be due to deformation and is

$$\phi = \frac{4\pi}{\lambda} \delta\rho_d \quad (8)$$

where $\delta\rho_d$ is the magnitude of the displacement in the direction of the satellite LOS. Each fringe in Plates 2 and 3b-5b represents 2.8 cm of displacement in the satellite LOS direction.

The geometric relationship between an Earth-based rectangular coordinate system and a satellite referenced system is illustrated in Figure 1. Assuming that the radar LOS and satellite groundtrack directions are orthogonal, we define a right-handed rectangular coordinate system in the satellite reference frame in which the directions of the first, second, and third rectangular vector components are in the satellite LOS direction, the satellite



a)

	LOS	Satellite Track	z
E	$-\sin\theta \cos\psi$	$\sin\psi$	$-\cos\theta \cos\psi$
N	$\sin\theta \sin\psi$	$-\cos\psi$	$\cos\theta \sin\psi$
U	$-\cos\theta$	0	$\sin\theta$

b)

Figure 1. (a) Rectangular coordinate systems for Earth-based geometry (E, N, U) and satellite-based geometry (LOS, satellite track, z); θ is the look angle of the radar, and ψ is the angle between the satellite track and south. (b) Rotation matrix to transform Earth-based coordinates into satellite-based coordinates.

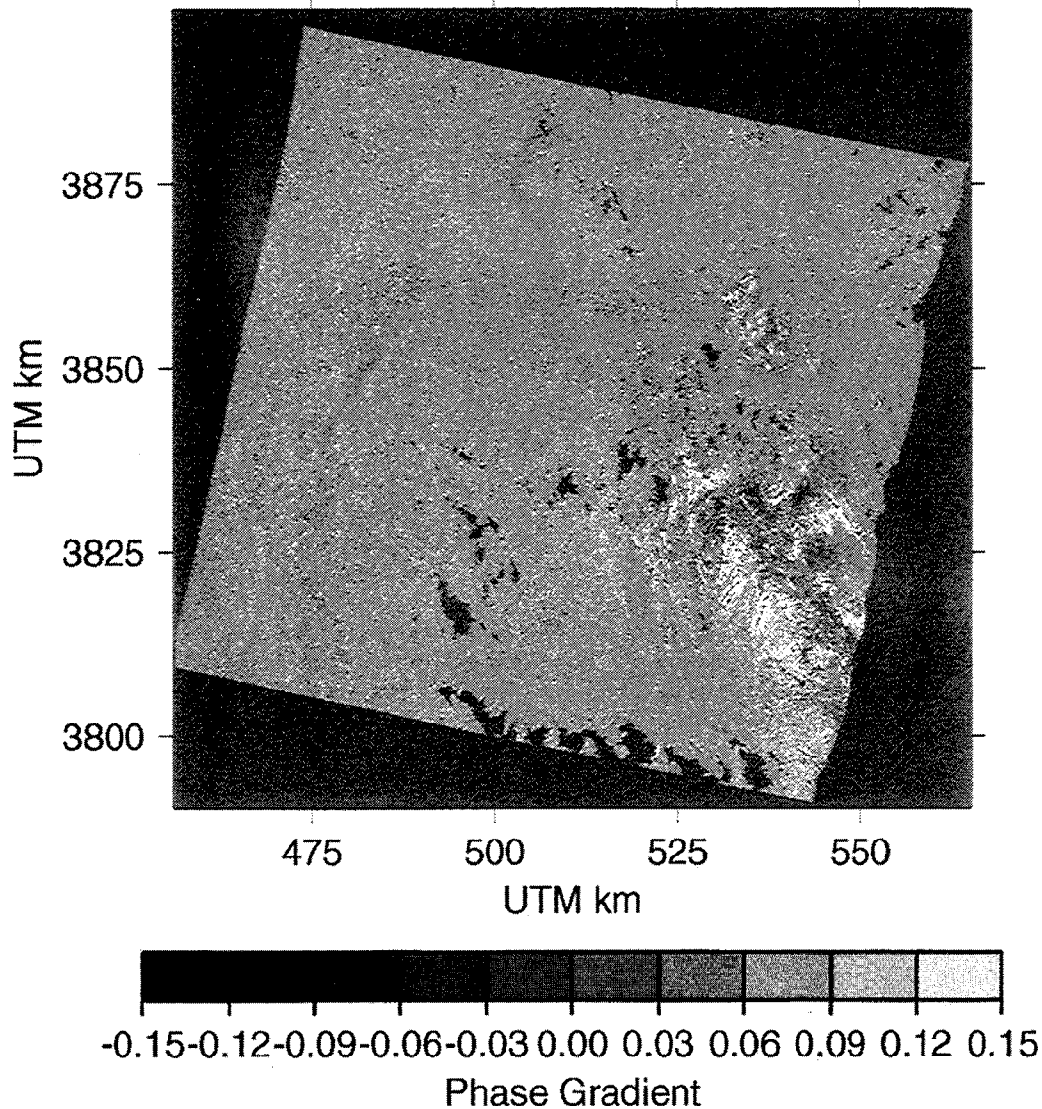


Figure 2. Interferogram deformation phase gradient formed by subtracting scaled topographic phase gradient from April 24 to August 7, 1992, interferogram phase gradient.

along-track direction, and the direction perpendicular to the plane of imaging (z), respectively. We then find the rotation matrix (\mathbf{A}) that transforms Earth-based rectangular coordinates (east (E), north (N), up (U)) into the satellite coordinate system. The rotation matrix \mathbf{A} is fully determined (for a descending pass geometry) by defining the along-track axis to lie in the Earth-referenced E-N plane and to make an angle of $180^\circ - \psi$ with the N axis (where ψ is the angle between the satellite groundtrack and south), the LOS axis to make an angle $180^\circ - \theta$ with the U direction (where θ is the radar look angle), and the base vector perpendicular to the plane of imaging to make an angle $90^\circ - \theta$ with the U direction (Plate 2). The assumption that the LOS and along-track directions are orthogonal is reasonable in our case since the angle between them (in the imaging plane) is $90^\circ \pm \sigma$, where σ , the squint angle, is less than 0.03° for the ERS imaging radars.

If \mathbf{u} is the displacement in the satellite coordinate system and \mathbf{u} is the displacement in the Earth-based coordinate system,

$$\mathbf{u} = \mathbf{A}\mathbf{u} \quad (9)$$

and the displacement measured by the radar interferometer is the LOS component of \mathbf{u} which is \underline{u}_1 .

The gradient of the displacement in the Earth-based coordinate system can be transformed using the same rotation matrix to yield tensor components proportional to the phase gradient of deformation. If the deformation gradient tensor [e.g., *Malvern, 1969*] in the Earth-based coordinate system is \mathbf{J} and the deformation gradient tensor in the satellite coordinate system is \mathbf{J} , then

$$\mathbf{J} = \mathbf{A}\mathbf{J}\mathbf{A}^T \quad (10)$$

The two components of phase gradient due to deformation that we can measure using InSAR are proportional to two components of \mathbf{J} : \mathbf{J}_{11} is the derivative of \underline{u}_1 in the LOS direction, and \mathbf{J}_{12} is the derivative of \underline{u}_1 in the along-track direction. Our phase gradient maps plot only the deformation gradient component that is in the LOS direction because this component highlights the predominantly N-S structures. Note that the deformation gradient tensor includes both strain and rotation.

As is evident from this analysis, the LOS component of deformation is a linear combination of all the components of the Earth-referenced deformation as are the two phase gradient components a linear combination of all the deformation gradient components in an Earth-based coordinate system. Because of this, other information including geologic mapping, GPS measurements, earthquake orientations, and/or assumptions about the nature of the deformation is necessary to interpret radar interferometric measurements. Even in the case where ascending and descending passes of the satellite are available for a given deformation event, information about the magnitude of the horizontal displacement vector or its orientation is necessary to determine its three components.

The phase gradient presented in Figure 2 and Plates 3a-5a, is capable of both adding to the knowledge about the earthquake rupture pattern and mapping extensions of faults difficult to trace geologically by highlighting strain concentrations on secondary fractures and triggered or sympathetic slip on major faults. The larger-scale deformation patterns are best observed as variations in the wrapped phase since their contribution to the phase gradient measurements is that of a regional constant shift.

4. Results

The stacked LOS phase gradient (equation (5)) of two ERS-1/ERS-2 tandem mission interferograms was scaled and subtracted from the phase gradient of the ERS-1 April 24 to August 7, 1992, interferogram to produce the gradients shown in Figure 2 and Plates 3a-5a. The unwrapped phase of the December 3-4, 1995, tandem interferogram was scaled and subtracted from the phase of the April-August 1992 interferogram to produce the fringes in Plates 2, 3b-5b. Because each image was collected during a descending pass of the right-looking ERS satellite, the nearest range to the satellite is on the right-hand side of the figures.

Plate 2 and Figure 2 show the relationship of the deformation phase gradient to the deformation fringe phase for the entire area of the study (100 km by 100 km) defined by an ERS data frame. The deformation fringe phase is comparable to maps shown in other studies [Massonnet *et al.*, 1993; Zebker *et al.*, 1994]. The most obvious feature in the map is the region of phase decorrelation around the main rupture. Ground scatterers in this region underwent random motions between the two imaging times with length scales greater than the wavelength of the SAR. The phase cannot be recovered here. Three areas outside the decorrelated rupture signature show remarkable deformation fringe and phase gradient signatures. Area A (Plate 3) surrounds the end of the rupture and includes the Camp Rock (CRF), Emerson (EmF), Johnson Valley (JVF), and Lenwood (LF) Faults and small parts of the Calico Fault (CF). Area B (Plate 4) includes the Calico and Pisgah (PF) Faults as they traverse the latitude of the Mojave Valley (MV) as well as deformation related to structures which have been dubbed the Newberry fractures [Unruh *et al.*, 1994]. Area C (Plate 5) includes Coyote Dry Lake (CDL) and the Barstow earthquake cluster [Hauksson *et al.*, 1993].

4.1. End of the Main Rupture

The fringe pattern between the Johnson Valley Fault and the main rupture is dense and elongated parallel to the azimuth of the rupture (Plate 3b). The density of fringes decreases logarithmically across the Johnson Valley from east to west as is expected from elastic half-space modeling of the lithosphere [see Massonnet *et al.*, 1993]. Because of the viewing geometry

mentioned above, this pattern is indicative of either a left-lateral shear in the direction of earthquake rupture or a tilt of the region between the Camp Rock-Emerson and Johnson Valley Faults. Between the Camp Rock-Emerson and Johnson Valley Faults, negative phase gradients occur in linear patterns striking N-NE (Plate 3a). It is likely that these correspond to secondary fault rupture at depth. The fringes across these secondary faults ramp downward with increasing range, indicating relative ground movement away from the satellite on the western sides of the faults. If no vertical deformation is assumed, this evidence, combined with the observation of negative phase gradients and the orientations of the fractures, indicates left-lateral displacements across these secondary structures. Offsets along each of the secondary faults between the Johnson Valley Fault and the main rupture are typically 2 rad which is equivalent to 9 mm of LOS displacement.

The elongated fringe pattern in the upper Johnson Valley is limited to the north by an arcuate feature seen in the phase gradient map (Plate 3a) which defines the transition of the surface morphology from alluvial fill to mountainous. This feature demarcates the northern extension of the Fry Mountains (area marked B in Plate 3a) and is one of the bounds on a zone of complex deformation [Zebker *et al.*, 1994, Plate 6, area B] that extends west to the Ord Mountains, north to the rupture on the Camp Rock Fault, and south to the Fry Mountains. Although previous workers have interpreted this region to contain "cracking" [Zebker *et al.*, 1994], analysis of the azimuth and range gradient maps indicates drainage patterns intersecting a fracturing pattern consistent with the style of deformation in the upper Johnson Valley. While geologic maps [Dibblee, 1964] of the area show the termination of the Johnson Valley Fault near its intersection with the Fry Mountains, the interferometric phase gradient shows an offset along a fracture connecting the mapped terminus of the Johnson Valley Fault with the Camp Rock Fault near the terminus of the earthquake rupture (Plates 3a and 3c). This linkage is not obvious in the fringe map (Plate 3b). This extension of the Johnson Valley Fault is the only coherent feature within the zone of complex deformation. Geologic mapping results show an east-side-down offset along a short fracture intersecting the end of the rupture on the Camp Rock Fault near GPS site 7000 (Plate 3c) that may correspond to this northward extension of the Johnson Valley Fault (K. LaJoie, personal communication, 1997).

While the northern end of the Fry Mountains intersects the main rupture trace, from the west, at the north end of the step-over region linking the Emerson Fault and the Camp Rock Fault, the south end of the step-over region is flanked to the east by a northeastwardly trending Mesozoic structure called Iron Ridge (Plate 3c). After the earthquake, two NE to east striking zones of aftershocks bordered Iron Ridge to the north and south (Plate 1) [Hauksson *et al.*, 1993]. The northern zone of aftershocks is associated with triggered slip on left-lateral, NE striking fractures [Hart *et al.*, 1993; K. LaJoie, personal communication, 1997].

Iron Ridge corresponds directly to a region of rounded, nearly circularly enclosed fringes in the interferogram (Plate 3b, label C). Fringes ramp upward to the west with positive phase gradient on the satellite side of Iron Ridge and ramp downward to the west with negative phase gradient on the opposite side. The semi-circular fringes are most likely indicative of uplift during the time period surrounding the earthquake with the central fringe representing maximum displacement toward the satellite. The phase variation across this feature is 37.5 rad representing 16.8 cm of

LOS displacement. The zone of semicircular fringes is cut to the northeast by the West Calico Fault (WCF) (Plate 1) and bounded farther to the east by a southeastward extension of the Calico Fault as evidenced in the interferometric phase gradient map (Figure 5a) and previously mapped fault locations (Plate 3c).

The phase gradient is positive along linear features (Plate 3c, label D) located southwest of the Johnson Valley which correspond to the Lenwood Fault, a northern extension of the Old Woman Fault, and an unidentified fault west of the Old Woman Fault (Plate 3c). The fringe map exhibits upward ramping of fringes across these structures from east to west indicating relative displacement toward the satellite on the west sides of the faults. LOS displacements across the faults are typically 15 mm. If the displacement across these faults was purely horizontal, the phase gradient features and fringe patterns indicate left-lateral sympathetic slip. If the displacement is vertical, there was uplift on the west sides of these faults relative to the east sides.

4.2. Calico Fault and Newberry Fractures

The Calico Fault (Plates 1 and 4) runs beneath the Mojave Valley in the left half of Plate 4. The phase gradient is negative along this fault while the deformation fringe phase shows down-ramping from east to west, indicating relative displacement away from the satellite on the west side of the fault. A strain concentration on this fault is not obvious in the fringe map. The LOS displacement across this fault is 8-9 mm. Assuming only horizontal offset, the interferometric evidence suggests that the offset was right-lateral. This agrees with mapping results reported by *Hart et al.* [1993].

The fractures in the center of Plate 4 have been mapped and named the Newberry fractures [*Unruh et al.*, 1994; K. LaJoie, personal communication, 1997]. Geologic mapping shows that they are purely extensional in a NE-SW direction. LOS displacements across the fractures range from 5 to 22 mm. Associated with these fractures, the interferometry results show two regions of enclosed fringe patterns. A relative LOS displacement of 13 mm is present across the northern fringe pattern, while a relative LOS displacement of 44 mm is present across the southern fringe pattern. The interferogram fringes ramp down toward the centers of the patterns, and the phase gradients are negative on the satellite sides of the fringe patterns and positive on the sides farther from the satellite. Because of their association with the extensional Newberry fractures and their location near Troy Dry Lake, the ground features are here interpreted as subsidence basins.

4.3. Barstow Aftershock Cluster and Coyote Lake

The Barstow earthquake cluster trended north to northwest (Plates 1 and 5b) and did not occur on known surface faults. The maximum magnitude earthquake in the cluster occurred on August 5, 1992 [*Hauksson et al.*, 1993], with magnitude 4.7 (Council of the National Seismic System (CNSS) earthquake database). The fringe pattern in the left-hand portion of Plate 5 consisting of two, coupled bull's-eyes (one positive LOS displacement and one negative LOS displacement) straddles the intersection of the Barstow cluster, the Calico Fault and the Coyote Lake Fault (Plate 5c). Several earthquakes with magnitude greater than 3.5 occurred at or near this location during the time period between April 24 and August 7, 1992 (Plates 1 and 5b; stars). The phase gradient image shows little indication of a surface fault rupture. The fringes indicate right-lateral offset across the Calico Fault with vertical uplift of the Calico

Mountains, or left-lateral offset across the conjugate Coyote Lake Fault. The shocks in the Barstow cluster had a predominantly right-lateral, strike-slip focal mechanism [*Hauksson et al.*, 1993]. The relative LOS displacement measured across the enclosed fringes is 5.3 cm.

Flanking the east side of the Calico Mountains, a structure which may be a northeastern branch of the Calico Fault is apparent in the phase gradient map (Plate 5a, label C; Plate 5c). The fault appears to include a series of right-lateral strike-slip offsets connected by extensional cracks. This is evidenced by the change in phase gradient signature from negative to a negative-positive double as the fracture changes orientation. Typical LOS displacements of 5 mm are associated with right-lateral offsets across this fault.

Northeast of this apparent northeastern branch of the Calico Fault is Coyote Dry Lake (Plate 5a, label D; Plate 5c). The deformation fringe phase and phase gradient maps show deformation of the lake shore between the time period April 24 and August 7, 1992, and a small amount of what can be interpreted as subsidence within the lake bed itself. Subsidence in the interior of the lake bed was 9-10 mm LOS, while deformation along the shoreline reached 13 mm LOS across some features. This deformation could be either earthquake related or indicate a seasonal change of the lakebed between spring and summer.

5. Discussion

The interferometric results presented here indicate that small-scale LOS deformations associated with the Landers earthquake occurred within 75-100 km of the main rupture. These small-scale deformations are superimposed on a deformation field such as might be expected from the response of an elastic lithosphere to the Landers earthquake [e.g., *Massonnet et al.*, 1993, Figure 3b]. These small-scale deformations are associated with secondary fractures, preexisting faults, dry lake beds, and mountainous regions; they provide insight into the formation of such geomorphic features and help define the role of these features in fault interactions. Furthermore, interferometric maps showing small-scale deformations could be used as a reconnaissance tool for mapping faults and coseismic displacements and for decisions involving GPS receiver location or GPS data exclusion from inversions that assume elastic behavior.

The long, linear secondary faults superimposed on the dense, elongated fringe pattern between the Johnson Valley Fault and the main rupture (Plate 3) indicates a shear zone between the main rupture trace and the Johnson Valley Fault with probable faulting of the basement rock. Faulting is believed to extend to the basement because it is unlikely that the overlying alluvium is cohesive enough to sustain fractures with lengths of 10 km. Geologic mapping of surface ruptures indicative of shear zones in alluvium due to the Landers earthquake shows a maximum length of shear fractures to be of the order of 500 m [e.g., *Johnson et al.*, 1994; *Sowers et al.*, 1994].

The fractures between the rupture on the Camp Rock-Emerson Faults and the Johnson Valley Fault are similar in style to fracture patterns seen in much smaller versions of shear zones associated with the Landers earthquake [e.g., *Johnson et al.*, 1994]. As the orientation of a fracture changes with respect to the look direction of the radar, the sense of slip on a fracture with the same phase gradient sign changes. Hence the smaller fractures close to the Johnson Valley Fault (Plate 3c) most likely

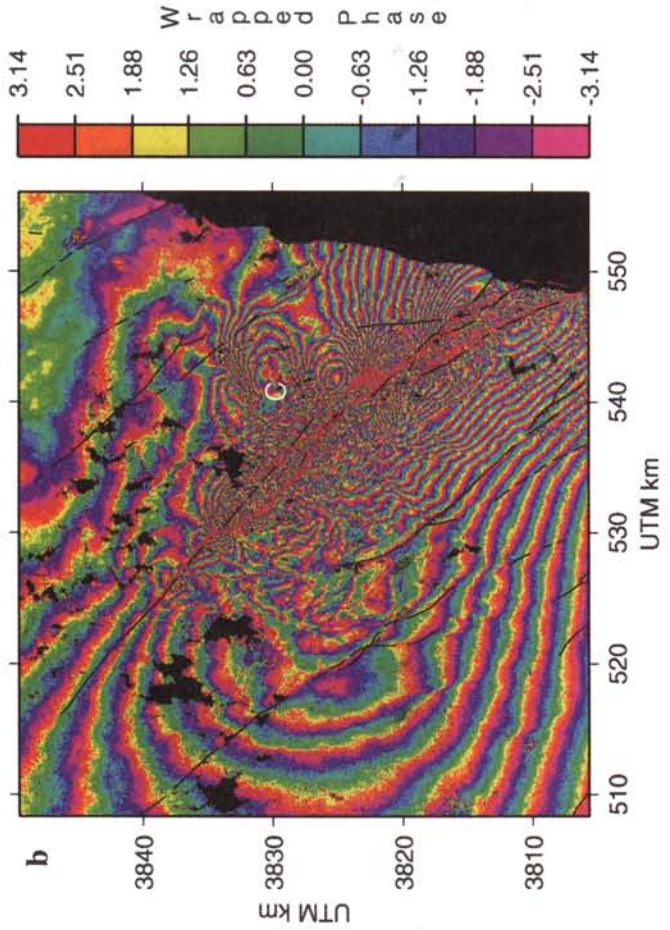
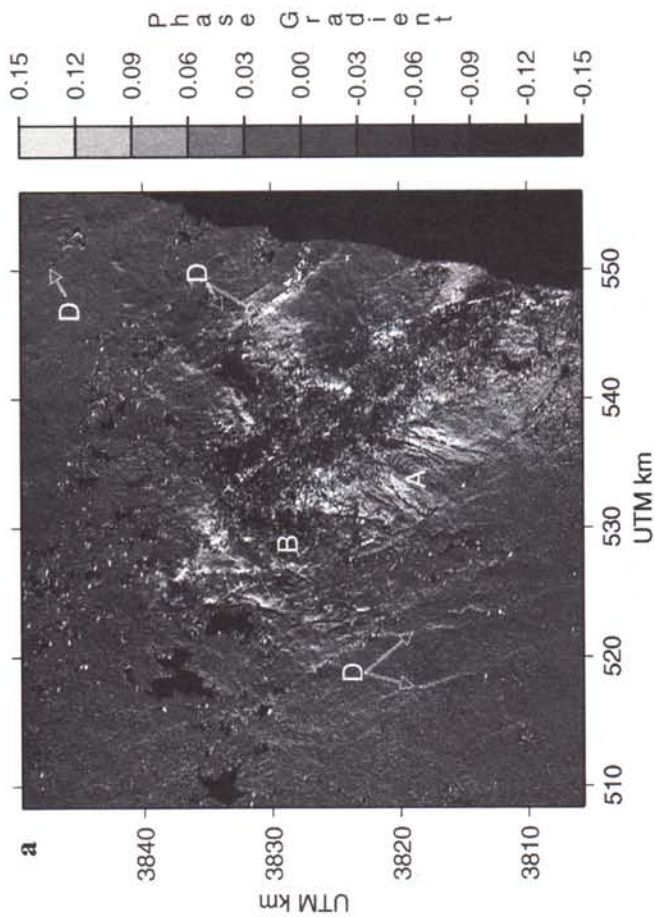
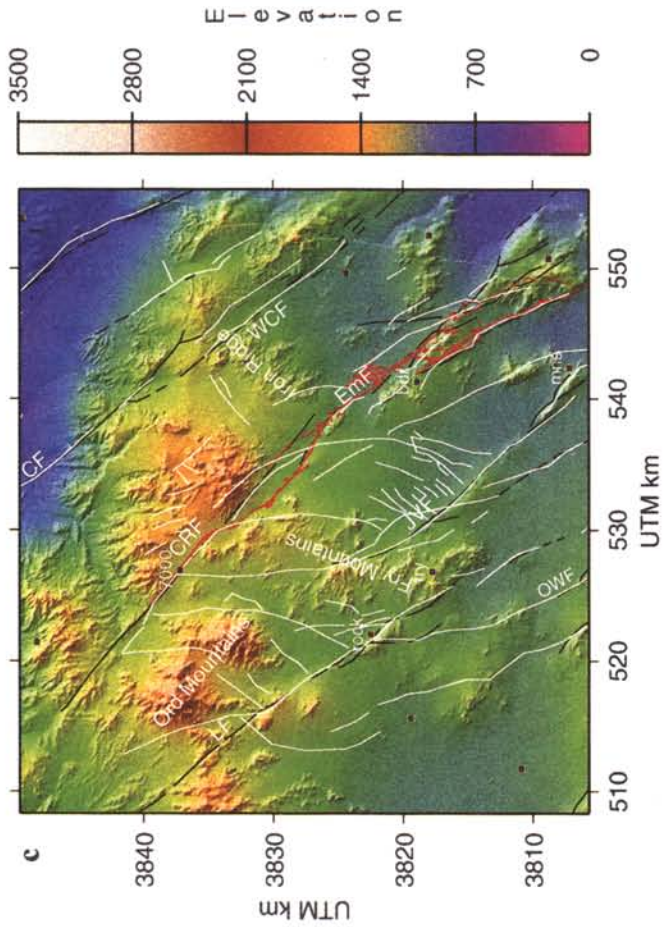
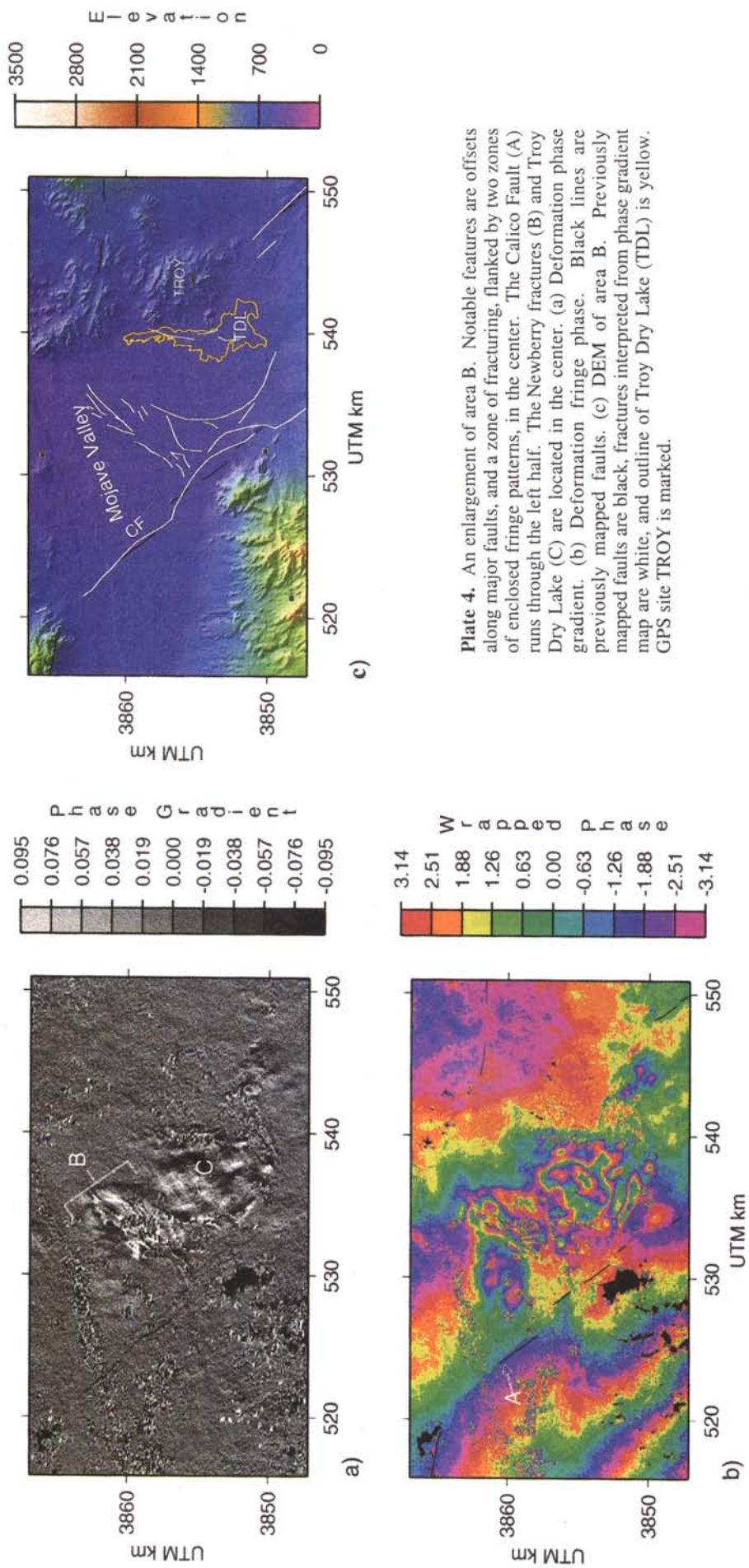


Plate 3. An enlargement of area A. Notable features include long secondary fractures (A) between the Johnson Valley Fault and the main rupture on the Camp Rock-Emerson Faults, complex zones of fracture (B) to the south of the end of rupture delimited by arcuate traces in the phase gradient map, nearly enclosed fringe patterns (C) on the northeast side of the rupture, and small offsets along major faults (D) excluding those directly involved in the earthquake rupture. (a) Deformation phase gradient. (b) Deformation fringe phase with previously mapped faults in black and geologically mapped surface rupture [Sielh *et al.*, 1993] in red. (c) DEM of area A. Previously mapped faults are black, field-mapped earthquake rupture is red, and fractures interpreted from phase gradient map are white. Fault abbreviations are as in Figure 1. Labeled GPS sites are Rock, Fry, Means (mns), Boulder (bdr), and 7000.



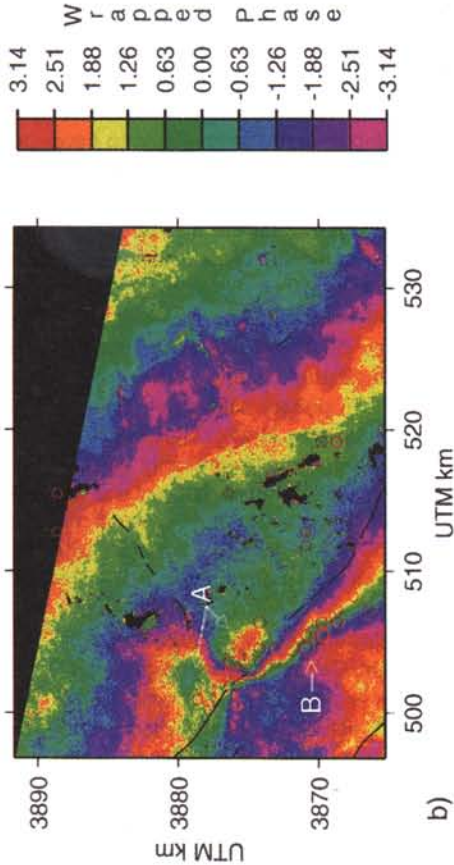
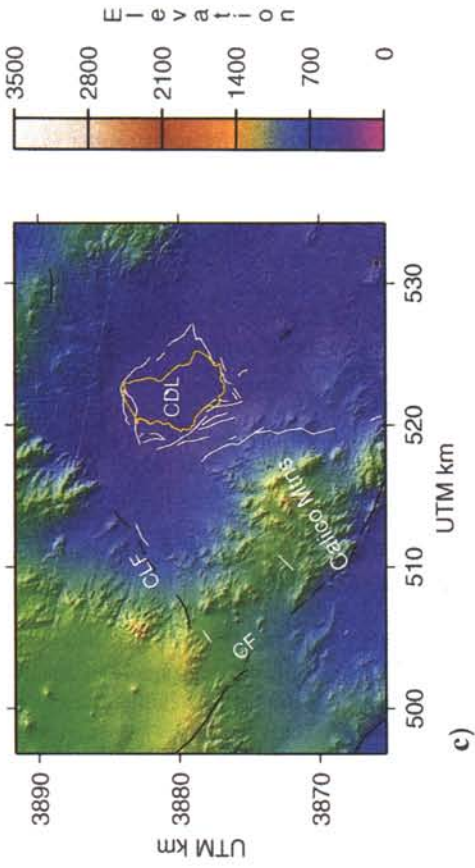


Plate 5. An enlargement of area C. The enclosed fringes labeled "A" indicate deformation related to the intersection of the Barstow Cluster and preexisting faults. A northern branch of the Calico Fault (C) and some deformation around the shoreline of Coyote Dry Lake (D) are apparent in the phase gradient image. (a) Deformation phase gradient. (b) Deformation fringe phase with faults in black and shocks in red. (c) DEM of area C. Previously mapped faults are black, fractures interpreted from phase gradient map are white, and outline of Coyote Dry Lake (CDL) is yellow.

have left-lateral offsets across them, while the larger fractures that traverse the entire valley floor to intersect with the main rupture most likely accommodate left-lateral offsets near the Johnson Valley Fault which change to right-lateral offsets as the fractures near the main rupture. This behavior is similar to that of a curved fracture in the Happy Trail shear zone observed by Johnson *et al.* [1994]. The fracture flanking the eastern side of the Fry Mountains (Plate 3c) probably also accommodated some east-side-up motion similar to some fractures seen in the Happy Trail shear zone. Because of their regular spacing between mountain ranges, the long fractures in the Johnson Valley and between the Lenwood Fault and the northwestward continuation of the earthquake rupture may be related to and/or facilitate the uplift of the Fry and Ord Mountains (Plate 3c).

The fractures in the upper Johnson Valley may have collectively accommodated some significant portion of right-lateral shear. Murray *et al.* [1993] require ~0.5 m of right-lateral slip on a northwest trending fault between stations Boulder and Means on the east and Old Woman, Fry, and Rock on the west (Plate 3c) to fit their trilateration data to an elastic half-space model. The tie lines between the above stations span the upper Johnson Valley. Because displacement on the upper Johnson Valley Fault (which runs through the upper Johnson Valley between the Johnson Valley Fault and the Camp Rock-Emerson Faults) was of the order of centimeters (K. LaJoie, personal communication, 1997), offset on another fault or over a region is necessary to fit the geodetic data. This discrepancy could be resolved with further modeling of the displacement expected from an elastically responding lithosphere and comparison of models to interferometric results.

Stress changes on faults not involved in the main rupture are indicated by published and preliminary modeling of the stress field induced by the earthquake in an elastic half-space [Harris and Simpson, 1992; Stein *et al.*, 1992; R. Simpson, personal communication, 1997]. Two lines of evidence suggest that InSAR observed displacements on the Lenwood and Old Woman Faults were vertical, west-side-up rather than left-lateral and sympathetic. First, Coulomb failure stress is predicted to have decreased by only as much as 17 bars across the Lenwood and northern portion of the Old Woman Fault [Harris and Simpson, 1992], while the calculated stress drop on the Landers earthquake surface rupture was ~85 bars; assuming that the level of stress on other faults in the Mojave Desert before the earthquake was similar to that on the faults involved in the Landers earthquake, a 17-bar stress drop would not be enough to induce sympathetic slip. Second, preliminary modeling results show vertical displacements across these faults, if present, should be west-side-up (R. Simpson, internet communication, 1997). Thus, while the Lenwood and northern Old Woman Faults probably relaxed subsequent to the Landers earthquake, the stress drop was not enough to induce left-lateral, sympathetic slip. Instead, the displacements measured in the SAR interferogram were probably vertical, west-side-up which is consistent with the geomorphology (Plate 1).

Geologic field mapping and tectonic modeling suggest that the offset observed by InSAR on the Calico Fault was right-lateral. The Calico Fault (Figure 6) lies in a region of the model of Stein *et al.* [1992] in which faults on optimally oriented planes were brought closer to failure by the Landers earthquake-induced stress field. Geologic mapping indicates right-lateral slip on the Calico Fault [Hart *et al.*, 1993]. Also, there are no geomorphic structures directly related to the Calico Fault that would indicate that it accommodates vertical motions (Plate 4c).

The Newberry fractures were mapped by geologists [Unruh *et al.*, 1994; K. LaJoie, personal communication, 1998] immediately after the Landers earthquake. The Unruh *et al.* [1994] study shows a series of parallel, linear fractures trending N-NE, while more detailed mapping by K. LaJoie in the field and using air photographs shows curved fractures similar to those seen in the SAR interferogram (Plates 4a and 4c). These fractures opened preexisting structures and exhibited normal dip-slip separation of as much as 12 cm and lateral offsets of 5 cm or less [Unruh *et al.*, 1994]. These structures are interpreted by Unruh *et al.* [1994] as evidence of pure northwest-southeast extension. The collocation of these fractures with extensional basins may show how, incrementally, the Troy Dry Lake bed was formed or may be related to internal deformation of the lake bed itself. The region surrounding the Newberry fractures and Calico Fault shows a deviation from the fringe pattern expected from modeling an elastic lithosphere's response to the earthquake [e.g., Massonnet *et al.*, 1993]. This deviation could be due to inhomogeneities in the crust and may account for some of the anomalous motion at Mojave GPS network station TROY (Plate 4c) where motion was 150% of that expected from elastic half-space models [Miller *et al.*, 1993].

Deformation near the Calico Fault related to the Barstow earthquake cluster is a further example of small-scale deformation associated with the Landers earthquake-induced stress field. Earthquakes of the Barstow Cluster were confined to depths less than 10 km and occurred along a linear trend not related to any geologically mapped fault. The Barstow shocks began 6-8 hours after the Landers main shock [Hauksson *et al.*, 1993]. In the interferogram (Plate 5b), the only clear fringe pattern associated with the Barstow Cluster occurs where its trend intersects the Calico and Coyote Faults. However, there is negative shading in the phase gradient map aligned with the cluster (Plate 5a) that indicates diffuse right-lateral shear likely related to faulting at depth. The enclosed fringe patterns at the intersection of the Calico and Coyote Lake Faults (Plate 5b) are probably indicative of uplift of the Calico Mountains on the southeast side of the Coyote Lake Fault and subsidence on the northwest side of the Coyote Lake Fault as the Calico Fault accommodated a right-lateral offset.

Because GPS results adequately fit far-field coseismic displacements as predicted by an elastic half-space model [Bock *et al.*, 1993; Blewitt *et al.*, 1993], such a model can be presumed to be a good one for the large-scale displacement pattern associated with the earthquake rupture. Small-scale anomalies in the displacement field are most likely confined to the region within 100 km of the earthquake rupture and are likely due to interaction of crustal and surficial structures with the earthquake induced stress field. These small-scale anomalies could account for some of the deviation from an elastic half-space model in the near-field such as noted by Miller *et al.* [1993], Murray *et al.* [1993], and Hudnut *et al.* [1994].

It is unfortunate that more detailed field observations of the Landers earthquake rupture are not available to ground truth InSAR observations. Air photographs show offsets along some fractures that corroborate InSAR observations (Newberry fractures) but do not exhibit fine details such as seen in the upper Johnson Valley region of the interferogram (K. LaJoie, personal communication, 1997). If InSAR observations including the displacement field and displacement phase gradient were made available within a few months of the earthquake, it might have been possible to plan field surveys to study features seen in the interferogram. Our own expedition into the field (January 1997)

indicated that much of the millimeter and centimeter scale deformation has been eroded by natural processes and recreational vehicles.

6. Conclusions

SAR interferometry allows near total spatial coverage of the radar LOS deformation and the gradient of the radar LOS deformation in the region of a major earthquake. This spatial coverage allows us to study heterogeneity in the deformation field. This heterogeneity can be investigated using the phase gradient map which highlights offsets on major faults, secondary fractures, and geologic structures that are not apparent in interferogram fringe maps. Interpretations of these interferogram fringe and phase gradient maps depend on ancillary information including geological field mapping, GPS measurements, and lithospheric modeling to determine meaningful displacements on and across geological structures.

Our observations show that there is localized heterogeneity in the deformation field of the Landers earthquake within 80-100 km of the main rupture. Unmapped faults or questionable extensions of previously mapped faults which experienced triggered slip are highlighted by the phase gradient observations. Secondary fractures in the upper Johnson Valley indicate a shear zone between the Johnson Valley Fault and the main rupture that may include the region between the Lenwood Fault and the Camp Rock Fault occupied by the Fry and Ord Mountains. Previously mapped fractures associated with extension in the Mojave Valley are apparent in the phase gradient map and corroborate field observations. Also, there are correlations between fringe patterns and geomorphology indicating incremental deformation of extensional and compressional structures including Iron Ridge, the Calico Mountains, Coyote Dry Lake, and Troy Dry Lake.

Appendix A: Interferometer Geometry and Equations

If λ is the wavelength of the radar and $\delta\rho$ is the range difference between the reference and repeat passes of the satellite, the interferogram phase of a point on the ground is $\phi = (4\pi/\lambda)\delta\rho$. We present the interferometer geometry and range difference attributable to three factors: (1) spheroidal Earth with no topography, (2) topography, and (3) surface deformation. We use these relationships to show how the phase gradient of interferograms may be scaled so that phase gradients of interferograms with different baselines may be added to and subtracted from each other.

A1. Range Difference Due to Spheroidal Earth

The relationship between the repeat-pass range to an Earth with no topography or surface deformation ($\rho + \delta\rho_e$), the reference-pass range (ρ), the baseline length (B), and the baseline elevation angle (α) is provided by the law of cosines [Zebker et al., 1994] (Figure A1). Applying the parallel ray approximation [Zebker and Goldstein, 1986], the range difference is

$$\delta\rho_e = -B \sin(\theta_0 - \alpha) \quad (A1)$$

where θ_0 is the look angle to a spheroidal Earth defined by $\cos \theta_0 = (c^2 + \rho^2 - r^2)/2\rho c$, where c is the distance from the center of the

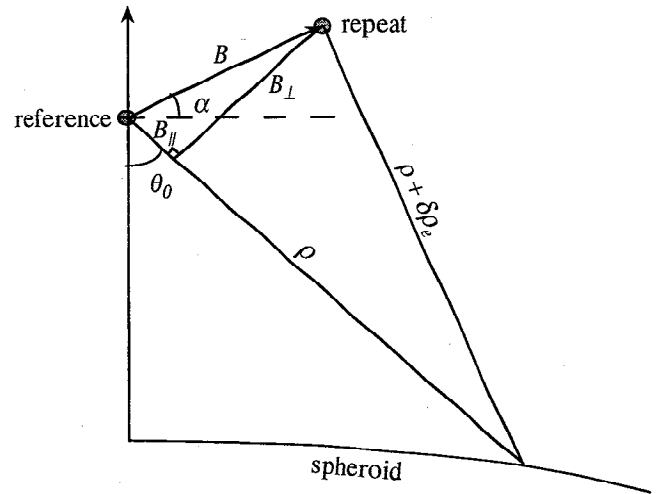


Figure A1. InSAR geometry for spheroidal Earth with no topography or surface deformation. Here ρ is range from the "reference" satellite pass to a location on the spheroid, $\rho + \delta\rho_e$ is range from the "repeat" satellite pass to the same location, θ_0 is the radar look angle, α is the baseline elevation angle, B is the baseline length, B_{\parallel} is the component of the baseline parallel to the satellite reference pass line of site, and B_{\perp} is the component of the baseline perpendicular to the satellite reference pass line of site.

Earth to the location of the satellite reference pass and r is the distance from the center of the Earth to the location on the Earth that is illuminated when the range from the satellite to the Earth is ρ .

We define the components of the baseline parallel (B_{\parallel}) and perpendicular (B_{\perp}) to the range ray referenced to a spheroidal Earth as

$$B_{\parallel} = B \sin(\theta_0 - \alpha) \quad (A2a)$$

$$B_{\perp} = B \cos(\theta_0 - \alpha) \quad (A2b)$$

The range difference due to a spheroidal Earth with no topography is equal to the parallel component of the baseline.

A2. Range Difference Due to Topography on a Spheroidal Earth

Here the range difference ($\delta\rho_e + \delta\rho_t$) is influenced by the topography (see Figure A2) so that

$$\delta\rho_e + \delta\rho_t = -B \sin(\theta_0 + \delta\theta_t - \alpha) \quad (A3)$$

where θ is the angle between the vertical and the reference pass range ray and is the sum of two terms: θ_0 is the look angle for a spheroidal Earth with no topography and $\delta\theta_t$ is the angular distortion caused by the presence of topography.

Since the spacecraft is far from the Earth, $\delta\theta_t$ is small and the range difference due to topography on a spheroidal Earth ($\delta\rho_e + \delta\rho_t$) is

$$\delta\rho_e + \delta\rho_t = -(B_{\parallel} + \delta\theta_t B_{\perp}) \quad (A4)$$

We perform the "flat Earth" correction by computing B_{\parallel} using equation (A1) and removing it from the interferogram phase.

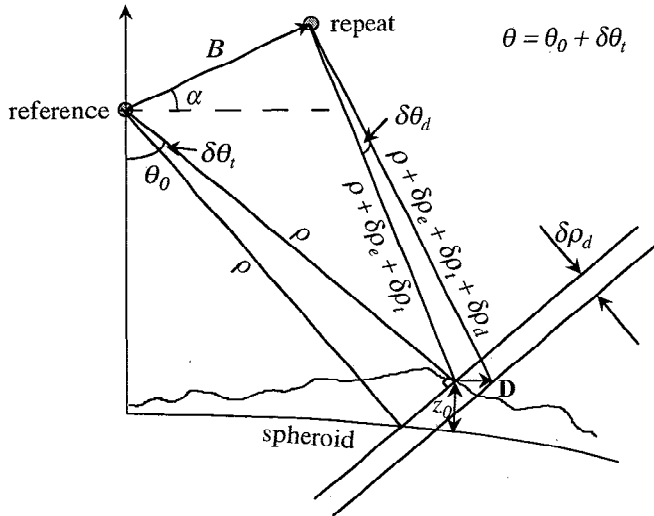


Figure A2. InSAR geometry for spheroidal Earth with topography and surface deformation. Here ρ is range from the “reference” satellite pass to a location on the surface of the Earth at elevation z_0 , $\rho + \delta\rho_e + \delta\rho_t$ is range from the “repeat” satellite pass to the same location, $\rho + \delta\rho_e + \delta\rho_t + \delta\rho_d$ is the range from the repeat pass of the satellite to the same piece of Earth after it has been displaced by \mathbf{D} , θ_0 is the radar look angle to the reference spheroid for range ρ , $\delta\theta_t$ is the topographic angular distortion, $\delta\theta_d$ is the displacement angular distortion, α is the baseline elevation angle, and B is the baseline length. When measuring deformations using space-based InSAR, the three range rays (excluding the one drawn to the reference spheroid) in the figure can be considered parallel to each other making $\delta\theta_d$ essentially zero. The InSAR measured component of the displacement, \mathbf{D} , is that which is in the direction of the satellite LOS. This displacement is equal to $\delta\rho_d$.

A3. Range Difference for Topography and Deformation on a Spheroidal Earth

By inspecting Figure A2 and making several assumptions, one comes to the conclusion that a displacement vector is projected into the satellite line-of-sight direction and it contributes additively to the range change due to topography and a spheroidal Earth. Because the spacecraft is far from the Earth (800 km), it can be assumed that the ray with length ρ is parallel to the ray with length $\rho + \delta\rho_e + \delta\rho_t$, and the ray with length $\rho + \delta\rho_e + \delta\rho_t + \delta\rho_d$. Implicit in this assumption is that $\delta\theta_d$ is essentially zero and the radar signal wavefronts are perpendicular to the above rays. Now, the range difference is

$$\delta\rho = \delta\rho_e + \delta\rho_t + \delta\rho_d = -(B_{\parallel} + \delta\theta_t B_{\perp} - \delta\rho_d) \quad (\text{A5})$$

To isolate the range change due to deformation, we remove the flat Earth range change (see above) and the topographic range change estimated from other interferograms (see below).

A4. Scale Factors for Interferograms Which Have Had the Flat Earth Correction Applied

Consider two interferograms which have both had the flat Earth correction applied. Interferogram 1 (ϕ_1) has phase due only to topographic angular distortion and interferogram 2 (ϕ_2) has phase due to topographic angular distortion and displacement. If the interferograms are matched to the same reference geometry,

the topographic angular distortion is assumed to be the same for both and interferogram 1 can be scaled by the ratio of the perpendicular baselines and subtracted from interferogram 2 to yield the displacement in the satellite LOS [Zebker *et al.*, 1994]:

$$\phi_2 - \frac{B'_1}{B_1} \phi_1 = \frac{4\pi}{\lambda} \delta\rho_d \quad (\text{A6})$$

where B_1 is the perpendicular component of the baseline for interferogram 1 and B'_1 is the perpendicular component of the baseline for interferogram 2.

The interferogram scale factor (see equation (6)) is the ratio of the perpendicular baselines of each starting interferogram. This scale factor can be applied directly to the interferogram phase gradient (in range) to extract the interferogram deformation phase gradient, $4\pi/\lambda (\partial\delta\rho_d/\partial\rho)$, using

$$\frac{\partial\phi_2}{\partial\rho} - \frac{B'_1}{B_1} \frac{\partial\phi_1}{\partial\rho} = \frac{4\pi}{\lambda} \frac{\partial\delta\rho_d}{\partial\rho} \quad (\text{A7})$$

The LOS displacement gradient, $\partial D_{\text{LOS}}/\partial\rho$, is then equal to the deformation range-difference gradient, $\partial\delta\rho_d/\partial\rho$.

Appendix B: Low-Pass and Gradient Filters

Interferograms formed from full-resolution, SAR images contain significant phase noise. The gradient operation amplifies the shortest-wavelength noise resulting in a noisy estimate of phase gradient. To suppress a portion of this noise, we filter the data before computing the gradient by forming a multilook average using a Gaussian-shaped filter. We have designed a convolution filter that is nearly isotropic in ground range/azimuth space consistent with the sampling frequency of the radar:

$$f(x, y) = \exp\left[-\frac{x^2 + y^2}{2\sigma^2}\right] \quad (\text{B1})$$

where x is range, y is azimuth, and σ is filter width. Based on visual inspection of a variety of interferograms, we have chosen $\sigma = 8$ m so that 0.5 gain occurs at a wavelength of 42 km in slant range (~ 107 m in ground range) and 84 m in azimuth. Based on a cross-spectral analysis of repeat tandem interferograms [Sandwell and Price, 1997], we found signal-to-noise ratios of 1 at a wavelength of 230 m in ground range and 180 m in azimuth. Thus the low-pass Gaussian is passing all of the relevant signals.

The gradient operation follows the low-pass Gaussian filter. We have designed a derivative filter using the Parks-McClellan approach. The filter coefficients and imaginary response are shown in Figure B1. The derivative filter is 17 points long (solid curve, Figure B1a), while the Gaussian filter is only 5 points long in range (dashed). Figure B1b shows the gain for a theoretical derivative (dotted) and the numerical derivative (solid). The convolution of the Gaussian and derivative filters (dashed) has a peak response at a wavelength of 50 m. The location of the peak can be adjusted by varying σ in equation (B1), although the derivative filter limits the best resolution to 30 m wavelength.

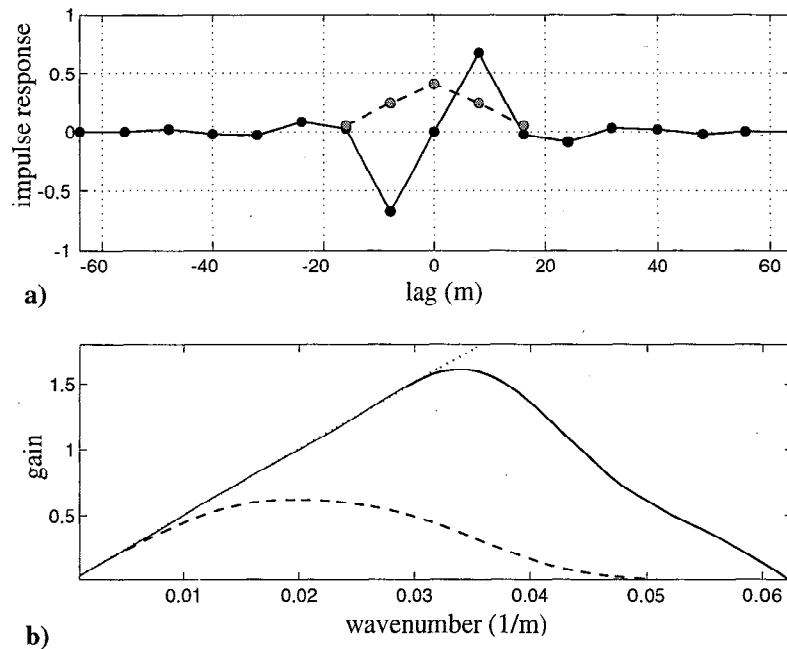


Figure B1. (a) Filters used in interferogram phase gradient formation. Solid line is the gradient filter, dashed line is the smoothing filter. (b) Gain for theoretical derivative filter (dotted line), numerical derivative filter (solid line), and the convolution of the Gaussian smoothing and numerical derivative filters (dashed line).

Acknowledgments. We thank Howard Zebker for help developing an InSAR processing system and for providing us with some of the algorithms used to process our data. Duncan Agnew suggested we formalize the relationship between the phase gradient and the deformation gradient tensor and pointed us toward important geodetic observations pertinent to this work. We thank Ken Laloie and Bob Simpson for discussions aiding in the interpretation of the data. We thank Bernard Minster for a careful and constructive internal review. Finally, we thank Paul Rosen and Howard Zebker for helpful external reviews. This research was supported by NASA (HPCC/ESS and SENH Programs) and NSF (EAR-19201). Evelyn Price was supported as a SIO/NASA/Goddard JCOSS student fellow.

References

- Blewitt, G., M.B. Heflin, K.J. Hurst, D.C. Jefferson, F.H. Webb, and J.F. Zumberge, Absolute far-field displacements from the 28 June 1992 Landers earthquake sequence, *Nature*, *361*, 340-342, 1993.
- Bock, Y., et al, Detection of crustal deformation from the Landers earthquake sequence using continuous geodetic measurements, *Nature*, *361*, 337-340, 1993.
- Carter, J.N., B.P. Luyendyk, and R.R. Terres, Neogene clockwise rotation of the eastern Transverse Ranges, California, suggested by paleomagnetic vectors, *Geol. Soc. Am. Bull.*, *98*, 199-206, 1987.
- Curlander, J.C., and R.N. McDonough, *Synthetic Aperture Radar: Systems and Signal Processing*, edited by J.A. Kong, John Wiley, New York, 1991.
- Dibblee, T.W., Geologic map of the Rodman Mountains quadrangle, San Bernardino County, California, *U.S. Geol. Surv. Publ.*, *1-430*, 1964.
- Dokka, R.K., and C.J. Travis, Late Cenozoic strike-slip faulting in the Mojave Desert, California, *Tectonics*, *9*, 311-340, 1990a.
- Dokka, R.K., and C.J. Travis, Role of the eastern California shear zone in accommodating Pacific-North American plate motion, *Geophys. Res. Lett.*, *17*, 1323-1326, 1990b.
- Doser, D.L., A re-examination of the 1947 Manix, California, earthquake sequence and comparison to other sequences within the Mojave Block, *Bull. Seismol. Soc. Am.*, *80*, 267-277, 1990.
- Feigl, K.L., A. Sergeant, and D. Jacq, Estimation of an earthquake focal mechanism from a satellite radar interferogram: Application to the December 4, 1992 Landers aftershock, *Geophys. Res. Lett.*, *22*, 1037-1040, 1995.
- Fuis, G.S., and A.G. Lindh, A change in fault-plane orientation between foreshocks and aftershocks of the Galway Lake earthquake, $M_1 = 5.2$, 1975, Mojave Desert, California, *Tectonophysics*, *52*, 601-602, 1979.
- Gabriel, A.K., and R.M. Goldstein, Crossed orbit interferometry: Theory and experimental results from SIR-B, *Int. J. Remote Sens.*, *9*, 857-872, 1988.
- Gabriel, A.K., R.M. Goldstein, and H.A. Zebker, Mapping small elevation changes over large areas: Differential radar interferometry, *J. Geophys. Res.*, *94*, 9183-9191, 1989.
- Garfunkel, Z., Model for the late Cenozoic tectonic history of the Mojave Desert and its relation to adjacent areas, *Geol. Soc. Am. Bull.*, *85*, 1931-1944, 1974.
- Goldstein, R.M., Atmospheric limitations to repeat-track radar interferometry, *Geophys. Res. Lett.*, *22*, 2517-2520, 1995.
- Goldstein, R.M., H.A. Zebker, and C.L. Werner, Satellite radar interferometry: Two-dimensional phase unwrapping, *Radio Sci.*, *23*, 713-720, 1988.
- Graham, L.C., Synthetic interferometer radar for topographic mapping, *Proc. IEEE*, *62*, 763-768, 1974.
- Harris, R.A., and R.W. Simpson, Changes in static stress on southern California faults after the 1992 Landers earthquake, *Nature*, *360*, 251-254, 1992.
- Hart, E.W., W.A. Bryant, and J.A. Treiman, Surface faulting associated with the June 1992 Landers earthquake, California, *Calif. Geol.*, *46*, 10-16, 1993.
- Hauksson, E., State of stress from focal mechanisms before and after the 1992 Landers earthquake sequence, *Bull. Seismol. Soc. Am.*, *84*, 917-934, 1994.
- Hauksson, E., L.M. Jones, K. Hutton, and D. Eberhart-Phillips, The 1992 Landers earthquake sequence: Seismological observations, *J. Geophys. Res.*, *98*, 19,835-19,858, 1993.
- Hill, R.L., and D.J. Beeby, Surface faulting associated with the 5.2 magnitude Galway Lake earthquake of May 31, 1975: Mojave Desert, San Bernardino County, California, *Geol. Soc. Am. Bull.*, *88*, 1378-1384, 1977.
- Hill, R.L., J.A. Treiman, and J.W. Given, Geologic Study of the Homestead Valley Earthquake Swarm of March 15, 1979, *California Geology*, 60-67, 1980.
- Hudnut, K.W., et al., Co-seismic displacements of the 1992 Landers earthquake sequence, *Bull. Seismol. Soc. Am.*, *84*, 625-645, 1994.
- Johnson, A.M., R.W. Fleming, and K.M. Cruikshank, Shear zones formed along long straight traces of fault zones during the 28 June 1992

- Landers, California, earthquake, *Bull. Seismol. Soc. Am.*, *84*, 499-510, 1994.
- Kanamori, H., H.K. Thio, D. Dreger, E. Hauksson, and T. Heaton, Initial investigation of the Landers, California earthquake of 28 June 1992 using TERRASCOPE, *Geophys. Res. Lett.*, *19*, 2267-2270, 1992.
- Li, F.K., and R.M. Goldstein, Studies of multibaseline spaceborne interferometric synthetic aperture radars, *IEEE Trans. Geosci. Remote Sens.*, *28*, 88-97, 1990.
- Malvern, L.E., *Introduction to the Mechanics of a Continuous Medium*, Prentice-Hall, Englewood Cliffs, N.J., 1969.
- Massonnet, D., and K.L. Feigl, Discrimination of geophysical phenomena in satellite radar interferograms, *Geophys. Res. Lett.*, *22*, 1537-1540, 1995a.
- Massonnet, D., and K.L. Feigl, Satellite radar interferometric map of the coseismic deformation field of the $M = 6.1$ Eureka Valley, California earthquake of May 17, 1993, *Geophys. Res. Lett.*, *22*, 1541-1544, 1995b.
- Massonnet, D., M. Rossi, C. Carmona, F. Adragna, G. Peltzer, K. Feigl, and T. Rabaut, The displacement field of the Landers earthquake mapped by radar interferometry, *Nature*, *364*, 138-142, 1993.
- Massonnet, D., K. Feigl, M. Rossi, and F. Adragna, Radar interferometric mapping of deformation in the year after the Landers earthquake, *Nature*, *369*, 227-230, 1994.
- McDonough, R.N., B.E. Raff, and J.L. Kerr, Image formation from spaceborne synthetic aperture radar signals, *Johns Hopkins APL Tech. Dig.*, *6*, 300-312, 1985.
- Miller, M.M., F.H. Webb, D. Townsend, M.P. Golombek, and R.K. Dokka, Regional coseismic deformation from the June 28, 1992, Landers, California, earthquake: Results from the Mojave GPS network, *Geology*, *21*, 868-872, 1993.
- Murray, M.H., J.C. Savage, M. Lisowski, and W.K. Gross, Coseismic displacements: 1992 Landers, California, earthquake, *Geophys. Res. Lett.*, *20*, 623-626, 1993.
- Peltzer, G., K.W. Hudnut, and K.L. Feigl, Analysis of coseismic surface displacement gradients using radar interferometry: New insights into the Landers earthquake, *J. Geophys. Res.*, *99*, 21,971-21,981, 1994.
- Peltzer, G., P. Rosen, F. Rogez, and K. Hudnut, Postseismic rebound in fault step-overs caused by pore fluid flow, *Science*, *273*, 1202-1204, 1996.
- Richter, C.F., The Manix (California) earthquake of April 20, 1947, *Bull. Seismol. Soc. Am.*, *37*, 171-179, 1947.
- Rosen, P.A., S. Hensley, H.A. Zebker, F.H. Webb, and E. Fielding, Surface deformation and coherence measurements of Kilauea Volcano, Hawaii from SIR-C radar interferometry, *J. Geophys. Res.*, *101*, 23,109-23,125, 1996.
- Sandwell and Price, Sums and Differences of Interferograms, *Eos Trans. AGU*, *78*(46), Fall Meet. Suppl., F144, 1997.
- Sauber, J., W. Thatcher, and S.C. Solomon, Geodetic measurement of deformation in the central Mojave Desert, California, *J. Geophys. Res.*, *91*, 12,683-12,693, 1986.
- Savage, J.C., M. Lisowski, and W.H. Prescott, An apparent shear zone trending north-northwest across the Mojave Desert into Owens Valley, eastern California, *Geophys. Res. Lett.*, *17*, 2113-2116, 1990.
- Scharoo, R., and P.N.A.M. Visser, Precise orbit determination and gravity field improvement for the ERS satellites, *J. Geophys. Res.*, *103*, 8113-8127, 1998.
- Sieh, K., et al., Near-field investigations of the Landers earthquake sequence, April to July 1992, *Science*, *260*, 171-176, 1993.
- Sowers, J.M., J.R. Unruh, W. R. Lettis, and T.D. Rubin, Relationship of the Kickapoo Fault to the Johnson Valley and Homestead Valley Faults, San Bernardino County, California, *Bull. Seismol. Soc. Am.*, *84*, 528-536, 1994.
- Stein, R.S., G.C.P. King, and J. Lin, Change in failure stress on the southern San Andreas fault system caused by the 1992 magnitude = 7.4 Landers earthquake, *Science*, *258*, 1328-1332, 1992.
- Tarayre, J., and D. Massonnet, Atmospheric propagation heterogeneities revealed by ERS-1 interferometry, *Geophys. Res. Lett.*, *23*, 989-992, 1996.
- Unruh, J.R., W.R. Lettis, and J.M. Sowers, Kinematic interpretation of the 1992 Landers earthquake, *Bull. Seismol. Soc. Am.*, *84*, 537-546, 1994.
- Werner, C.L., S. Hensley, R.M. Goldstein, P.A. Rosen, and H.A. Zebker, Techniques and applications of SAR interferometry for ERS-1: Topographic mapping, change detection, and slope measurement, *First ERS-1 Symposium - Space at the Service of our Environment*, Cannes, France, 205-210, 1992.
- Wesnousky, S.G., Earthquakes, Quaternary Faults, and Seismic Hazard in California, *J. Geophys. Res.*, *91*, 12,587-12,631, 1986.
- Zebker, H.A., and R.M. Goldstein, Topographic mapping from interferometric synthetic aperture radar observations, *J. Geophys. Res.*, *91*, 4993-4999, 1986.
- Zebker, H.A., and J. Villasenor, Decorrelation in interferometric radar echoes, *IEEE Trans. Geosci. Remote Sens.*, *30*, 950-959, 1992.
- Zebker, H.A., P.A. Rosen, R.M. Goldstein, A. Gabriel, and C.L. Werner, On the derivation of coseismic displacement fields using differential radar interferometry: The Landers earthquake, *J. Geophys. Res.*, *99*, 19,617-19,643, 1994.
- Zebker, H.A., P.A. Rosen, and S. Hensley, Atmospheric effects in interferometric synthetic aperture radar surface deformation and topographic maps, *J. Geophys. Res.*, *102*, 7547-7563, 1997.

E.J. Price and D.T. Sandwell, IGPP 0225, Scripps Institution of Oceanography, University of California, San Diego, La Jolla, CA 92093-0225. (e-mail: evelyn@seasat.ucsd.edu; sandwell@geosat.ucsd.edu)

(Received September 19, 1997; revised May 6, 1998; accepted May 22, 1998.)

Chapter 4

Vertical Displacements on the 1992 Landers, California Earthquake Rupture From InSAR and Finite-Fault Elastic Half-Space Modeling

4.1. ABSTRACT

The radar line-of-sight displacements predicted by the coseismic dextral slip model of *Wald and Heaton*, [1994] are subtracted from an imaging radar interferogram that temporally spans the 1992 Landers earthquake and the residuals are interpreted as due to vertical slip on the earthquake rupture. The residuals range in amplitude from -0.3 meters to 0.25 meters with highest variations to the east of the earthquake rupture. The main features of the residual displacement field are lobes of subsidence and uplift associated with the two main slip events involved in the earthquake rupture: the hypocentral event on the Johnson Valley fault and the maximum buried slip in the stepover between the Homestead Valley and Emerson faults. Also, 0.25 meters of vertical displacement on the Iron Ridge fault, when combined with the field measured left-lateral offset, suggests oblique slip on this fault. In addition, we construct a map of vertical coseismic displacements. This type of map cannot be obtained using any other method (e.g. campaign GPS).

The distribution of vertical slip on the rupture inferred from an inversion of the residual displacements indicates two major pairs of east-side-up and east-side-down motions associated with the two main earthquake slip events. East-side-up motions are observed near the southern terminus of the rupture and adjacent to the region of maximum buried slip. East-side-down motions are inferred deep within the Kickapoo

stepover and shallow on the northern portion of the rupture. The depths of the vertical motions follow the depths of maximum slip along the rupture. Forward modeling was performed to test the assumption of *Deng et al.*, [1998] that there was 0.7 meters of vertical east-side-down slip on the model segment corresponding to the Camp Rock and Emerson faults. A best fitting model indicates that 0.7 meters of vertical east-side-down slip on the Emerson and Camp Rock faults was possible but the locking depth was only 7.5 km.

4.2. INTRODUCTION

On June 28, 1992 the M_w 7.3 Landers earthquake originated on the Johnson Valley fault in California's Mojave Desert and ruptured northward by stepping right onto more northwestwardly oriented faults. The slip on the rupture was predominantly dextral with a maximum of 6.1 meters of offset measured in the field [*Hart et al.*, 1993; *Sieh et al.*, 1993]. Vertical offsets of as much as 1 meter or more were measured on some fault segments [*Sieh et al.*, 1993; *Hart et al.*, 1993; *Irvine and Hill*, 1993; *Sowers et al.*, 1994; *Johnson et al.*, 1994; *Arrowsmith and Rhodes*, 1994; *Spotila and Sieh*, 1995; *Zachariassen and Sieh*, 1995; *Aydin and Du*, 1995; *Fleming and Johnson*, 1997; *McGill and Rubin*, 1999]. However, vertical displacements measured on faults that are part of a complex rupture geometry with, on average, a large horizontal displacement may be due to localized uplift and subsidence of individual fault-bounded blocks and not representative of vertical slip on the rupture as a whole. In this study, an attempt is made to estimate the amount and distribution of vertical slip on the rupture surface using InSAR measurements and finite fault elastic half-space modeling.

Numerous authors inferred the distribution of right-lateral slip on the buried Landers earthquake rupture fault surface by inverting different data sets assuming finite dislocations in an elastic half-space [Murray *et al.*, 1993; Hudnut *et al.*, 1994; Freymueller *et al.*, 1994; Johnson *et al.*, 1994; Wald and Heaton, 1994; Cohee and Beroza, 1994]. In this study, the synthetic interferogram predicted by the model of Wald and Heaton, [1994] is subtracted from an interferogram that temporally spans the earthquake (the coseismic interferogram) and the residual interferogram (the vertical interferogram) is inverted for a distribution of vertical slip on the same fault patches. This particular right-lateral slip model is chosen because it was derived from an analysis of a combination of field measured offsets, GPS displacements, strong motion, and teleseismic data and a reasonable amount of consistency was found between the slip models resulting from the inversion of the last three data sets.

The assumption that the residuals represent a displacement signal due to vertical motions on the main rupture may be challenged by noting that the complex rupture geometry and significant breakage of numerous faults close to the rupture (e.g. the Galway Lake fault, the Iron Ridge fault, and the Upper Johnson Valley fault) may not be modeled adequately by a three-plane rupture model. However, effects from rupture complexities should be responsible for short wavelength signals close to the rupture. Adequate smoothing of the model can lessen the effects of such signals on the inversion. Also, the largest difference between the horizontal motions predicted by the right lateral slip model and GPS observations near the rupture is approximately 7.4 cm in the direction of the radar line-of-sight (LOS) at site 7002 (there is a 10 cm LOS residual at site 7000, but this site is very close to the rupture). It is shown below that this is less than

25% of the maximum amplitude of observed signal in the vertical interferogram. A consideration of the vertical component of slip can add to our understanding of earthquake rupture mechanics and dynamics. Furthermore, models of other components of the earthquake cycle, such as postseismic deformation, rely on assumptions about the magnitudes and locations of the vertical displacements on the earthquake rupture planes [e.g. *Deng et al.*, 1998].

4.3. INTERFEROMETRIC METHOD

Radar imagery (Figure 4.1) collected by the ERS-1 and ERS-2 satellites during their 35 day repeat and tandem mission phases is combined to form a map of the coseismic displacement in the direction of the radar line-of-sight (LOS) (Figure 4.2) using an interferometric method (InSAR). This map of coseismic displacement is similar to the ones published by *Massonnet et al.*, [1993]; *Zebker et al.*, [1994]; and *Peltzer et al.*, [1994]. The specific methodology used in this study is similar to that which is outlined in *Price and Sandwell*, [1998] which is, itself, similar to what is standard. (Note that a number of InSAR reviews from multiple points of view have recently been published or are in press [*Bamler and Hartl*, 1998; *Massonnet and Feigl*, 1998; *Bürgmann et al.*, 1999].)

Each time the satellite passes over a specific area on the ground, there exists the potential to form an interferogram by combining the imagery collected at that time with an image collected at a different time over the same area. The interferogram represents the change in two-way distance (the range change) to points on the ground measured at the two times of imaging. When the satellite does not exactly repeat its orbit a parallax

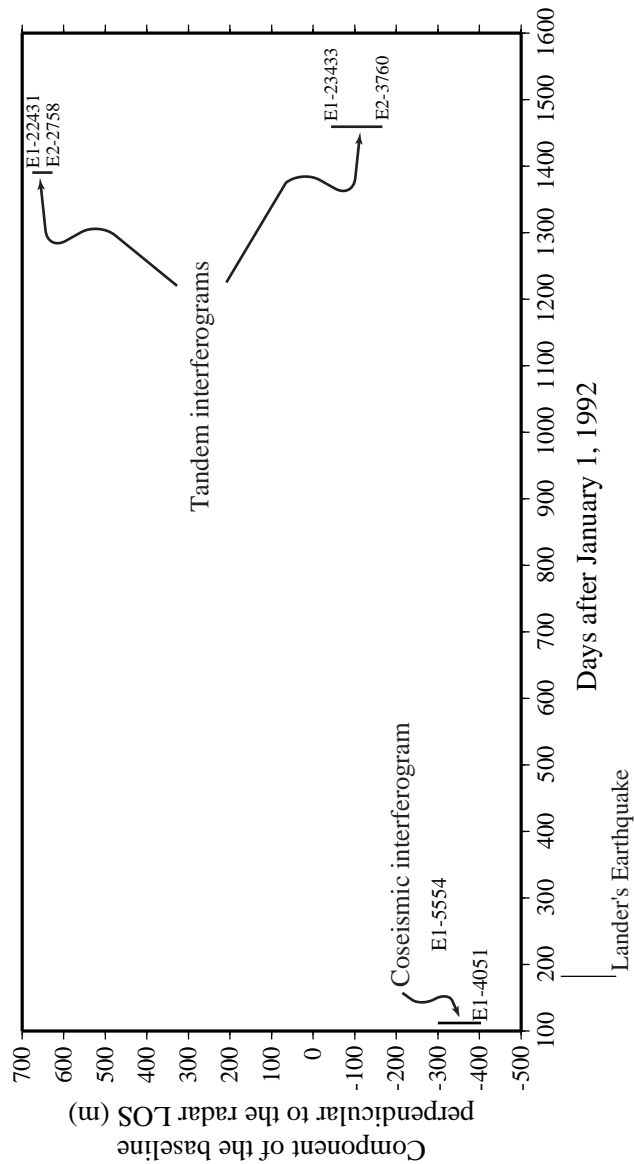
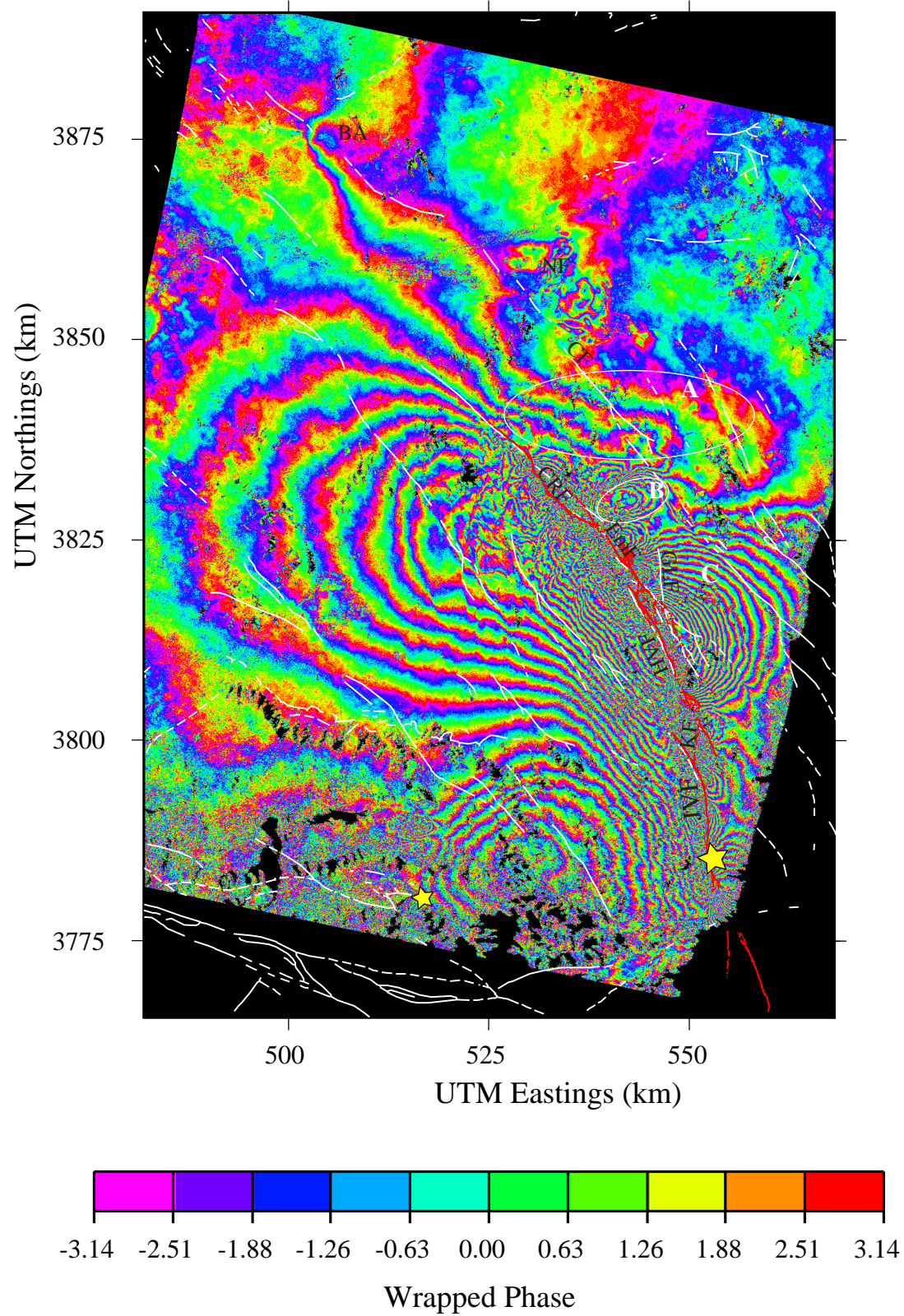


Figure 4.1. The ERS-1 and ERS-2 radar imagery used in this study plotted in time-space coordinates. The Landers earthquake occurred on June 28, 1992 (day 180). The coseismic interferogram is derived from two images taken by the ERS-1 radar on April 24, 1992 and August 7, 1992 and has a baseline of 147.1 meters. The two topographic interferograms are derived from images taken during the ERS-1 and ERS-2 tandem mission. The first has a baseline of 52.4 meters and is composed of an image taken by the ERS-1 radar on October 29, 1995 (orbit 22431) and an image taken by the ERS-2 radar on October 30, 1995 (orbit 2758). The second has a baseline of 137.0 meters and is composed of an image taken by the ERS-1 radar on January 7, 1996 (orbit 23433) and an image taken by the ERS-2 radar on January 8, 1996 (orbit 3760).

Figure 4.2. The coseismic interferogram. The white lines indicate the locations of faults mapped previously to the Landers earthquake from a California fault database. The red lines compose the earthquake rupture trace as mapped by *Sieh et al.*, [1993]. The yellow stars are at the locations of the Landers (the larger star) and the Big Bear (the smaller star) epicenters. Regions A, B, and C are discussed in the text. Region A contains subsidence to the northeast of the rupture, Region B surrounds Iron Ridge, and Region C is adjacent to the maximum buried slip. The yellow stars indicate the two major shocks that occurred during the time span of the interferogram: the larger star at the location of the Landers epicenter, the smaller star is at the location of the Big Bear epicenter. The abbreviated labels stand for: Calico fault (CF), Camp Rock fault (CRF), Emerson fault (EmF), Galway Lake fault (GLF), Homestead Valley fault (HVF), Johnson Valley fault (JVF), Kickapoo fault (KF), Newberry Fractures (NF), and north of the Barstow aftershocks (BA).



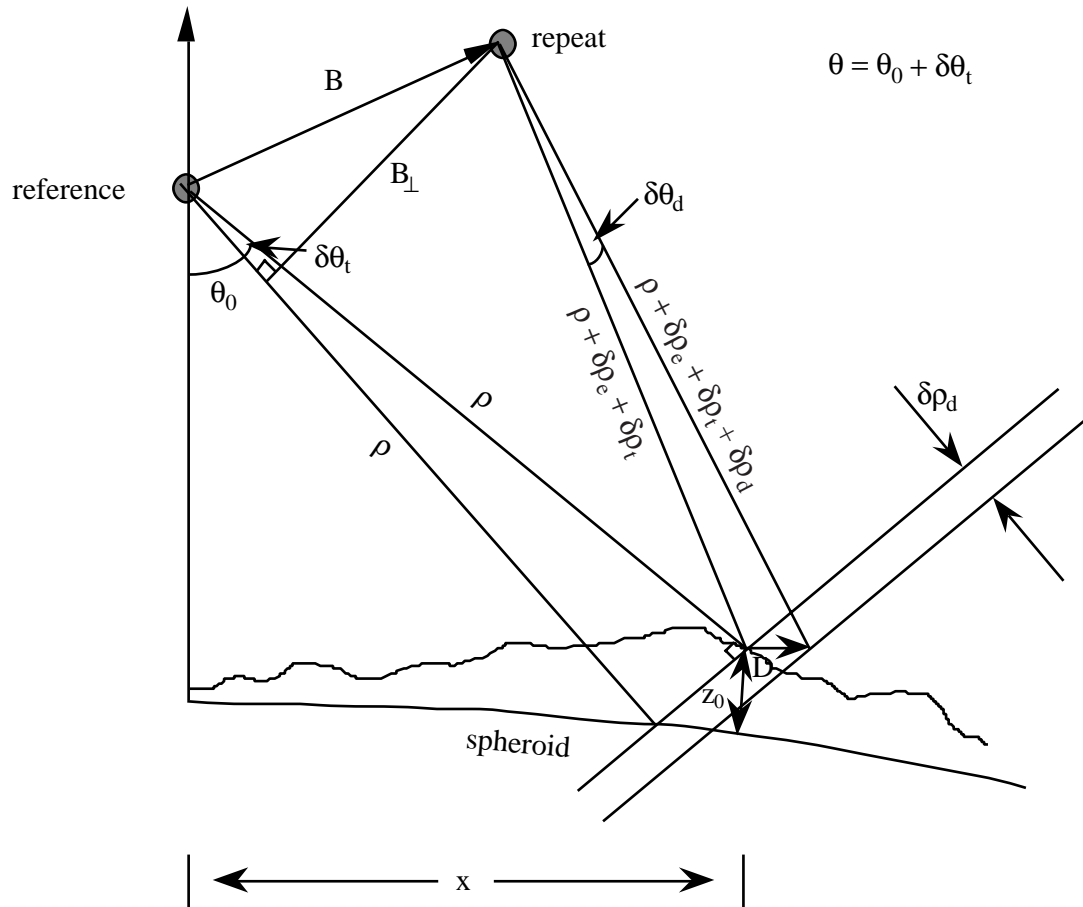
effect enables the measurement of topography. If the Earth's surface moves between the two times of imaging, the displacement measured in a single interferogram is that component which is in the direction of the radar line-of-sight and that component only. While InSAR cannot differentiate between horizontal and vertical displacements, it does give a high spatial density of LOS displacement measurements and methods of interpretation allow extraction of physically meaningful information.

The distance between the positions of the satellite(s) during the two passes is called the interferometric baseline (see Figure 4.3a). The phase of the product of one complex image and the complex conjugate of the second is the interferometric phase. The interferometric phase is related to the range change by $\phi = 4\pi/\lambda \delta\rho$ where ϕ is the interferometric phase, λ is the wavelength of the radar, and $\delta\rho$ is the range change. This range change (Figure 4.3a) is the sum of contributions from the imaging geometry, the topography, displacement of the Earth's surface, atmospheric delay, and phase noise

$$\delta\rho = \delta\rho_e + \delta\rho_t + \delta\rho_d + \delta\rho_\epsilon \quad (4.3.1)$$

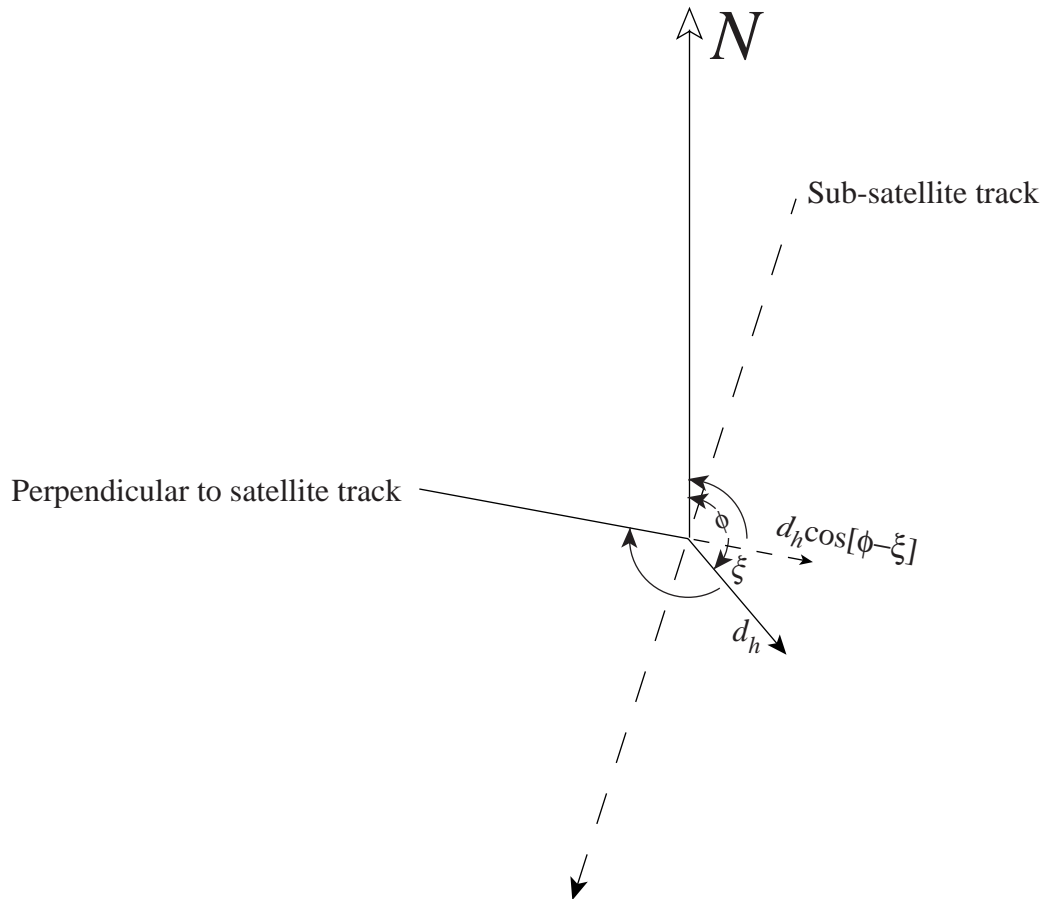
Where $\delta\rho_e$ is the contribution due to the imaging geometry and is equal to the component of the baseline parallel to the radar LOS, $\delta\rho_t$ is the component of range change due to topography and is equal to the product of the perpendicular component of the baseline and the topographic angular distortion, $\delta\rho_d$ is the contribution due to displacement of the Earth's surface, and $\delta\rho_\epsilon$ is the range change due to changes in the refractivity of the atmosphere and phase noise. Both $\delta\rho_d$ and $\delta\rho_\epsilon$ map directly into the radar LOS.

Errors in repeat pass interferometric measurements include phase noise and atmospheric noise, which can give spurious estimates of displacement subject to misinterpretations. In a multi-look interferogram with the number of looks greater than



a)

Figure 4.3. a) The InSAR geometry. The range from the "reference" satellite pass to a location on the surface of the earth at elevation z_0 is ρ , the range from the "repeat" satellite pass to the same location is $\rho + \delta\rho_e + \delta\rho_t$, the range from the repeat pass of the satellite to the same piece of earth after it has been displaced by D is $\rho + \delta\rho_e + \delta\rho_t + \delta\rho_d$, the radar look angle to the reference spheroid is θ_0 , the topographic angular distortion is $\delta\theta_t$, the displacement angular distortion is $\delta\theta_d$, the baseline length is B , the length of the component of the baseline perpendicular to the radar LOS is B_{\perp} . The subscripted range changes are explained in the text (Section 4.3). When measuring displacements using space-based InSAR, the three range rays (excluding the one drawn to the reference spheroid) in the figure can be considered parallel to each other making $d\rho_d$ essentially zero. The InSAR measured component of the displacement, D , is that which is in the direction of the radar LOS. This displacement is equal to $\delta\rho_d$.



b)

Figure 4.3. b) The geometrical construction for computing the component of horizontal displacement perpendicular to the satellite track $-d_h \cos[\phi - \xi]$. The perpendicular to the satellite track has an azimuth ξ of 283° . The horizontal displacement has a magnitude d_h and an orientation of ϕ degrees clockwise from north.

4, the phase noise variance can be estimated using the complex correlations between matching pixels in the two images [Rodriguez and Martin, 1992]. Errors due to atmospheric delay are due to changes in the refractive index of the medium through which the radar signals pass and can be due to both turbulence and longer wavelength differences in the troposphere and ionosphere, or systematic changes in humidity with topography [e.g. Tarayre and Massonnet, 1996] at the two times of imaging. The character and level of atmospheric noise is different in each interferogram [Hanssen, 1998] and an automated method for its removal has yet to be developed.

The range change error due to a given error in elevation of a target located at a distance x from the sub-satellite ground track is proportional to the length of the perpendicular component of the baseline

$$d\delta\rho = \frac{B}{x} dH \quad (4.3.2)$$

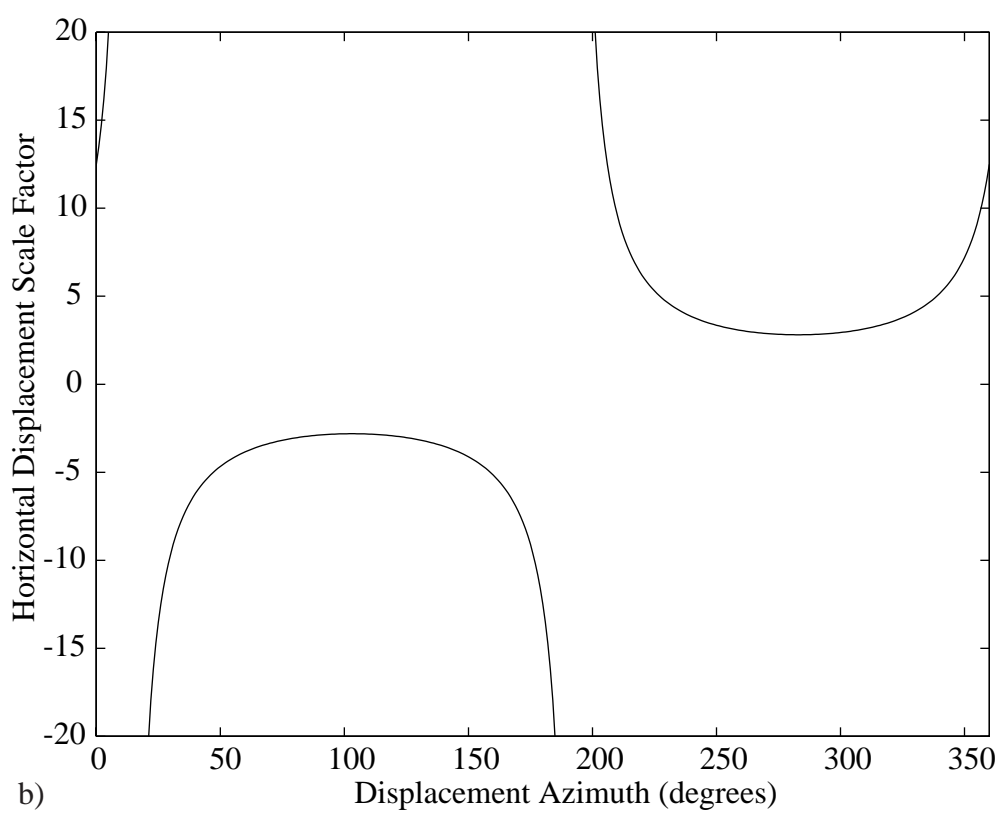
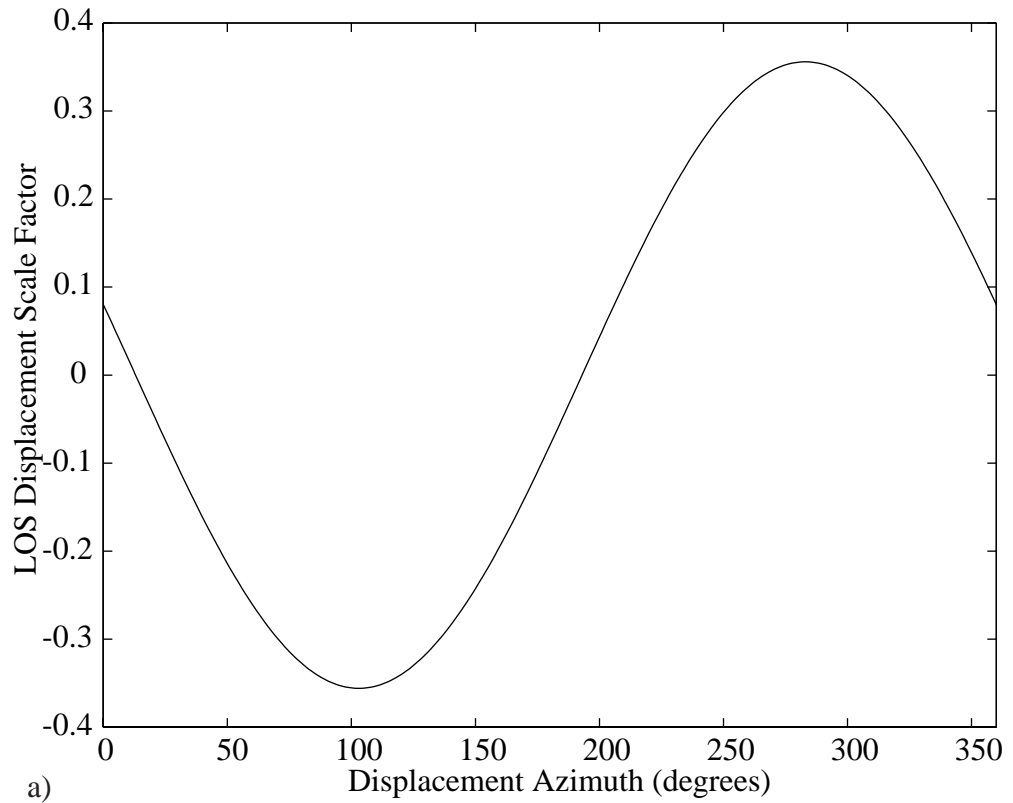
Where $\delta\rho$ is range change, H is elevation, x is the distance between the sub-satellite ground track and the target, and B is the component of the baseline perpendicular to the reference pass range ray (Figure 4.3a). Hence, given the length of the perpendicular component of the baseline corresponding to the coseismic interferogram (99 meters), a 10-meter error in elevation of a target in the middle of the interferogram gives a 3-mm error in range change.

4.3.1. SCALING VERTICAL AND HORIZONTAL DISPLACEMENTS INTO THE SATELLITE LOS

Because we cannot distinguish between vertical and horizontal displacements using a single interferogram, interpretations should be based on plausible ground

Figure 4.4. a) The radar LOS displacement scale factor versus the azimuth of the horizontal displacement given the 193° azimuth of the sub-satellite track and a signal incidence angle of 20.8° . Horizontal displacements perpendicular to the sub-satellite track are scaled by the sine of the incidence angle while horizontal displacements parallel to the sub-satellite track cannot be measured.

b) The horizontal displacement scale factor versus the azimuth of the horizontal displacements given the 193° azimuth of the sub-satellite track and a signal incidence angle of 20.8° . If the radar LOS displacement across a fault is assumed to be a horizontal displacement, the magnitude of the horizontal displacement is the product of the LOS displacement and the horizontal displacement scale factor. Assuming a horizontal displacement across a fault that is parallel to the satellite track implies that its magnitude is infinite. A minimum scale factor is about 3 (the reciprocal of the sine of the incidence angle) for computing displacements oriented perpendicular to the satellite track direction.



movement, ancillary data (such as GPS and field measurements and mapping), and the imaging geometry. The scaling of a vertical displacement on the ground into a LOS displacement is proportional to the cosine of the angle of incidence (20.8° in this study). The scaling of a horizontal displacement on the ground into the radar LOS direction depends on the azimuth of the displacement and the azimuth of the satellite track (approximately 13° at the latitude of the Mojave Desert). For example horizontal displacements parallel to the satellite track cannot be measured while horizontal displacements orthogonal to the satellite track are scaled by the cosine of the incidence angle (Figure 4.4a). The relationship between LOS displacement and horizontal displacement is:

$$D = d_h \cos[\phi - \xi] \sin[\iota] \quad (4.3.3)$$

Where D is LOS displacement, d_h is horizontal displacement, ξ is the azimuth of the perpendicular to the satellite track, ϕ is the azimuth of the displacement, and ι is the incidence angle (see Figure 4.3b).

When attempting to discriminate between horizontal displacements and vertical displacements across a structure such as a fracture or fault, it is important to consider the orientation of that structure with respect to the radar. Interpreting a measured LOS displacement as a horizontal displacement parallel to the satellite track implies infinite horizontal displacement while, at minimum, the scaling of a measured LOS displacement into a horizontal displacement is approximately 3 times the measured LOS displacement (Figure 4.4b). Scaling point-wise displacements into the satellite LOS is not the only way to interpret interferograms: an excellent discussion of the interferogram fringe patterns caused by shear and rotations of blocks is given by *Peltzer et al.*, [1994].

4.4. DATA PROCESSING AND REDUCTION

To extract estimates of displacement from a single interferogram, it must first be "flattened": the geometric range change contribution $\delta\rho_e$ is removed. An estimate of the topographic contribution to the phase $\delta\rho_t$ must then be made and removed from the interferogram, and the resulting deformation interferogram can then be unwrapped or left in modulo 2 increments and geometrically rectified (orthorectified and geolocated). Here, 6 images from track 399 of the ERS-1 and ERS-2 satellites (Figure 4.1) are combined to form the LOS displacement map over a region surrounding the Landers earthquake rupture (Figure 4.2). Four images from the ERS-1/ERS-2 tandem mission are used to make two interferograms that are stacked to estimate topographic phase and make a DEM for orthorectification. Two additional images that temporally span the earthquake; taken on April 24, 1992 and August 7, 1992; are used to generate an interferogram from which the topographic phase estimate is subtracted to derive coseismic displacement. After the topographic phase estimate has been subtracted from the interferogram spanning the earthquake, the result is unwrapped using a "tree" algorithm [Goldstein *et al.*, 1988], orthorectified using elevations derived from the stacked tandem interferograms, gridded at 60 m spacing, and geolocated using tie-points.

A synthetic coseismic interferogram (Figure 4.5) is formed by using the dextral dislocations of the "combined" model of Wald and Heaton, [1994] as input to the "RNGCHN" software [Feigl and Dupre, 1999] which analytically computes the displacement at the Earth's surface due to dislocations in an elastic half-space using the formulation of Okada, [1985]. In addition, the contribution to the displacement field by the Big Bear earthquake, an M_w 6.2 event that happened three hours after the Landers

Figure 4.5. The synthetic interferogram predicted by the Landers earthquake dextral slip model of *Wald and Heaton*, [1994]. The white lines compose the earthquake rupture trace as mapped by *Sieh et al.*, [1993]. The yellow lines indicate the locations of the three model segments defined by *Wald and Heaton*, [1994]. Regions A, B, and C are as in Figure 2.

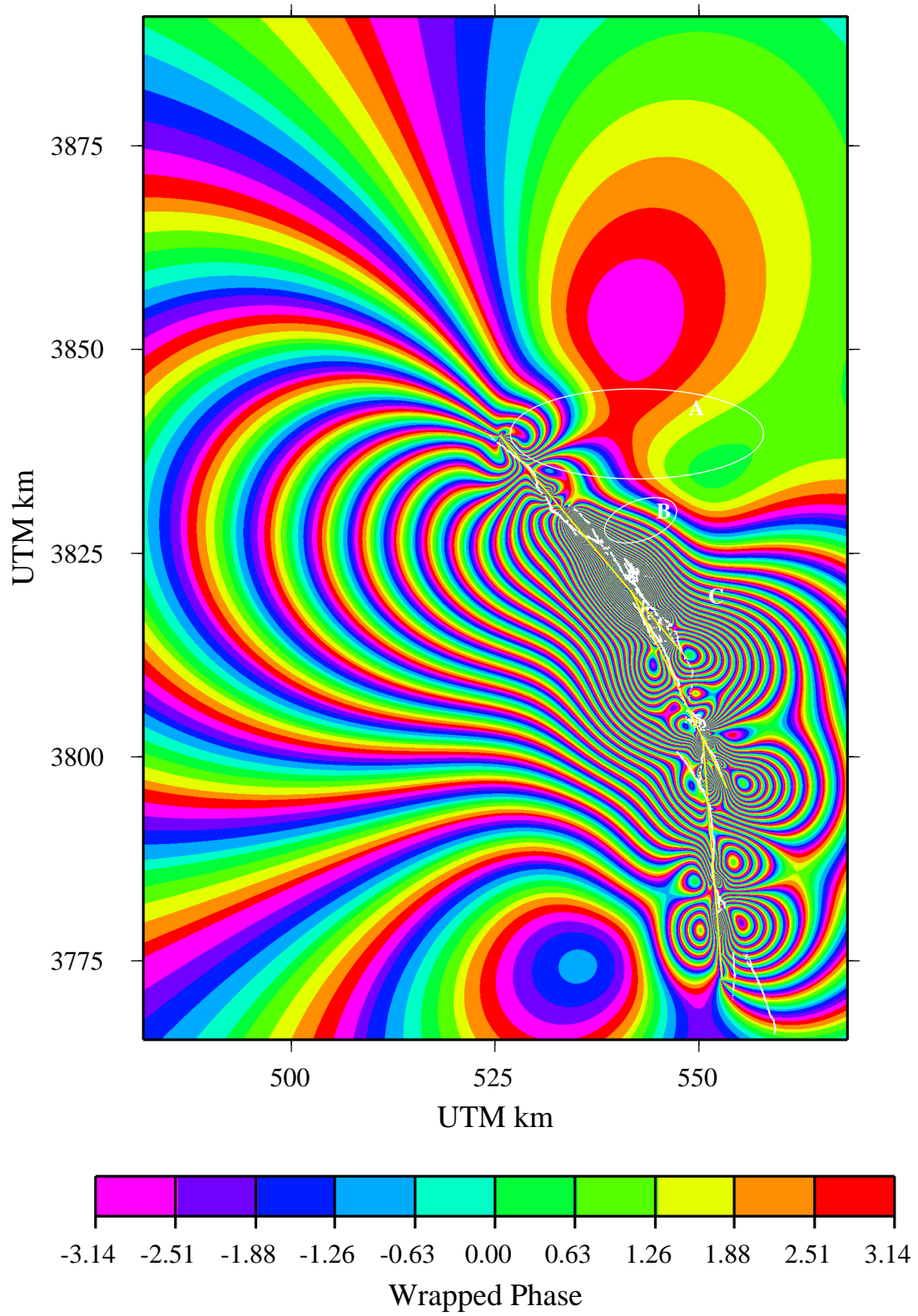


Figure 4.6. The unwrapped "vertical interferogram". This is the full-resolution map of the residual displacements obtained by differencing the synthetic interferogram (Figure 5) and the coseismic interferogram (Figure 2). The white lines indicate the locations of faults mapped previously to the Landers earthquake from a California fault database. Regions A, B, and C are as in Figure 2. Profiles AS-AS', EC-EC', H-H', and J-J' are across-strike, parallel to the Emerson/Camp Rock model segment, parallel to the Homestead Valley model segment, and parallel to the Johnson Valley model segment, respectively. Profiles EC-EC' and H-H' are located 6 km east of the corresponding model segments while profile J-J' is located 2.5 km east of the Johnson Valley model segment. The pluses and minuses are the LOS-projected differences between the horizontal displacements measured at GPS sites by *Freymueller et al.*, [1994] and those predicted by the dextral slip model. The circles are the LOS-projected GPS displacement measurement errors. The GPS sites 6054, 7000, 7002, and Ricu are labeled.

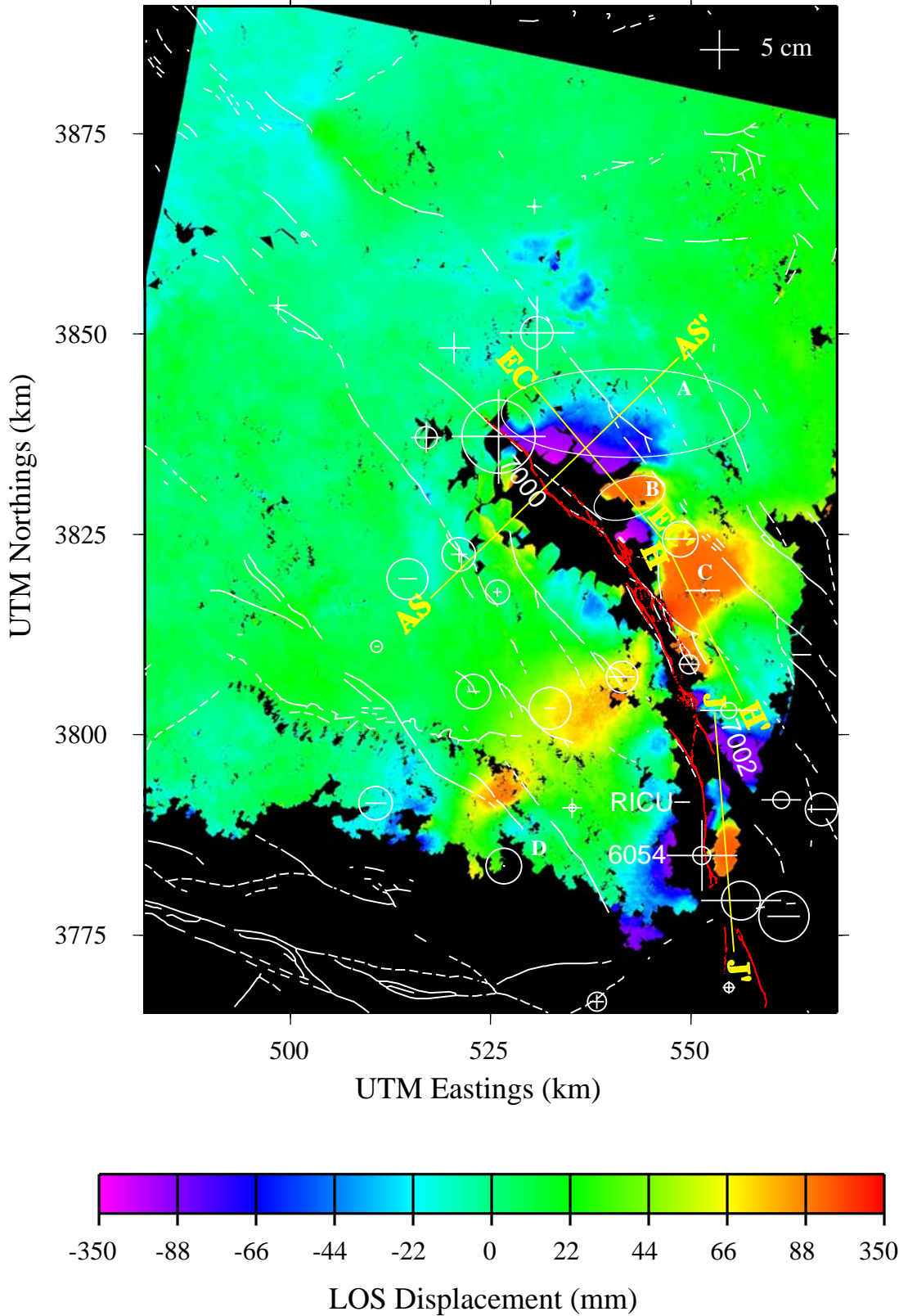
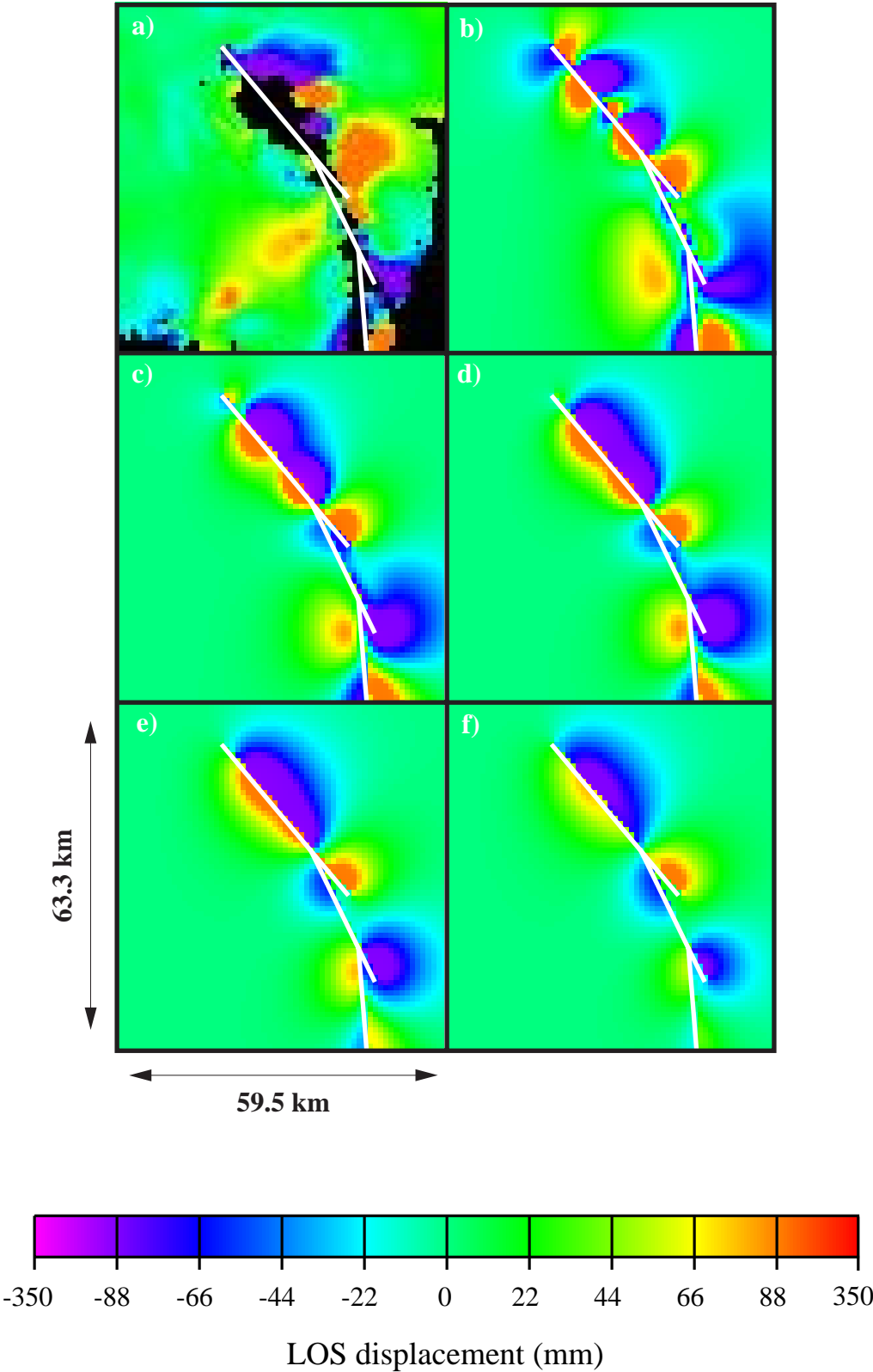


Figure 4.7. The data and inverse model predictions. The white lines are the model segments. a) The reduced resolution data that were inverted for vertical slip on the rupture plane (The full resolution data are shown in Figure 6). b), c), d), e), and f) are the predicted LOS displacements for inverse models with smoothing parameters β equal to 1, 3.1, 5, 10, and 20 respectively.



earthquake in the San Bernardino Mountains, was computed by modeling it as 1.15 meters of dextral slip between 2.5 and 15 km of depth on a fault striking 57° . The LOS displacements comprising the synthetic interferogram are subtracted from the full resolution (2853x2850 data samples at 60-m spacing) coseismic interferogram to form the vertical interferogram (Figure 4.6). A two-dimensional smoothing filter is then applied to the full resolution vertical interferogram to limit its bandwidth before sampling to a 960-m grid spacing to avoid aliasing short wavelengths into long ones. The down-sampled vertical interferogram has 63x67 data values (Figure 4.7a), 14% of which are null due to inability to unwrap the phase. While the inability to unwrap the phase leads to less spatial coverage, it eliminates data values with high phase variance, which would have to be severely down-weighted in an inversion.

Because of orbital errors, long-wavelength atmospheric signals, or a lack of the phase unwrapping algorithm to determine the appropriate integer multiple of 2π offset in the interferogram, deformation interferograms typically must be calibrated by removing a constant offset and slope. Here, the slope and constant offset are found by an integration of the measured displacements with the modeled displacements. Four fringes in the along-track direction, corresponding to a slope of $7.3 \mu\text{rad}$, were removed from the residual interferogram. The constant offset of the data was then found iteratively by adding a constant to the interferogram and solving for the best fit least squares solution (similar to the way such a constant would be found in a non-linear inversion). The constant found here was 3.3 mm.

4.5. MODELING METHOD

Both forward and inverse modeling of LOS displacements caused by vertical displacements on patches defined by *Wald and Heaton*, [1994] are performed. The models consist of finite-fault, vertical dislocations in an elastic half-space with Poisson's ratio equal to 0.25. There are 186 model patches each 3 km long by 2.5 km wide on three overlapping fault segments. The forward modeling effort was to test the assertion by *Deng et al.*, [1998] that there was 0.7 meters of vertical, east-side-down offset on the Emerson/Camp Rock segment of the rupture and to determine the depth to which vertical offset of such magnitude could have occurred. Inverse modeling was used to solve for a reasonable distribution of vertical displacement on the rupture that could account for some of the deformation signal in the vertical interferogram. The inversion is carried out by minimizing

$$\| \mathbf{C}^{-1/2} (\mathbf{A}\bar{\mathbf{x}} - \bar{\mathbf{d}}) \| + \beta^2 \| \mathbf{L}\bar{\mathbf{x}} \| \quad (4.5.1)$$

Where $\| \cdot \|$ denotes the 2-norm, $\mathbf{C}^{-1/2}$ is the square root of the inverse of the data covariance matrix, \mathbf{A} is a matrix of Green's functions relating a unit slip on each model patch to LOS displacements at the Earth's surface, $\bar{\mathbf{x}}$ is a vector of model coefficients, $\bar{\mathbf{d}}$ is a vector of data values, β is an arbitrary constant that controls the smoothness of the model, and \mathbf{L} is a discretized Laplacian operator. The first term in the above equation is called the misfit while the second term is called the roughness. Although the system is overdetermined (there are 3635 data values and 186 model elements), significant smoothing is required to mitigate the effects of the short-wavelength deformation signals in the vertical interferogram.

The displacement measurements were assumed to be independently and identically distributed with standard deviation equal to 5 cm. In fact, atmospherically induced errors in the data are spatially correlated leading to off-diagonal terms in the data covariance matrix [Williams *et al.*, 1998]. Less than obvious displacements on faults other than the main rupture and localized displacements not representative of the elastic response of the lithosphere as a whole can reach 1-2 cm and can be spatially correlated [Massonnet *et al.*, 1994; Peltzer *et al.*, 1994; Price and Sandwell, 1998]. Furthermore, the postseismic LOS displacements that occurred within the month following the earthquake have been measured to be as high as 5 cm [Massonnet *et al.*, 1996; Price, 1999]. In spite of these unspecified errors, the similarity between the LOS displacements predicted by the inverse models and the vertical interferogram (Figure 4.7) gives confidence in the general features of the models.

4.6. RESULTS

4.6.1. INTERFEROMETRIC OBSERVATIONS

The coseismic interferogram spanning the time period -65 to +41 days surrounding the Landers earthquake and the interferogram predicted by the model of Wald and Heaton, [1994] are shown in Figures 4.2 and 4.5 respectively. There are multiple regions where the fringe patterns in the coseismic interferogram deviate from those predicted by the model. The regions surrounding the Newberry Fractures (Figure 4.2, label NF) and near the Barstow aftershock's epicenters (Figure 4.2, label BA) were discussed by Price and Sandwell, [1998]. Three new regions related to possible vertical slip on the rupture are noted here. The first is a region of flattened fringes to the north-

east of the rupture (Figure 4.2, label A) between the Camp Rock fault and the Calico Fault that has never been modeled well using elastic half-space models with only right-lateral slip [Massonnet *et al.*, 1993; Massonnet and Feigl, 1998]. The second is the pattern of circular fringes surrounding Iron Ridge (Figure 4.2, label B) discussed by Price and Sandwell, [1999]. The third is the underestimation by the dextral slip model of the number of hemispherical fringes southeast of the stepover between the Homestead Valley and Emerson faults (Figure 4.2, label C). This underestimation was discussed by Massonnet *et al.*, [1993] and attributed to "simple discretization of the elastic model."

The differences between the LOS-projected horizontal displacements predicted by the dextral slip model and those measured at GPS sites by Freymueller *et al.*, [1994] are shown as pluses and minuses in Figure 4.6. Pluses indicate that the dextral slip model predicts a residual towards-the-satellite motion while minuses indicate that the dextral slip model predicts a residual away-from-the-satellite motion. Because neither the magnitudes nor the signs of the horizontal residuals appear to be correlated with the towards and away-from the satellite motions observed in the residual interferogram, it is plausible that the signal in the residual interferogram is associated with vertical slip on the rupture rather than dextral slip model errors.

The first striking characteristic of the unwrapped vertical interferogram (Figure 4.6) is that the signals due to possible vertical motions on the rupture plane have highest amplitudes to the east of the rupture. The maximum LOS displacement in the vertical interferogram is 25.6 cm while the minimum is -38.7 cm. (To scale LOS displacements into vertical displacements, multiply them by 0.935.) There is a large region of apparent subsidence to the north-east of the rupture bounded to the south by the Galway Lake fault

(the north striking fault near the letter "H" in Figure 4.6) and interrupted by uplift of Iron Ridge (Figure 4.6, Region B). A comparison of displacements extracted from the unwrapped coseismic interferogram and the synthetic interferogram along profile AS-AS', which is perpendicular to the rupture strike in this region, indicates that the LOS displacement is overestimated on the east side and slightly underestimated on the west side of the rupture by the predictions of the dextral slip model (Figure 4.8b). This indicates vertical, east-side-down motion on the north-east side of the rupture as shown by the signal along profile AS-AS' extracted from the vertical interferogram and displayed in Figure 4.8c. Note that the apparent vertical displacements along this profile are negatively correlated with the corresponding topography (Figure 4.8c,d) extracted from both USGS and InSAR digital elevation models.

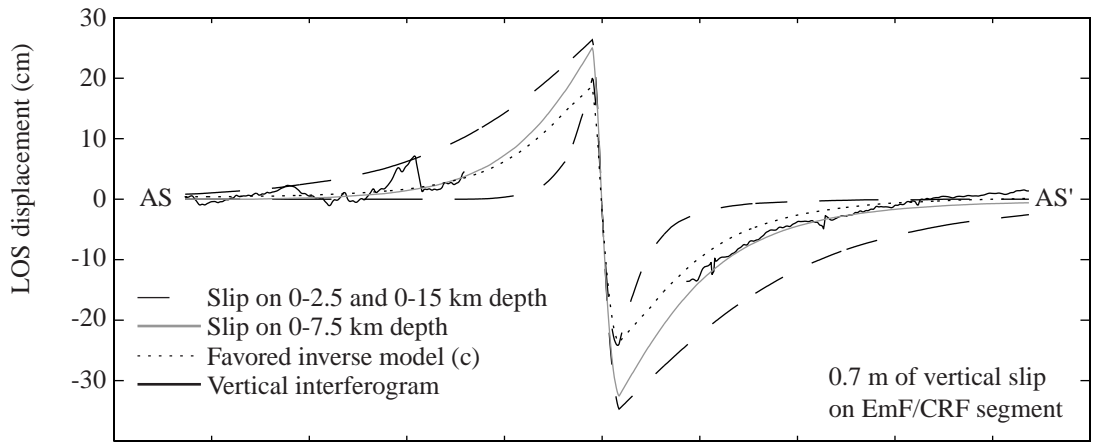
LOS displacements extracted from the vertical interferogram along profile EC-EC', which is parallel to the Emerson/Camp-Rock fault model segment, indicates subsidence interrupted by 28 cm of positive LOS displacement on the Iron Ridge fault (Figure 4.9b). While 25 cm of left-lateral displacement was measured by field geologists on the Iron Ridge fault [*Hart et al.*, 1993], this scales to only 4.2 cm of LOS displacement across a structure striking 221.5° . The remaining 24-cm of LOS displacement must be due to vertical displacement on this fault. This suggests oblique displacement on the Iron Ridge Fault with a rake of nearly 45° . If the signal in the vertical interferogram over Iron Ridge is assumed to be uplift, there is 15.8 cm of LOS displacement consistent, to within error, with the 16.8 cm cited by *Price and Sandwell*, [1998].

A region of towards-the-satellite LOS deformation is bounded to the west by the

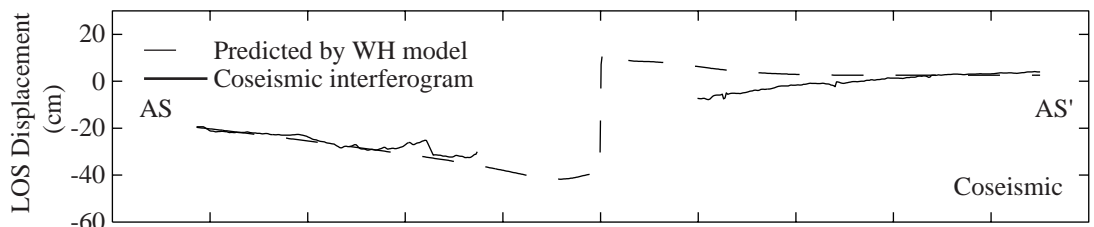
Galway Lake fault, to the east-northeast by the West Calico fault, and to the west-southwest by the Emerson fault (Figure 4.6, label C). This region is adjacent to the location of maximum buried dextral slip on the rupture, which is within the southern portion of the step-over between the Homestead Valley and the Emerson faults (e.g. Figure 4.9a). A comparison between the LOS displacements extracted from the coseismic interferogram along profile H-H' (which crosses this region and is parallel to the Homestead Valley fault model segment) and the LOS displacements predicted by the dextral slip model along the same profile indicates underestimation of the LOS displacement by the dextral slip model by as much as 16 cm (Figure 4.9b). One of the largest differences between the observed GPS horizontal displacements and those predicted by the right lateral slip model occurs in this region at station LEDG (see Figure 4.6 for location). This difference is approximately 4.3 cm of LOS displacement, which is not enough to account for the 16-cm discrepancy between the coseismic interferogram measurements and the dextral slip model predictions. This indicates that the vertical displacement is significant.

High amplitude signals in the vertical interferogram are also observed surrounding the Johnson Valley fault but we do not have interferometric data far to the east of the fault in this area that would help constrain the depths of possible vertical displacements. However, horizontal displacements measured at benchmarks 6054 and Ricu (see Figure 4.6 for the locations), which are within 4 km of the rupture on the Johnson Valley fault agree to within 10 cm and 2 cm respectively with the dextral slip model. The residual at mark 7002 (see Figure 4.6 for the location) is 7.4 cm LOS. The LOS displacements along profile J-J' extracted from the vertical interferogram measure

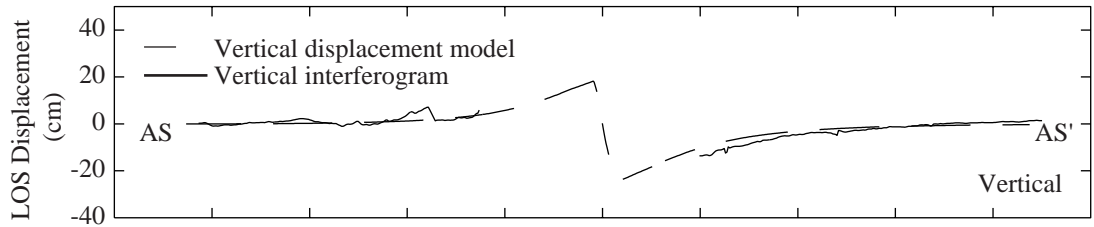
Figure 4.8. The measured and modeled radar LOS displacements along profile AS-AS'. a) The profiles extracted from forward-modeled predictions assuming 0.7 meters of vertical displacement on the northern 9 patches of the Emerson/Camp Rock model segment for various locking depths. The two dashed lines are the predicted LOS displacements assuming 0.7 meters of vertical east-side-down motion within the 0-2.5 km depth range (the lower amplitude, shorter wavelength dashed line) and the 0-15 km depth range (the higher amplitude, longer wavelength dashed line). The gray line is the profile extracted from the forward-modeled predictions that best fit the data: 0.7 meters of vertical, east-side-down slip within the 0-7.5 km depth range. The dotted line is the prediction of the favored inverse model "c". b) The LOS displacements predicted by the dextral slip model of *Wald and Heaton*, [1994] (the dashed line) and the LOS displacements extracted from the coseismic interferogram (the solid line). c) The LOS displacements predicted by the vertical slip model "c" (the dashed line) and the LOS displacements extracted from the "vertical interferogram" (the solid line). d) The elevation extracted from a USGS 1° DEM (the solid line) and the elevation extracted from the InSAR DEM plus a 100 m shift (the dotted line). The abbreviated labels indicate the locations of the intersections of the following faults with the across-strike profile: Lenwood fault (LF), Johnson Valley fault (JVF), Calico fault (CF), and Rodman fault (RF).



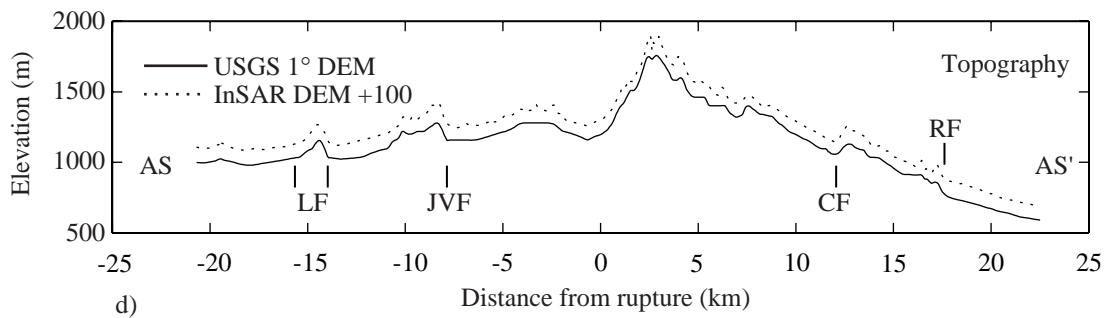
a)



b)

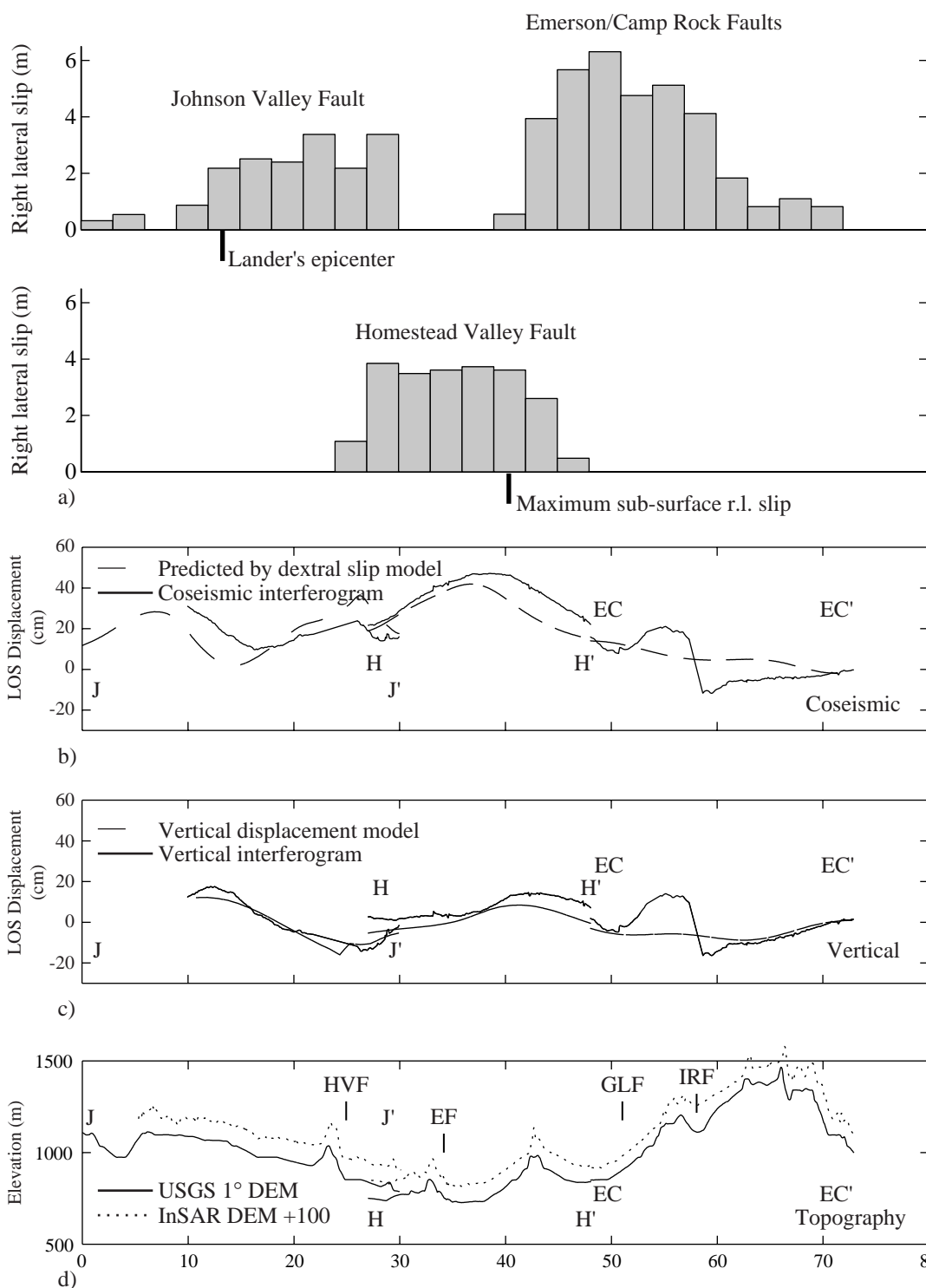


c)



d)

Figure 4.9. The measured and modeled displacements along profiles parallel to the strike of the model segments. The locations of the profiles J-J', H-H', and EC-EC' are marked in Figure 6. a) The dextral slip along the top-most layer of the model of *Wald and Heaton*, [1994]. b) The LOS displacements predicted by the dextral slip model of *Wald and Heaton*, [1994] (the dashed line) and the LOS displacements extracted from the coseismic interferogram (the solid line). c) The LOS displacements predicted by the vertical slip model "c" (the dashed line) and the LOS displacements extracted from the "vertical interferogram" (the solid line). d) The elevation extracted from a USGS 1° DEM (the solid line) and the elevation extracted from the InSAR DEM plus a 100 m shift (the dotted line). The abbreviated labels indicate the locations of the intersections of the following faults with the rupture-parallel profiles: Homestead Valley fault (HVF), Emerson fault (EF), Galway Lake fault (GLF), and Iron Ridge fault (IRF).



18 cm of LOS displacement near the Landers epicenter and -9 cm of LOS displacement just east of the Kickapoo stepover. These signals are larger than signals due to horizontal displacement differences between GPS measurements and the dextral slip model predictions.

4.6.2. FORWARD MODELING RESULTS

A recent viscoelastic model of postseismic deformation following the Landers earthquake by *Deng et al.*, [1998] uses 0.7 meters of dip-slip motion on the Emerson/Camp-Rock fault plane as an input parameter. There is neither conclusive field evidence nor is there accurate enough GPS evidence that this amount of dip-slip motion, if any, occurred during the earthquake. This assumption is tested by allowing 0.7 meters of dip-slip motion on the northern 9 columnar patches of the Emerson/Camp Rock model segments. The locking depth was then varied to determine the depth to which 0.7 meters of vertical slip might have occurred.

The results of the forward modeling are shown in Figure 4.8a. The two dashed lines are the predicted LOS displacements along profile AS-AS' assuming 0.7 meters of vertical east-side-down motion on a 0-2.5 km (the lower amplitude, shorter wavelength dashed line) and a 0-15 km depth range (the higher amplitude, longer wavelength dashed line). The gray line is the profile extracted from the forward model predictions that best fit the data: 0.7 meters of vertical, east-side-down slip within the 0-7.5 km depth range. 0.7 meters of vertical slip on the Emerson/Camp Rock model segment between 0 and 15 kilometers depth rupture predicts a LOS displacement that is 10 cm less than what is observed in the vertical interferogram 5 km northeast of the rupture (Figure 4.8a). For

reference, the dotted line in Figure 4.8a is the profile from the favored inverse model "c" (see below). Because the absolute phase (and hence the LOS displacement) near the rupture could not be recovered due to high phase variance, it cannot be determined whether vertical displacements on the rupture broke to the surface or remained buried or what their absolute amplitudes might have been. Even if the phase near the rupture could be determined, there may be short wavelength horizontal displacement residuals due to the complexity of faulting that would contaminate the apparent vertical signal.

4.6.3. INVERSE MODELING RESULTS

The vertical interferogram was inverted for a vertical slip distribution on the rupture using a linear least-squares scheme (Eqn. 4.5.1). The roughness parameter β was varied between values of 0.0005 and 30. The trade-off between roughness and misfit is plotted in Figure 4.10. Recall that misfit and roughness were defined as the first and second terms of Eqn. 4.5.1. Models corresponding to representative values of β are shown in Figure 7. (The letters "b-f" in Figures 4.7, 4.10, and 4.11 refer to corresponding predicted surface displacements, roughness parameters, and models respectively.)

The roughness versus misfit curve indicates more than one value of misfit for roughness values above 0.45. This is attributed to the fact that as the roughness parameter increases, high spatial frequency features in the data are so severely penalized by the inversion process that they no longer contribute significantly to the complexity of the model (see Figure 4.7). For example, when the roughness parameter exceeds $\beta = 5$, there is very little uplift predicted at Iron Ridge. It is reasonable to assume that this uplift is due to slip on the Iron Ridge Fault rather than on the main Landers earthquake rupture.

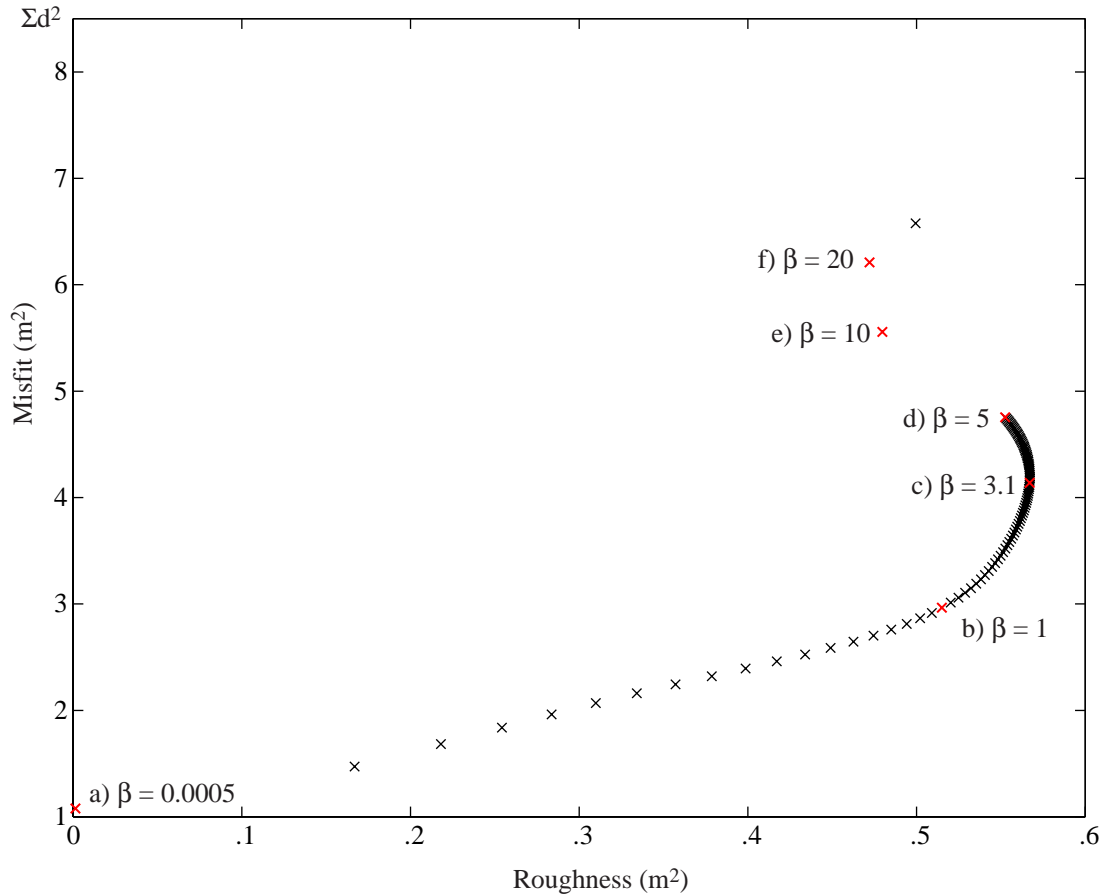


Figure 4.10. The plot of roughness versus misfit for the vertical displacement inverse models. The coordinate locations of the roughness parameters corresponding to the models shown in Figure 11 are each marked by a red x and labeled with letters a)-f) corresponding to the same letter labels in Figure 11. Σd^2 indicates the sum of the squares of the data: the maximum possible misfit.

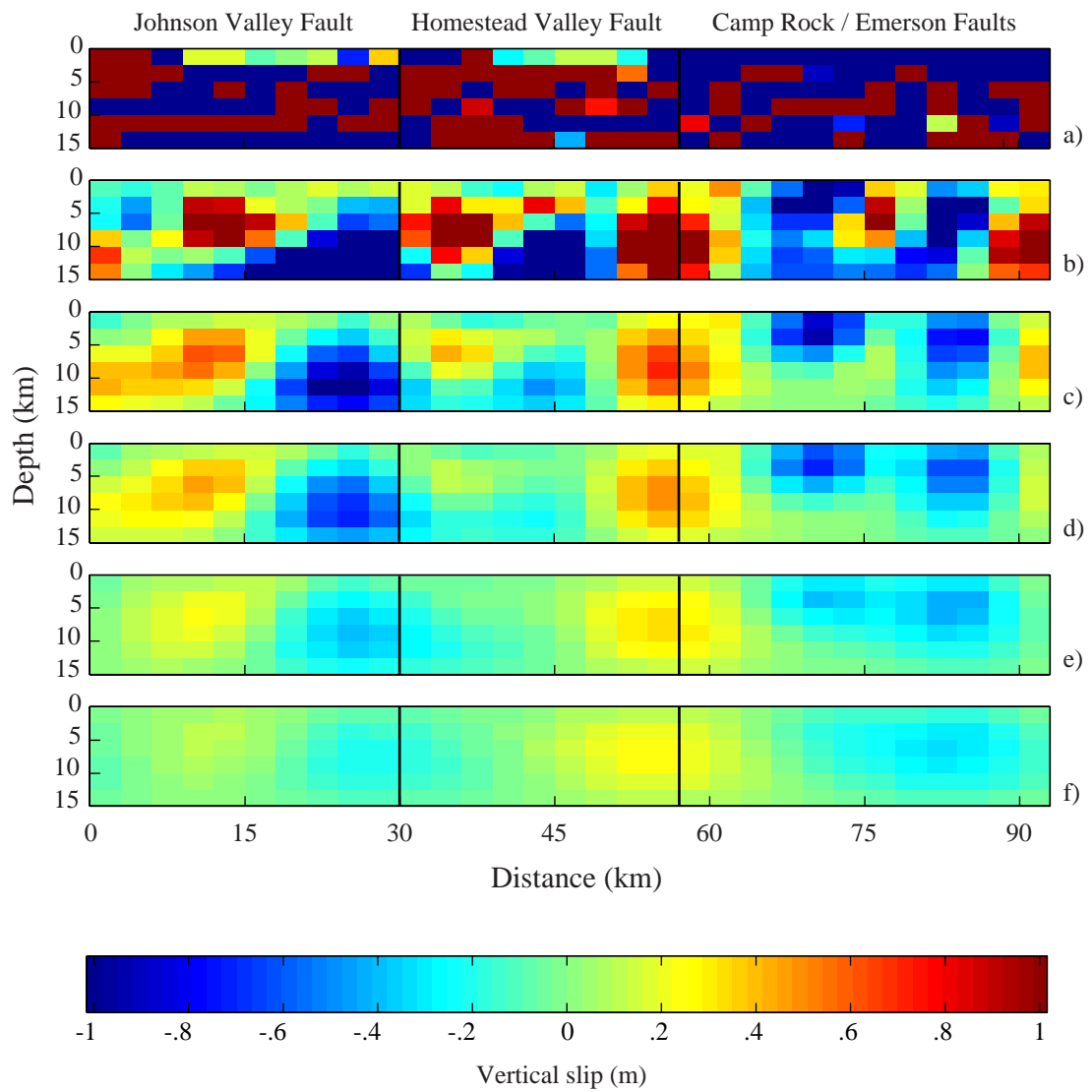


Figure 4.11. The vertical slip models corresponding to increasing roughness parameter: a) $b = 0.00005$, b) $b = 1$, c) $b = 3.1$, d) $b = 5$, e) $b = 10$, and f) $b = 20$.

The favorite model "c" has a roughness parameter β equal to 3.1. This model is chosen because it retains as much high frequency detail in the model and predicted data without over or under smoothing. Model "c" reduces the data variance by 51%: the variance of the data is 8.5 m^2 while the variance of the residuals is 4.2 m^2 . Displacements along profiles AS-AS', EC-EC', H-H' and J-J' are extracted from the surface displacements predicted by model "c" (Figure 4.7c) and plotted with corresponding profiles extracted from the vertical interferogram in Figures 4.8c and 9c. The model predictions along profile AS-AS' fit the corresponding vertical interferogram data to within 2.5 cm (Figure 4.8c) but the amplitudes along the model profile are slightly less than those along the data profile due to the weight of the roughness factor β . The displacements predicted by model "c" along profiles J-J' and H-H' match the corresponding data extracted from the vertical interferogram to within 10 cm (Figure 4.9c) although, again, the predicted amplitudes are underestimated. The model predicted displacements along profile EC-EC' (Figure 4.9c) indicates that most of the signal from slip on the Iron Ridge fault was eliminated by the chosen degree of model smoothing.

A reconstruction of the distribution of vertical slip along the rupture is shown in Figure 4.12 below the "combined" dextral slip model made available by *Wald*, [1996]. A main feature of the vertical slip model is pairs of east-side-up and east-side-down vertical motions. Regions of maximum east-side-up slip are adjacent to the earthquake's hypocenter on the Johnson Valley fault and the location of maximum sub-surface dextral slip within the stepover between the Homestead Valley fault and the Emerson fault. At the locations along the rupture trace where the maximum horizontal slip was deep, the model inferred vertical slip is also deep while at the locations where the maximum

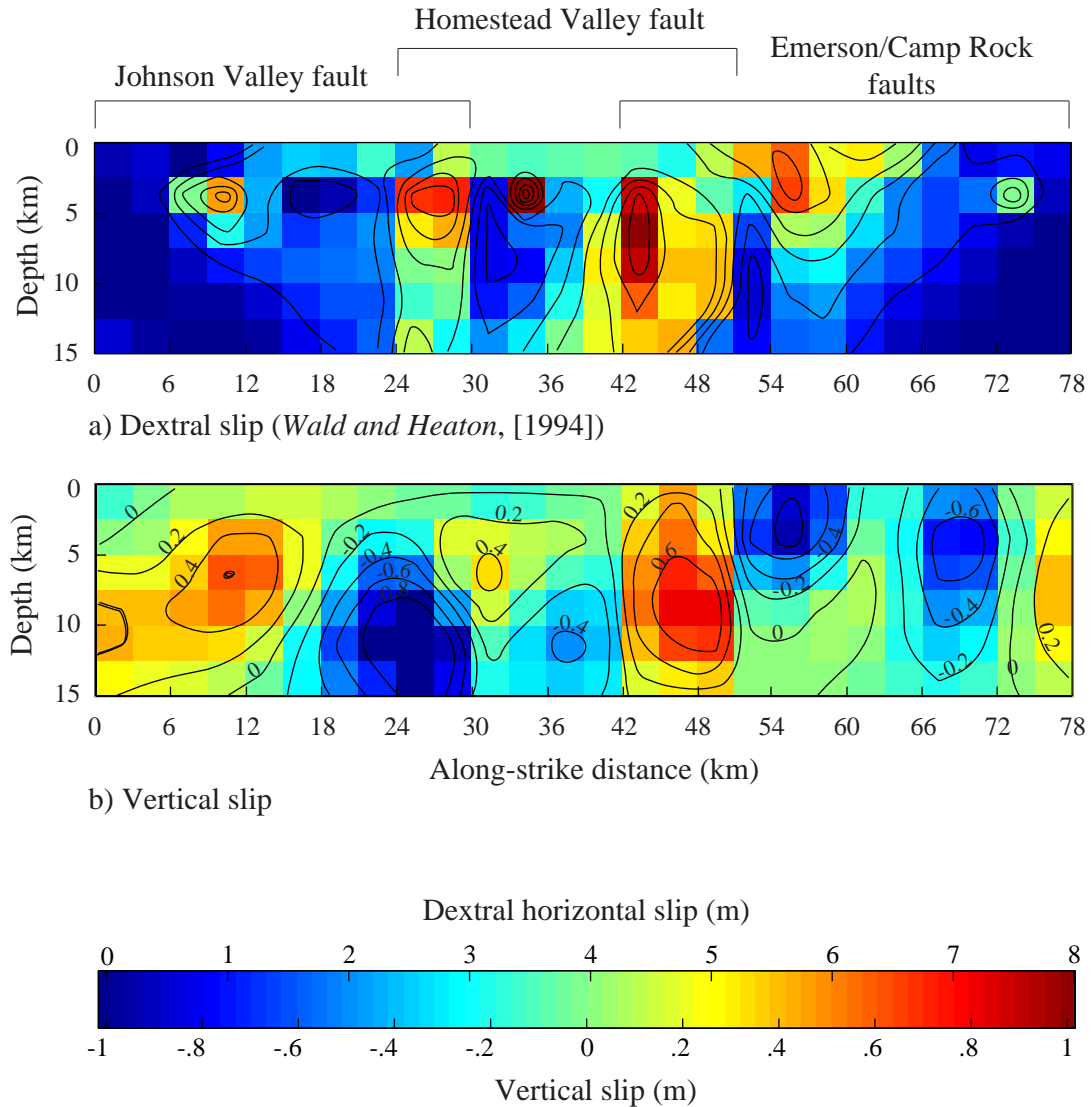


Figure 4.12. The vertical slip on the rupture compared to the dextral slip on the rupture. a) The dextral slip on the earthquake rupture inferred by Wald and Heaton, [1994] re-plotted and re-contoured for this study. b) The vertical slip on the earthquake rupture inferred by model "c". The slips within the stepovers are the sum of the slips on the overlapping segments of the faults flanking the stepovers.

horizontal slip was shallow, the model inferred vertical slip is also shallow. The model indicates deep, east-side-down slip on the Johnson Valley fault at the latitude of the Kickapoo step-over and a region of shallow east-side-down vertical slip on the end of the rupture that deepens to the north. The maximum-modeled east-side-down slip on the Emerson/Camp Rock segment was 0.8 meters on a patch in the 2.5-5 km depth range. This may be a localized overestimate of slip since effects from the uplift of Iron Ridge are still apparent in the predicted data and the model (Figures 4.7c and 4.11c).

4.6.4. MOMENT ANALYSIS OF THE SLIP MODEL

The contribution to the moment M_v from vertical displacements is computed by

$$M_v = \mu \sum_{n=1}^m A_n |s_n| \quad (4.6.1)$$

Where M_v is the amount of moment due to vertical slip on fault patches, μ is the modulus of rigidity (30 GPa), m is the number of model patches, A_n is the area of patch n , and s_n is the vertical slip on patch n . The moment predicted by model "c" is $M_v = .12 \times 10^{20}$ N-m. The moment, quoted by *Wald and Heaton*, [1994], due to dextral slip on fault patches of a model inferred from horizontal GPS coseismic displacements is 0.69×10^{20} N-m which is smaller than the 0.77×10^{20} N-m moment of the dextral slip model derived from a combination of geodetic, teleseismic, and strong motion data [*Wald and Heaton*, 1994]. Vertical slip on fault patches may account for some of this difference in moment.

4.6.5. RESOLUTION ANALYSIS OF THE VERTICAL SLIP MODEL

A resolution analysis indicates the inversion routine's ability to recover the slip distribution at the resolution of the fault model parameterization using the roughness parameter of model "c" (Figure 4.13). This is a function of the roughness parameter and type of roughening filter (a Laplacian in this study), the data distribution, and the data covariance. Two tests were performed. In the first test 10 meters and 30 meters of vertical slip were placed on single shallow and single deep fault patches, respectively. The shallow patch spans the 2.5-5 km depth range while the deep patch spans the 10-12.5 km depth range (Figure 4.13a). In the second test (Figure 4.13b), vertical dislocations were placed on patches inferred to slip the most by model "c". The amount of vertical slip placed on the test patches was the amount on the same patches inferred by model "c" multiplied by 5.

The first test (Figure 4.13a) indicates that the recovery of the amplitude of displacement on the shallow patch is 20% while the amplitude recovery is 5% on the deep patch. All of the vertical slip on the shallow test patch is recovered in the 9 model patches surrounding the patch while 30% of the vertical slip on the deep test patch is recovered in the surrounding 9 model patches. Hence, the deeper an actual slip on a patch on the earthquake rupture the more attenuated and spread out its image in a model inferred by the inversion process. The sum of the elements of the patch-wise slip model is equal to the sum of the elements of the smoothed output model but a moment estimate (Eqn. 4.6.1) is 1.5 times that of the patch-wise slip model. This is because negative side-lobes offset the patch-wise slip on the shallow patch. Also, slip on a patch near the top layer is pushed deeper while slip on a patch near the bottom layer is pushed shallower.

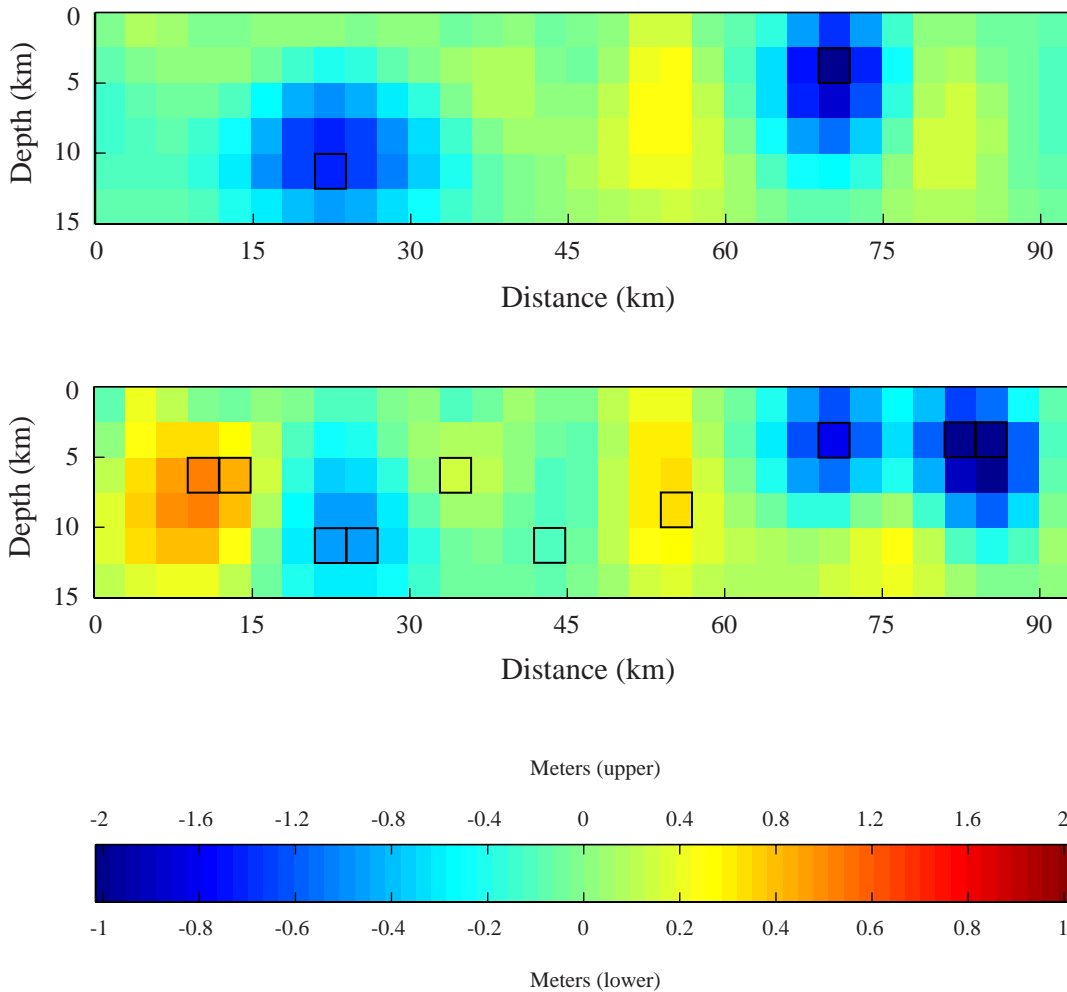


Figure 4.13. The resolution analysis. a) The model resulting from inversion of synthetic data using the roughness parameter of model "c" showing the inversion routine's ability to resolve impulsive slip on deep and shallow patches. The synthetic data was produced by placing 10 meters of vertical slip on the shallow patch outlined by a black box and 30 meters of slip on the deep patch outlined by a black box. b) The model resulting from inversion of synthetic data using the roughness parameter of model "c". The synthetic data was produced by placing 5 times the vertical slip indicated by model "c" at each patch outlined by a black box.

The second test (Figure 4.13b) indicates that near surface vertical slip is resolved better than deeper vertical slip and that although the patch-wise displacements are smoothed considerably, the character of the model is preserved.

4.7. DISCUSSION

4.7.1. A COMPARISON BETWEEN THE FIELD MEASURED AND THE INTERFEROMETRICALLY MEASURED VERTICAL SLIP

During the months following the Landers earthquake, a multitude of field researchers measured both horizontal and vertical slip on and in the vicinity of the surface rupture trace. The surface expression of the rupture trace can, in general, be described as broad and complex. Offsets on structures within different surface faulting environments inferred by the presence of compressional and extensional bends in the rupture and shear zones, some as wide as 200 meters (e.g. *Johnson et al.*, [1994]), were documented. Even in locations where the rupture was a long, straight trace, its surface expression could consist of a mole track in desert alluvium measuring 15 meters in width flanked by a zone of fractures extending as far as 30 meters to either side [*Hart et al.*, 1993].

Many of the published studies that discuss vertical displacements that occurred during the earthquake focus on regions surrounding the compressional and extensional bends in the rupture trace. Measurements of vertical slip ranging in amount from 0.5 to 1 meter were not uncommon. On the northern end of the rupture, *Fleming and Johnson*, [1997] found 0.5-0.6 meters of vertical, east-side-down displacement on a ladder of quadrilaterals spanning the Emerson fault. However, this study was done in a region spanning a compressional ridge on the west side of the extensional stepover between the

Emerson and Camp Rock faults. Further to the southeast along the rupture, *Irvine and Hill*, [1994] find 1 meter of vertical east-side-up displacement on the rupture near its intersection with the southern northeast striking zone of aftershocks but there are fractures directly east of this measurement that may have a west-side-up sense of slip. At a distance 6-km away to the south along the rupture, they measure 1 meter of vertical, west-side-up displacement just north of the stepover between the Homestead Valley and Emerson faults. This stepover was studied in detail by *Zachariassen and Sieh*, [1995] whose measurements of vertical slip, while they were as much as 0.6 meters, west-side-up on the Homestead Valley fault, were typically offset by east-side-up vertical slip on the Emerson fault indicating that the vertical motion was more likely related to down-drop of the block within the extensional stepover than to vertical slip on the rupture as a whole. Vertical slip on structures near the extensional Kickapoo stepover was measured by *Sowers et al.*, [1994]; *Johnson et al.*, [1994]; and *Spotila and Sieh*, [1995]. There vertical slip reached as much as 1 meter, west-side-up near the slip gap north of the stepover but was typically 0-0.5 meters within the stepover and related to the down-drop of the block to the southeast of the Kickapoo fault [*Spotila and Sieh*, 1995] and/or rotation of the block to the north of the Kickapoo fault [*Peltzer et al.*, 1994; *Spotila and Sieh*, 1995] inferred from thrust faulting observed at the slip gap [*Spotila and Sieh*, 1995].

The deformation within the areas addressed by the detailed field studies could not be measured with the interferometric method due to decorrelation between the images near the rupture. Even if it could have been, the dextral slip model parameterization is not complex enough to account for all the possible near fault displacements. There seems to be little apparent correlation between the displacement patterns seen adjacent to the

areas of detailed study in the vertical interferogram and the vertical displacements measured in the field. Exceptions to this are east-side down motion seen in the vertical interferogram adjacent to the slip gap and possibly the 0.3 meters of vertical displacement measured 2.5 km south of epicenter and 0.4 meters vertical 6 km north of epicenter reported by [Hart *et al.*, 1993] (although they do not indicate whether slip was west-side-up or east-side-up).

4.7.2. DID THE IRON RIDGE FAULT STOP THE RUPTURE?

The Landers earthquake rupture was modeled teleseismically as two events [Kanamori *et al.*, 1992]. (The following description of the rupture is an interpretation of Wald and Heaton, [1994], their Figure 4.16.) The first slip event had a duration of 7 seconds beginning at the hypocenter on the Johnson Valley fault and ruptured northward to the Kickapoo stepover where it nearly stopped. During the following 4 seconds, rupture on the Homestead Valley fault was diffuse. Then, a second slip event originated deep on the rupture plane just south of the stepover between the Homestead Valley fault and the Emerson fault. Here, slip grew towards the surface while the rupture stalled for 4 seconds in the stepover. Finally, the rupture broke through the northern part of the stepover and continued on shallower portions of the Emerson and Camp Rock faults. At the location of the intersection of the Iron Ridge fault and the main rupture, the dextral slip model shows that slip was continuous in the 19-20 second time window and discontinuous at the surface in the 20-21 second time window. A small area near the Earth's surface at the intersection of the Iron Ridge fault and the main rupture has less

right-lateral slip than the surroundings while the slipping surface, as a whole, deepens slightly to the northwest. After this point, the rupture stops.

The Iron Ridge fault is here inferred to have broken 20-21 seconds after the rupture initiation because of the discontinuity in slip at its intersection with the main rupture within the 20-21 second time window [Wald and Heaton, 1994; their Figure 4.16]. When this happened, the Iron Ridge fault underwent both vertical and left-lateral displacement irrecoverably accommodating some of the extensional strain propagating through the block east of the rupture. While the Iron Ridge fault may have played a role in stopping the rupture by weakening the block to the east of it, other factors were probably as or more important: on the northern Emerson and Camp Rock faults, the rupture propagated in a weaker, shallower layer and its potency had diminished considerably [Wald and Heaton, 1994; their Figure 4.16].

On the other hand, various lines of evidence indicate that not all of the earthquake's rupture energy had been converted to displacement at the end of the main rupture suggesting that if the rupture had more competent material on its tensional side, it might have continued further. Surface strain events to the north and west in the near-field included triggered slip on the Calico fault [Hart *et al.*, 1993; Price and Sandwell, 1998], extensional deformation surrounding the Newberry Fractures [Unruh *et al.*, 1994; Price and Sandwell, 1998], and compressional deformation near the Barstow aftershock cluster [Price and Sandwell, 1998] which is now believed to be coseismic since it does not have any expression in an interferogram whose time span begins five days after the earthquake.

4.7.3. A COMPARISON BETWEEN MODELED VERTICAL DISPLACEMENTS AND MODELED RIGHT-LATERAL SLIP

Static models of lateral dislocations that cut the surface of an elastic half-space predict patterns of tensional and compressional strains in the material surrounding the dislocations whose distributions depend on the geometry of and distribution of slip on the cuts in the elastic material [*Bilham and King*, 1989]. Dynamic models of mode II crack propagation in an elastic medium with a process zone at the crack tip predict compressional and tensional stresses with axes oriented 20° away from and on opposite sides of the propagating end [*Scholz et al.*, 1993]. In the most simple case, the elastic material surrounding a right-lateral dislocation on a cut striking north exhibits lobes of tensional strain to the northeast and southwest and compressional strain to the northwest and southeast. Because elastic dislocation modeling predicts that the material surrounding a fault that has slipped laterally undergoes vertical motions, it seems probable that vertical slip may occur on a fault near locked sections or the ends of a fault in response to lateral motions on it.

The pattern of up and down motion on the rupture inferred from the inverse model is correlated with slip heterogeneities on the rupture plane. Two major pairs of east-side-up and east-side-down slip are inferred from model "c". The first pair occurs on the Johnson Valley Fault with the maximum east-side-up slip occurring in the same model cell as the earthquake hypocenter. The corresponding east-side-down slip is deep on the Kickapoo stepover. The second pair is probably completely on the Emerson/Camp Rock segment of the model: The west-side-down slip is inferred to have occurred on the Homestead Valley model segment but the Homestead Valley and Emerson/Camp Rock

model segments are close together and there is no data between them to help constrain which segment accommodated the vertical slip. The maximum east-side-up slip is about 3 km north of the maximum dextral slip on the rupture and the east-side-down slip is along the Emerson/Camp Rock segment outside of the stepover region. The east-side-up motion may be due to southeastward propagation of energy on the Emerson fault at the stepover. A third, weaker pair of east-side-up and east-side-down slip on the Homestead Valley fault may or may not be significant. This pair indicates east-side-up motion on the Homestead Valley Fault at and south of the Kickapoo stepover changing to east-side-down slip between the slip gap and the maximum in dextral slip on the main rupture.

4.7.4. INTERPRETATION- TRANSIENT AND LONG TERM STRAIN FIELDS

Because vertical motions of the material surrounding the earthquake rupture indicate regions of contraction and extension, their association with surface fractures, and aftershocks can be used to interpret the local strain field induced by the earthquake. Figure 4.14 shows just such an interpretation. Arrows indicate the directions of maximum tension and compression near maximums in uplift and subsidence. Except for the orientation of maximum extension near Troy Dry Lake inferred from the orientations of the Newberry Fractures by *Unruh et al.*, [1994], the azimuths of maximum tension and compression are adopted from an inversion of slip on aftershock planes for the post-earthquake stress field by *Hauksson*, [1994].

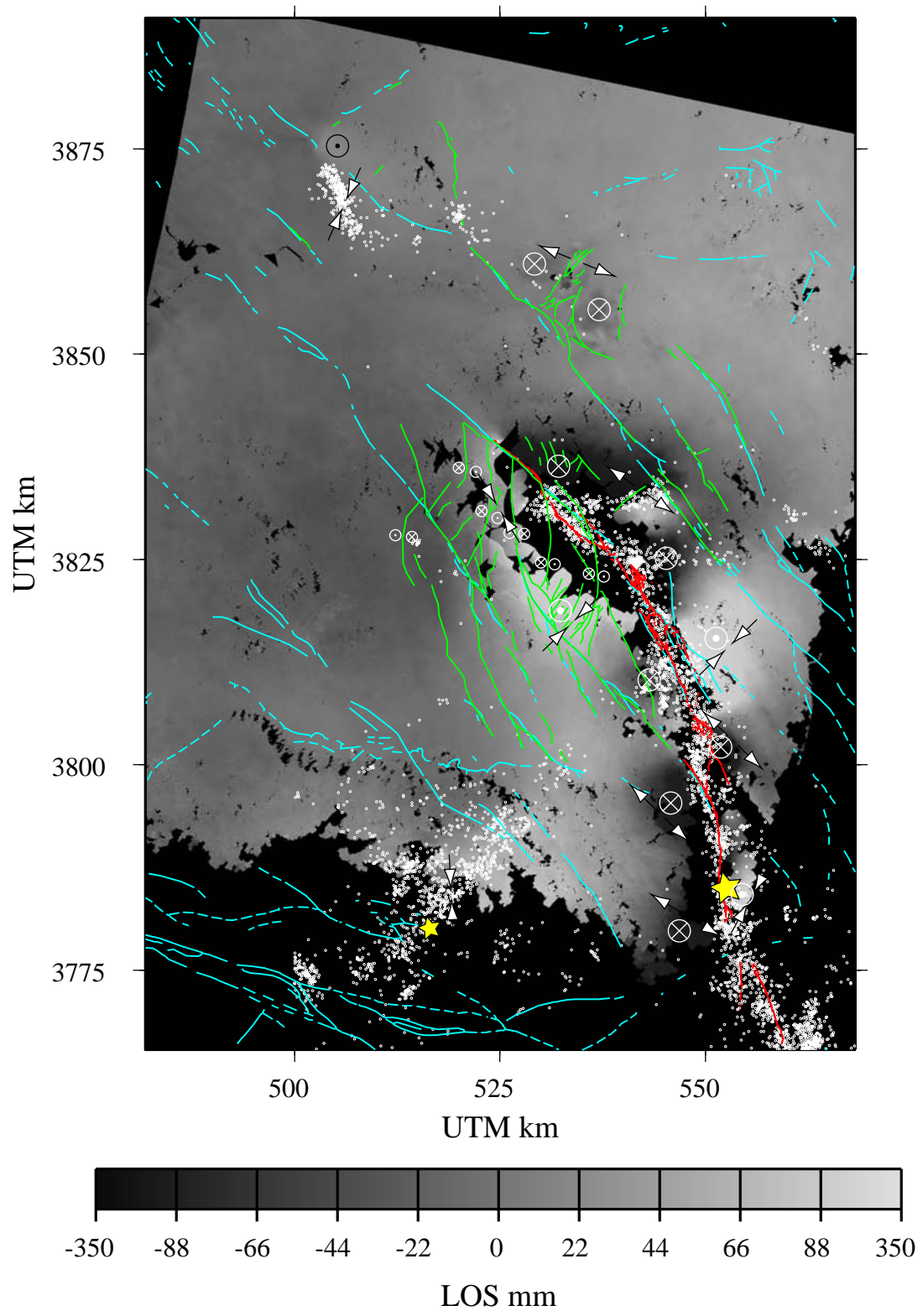
Near the main rupture, extensional and compressional lobes are associated with the two earthquake sub-events. Lobes of compression and extension are observed just south of the earthquake epicenter indicated by the larger yellow star in Figure 4.14. The

extension on the west side of the rupture continues north to the Kickapoo stepover. A quadrupolar pattern of extension and compression on the Northern part of the rupture is associated with the beginning of the large slip event on the stepover between the Homestead Valley fault and the Emerson fault and its propagation to the end of the rupture. This quadrupolar pattern consists of uplift east of the stepover (Figure 4.6, label C), subsidence west of the stepover, subsidence northeast of the end of the rupture, and compression southwest of the tip of the rupture.

Close inspection of the fractures west of the end of the rupture indicate that vertical motions were down to the inner concave sides of the curved fractures (Figure 4.14). These vertical motions are opposite to what would be expected given the topographic features in these areas indicating that normal and reverse faults associated with long-term formation of ridges and valleys that, over the long term, accommodate strain within a northwest-southeast directed extensional environment were subjected to a transient compressional environment by the rupture. For example, offsets across fractures indicate that the block containing the northern Fry Mountains dropped down and the valley between the Fry Mountains and the Ord Mountains lifted up.

If topography is an indicator of long-term strain, a comparison of topography with vertical coseismic deformation can determine whether the vertical displacements were typical of long-term deformation or were a result of the transient, local stress field induced by the earthquake. For example, a direct correlation was found between the vertical motions on the Loma Prieta earthquake rupture and the uplifts of the Santa Cruz Mountains and adjacent marine terraces [*Valensise, 1994*]. The profiles extracted from the vertical interferogram and the DEM indicate that the relative vertical displacements

Figure 4.14. The interpretational map of vertical displacements and fractures. The blue lines indicate the locations of major faults mapped prior to the Landers earthquake taken from a California fault database. The green lines indicate the locations of fractures mapped by *Price and Sandwell*, [1998]. The red line is the rupture trace mapped by *Sieh et al.*, [1993]. The yellow stars indicate the locations of the Landers (the larger star) and Big Bear (the smaller star) epicenters. Small white circles indicate the epicenters of aftershocks that occurred between April 24 and August 7, 1992 from the CNSS fault database with residuals less than .12 seconds. Circles with dots and crosses in their middles indicate up and down vertical motions, respectively. Arrows indicate the directions of extension and compression. The direction of extension surrounding the Newberry Fractures is adopted from *Unruh et al.*, [1994]. The other directions of extension and compression are adapted from *Hauksson*, [1994].



east of the rupture are correlated with the relative topography along profiles J-J' and H-H' which run parallel to the Johnson Valley and Homestead Valley faults (Figure 4.9). However, the subsidence northeast of the end of the rupture along profile EC-EC' (Figure 4.9) occurs in a region surrounding the Rodman Mountains which are some of the highest mountains near the end of the rupture. This mismatch between vertical displacement and elevation is further evident along the across-strike profile AS-AS' (Figure 4.8). This indicates that the vertical displacements that occurred on the end of the rupture were induced by the local, transient stress field associated with the propagating rupture and are not representative of long-term strain.

4.8. CONCLUSIONS

Integration of InSAR and finite-fault elastic half-space modeling can be used to measure the distribution of vertical displacement surrounding a major earthquake. This distribution can be inverted for vertical slip on the rupture plane and interpreted in the framework of the earthquake dynamics and regional strain. The distribution of vertical slip on the Landers earthquake rupture, like the distribution of dextral slip, was heterogeneous. East-side-up/down pairs are associated with the two main slip events on the rupture. While the relative vertical displacements surrounding the southern part of the rupture follow the relative topography, the relative vertical displacements surrounding the northern part of the rupture are not correlated with the topography. Rather than being indicative of long-term incremental strain, the vertical displacements surrounding the end of the rupture occurred in response to the local stress field induced by the earthquake. A realistic coseismic vertical slip distribution could be used as input to time-dependant

models that describe other phases of the earthquake cycle, such as viscoelastic rebound, to help constrain the contribution of the proposed mechanisms to the postseismic deformation signal.

4.9. REFERENCES

- Arrowsmith, J.R., and D. D. Rhodes, Original forms and initial modifications of the Galway Lake road scarp formed along the Emerson fault during the 28 June 1992 Landers, California, earthquake, *Bull. Seism. Soc. Am.*, 84 (3), 511-528, 1994.
- Aydin, A., and Y. Du, Surface Rupture at a Fault Bend: the 28 June 1992 Landers, California, Earthquake, *Bull. Seism. Soc. Am.*, 85 (1), 111-128, 1995.
- Bamler, R., and P. Hartl, Synthetic aperture radar interferometry, *Inverse Problems*, 14, R1-R54, 1998.
- Bilham, R., and G. King, The morphology of strike-slip faults: examples from the San Andreas fault, California, *J. Geophys. Res.*, 94(B8), 1989.
- Bürgmann, R., Rosen, P.A., and E.J. Fielding, Synthetic aperture radar interferometry to measure Earth's surface topography and its deformation, *Annu. Rev. Earth Planet. Sci.*, (in press) 1999.
- Cohee, B.P., and G.C. Beroza, Slip distribution of the 1992 Landers earthquake and its implications for earthquake source mechanics, *Bull. Seism. Soc. Am.*, 84 (3), 692-712, 1994.
- Deng, J., M. Gurnis, H. Kanamori, and E. Hauksson, Viscoelastic flow in the lower crust after the 1992 Landers, California, earthquake, *Science*, 282, 1689-1692.
- Feigl, K.L., and E. Dupre, RNGCHN: a program to calculate displacement components from dislocations in an elastic half-space with applications for modeling geodetic measurements of crustal deformation, *Comput. Geosci.*, 25 (6), 695-704, 1999.
- Fleming, R.W., and A. M. Johnson, Growth of a tectonic ridge during the Landers earthquake, *Geology*, 25 (4), 323-326, 1997.
- Freytmuller, J., N.E. King, and P. Segall, The co-seismic slip distribution of the Landers earthquake, *Bull. Seism. Soc. Am.*, 84 (3), 646-659, 1994.
- Goldstein, R.M., H.A. Zebker, and C.L. Werner, Satellite radar interferometry: Two-dimensional phase unwrapping, *Radio Science*, 23 (4), 713-720, 1988.
- Hanssen, R., Atmospheric heterogeneities in ERS tandem SAR interferometry, *DEOS Rep.*, no. 98.1, 1998.
- Hart, E.W., W.A. Bryant, and J.A. Treiman, Surface faulting associated with the June 1992 Landers earthquake, California, *Calif. Geol.*, 46, 10-16, 1993.

- Haukkson, E., L.M. Jones, K. Hutton, and D. Eberhart-Phillips, The 1992 Landers Earthquake Sequence: Seismological Observations, *J. Geophys. Res.*, 98 (B11), 19,835-19,858, 1993.
- Haukkson, E., State of stress from focal mechanisms before and after the 1992 Landers earthquake sequence, *Bull. Seism. Soc. Am.*, 84 (3), 917-934, 1994.
- Hudnut, K.W., and 16 others, Co-seismic displacements of the 1992 Landers earthquake sequence, *Bull. Seism. Soc. Am.*, 84 (3), 625-645, 1994.
- Irvine, P.J., and R. L. Hill, Surface rupture along a portion of the Emerson fault, *Calif. Geol.*, 46, 23-26, 1993.
- Johnson, A.M., R.W. Fleming, and K.M. Cruikshank, Shear zones formed along long, straight traces of fault zones during the 28 June 1992 Landers, California, earthquake, *Bull. Seism. Soc. Am.*, 84 (3), 499-510, 1994.
- Johnson, H.O., D.C. Agnew, and K. Hudnut, Extremal bounds on earthquake movement from geodetic data: Application to the Landers earthquake, *Bull. Seism. Soc. Am.*, 84 (3), 660-667, 1994.
- Massonnet, D., M. Rossi, C. Carmona, F. Adragna, G. Peltzer, K. Feigl, and T. Rabaute, The displacement field of the Landers earthquake mapped by radar interferometry, *Nature*, 364 (8 July), 138-142, 1993.
- Massonnet, D., K. Feigl, M. Rossi, and F. Adragna, Radar interferometric mapping of deformation in the year after the Landers earthquake, *Nature*, 369, 227-230, 1994.
- Massonnet, D., and K. L. Feigl, Radar interferometry and its application to changes in the Earth's surface, *Rev. Geophys.*, 36 (4), 441-500, 1998.
- McGill, S.F., and C. M. Rubin, Surficial slip distribution on the central Emerson fault during the June 28, 1992, Landers earthquake, California, *J. Geophys. Res.*, 104 (B3), 4,811-4,834, 1999.
- Murray, M.H., J.C. Savage, M. Lisowski, and W.K. Gross, Coseismic displacements: 1992 Landers, California, earthquake, *Geophys. Res. Lett.*, 20, 623-626, 1993.
- Okada, Y., Surface deformation to shear and tensile faults in a half-space, *Bull. Seismol. Soc. Am.*, 75 (4), 1135-1154, 1985.
- Peltzer, G., K.W. Hudnut, and K.L. Feigl, Analysis of coseismic surface displacement gradients using radar interferometry: New insights into the Landers earthquake, *J. Geophys. Res.*, 99 (B11), 21,971-21,981, 1994.

- Price, E.J. and D.T. Sandwell, Small-scale deformations associated with the 1992 Landers, California, earthquake mapped by synthetic aperture radar interferometry phase gradients, *J. Geophys. Res.*, 103 (B11), 27,001-27,016, 1998.
- Price, E.J., SAR interferogram displacement maps constrain depth, magnitude, and duration of postseismic slip on the 1992 Landers, California earthquake rupture, *Eos Trans. AGU*, 80 (17), Spring Meet. Suppl., S77, 1999.
- Rodriguez, E., and J.M. Martin, Theory and design of interferometric synthetic aperture radars, *IEE Proc.-F*, 139 (2), 147-159, 1992.
- Sieh, K., L. Jones, E. Hauksson, K. Hudnut, D. Eberhart-Phillips, T. Heaton, S. Hough, K. Hutton, H. Kanamori, A. Lilje, S. Lindvall, S.F. McGill, J. Mori, C. Rubin, J.A. Spotila, J. Stock, H.K. Thio, J. Treiman, B. Wernicke, J. Zachariasen, Near-Field Investigations of the Landers Earthquake Sequence, April to July 1992, *Science*, 260 (9 April), 171-176, 1993.
- Scholz, C.H., N.H. Dawers, J.-Z. Yu, and M.H. Anders, Fault growth and fault scaling laws: Preliminary results, *J. Geophys. Res.*, 98 (B12), 21,951-21,961.
- Sowers, J.M., J.R. Unruh, W.R. Lettis, and T.D. Rubin, Relationship of the Kickapoo fault to the Johnson Valley and Homestead Valley faults, San Bernardino County, California, *Bull. Seism. Soc. Am.*, 84 (3), 528-536, 1994.
- Spotila, J.A., and K. Sieh, Geologic investigations of a "slip gap" in the surficial ruptures of the 1992 Landers earthquake, southern California, *J. Geophys. Res.*, 100 (B1), 543-559, 1995.
- Tarayre, J. and D. Massonnet, Atmospheric propagation heterogeneities revealed by ERS-1 interferometry, *Geophys. Res. Lett.*, 23 (9), 989-992, 1996.
- Valensise, G., Geologic assessment of the relative contribution of strike-slip faulting, reverse-slip faulting, and bulk squeezing in the creation of the central Santa Cruz Mountains, California, U.S. Geol. Sur. Prof. Pap., 1550-F, 131 pp., 1994.
- Wald, D.J., and T.H. Heaton, Spatial and temporal distribution of slip for the 1992 Landers, California, earthquake, *Bull. Seism. Soc. Am.*, 84 (3), 668-691, 1994.
- Wald, D.J., U.S. Geological Survey variable-slip, finite-fault source model repository, <http://www-socal.wr.usgs.gov/slipmodels.html>, 1996.
- Williams, S., Y. Bock, and P. Feng, Integrated satellite interferometry: Tropospheric noise, GPS estimates and implications for interferometric synthetic aperture radar products, *J. Geophys. Res.*, 103 (B11), 27,051-27,067, 1998.

Zachariasen, J. and K. Sieh, The transfer of slip between two en echelon strike-slip faults: A case study from the 1992 Landers earthquake, southern California, *J. Geophys. Res.*, 100 (B8), 15,281-15,301, 1995.

Zebker, H.A., P.A. Rosen, R.M. Goldstein, A. Gabriel, and C.L. Werner, On the derivation of coseismic displacement fields using differential radar interferometry: The Landers earthquake, *J. Geophys. Res.*, 99 (B10), 19,617-19,643, 1994.

Chapter 5

Postseismic Deformation Following the June 28, 1992 Landers, California, Earthquake

5.1. INTRODUCTION

The Landers earthquake occurred on June 28, 1992 in California's Mojave Desert. Summary descriptions of the rupture and the regional tectonics can be found in Chapters 3 and 4 of this dissertation. During the months after the earthquake, the Earth's lithosphere in the Mojave Desert region continued to deform at a rate that was higher than the long-term strain rate which had been measured geodetically by *Sauber et al.*, [1986] and inferred geologically by *Dokka and Travis*, [1990]. Total postseismic displacements measured at GPS stations were 10-20% of the measured coseismic displacements with 90% of the postseismic displacement occurring within the first six months after the Landers mainshock [*Bock et al.*, 1997].

A goal of studying postseismic deformation is to identify the mechanisms by which the Earth's lithosphere deforms following a major earthquake in order to gain insight into its rheology and the processes involved in the earthquake cycle. Various workers have proposed a number of postseismic deformation mechanisms to describe the spatial and temporal characteristics of geodetic data collected after the Landers earthquake. These mechanisms include deep afterslip [*Shen et al.*, 1994; *Savage and Svarc*, 1997; *Bock et al.*, 1997], viscoelastic relaxation [*Deng et al.*, 1998], poroelastic relaxation [*Peltzer et al.*, 1996], hydrothermal deformation [*Wyatt et al.*, 1994], re-equilibration of fluids in a highly fractured stratum [*Wyatt et al.*, 1994], crustal

anelasticity [Wyatt *et al.*, 1994], and fault zone collapse [Massonnet *et al.*, 1996; Savage and Svarc, 1997].

In this study, radar line-of-sight (LOS) displacement maps (interferograms) formed using images spanning 5-215 days, 40-355 days, and 355-1253 days after the earthquake (Figure 5.1) are inverted for the amount of right-lateral slip on planes approximating the rupture and its deep extension between 4 and 30 km of depth. Because displacements of the Earth's surface measured using GPS geodesy indicate postseismic displacements at GPS stations in the same direction as the coseismic displacements [Shen *et al.*, 1994; Savage and Svarc, 1997; Bock *et al.*, 1997], a significant portion of the postseismic deformation has been inferred to be slip on the rupture plane or its down-dip extension with the same sense as the coseismic slip. The models derived from inverting interferograms indicate that slip occurred within a zone 7.5-10 km deep causing an 80 km-wide displacement pattern that decayed remarkably within 40 days of the earthquake. This inference of shallow slip agrees qualitatively with the conclusions of Shen *et al.*, [1994] who invert for slip on both shallow (0-10 km depth range) and deep (10-30 km depth range) patches finding that slip on the shallow patches is significant, and those of Massonnet *et al.*, [1996] whose best-fitting model describing a pattern of postseismic deformation on the northern part of the rupture indicates right-lateral slip in the 6-11 km depth range.

Attempting to measure postseismic deformation using InSAR pushes the method to its limits [Massonnet *et al.*, 1994]. The amplitude of the postseismic displacement signal is much smaller than the amplitude of the coseismic displacement signal and is of the magnitude of possible atmospheric delay. Hence, a visual interpretation of the

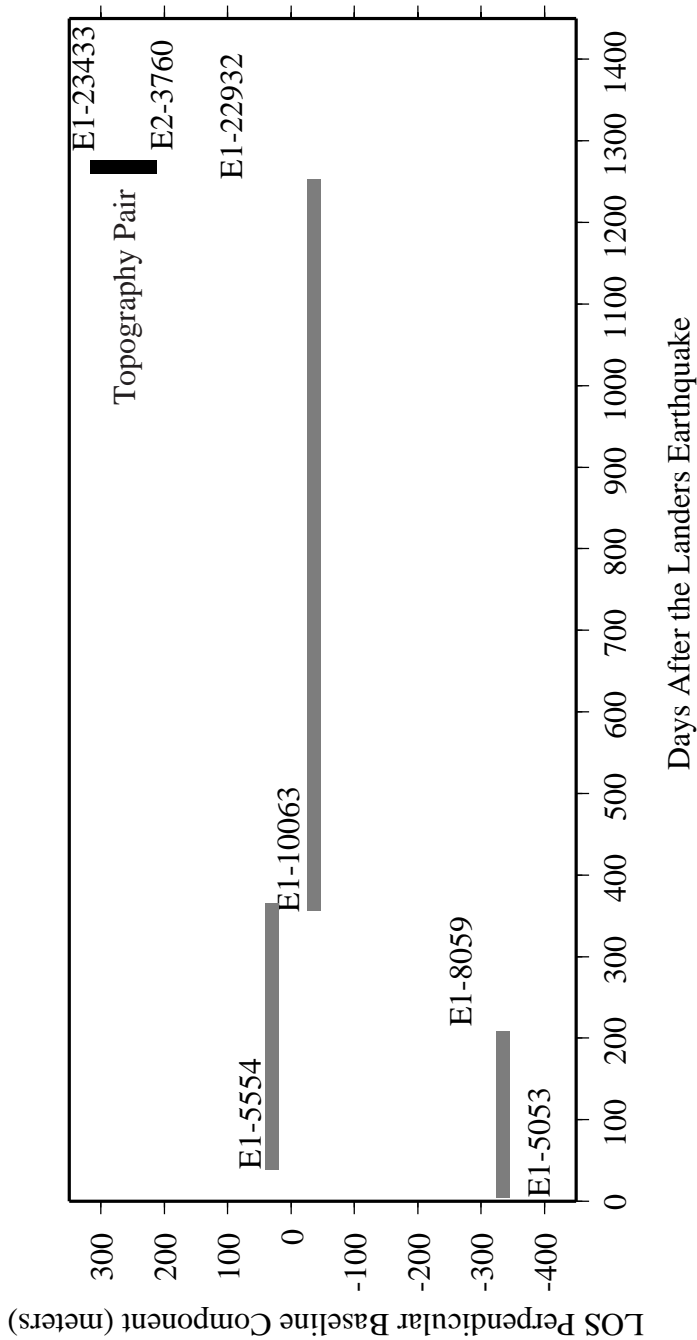


Figure 5.1. The SAR imagery used in this study from ERS frame 2907. The orbit numbers of the frames are plotted at their respective times in days after the Landers Earthquake and relative components of the interferometer baseline perpendicular to the satellite LOS. Displacement maps are formed for the three time intervals spanned by the grey bars. The topographic range change was removed from the interferograms using the ERS-1 orbit 23433_ ERS-2 orbit 3760 pair.

interferometric signal becomes important. Variations in the interferograms near pre-existing structures and the continuity of the displacement patterns can be used as discriminative criteria. Furthermore, inverting the interferometric displacement maps using an afterslip models and comparing them with the model predictions can help us gain insight into possible distributions of afterslip.

5.2. POSTSEISMIC DEFORMATION MECHANISMS

Although there are many possible mechanisms of postseismic deformation, three of the most accepted are deep afterslip, viscoelastic relaxation, and poroelastic relaxation (Figure 5.2). During an earthquake, the shallow part of the Earth's crust breaks between depths of 0 and 15 km. The resulting strains cause time-dependant deformation of the crust around the rupture. Deep afterslip and viscoelastic relaxation are proposed to occur in the lower crust between base of the earthquake rupture and the top of the moho (between 15 and 28 km in the Mojave desert). The major difference between the two mechanisms is that deep afterslip is localized while viscoelastic relaxation is a bulk deformation process. Poroelastic relaxation occurs in the upper crust.

5.2.1. DEEP AFTERSLIP

The fact that there was a significant horizontal component of displacement measured at far-field GPS stations following the Landers earthquake indicates that deep afterslip was a significant postseismic deformation mechanism [*Shen et al.*, 1994; *Savage and Svarc*, 1997; *Bock et al.*, 1997]. However, models of postseismic deformation due to deep afterslip indicate motion towards the satellite in a region to the west of the rupture

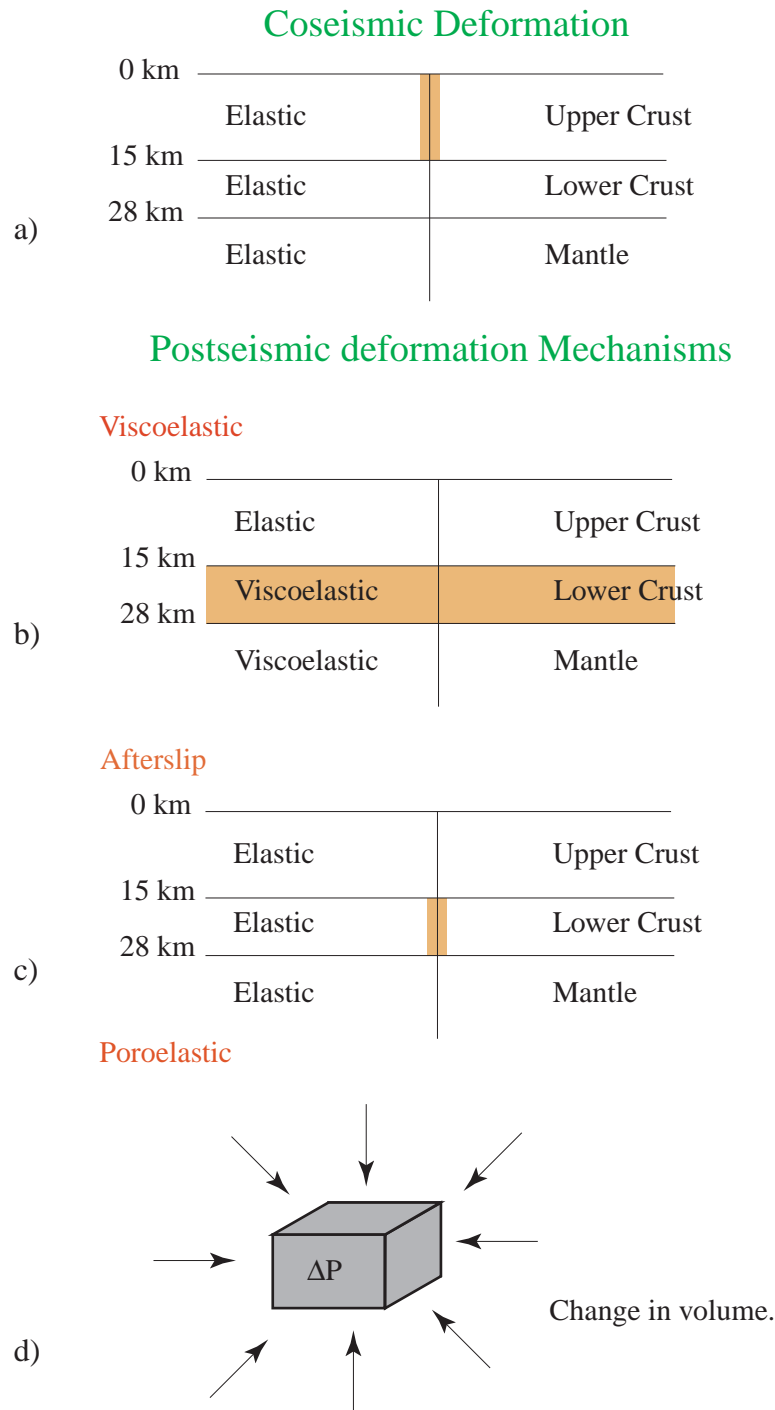


Figure 5.2. The postseismic deformation mechanisms. a) Coseismic slip occurs in the upper crust. b) Viscoelastic relaxation occurs throughout the lower crust. c) Deep afterslip is localized on the down-dip extension of the rupture. d) Pore pressure gradients induced by the earthquake cause water to flow into and out of extensional and compressional areas along the rupture.

which is not present in any of the interferograms [*Peltzer et al.*, 1998]. A combination of deep afterslip and a change in Poisson's ratio of the crust, due to pore fluid flow, in the region surrounding the earthquake can reconcile InSAR observations with deep afterslip theory [*Peltzer et al.*, 1998]. However, the decay time of the afterslip signal inferred from the 5-215 and 40-355 day interferograms by this study, about 40 days, is too short to be due to poroelastic deformation which has a decay constant of 270 ± 45 days.

5.2.2. VISCOELASTIC REBOUND

A viscoelastic mechanism may be used to model the postseismic deformation [*Deng et al.*, 1998]. Assuming that 0.7 meters of east-side down dip-slip coseismic motion occurred on the Emerson and Camp Rock faults, *Deng et al.* argue that a viscoelastic mechanism is the only one that can predict the fault-normal and vertical motions measured by *Savage and Svarc*, [1997] along a linear GPS array normal to the rupture south of the stepover between the Emerson and Camp Rock faults (the locations of the GPS sites surveyed by *Savage and Svarc* are shown in Figure 5.3a). They also argue that certain features observed in the "combined" postseismic interferogram presented by *Massonnet et al.*, [1996] indicate viscous flow of the lower crust. These features are a linear ridge of towards the satellite motion to the east of the rupture and an oval-shaped region of subsidence to the west of the rupture (e.g. Figure 5.3b). However, the interferometric signal that they model, assumed to be due to vertical displacement only, is a combination of two interferograms spanning 5-1008 and 40-355 days after the earthquake. Therefore the deformation signal D in the combined interferogram is $D = D(5-40 \text{ days}) + 2 \cdot D(40-355 \text{ days}) + D(355-1008 \text{ days})$. Thus the deformation between

7/3/92-1/29/93 (5-215 days post-Landers)

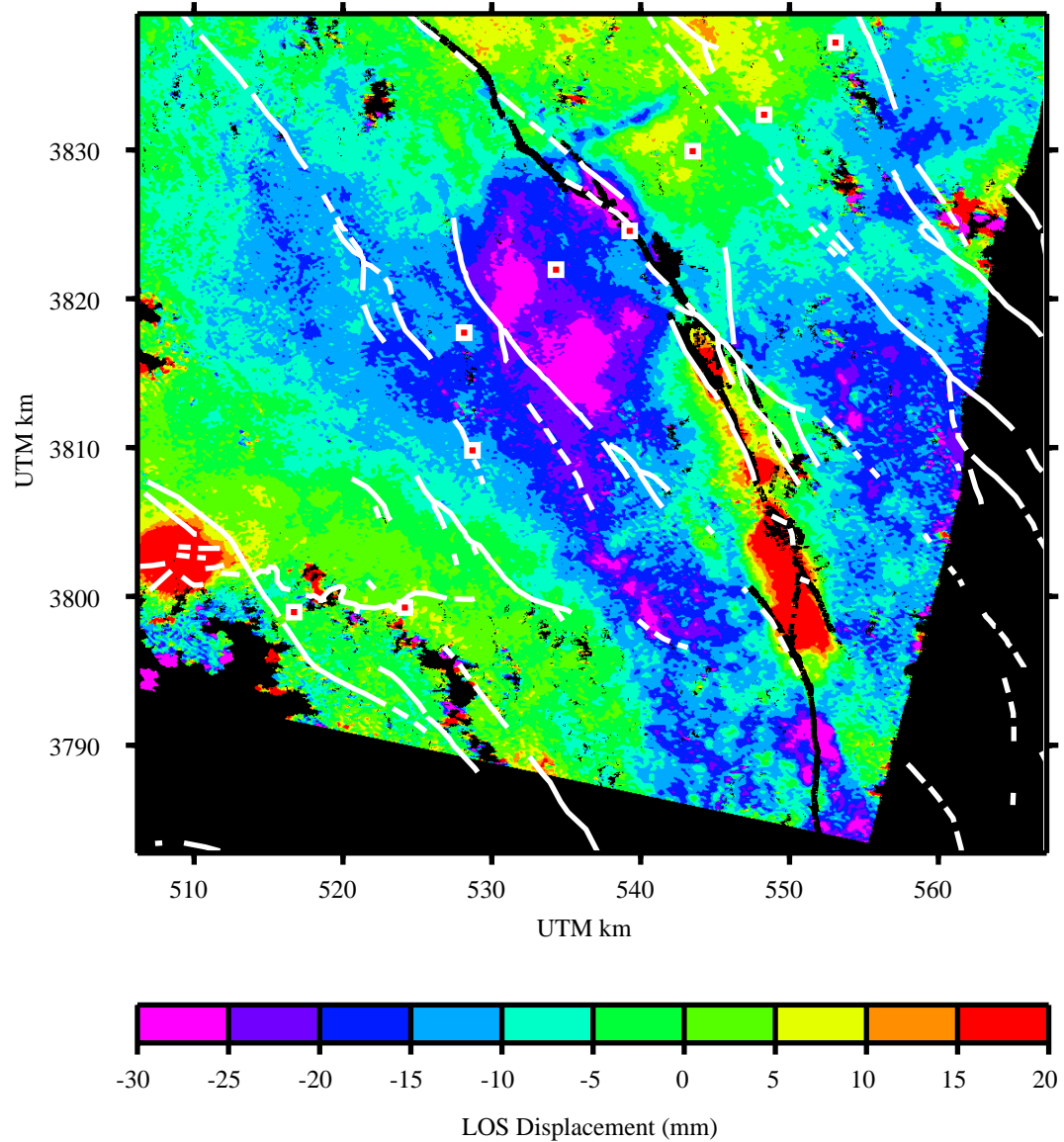


Figure 5.3a. The 5-215 day interferogram. The black lines indicate the rupture trace. The white lines are faults mapped previously to the Landers earthquake. The red squares are GPS sites surveyed by *Savage and Svarc*, [1997].

8/7/92-6/18/93 (40-355 days post-Landers)

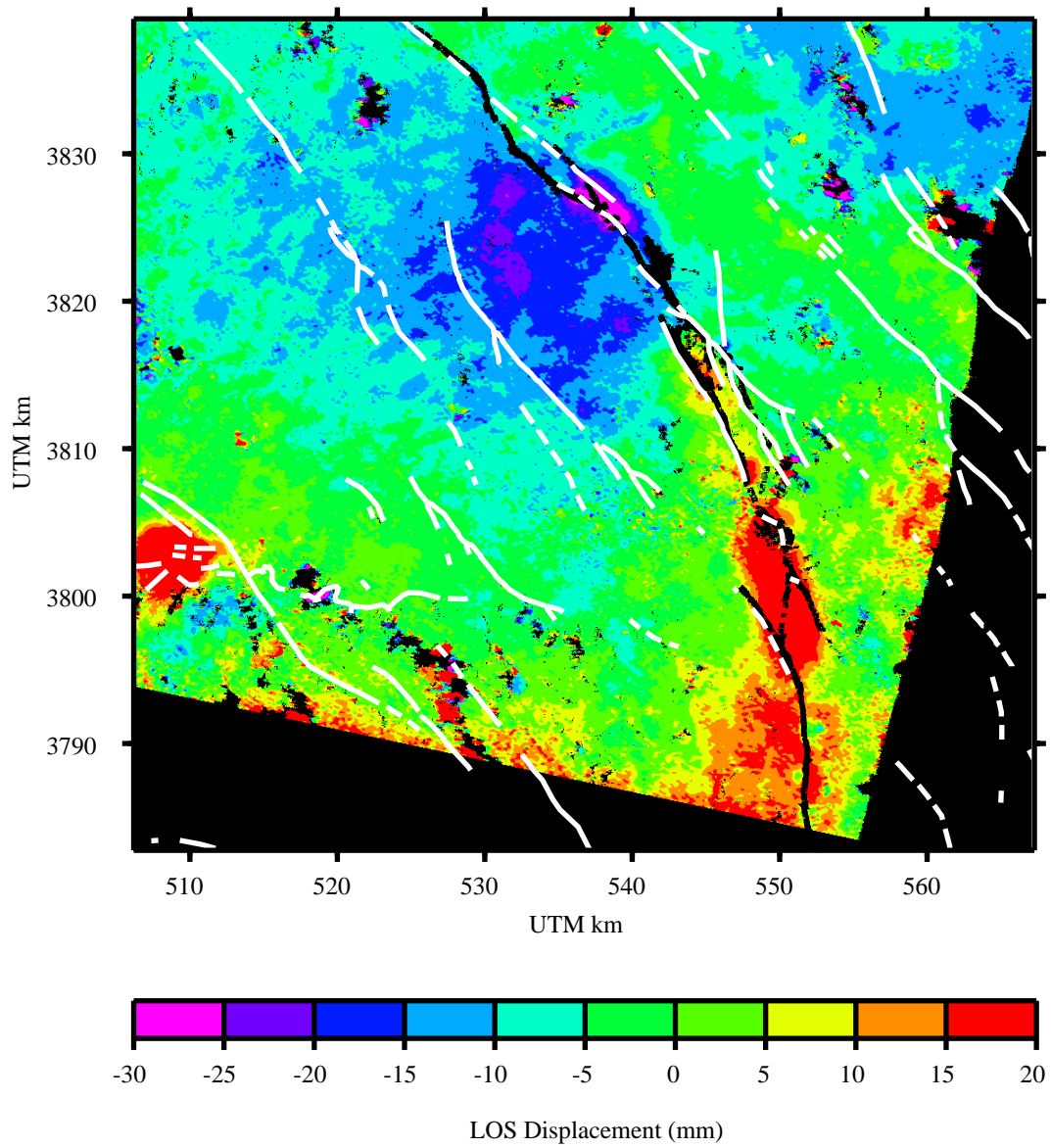


Figure 5.3b. The 40-355 day interferogram.

days 40 and 355 is weighted twice as much as the deformation in the other time periods. The long-wavelength signal measured after day 40 may be viscoelastic but the signal in the 5-215 day interferogram does not simply show the qualities described above that indicate viscoelastic deformation. For example, east of the rupture, there is uplift to the north of the stepover between the Homestead Valley and Emerson faults and subsidence to the south (Figure 5.3a) rather than a continuous "ridge" of uplift.

5.2.3. FAULT ZONE COLLAPSE

A mechanism for postseismic deformation first proposed by *Savage et al.*, [1994] is fault zone collapse [*Massonnet et al.*, 1996; *Savage and Svarc*, 1997]. This mechanism is described by displacement normal to the rupture plane due to closing of cracks opened during the earthquake in a fluid saturated rupture zone. This mechanism is proposed by *Massonnet et al.*, [1996] to explain a variation in style of postseismic deformation in their combined interferogram: On the portion of the rupture north of the stepover between the Homestead Valley and Emerson faults, the interferogram indicates dextral slip while on the southern portion of the rupture, the interferometric signal can be modeled using fault-normal displacement. Such a mechanism could also account for the apparent strengthening of the fault zone following the earthquake suggested by *Li et al.*, [1998] to explain an increase in seismic velocity with time measured by repeated seismic surveys after the earthquake.

5.2.4. PORE FLUID PRESSURE RE-EQUILIBRATION

Pore fluid pressure re-equilibration after an earthquake can cause poroelastic deformation due to increased pressure gradients near extensional and compressional rupture fault stepovers, coseismic hydraulic fracturing, and hydrothermal mechanisms. In the first case, pore fluid flow due to pressure gradients in fault stepovers arising from rapid coseismic deformations can cause deformation on a spatial scale of about 10 km with a time constant due to exponential rate of decay of 270 ± 45 days [Peltzer *et al.*, 1996; Peltzer *et al.*, 1998]. Coseismic hydraulic fracturing is proposed by Wyatt *et al.*, [1994] to explain the discrepancy between strains measured at the laser strain meters and the borehole tensor strain meter at the Piñon Flat Observatory (PFO). This coseismic fracturing could be caused by the pumping of fluids in an already highly fractured stratum such as is present at the PFO. The surface deformation measured in this case should have a time constant of a few days. A final possible pore fluid mechanism is a hydrothermal one described by an expansion of rocks after contact with warming fluids from below. The strain due to this effect would be quite small [Wyatt *et al.*, 1994] and undetectable with anything but the most accurate of geodetic instruments (such as the laser strain meters at the PFO). This last mechanism is unlikely to account for any of the Landers earthquake postseismic deformations measured.

5.3. DATA PROCESSING AND REDUCTION

The approach to processing the data in this study is similar to that outlined in Chapter 3, Appendix A and Chapter 4 of this dissertation. The SAR imagery (Table 5.1)

was collected during the ERS-1 orbital phase C and the ERS-1/ERS-2 tandem mission and is located in ERS track 399 and frame 2907.

First, an estimate of the topographic contribution to the phase was made using an interferogram formed from images collected during the ERS-1/ERS-2 tandem mission (Figure 5.1). Then, this topographic phase is subtracted from interferograms spanning 5-215, 40-355, and 355-1253 days after the earthquake. Since 5 pairs of images from the ERS-1/ERS-2 tandem mission were available (Table 5.1), the utility of stacking them to form an estimate of topographic phase was investigated. Stacking interferograms can reduce atmospheric and orbital errors [*Sandwell and Price*, 1998]. However, it was found that one of the interferograms had significantly less atmospheric noise than the other four and that stacking only increased atmospheric phase anomalies. Hence, only one was used to estimate the topographic phase. Combination of a large number of images should improve the recovery of the topographic phase if the noise can be averaged out [*Sandwell*, 1998].

Table 5.1. InSAR pairs considered in this study from ERS track 399, frame 2907

Reference		Repeat	
Satellite: Orbit	Acquisition Date	Satellite: Orbit	Acquisition Date
ERS1: 5053	Jul. 3, 1992	ERS1: 8059	Jan. 29, 1993
ERS1: 5554	Aug. 7, 1992	ERS1: 10063	Apr. 24, 1992
ERS1: 10063	Apr. 24, 1992	ERS1: 22932	Dec. 3, 1995
ERS1: 21930	Sep. 24, 1995	ERS2: 2257	Sep. 25, 1995
ERS1: 22431	Oct. 29, 1995	ERS2: 2758	Oct. 30, 1995
ERS1: 22932	Dec. 3, 1995	ERS2: 3259	Dec. 4, 1995
ERS1: 23433	Jan. 7, 1996	ERS2: 3760	Jan. 8, 1996
ERS1: 25437	May 26, 1996	ERS2: 5764	May 27, 1996

After removing the topographic phase, we scaled the result by the radar's wavelength to convert phase radians to millimeters. An attempt to calibrate InSAR LOS displacements with published GPS derived displacements [*Savage and Svarc, 1997*] failed since the published GPS displacements were measured relative to site Sanh which is near the rupture and hence should have a significant postseismic displacement of its own. Offsetting the LOS projected GPS horizontal displacements so that they are relative to CGPS site Gold, far from the rupture, would increase their values by 25 mm while offsetting them relative to Pin1, on the other side of the San Andreas fault from the rupture, would increase their values by 34 mm. Without reprocessing the GPS data, it is difficult to ascertain what the absolute displacement should be. Instead of using GPS displacements, the InSAR LOS displacements were calibrated iteratively by first adding a constant to each displacement map and then inverting it using a least-squares scheme to find the smallest misfit as a function of the added constant (similar to the way the vertical interferogram was calibrated in Chapter 4 of this dissertation). The calibrated interferograms are shown in Figures 5.3a, 5.3b, and 5.3c.

After forming the full resolution interferogram displacement maps (60 m pixel spacing), the two-dimensional data were filtered and down-sampled to a 970 meter resolution ($63 \times 58 = 3654$ pixels) to enable their subsequent inversion. The down-sampled data retained both the long-wavelength elastic (or viscoelastic) signal and much of the short-wavelength signal near the rupture due to faulting complexity, poroelastic deformation, or fault-zone collapse.

6/18/93-12/3/95 (355-1253 days post-Landers)

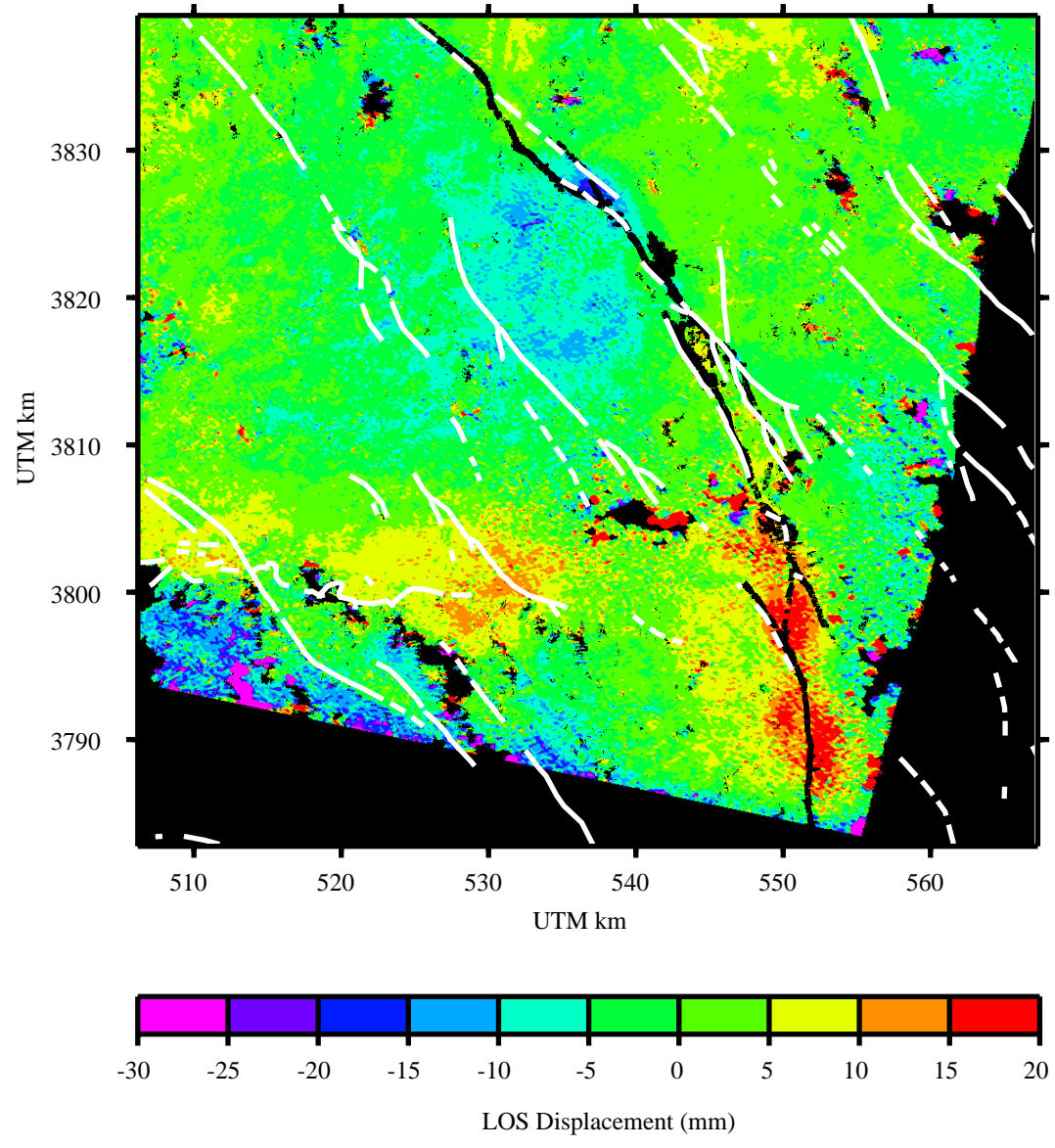


Figure 5.3c. The 355-1253 day interferogram.

5.4. MODELING METHOD

Linear least-squares inversions of the interferograms were performed in an attempt to determine whether afterslip in an elastic half-space was a viable mechanism for postseismic deformation, and, if so, to then determine the depth distribution and time duration of the afterslip. The same formulation as described in Chapter 4 of this dissertation, Eqn. 4.4, was used: the sum of the squares of the differences between the model predictions and the InSAR displacement data was minimized. A multitude of different model parameterizations was studied and the one shown in Figure 5.4 gave the best results. This parameterization is a down-dip extension of a trace along the rupture beginning near the southern terminus of the Johnson Valley fault north of the Pinto Mountain fault and following the trace of the rupture on its easternmost side. It is interesting to note that the coseismic slip measured in the field was concentrated on the Homestead Valley fault while the preferable model parameterization follows portions of the Emerson fault, parallel to the Homestead Valley fault, that ruptured only slightly during the earthquake.

The Green's functions relating a unit slip on each model patch to LOS displacements at the Earth's surface (Eqn. 4.4, matrix **A**) were computed by placing a unit slip on each model patch and solving for the displacement at the surface of an elastic half-space using the RNGCHN software [*Feigl and Dupre, 1999*]. A minimal amount of model smoothing was imposed using a Laplacian roughening filter (Eqn 4.4, matrix **L**). The data values were assumed to be independently and identically distributed with a variance of 1 cm estimated from data histograms (Figure 5.7a) and hence the covariance matrix (Eqn. 4.4, matrix **C**) was assumed to be diagonal.

Model Segments

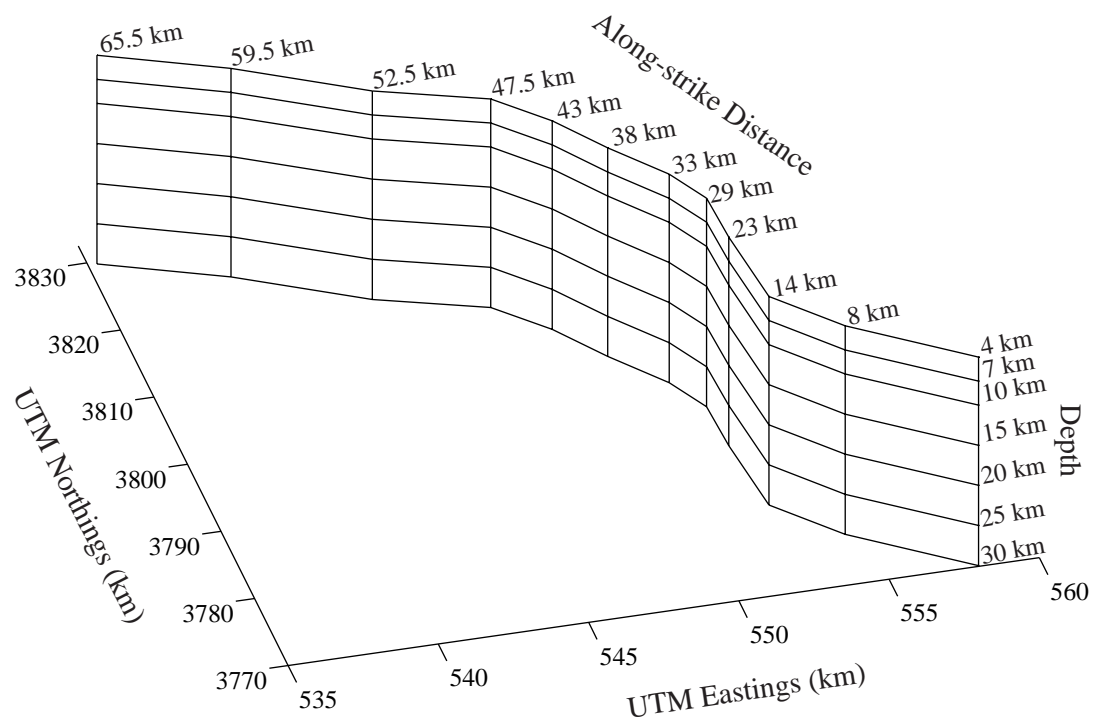


Figure 5.4. The model parameterization.

5.5. RESULTS

5.5.1. INTERFEROMETRIC OBSERVATIONS

The portions of the unwrapped interferograms that were inverted are shown in Figure 5.3. The displacement maps surround the rupture trace. Figure 5.3a is the displacement map spanning 5 to 215 days after the earthquake, Figure 5.3b is the displacement map spanning 40 to 355 days after the earthquake, and Figure 5.3c is the displacement map spanning 355 to 1253 days after the earthquake. An interesting feature in both the day 5-215 and day 40-355 day displacement maps is the round region of uplift near the location (UTM coordinate 510, 3802) of a magnitude 5.4 aftershock that occurred on December 4, 1992 and was subsequently inverted for the aftershock's focal mechanism by *Feigl et al.*, [1995]. Other interesting features in the displacement maps are discontinuities associated with major faults. For example, in the day 5-215 displacement map there appears to be some offset on the Calico fault and deformation on the Iron Ridge fault is clear.

The first striking features of the day 5-215 interferogram are the towards-the-satellite motion associated with extensional steps in the rupture and the away from the satellite motion near compressional stepovers. The ridge-like feature extending from the Kickapoo stepover to the northern stepover between the Homestead Valley and Emerson faults indicates uplift in a coseismic extensional region. The away-from-the-satellite motions near the stepover between the Emerson and the Camp Rock faults and the north-trending fault splay just south of the intersection of the GPS array and the rupture indicate subsidence in near-rupture coseismic compressional regions. The position of these regions of displacement near the rupture indicates that they do indeed represent

movements of the ground and are not due to atmospheric delay. These are the deformations attributed to pore-fluid flow by *Peltzer et al.*, [1998].

The second striking feature of the day 5-215 interferogram is the butterfly-shaped region of away-from-the-satellite motion that extends throughout the displacement map. This displacement pattern is here inferred to be due to shallow slip on the rupture plane with a distribution as shown in Figure 5.5a. A second deformation interferogram (not shown here) formed from images collected on July 3, 1992 and December 25, 1992 (day 5-180) shows this same pattern. Because of its low amplitude, it may represent an atmospheric signal in the July 3, 1992 image. However, it is more likely to represent the long-wavelength signal due to dextral afterslip on the rupture plane as suggested by GPS displacement data. A third striking feature of this interferogram is the region of away from the satellite motion in the Upper Johnson Valley. It is interesting to note that the higher amplitude portions of this signal follow fractures mapped by *Price and Sandwell*, [1998].

The day 40-355 interferogram indicates that the towards-and away-from-the-satellite motion in the Kickapoo stepover and the stepover between the Emerson and Camp Rock faults, respectively, still have high amplitudes 40 days after the earthquake. Away from the satellite motion in the Upper Johnson Valley is still apparent as well but the amplitude is much reduced. The butterfly-shaped deformation pattern is no longer apparent. This interferogram shows the displacement pattern indicative of viscoelastic deformation as described by *Deng et al.*, [1998]: namely, a slight ridge of relative uplift to the east of the rupture and an oval-shaped region of away from the satellite displacement west of the rupture.

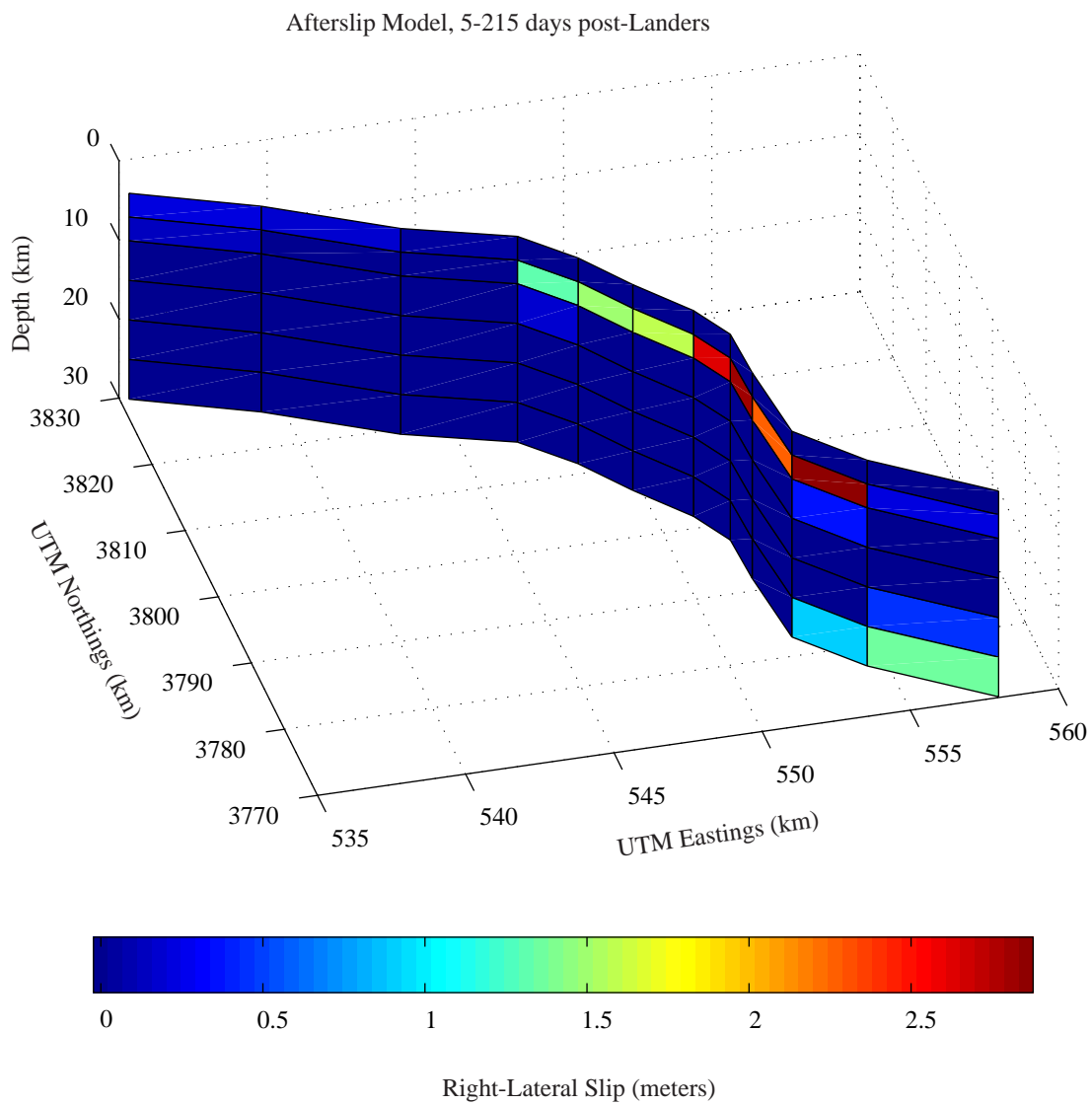


Figure 5.5a. The 5-215 day afterslip model.

The day 355-1253 interferogram indicates virtually no deformation far from the rupture. However, uplift surrounding the Kickapoo stepover and the Johnson Valley fault south of the stepover is still apparent. Also, there is still some away from the satellite motion in the Upper Johnson Valley but it is less than 15 mm in the LOS direction.

5.5.2. MODELING RESULTS

5.5.2.1. SLIP MODELS

The slip models corresponding to the displacement maps are shown in Figure 5.5a, Figure 5.5b, and Figure 5.5c. The slipping surface is split up into 66 patches extending from 4 km of depth to 30 km of depth (Figure 5.4). The two shallow-most layers are 3 km thick while the deeper layers are each 5 km thick. This change in thickness with depth is consistent with resolution analysis of geodetic inverse models that commonly show decreased resolution with depth (e.g. Chapter 4, section 7.4).

The model corresponding to the day 5-215 interferogram indicates that afterslip was concentrated within the layer between 7.5 and 10 km of depth. As much as 3 meters of afterslip may have occurred on the Johnson Valley fault near its intersection with the Kickapoo stepover. Slip is inferred to have been approximately 2.5 meters on the Kickapoo stepover and decreased to the north. No afterslip is inferred on the rupture surface north of the northern stepover between the Homestead Valley and Emerson faults during this time period.

The model corresponding to the day 40-355 interferogram indicates 1 meter of slip on the Kickapoo and Emerson faults increasing to a little more than 1.5 meters south of the northern stepover between the Homestead Valley and Emerson faults. The model

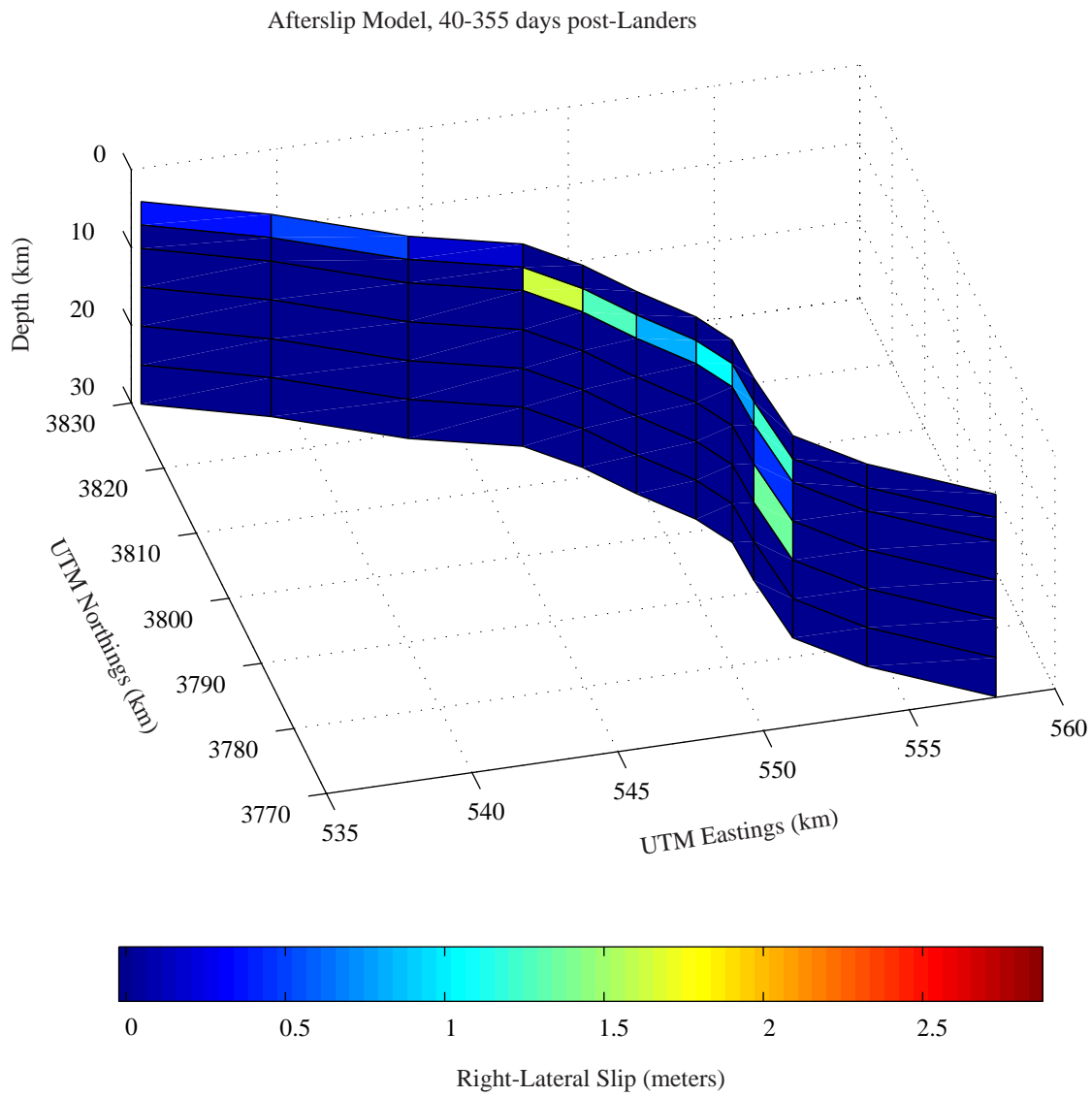


Figure 5.5b. The 40-355 day afterslip model.

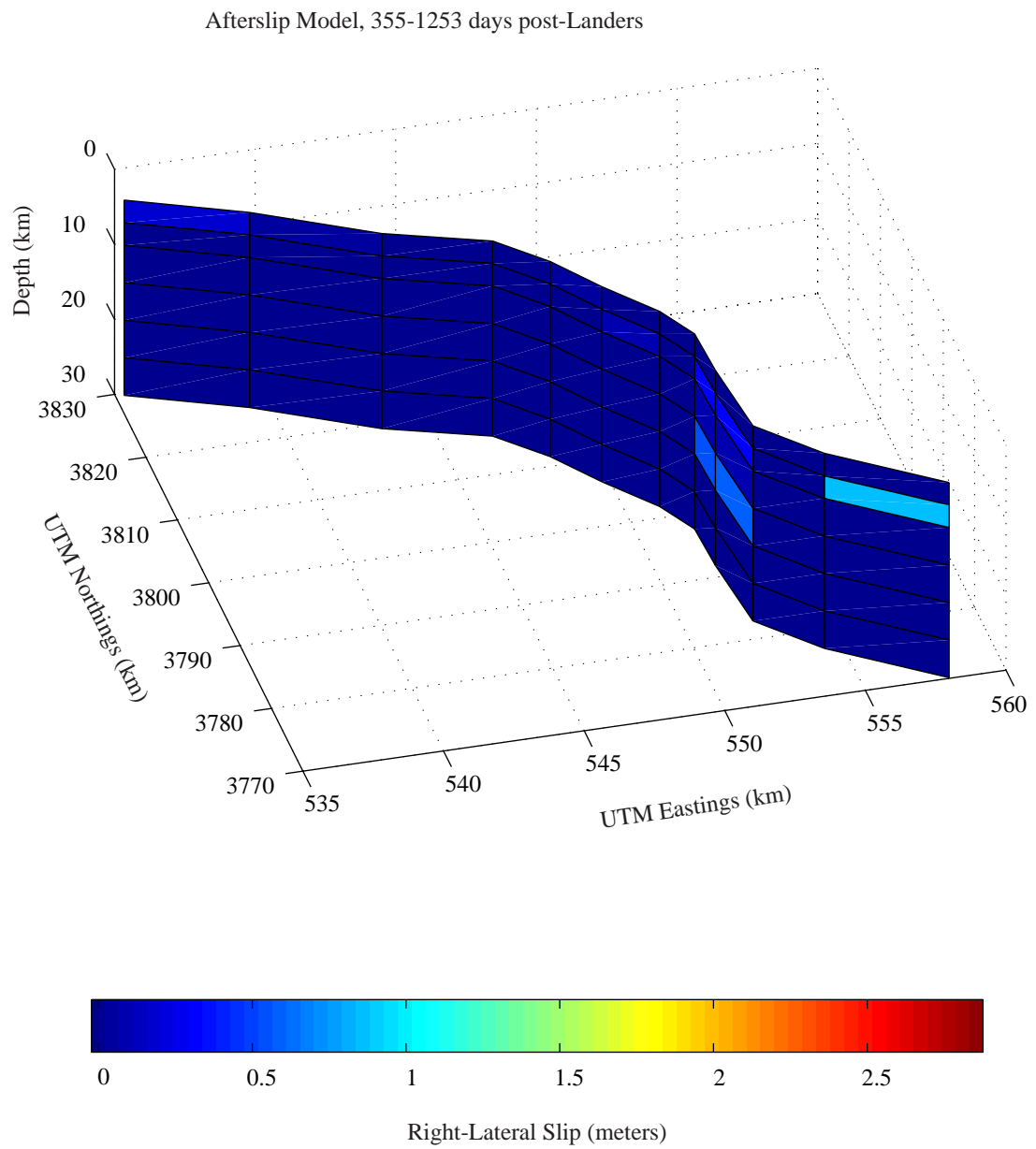


Figure 5.5c. The 355-1253 day afterslip model.

corresponding to day 355-1253 interferogram indicates very little slip on the rupture. The nearly one meter of slip on the southern Johnson Valley fault results in displacement at the surface that is believed to be atmospheric noise (the region of apparent subsidence to the northeast of the Kickapoo stepover). This model, which should produce virtually no slip, is indicative of the level of error in the model slips: approximately 1 meter.

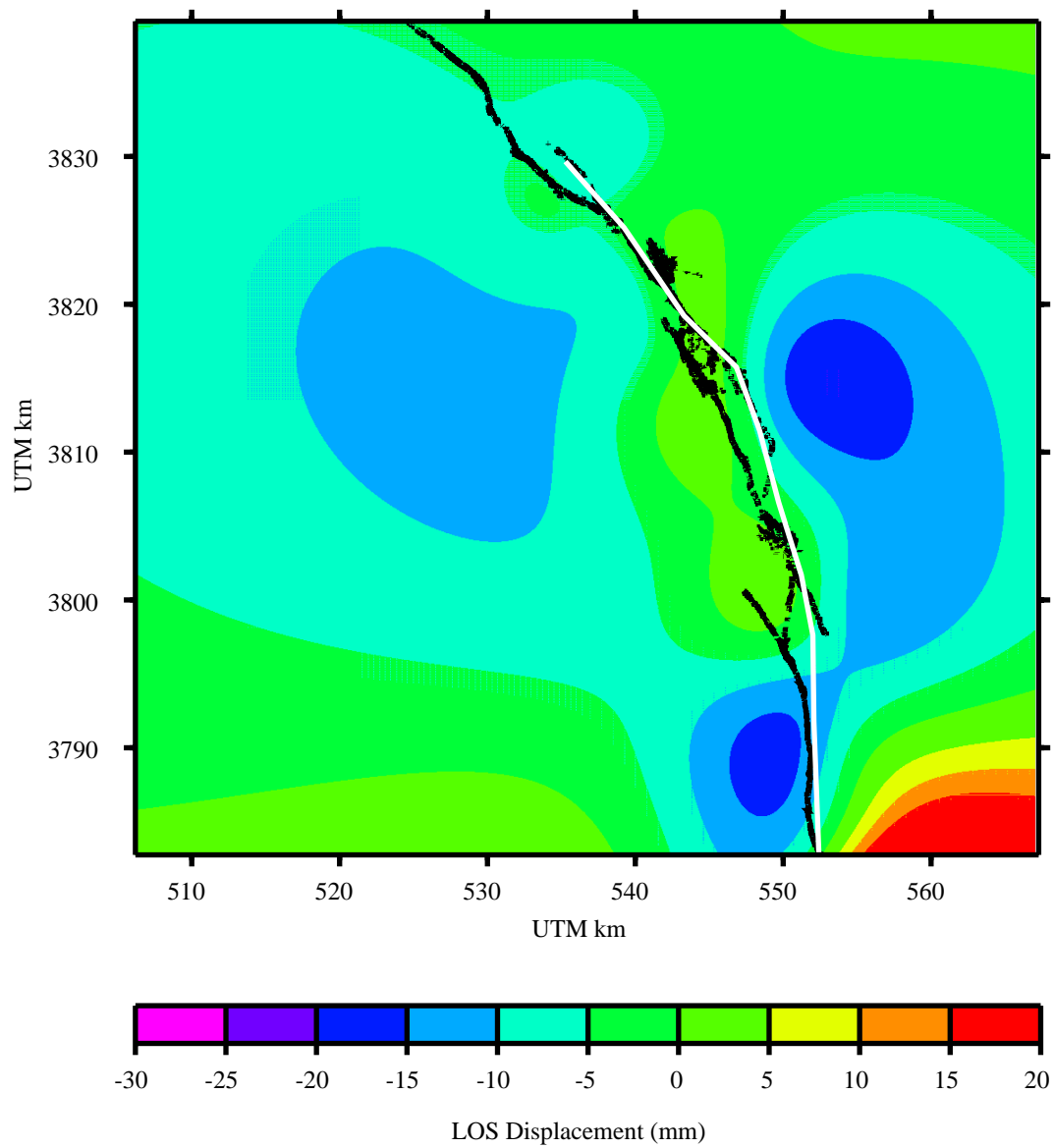
5.5.2.2. FORWARD PREDICTIONS

The predictions of the model corresponding to the day 5-215 interferogram (Figure 5.6a) indicate subsidence on both sides of the fault and minimal uplift near the along-strike locations of uplift thought to be due to pore-fluid flow. The predictions of the model corresponding to the day 40-355 interferogram (Figure 5.6b) indicate subsidence to the northwest of the rupture corresponding to the subsidence in the Upper Johnson Valley. The predictions of the model corresponding to the day 355-1253 interferogram (Figure 5.6c) indicate very little surface displacement: the largest signal is associated with atmospheric noise to the east of the Kickapoo stepover.

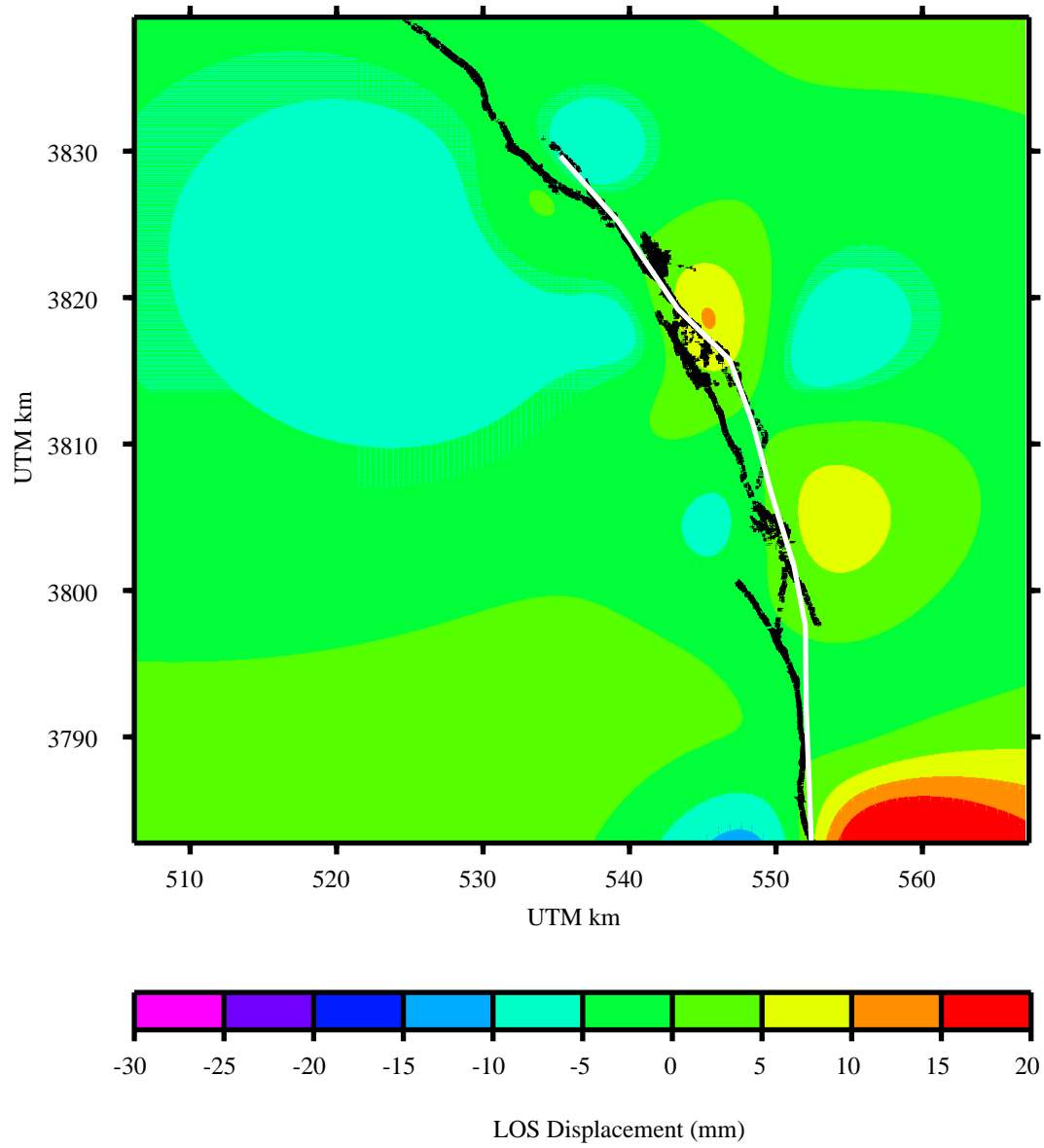
5.5.2.3. VARIANCE REDUCTION

Histograms of the LOS displacement values (Figure 5.7a) indicate that the modal displacement tends towards zero as time goes on. This trend can not be due to the temporal sampling frequency since the time duration spanned by the successive interferograms increases (210 days, 315 days, 898 days). The variance of the distributions is one centimeter for the first two interferograms and 6 millimeters for the last interferogram. Histograms of the residuals (Figure 5.7b) computed by subtracting the

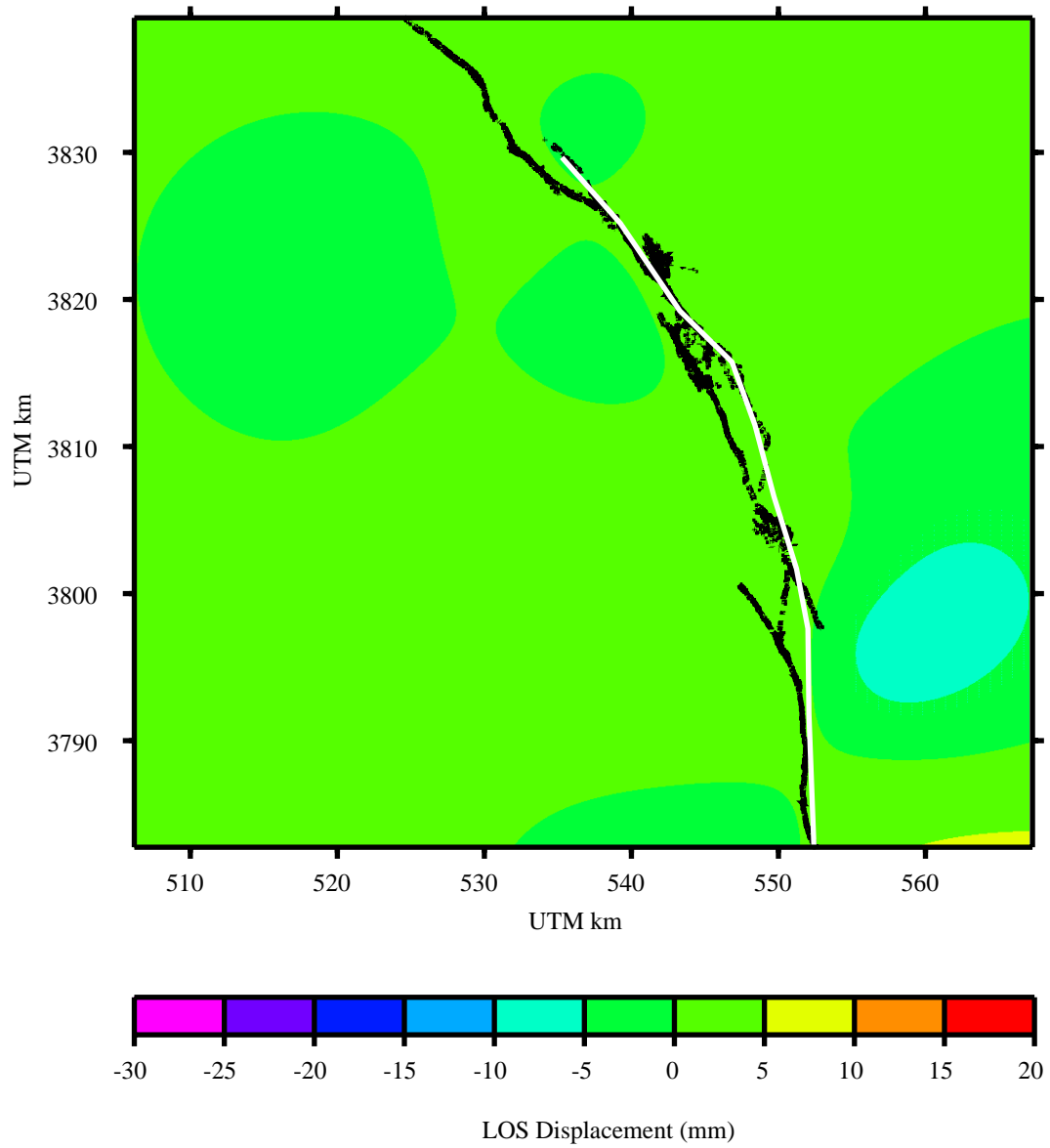
Modeled LOS Displacement, 5-215 days post-Landers

**Figure 5.6a.** The 5-215 day model predictions.

Modeled LOS Displacement, 40-355 days post-Landers

**Figure 5.6b.** The 40-355 day model predictions.

Modeled LOS Displacement, 355-1253 days post-Landers

**Figure 5.6c.** The 355-1253 day model predictions.

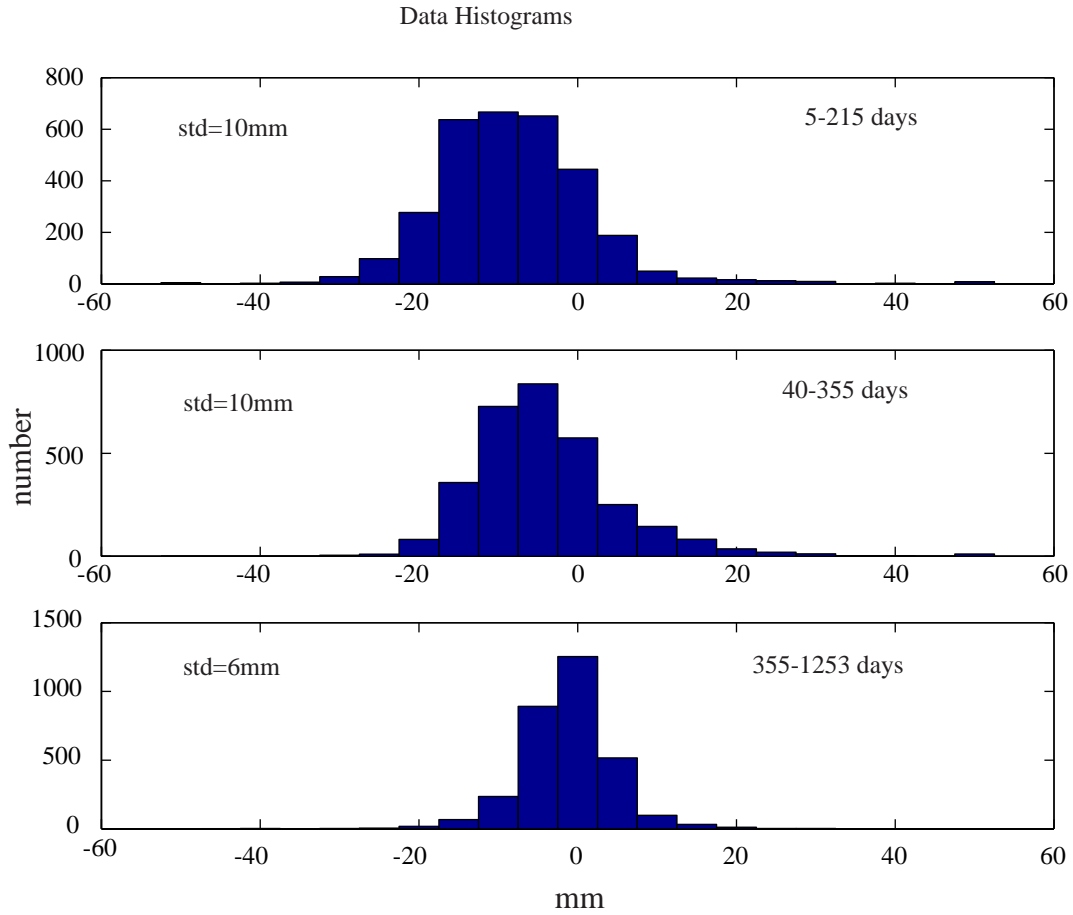


Figure 5.7a. Data histograms. As time goes on, the mean LOS displacement approaches zero.

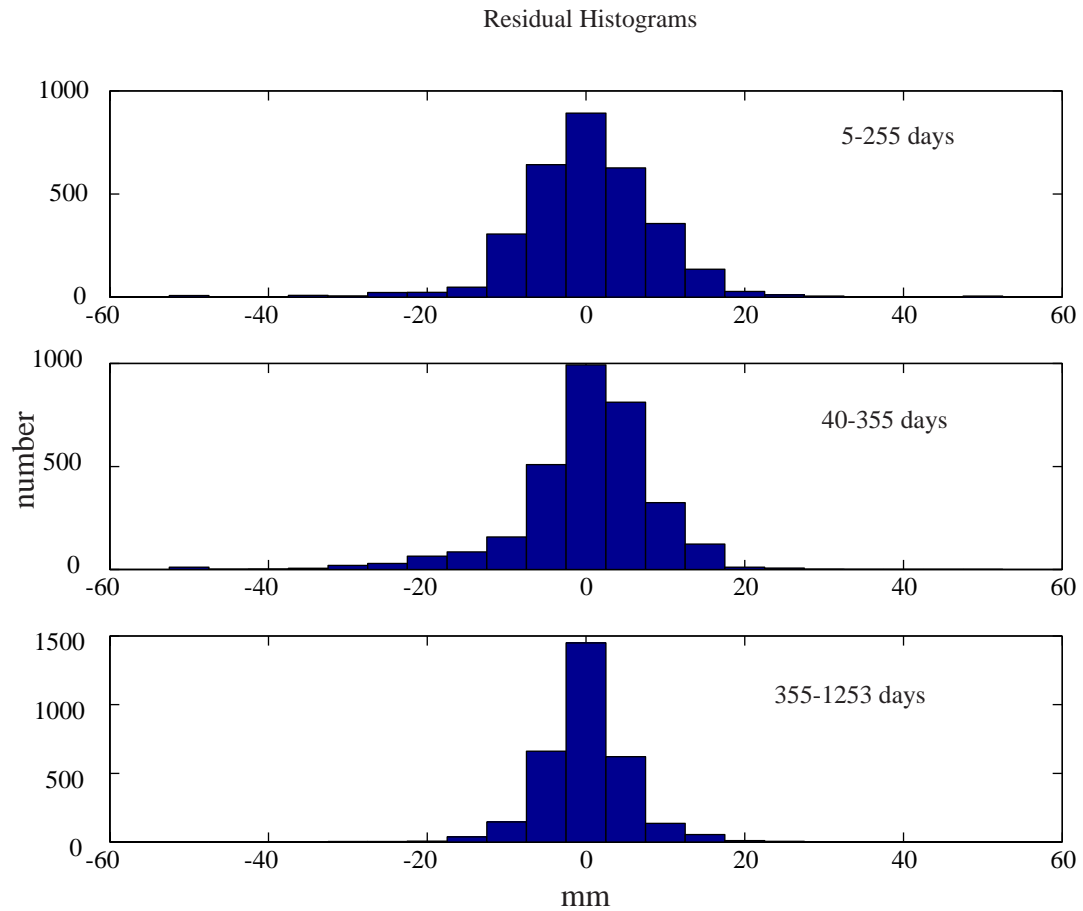


Figure 5.7b. Model residual histograms. The mean residual is zero but the standard deviation has not decreased. If our errors were Gaussian distributed (which they aren't) with standard deviation 10 mm, their χ^2 value gives 99% confidence in the models. Note that the errors in InSAR measurements are in large part due to changes in the atmosphere which has a power-law structure function.

model predictions from the data indicate that the modeling moved the centers of the distributions to zero but did not reduce the variance about the mean. This is illustrative of the fact that the InSAR method is being pushed to its typical artifact level.

5.5.2.4. MOMENT ANALYSIS

Model moments were computed using Eqn. 4.5. The moment computed for the day 5-215 model is 8.2×10^{18} N-m. The moment computed for the day 40-355 model is 4×10^{18} N-m. The moment computed for the day 355-1253 model is 1.3×10^{18} N-m. The moment of each model is within an order of magnitude of the moment estimated from the aftershocks that occurred within 6 months of the earthquake which is 2×10^{18} N-m [Shen *et al.*, 1994]. The moment estimated from the InSAR inversions is clearly larger than the moment estimated from aftershocks. This indicates a significant aseismic release of strain in 7.5-10 km depth layer.

5.6 DISCUSSION

5.6.1. COMPARISON OF LOS DISPLACEMENTS WITH GPS HORIZONTAL DISPLACEMENTS

Measured LOS displacements and model predicted displacements extracted from each deformation interferogram along a profile connecting GPS sites are shown above the LOS projected horizontal GPS displacements published by *Savage and Svarc*, [1997] in Figure 5.8. The amplitude of the LOS displacement signal along the profile extracted from the 5-215 day interferogram is 2 cm, the amplitude of the LOS displacement signal along the profile extracted from the 40-355 day interferogram is 1.3 cm, and the

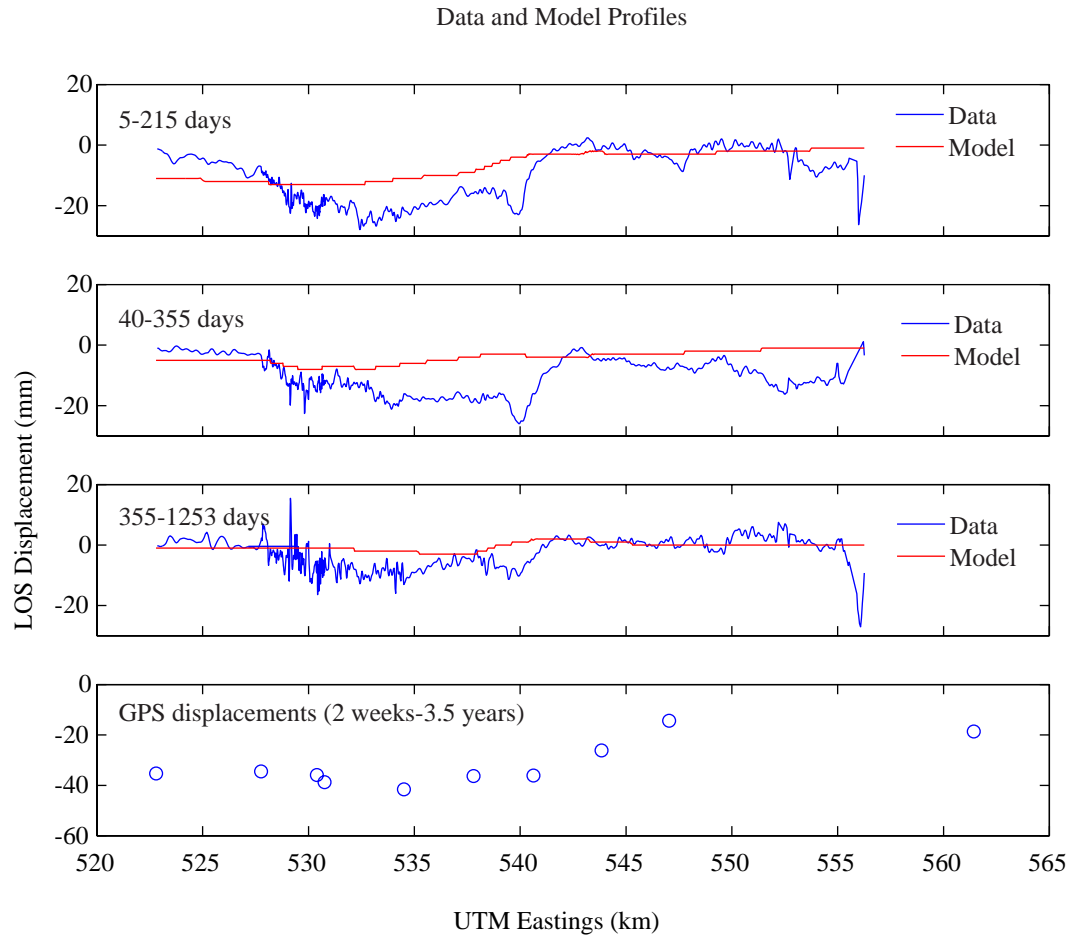


Figure 5.8. Data and model profiles along USGS geodetic array (see Figure 6a for geodetic marker locations). The plotted GPS displacements are the horizontal components projected into the radar LOS. The magnitudes of the projected horizontal displacements along the profile are comparable to the relative magnitudes of the InSAR displacements indicating that they are significant in the InSAR data.

amplitude of the LOS displacement signal extracted from the 355-1253 day interferogram is 0.95 cm. The amplitude of the LOS displacement signal due to horizontal motions as indicated by the GPS displacements measured over a period of 2 weeks to 3.5 years after the earthquake is approximately 2.5 cm. If we use an 84-day time constant and exponential decay of the amplitude, 84% of the deformation should have occurred between days 14 and 1277, 86% of the deformation should have occurred between days 5 and 215, 60% of the deformation should have occurred between days 40 and 355 and 1% of the deformation should have occurred between days 355 and 1253. Because the amplitude of the signal in the day 5-215 interferogram is similar, within a standard deviation, to the amplitude of the LOS-projected horizontal signal, a significant component of the signal in the interferogram must be due to horizontal motions.

If the postseismic displacement amplitude followed an exponential rate of decay with a time constant equal to 84 days (e.g. *Savage and Svarc*, [1997]), the ratio of displacement amplitudes in the consecutive interferograms should be 1.43:1:0.02. If the time constant was 270 days, the ratio of amplitudes in the consecutive interferograms should be 0.89:1:0.44. The amplitude ratios are 1.54:1:0.73. The ratio between the amplitudes extracted from the day 5-215 and day 40-355 interferograms agrees well with the 84-day time constant. However, the ratio between the amplitudes extracted from the day 40-355 and day 355-1253 interferograms agrees well with the 273 day time constant. This last comparison is not entirely conclusive since the signal in the day 355-1253 interferogram is below the level of the expected error. However, the analysis indicates that relaxation with an 80-day time constant was the dominant mechanism contributing to

the signal in the first two interferograms while relaxation with a 273-day time constant was the dominant mechanism contributing to the signal in the last two interferograms.

5.6.2. POSTSEISMIC DEFORMATION MECHANISMS

The four possible mechanisms for postseismic deformation that could cause significant displacements near the rupture measurable by InSAR are poroelastic [*Peltzer et al.*, 1998], viscoelastic [*Deng et al.*, 1998], afterslip [*Shen et al.*, 1994; *Savage and Svarc*, 1997], and fault zone collapse or strengthening [*Massonnet et al.*, 1996; *Li et al.*, 1998]. The decay of the amplitude of deformation due to each of these mechanisms and the wavelength of the expected displacement pattern is different. For instance, if the deformation mechanism is assumed to be aseismic afterslip on the main rupture surface, a long-wavelength postseismic signal that has 10-20% of the magnitude of the coseismic signal with a decay constant of about 46 days is expected; if the deformation mechanism is poroelastic (decay constant on the order of 9 months) or shallow slip on secondary structures, small-scale deformation patterns are expected.

The three interferograms analyzed in this study indicate that a variety of postseismic deformation mechanisms may contribute to the displacement signal. The non-existence of the signal inferred here to be due to afterslip within the seismogenic zone in the interferograms spanning 40-355 and 355-1253 days after the earthquake indicates that the time duration of this phenomenon was less than 40 days. The displacement signal due to apparent viscoelastic rebound is strong in the 40-355 day interferogram but is not obvious in the others. The displacement signal due to near-

rupture poroelastic deformation or fault-zone collapse is clear in the day 5-215 and day 40-355 interferograms.

This analysis indicates that afterslip in the seismogenic zone was a significant contributor to the surface displacement field within 40 days after the earthquake. Viscoelastic deformation as a response to the large load imposed by an earthquake of Landers' magnitude is likely to have occurred during the entire postseismic period. Also, since the near-fault short-wavelength LOS displacement signals are apparent in each interferogram, poroelastic and fault-zone collapse deformation mechanisms are important contributors.

The likely importance of all these deformation mechanisms suggests a systems analysis of the postseismic deformation phenomena. However, before such thing can be done, the behavior of models describing each mechanism must be studied. The viscoelastic code of *Deng et al.*, [1998] is a significant step in this direction. However, it is difficult to ascertain the time duration of the viscoelastic signal attributed to deformation observed in an interferogram that is a combination of two interferograms spanning overlapping time periods. The conceptual poroelastic model of *Peltzer et al.*, [1998] makes sense but a more detailed analysis of its application to long-wavelength deformation signals which are combined with possible viscoelastic, afterslip, or fault-zone collapse signals ought to be performed.

5.7. CONCLUSIONS

A butterfly-shaped deformation pattern in an interferogram formed from images collected 5 and 215 days after the Landers earthquake is due to afterslip on the faults that

ruptured during the earthquake between 7.5 and 10 km of depth. Inverting three interferograms spanning time periods after the earthquake pushes the method to its typical error level: the deformation signal is nearly the same size as possible atmospheric delay errors. In spite of this, consistently similar deformation patterns observed in consecutive interferograms indicate a multitude of postseismic deformation. The contribution of each of these phenomena to the observed displacement pattern can be inferred from the wavelength, pattern, and temporal decay of the displacement amplitudes. While a decay constant for viscoelastic deformation is not available in the literature, a comparison of InSAR measurements to decay constants expected from afterslip (creep) and poroelastic mechanisms indicates that the substantial contribution of each of these mechanisms to the deformation signal was different in consecutive interferograms.

5.8. REFERENCES

- Bock, Y., S. Wdowinski, P. Fang, J. Zhang, S. Williams, H. Johnson, J. Behr, J. Genrich, J. Dean, M. van Domselaar, D. C. Agnew, F. K. Wyatt, K. Stark, B. Oral, K.W. Hudnut, R. W. King, T. A. Herring, S. J. Dinardo, W. Young, D. D. Jackson, W. Gurtner, Southern California permanent GPS geodetic array; continuous measurements of regional crustal deformation between the 1992 Landers and 1994 Northridge earthquakes, *J. Geophys. Res.*, *102*, (B8), 18,013-18,033, 1997.
- Deng, J., M. Gurnis, H. Kanamori, and E. Hauksson, Viscoelastic flow in the lower crust after the 1992 Landers, California, earthquake, *Science*, *282*, 1689-1692, 1998.
- Dokka, R. K. and C. J. Travis, Role of the eastern California shear zone in accommodating Pacific-North American plate motion, *Geophys. Res. Lett.*, *17*, 1323-1326, 1990.
- Feigl, K. L., A. Sargent, and D. Jacq, Estimation of an earthquake focal mechanism from a satellite radar interferogram: Application to the December 4, 1992 Landers aftershock, *Geophys. Res. Lett.*, *22*, 1037-1040, 1995.
- Feigl, K. L., and E. Dupre, RNGCHN: a program to calculate displacement components from dislocations in an elastic half-space with applications for modeling geodetic measurements of crustal deformation, *Comput. Geosci.*, *25* (6), 695-704, 1999.
- Li, Y., J. E. Vidale, K. Aki, F. Xu, and T. Burdette, Evidence of shallow fault zone strengthening after the 1992 *M*7.5 Landers, California, earthquake, *Science*, *279*, 217-219, 1998.
- Massonnet, D., K. Fiegl, M. Rossi, and F. Adragna, Radar interferometric mapping of deformation in the year after the Landers earthquake, *Nature*, *369*, 227-230, 1994.
- Massonnet, D., W. Thatcher, and H. Vadon, Detection of postseismic fault-zone collapse following the Landers earthquake, *Nature*, *382*, 612-616, 1996.
- Peltzer, G., P. Rosen, F. Rogez, and K. Hudnut, Postseismic rebound in fault step-overs caused by pore fluid flow, *Science*, *273*, 1202-1204, 1996.
- Sandwell, D. T., and E. J. Price, Phase gradient approach to stacking interferograms, *J. Geophys. Res.*, *103*, 30,183-30,204, 1998.
- Sandwell, D. T., Can interseismic strain be recovered from ERS SAR interferometry?, *Eos Trans. AGU*, *79* (45), Fall Meet. Suppl., F36, 1998.
- Sauber, J., W. Thatcher, and S.C. Solomon, Geodetic Measurement of Deformation in the Central Mojave Desert, California, *J. Geophys. Res.*, *91*, 12,683-12,693, 1986.

- Savage, J.C., M. Lisowski, and J.L. Svarc, Postseismic deformation following the 1989 ($M = 7.1$) Loma Prieta, California, earthquake, *J. Geophys. Res.*, *99*, 13,757-13,765.
- Savage, J.C., and J.L. Svarc, Postseismic deformation associated with the 1992 $M_w = 7.3$ Landers earthquake, Southern California, *J. Geophys. Res.*, *102*, 7565-7577, 1997.
- Scholz, C.H., *The Mechanics of Earthquakes and Faulting*, Cambridge University Press, Cambridge, 1990.
- Shen, Z.K., D.D. Jackson, Y. Feng, M. Cline, M. Kim, P. Fang, and Y. Bock, Postseismic deformation following the Landers earthquake, California, 28 June 1992, *Bull. Seism. Soc. Am.*, *84*, 780-791, 1994.
- Wdowinski, S., Y. Bock, J. Zhang, P. Fang, and J. Genrich, Southern California Permanent GPS Geodetic Array; spatial filtering of daily positions for estimating coseismic and postseismic displacements induced by the 1992 Landers earthquake, *J. Geophys. Res.*, *102*, 18,057-18,070, 1997.
- Wyatt, F.K., D.C. Agnew, and M. Gladwin, Continuous measurements of crustal deformation for the 1992 Landers earthquake sequence, *Bull. Seism. Soc. Am.*, *84*, 768-780, 1994.

Chapter 6

Conclusions

In this dissertation InSAR is used to map crustal deformations associated with the 1992 Landers, California earthquake. The technical approach is described in Chapter 2 and the appendices of Chapter 3. Applications are discussed in Chapters 3,4, and 5. While the Landers earthquake has been widely studied using a variety of geophysical tools, we push the limits of the InSAR method to examine small-scale deformations as well as vertical and postseismic displacements.

6.1. CONCLUSIONS TO CHAPTER 3

The gradient of the interferometric phase can be computed directly from the real and imaginary parts of the complex interferogram and is not subject to phase unwrapping errors. Using the phase gradient method, we were able to map the locations of secondary fractures and triggered slip on major faults due to the Landers earthquake. Some of these observations are new. For instance, other workers had not noticed the fractures we mapped in the Upper Johnson Valley. If the senses of offset on the secondary fractures can be interpreted, they can be used to infer the directions of maximum strain at the Earth's surface induced by the earthquake.

6.2. CONCLUSIONS TO CHAPTER 4

We inferred the distribution of vertical slip on the rupture using a combination of InSAR measurements and finite-fault elastic half-space modeling. It is possible that there was 0.7 meters of dip-slip on the end of the Landers earthquake rupture but the locking depth was approximately 7.5 ± 1 km. There are two east-side up-down pairs of vertical slip associated with the two main earthquake strike-slip events. A map of vertical displacements was used to interpret the fractures mapped in Chapter 3. This map of vertical displacements is difficult to obtain with any method other than InSAR. For example, the error in the vertical component of GPS displacement measurements is often larger than the vertical displacement measurement itself.

6.3. CONCLUSIONS TO CHAPTER 5

A butterfly-shaped long-wavelength displacement pattern in the interferogram spanning 5-215 days after the Landers earthquake may be due to after-slip in the 7.5-10 km depth range. This pattern decays quickly within the first 40 days after the earthquake. The effects of a viscoelastic rebound mechanism may dominate the displacement pattern in the 40-355 day interferogram. A number of deformation mechanisms most likely contribute to the postseismic surface displacement signal including afterslip, pore-fluid re-equilibration, and viscoelastic rebound.